Université de Lille 1 SCIENCES ET TECHNOLOGIES

NEUTRONS FOR SCIENCE

Numéro d'ordre : 42553

École doctorale n° 104 : Science de la Matière, du Rayonnement et de l'Environnement

A thesis submitted in fulfilment of the requirements for the degree of

DOCTOR IN PHYSICS AND MATERIALS SCIENCE

given by

Université de Lille 1

defended by

Frédéric NGONO MEBENGA

the 18th December 2017

Investigations from experiments and simulations of amorphous forms of lactulose obtained by different routes

Jury

M. R. LEFORT,	Maître de Conférences, U. de Rennes 1	Rapporteur
M. M. MICOULAUT,	Professeur, UPMC (Paris)	Rapporteur
Mme C. ALBA-SIMIONESCO,	DR CNRS, LLB (Paris)	Examinateur
Mme V. DUPRAY,	Maître de Conférences, U. de Rouen	Examinateur
M. F. AFFOUARD,	Professeur, U. de Lille 1	Directeur de thèse
M. J-F. WILLART,	DR CNRS, U. de Lille 1	Co-directeur de thèse
M. G. CUELLO,	Docteur, ILL (Grenoble)	Encadrant
Mme. M. JIMENEZ-RUIZ,	Docteur, ILL (Grenoble)	Co-encadrant

UFR de Physique
Unité Matériaux Et Transformations (UMET)
UMR CNRS 8207, 59650 Villeneuve d'Ascq, France

Université de Lille 1 SCIENCES ET TECHNOLOGIES

NEUTRONS FOR SCIENCE

Numéro d'ordre : 42553

École doctorale n° 104 : Science de la Matière, du Rayonnement et de l'Environnement

Thèse soumise en vue de l'obtention du grade de

DOCTEUR EN PHYSIQUE ET SCIENCES DES MATÉRIAUX

donné par

Université de Lille 1

soutenue par

Frédéric NGONO MEBENGA

le 18 Décembre 2017

Etudes expérimentales et numériques de formes amorphes de lactulose obtenues par différentes voies

Jury

M. R. LEFORT,	Maître de Conférences, U. de Rennes 1	Rapporteur
M. M. MICOULAUT,	Professeur, UPMC (Paris)	Rapporteur
Mme C. ALBA-SIMIONESCO,	DR CNRS, LLB (Paris)	Examinateur
Mme V. DUPRAY,	Maître de Conférences, U. de Rouen	Examinateur
M. F. AFFOUARD,	Professeur, U. de Lille 1	Directeur de thèse
M. J-F. WILLART,	DR CNRS, U. de Lille 1	Co-directeur de thèse
M. G. CUELLO,	Docteur, ILL (Grenoble)	Encadrant
Mme. M. JIMENEZ-RUIZ,	Docteur, ILL (Grenoble)	Co-encadrant

UFR de Physique
Unité Matériaux Et Transformations (UMET)
UMR CNRS 8207, 59650 Villeneuve d'Ascq, France

This PhD thesis has been carried out between Université de Lille 1 and Institut Laue-Langevin (Grenoble).
It has given rise to 3 oral communications (one national and two international) and two posters. The articles are being written.

Declaration of Authorship

I, Frédéric Ngono Mebenga, declare that this thesis titled, 'Investigations from experiments and simulations of amorphous forms of lactulose obtained by different routes' and the work presented in it are my own. I confirm that:

- This work was done wholly or mainly while in candidature for a research degree at this University.
- Where any part of this thesis has previously been submitted for a degree or any other qualification at this University or any other institution, this has been clearly stated.
- Where I have consulted the published work of others, this is always clearly attributed.
- Where I have quoted from the work of others, the source is always given. With the exception of such quotations, this thesis is entirely my own work.
- I have acknowledged all main sources of help.
- Where the thesis is based on work done by myself jointly with others, I have made clear exactly what was done by others and what I have contributed myself.

Signed :

Date :

Contents

Dedicace

À mes parents, MEBENGA NGONO Alphonse et MEWALI Marie-Odette.

Remerciements

"*If I have seen further than others, it is only because I was standing on the shoulders of Giants.*"

Isaac Newton

Un travail de thèse ne peut être accompli sans l'aide d'autres scientifiques, la complicité de ses amis et le soutien de sa famille. Les lignes suivantes rendent hommage à plusieurs personnes sans lesquelles ce travail n'aurait jamais abouti.

Je voudrais tout d'abord remercier le Seigneur Dieu pour la santé, la protection et l'intelligence qu'il m'a accordées depuis ma naissance jusqu'à ce jour.

Ce travail a été effectué au laboratoire UMET (Unité Matériaux et Transformations) de l'Université Lille 1, et dans le groupe diffraction de l'Institut Laue-Langevin (ILL). Je remercie le Professeur Alexandre Legris et le Professeur Helmut Schober, respectivement directeur de l'UMET et directeur scientifique de l'ILL au moment où je commençais ma thèse, pour m'avoir fait confiance et accepté dans leur groupe.

Je remercie vivement les membres du jury de ma thèse pour l'intérêt qu'ils ont porté à mon travail et pour leur disponibilité. Je tiens à remercier le Professeur Matthieu Micoulaut de l'Université Pierre et Marie Curie (Paris) et Monsieur Ronan Lefort, Maître de Conférences - HDR à l'Université de Rennes 1, qui ont accepté de juger ce travail et d'en être les rapporteurs scientifiques. Je remercie également Madame Christiane Alba-Simionesco, Directeur de Recherche CNRS et directeur du Laboratoire Léon Brillouin (Paris), et Madame Valérie Dupray, Maître de Conférences - HDR à l'Université de Rouen, pour avoir pris le temps de juger ce travail.

Je tiens à exprimer ma profonde reconnaissance à mes quatre superviseurs de thèse : Pr. Frédéric Affouard, DR-CNRS Jean-François Willart, Dr. Gabriel Cuello et Dr. Monica Jimenez-Ruiz. Vos compétences scientifiques variées et vos conseils d'experts m'ont été d'une grande aide dans l'accomplissement de ce travail. Vous avez été disponibles lorsqu'il fallait réorienter, améliorer et approfondir. Chacun de vous de par sa sympathie et ses encouragements m'a aidé à braver les difficultés auxquelles j'ai fait face durant ce travail de thèse. De nos multiples discussions scientifiques au laboratoire à nos échanges "extra scientifiques" devant une bière (le(s) concerné(s) se reconnaitra(ont)), je garderai toujours de vous l'image de fins pédagogues, dont le dévouement et l'habileté ont sans doute accru ma passion pour la recherche. Merci infiniment !

J'adresse mes remerciements à tous les permanents de l'équipe MMT de l'UMET pour leur bienveillance. Un remerciement spécial à Mme. Florence Danède, Ingénieur d'études, pour les expériences de diffraction des rayons X sur poudre et les expériences d'analyse thermogravimétrique.

Je remercie également le Dr. Nicolas Tabary et Mr. Marc Bria, Ingénieur de Recherche de l'Université Lille 1, pour leur précieuse aide dans la réalisation des expériences de NMR et l'interprétation des résultats obtenus.

Toutes les opérations d'atomisation et de lyophilisation effectuées dans ce travail ont été réalisées dans le groupe INSERM du Pr. Jurgen Siepmann (Université Lille 2). Un remerciement spécial au Dr. Mounira Hamoudi pour sa gentillesse et son aide dans la réalisation de ces expériences.

Une grande partie des résultats de ce travail est le fruit de multiples expériences de diffusion neutronique, et je voudrais ici saluer les principaux auteurs.

Je remercie tout d'abord les différents scientifiques, responsables de logiciels que j'ai utilisés, et responsables d'instruments sur lesquels j'ai mené des expériences, mais dont je n'ai présenté les résultats dans ce manuscrit, soit parce qu'ils n'étaient pas concluants, soit parce qu'il n'était pas possible de les insérer dans un chapitre sans en diminuer la cohérence : Dr. Peter Fouquet (IN13, ILL), Dr. Victoria Garcia Sakai (IRIS, ISIS), Dr. Giovanni Romanelli (VESUVIO, ISIS), Dr. Helen Playford (RMCProfile, ISIS). J'aurai beaucoup appris lors de nos échanges.

J'adresse également mes sincères remerciements au Dr. Anne Stunault (D3, ILL), Dr. Andrew Wildes (D7, ILL) et Dr. Jan Embs (FOCUS, PSI) pour leur gentillesse, et toutes les discussions que nous avons eues lors de la réalisation d'expériences sur leurs instruments, le traitement et l'analyse des données mesurées.

Je tiens aussi à exprimer ma gratitude au Dr. Miguel Gonzalez du CS groupe de l'ILL pour sa grande gentillesse, sa disponibilité, et pour toutes les discussions scientifiques - neutron vs simulation - que nous avons eues. Il a été presqu'aussi disponible qu'un directeur de thèse et j'aurai beaucoup appris avec lui. Merci du fond du coeur.

Finalement, un grand merci à tous les autres scientifiques et techniciens de l'ILL dont j'ai bénéficié du support, et que j'ai omis de mentionner ici.

Une grande partie de mon cursus académique s'est faite à l'université de Yaoundé 1 (UY1), et j'aimerais ici remercier mes enseignants, ceux-là qui m'ont donné mes premières bases de physicien.

Je commencerai tout d'abord par remercier le Pr. Jean-Marie Ndjaka pour la confiance dont il m'a fait preuve, et pour m'avoir brillamment initié dans le domaine de la recherche. Il est très certainement le véritable point de départ de ces trois années de recherche. Merci Professeur !

J'adresse également mes remerciements à tous les enseignants du département de Physique

de l'UY1 pour tous les enseignements reçus depuis mon entrée en 2009. Un merci particulier au Pr. Serge Zekeng et tous les autres enseignants du laboratoire de science des matériaux dont j'ai pu bénéficier de conseils.

J'aimerais aussi remercier tous mes amis à travers le monde, qui ont eu une influence directe ou indirecte sur ce travail.

Je vais débuter par mes camarades de lycée et mes camarades de fac dont j'ai toujours bénéficié des encouragements ! Même après de longs moments sans s'être vus, le souvenir de nos folies a souvent suffi à me redonner le morale pour avancer. Un merci spécial notamment à Gaelle, Gladice, Zanga, Heuteu, Brice, Ndzana, Francis, et tous les autres. Certains d'entre vous sont peu contents de mon "éloignement", mais c'était plus un manque de temps qu'autre chose. Votre estime à mes yeux est restée la même. Merci également à tous mes promotionnaires de Master pour tous les moments passés ensemble.

A tous mes amis et collègues, tant de l'UMET que de l'ILL : Elena, Tatiana, Joseph, Paulo, Schéhérazade, Sarah, Benjamin, Luisa [1], Lidia (my best friend, a model of loyalty, "crazy but not stupid"), Javier, Ana Carolina, Annalisia, Tatiana (the special one !), Thomas et les autres. Nous nous sommes soutenus lors des périodes de doute, nous avons cheminé ensemble. Que dire de ces vendredis et samedis soirs de boissons, rigolades et jeux. Sans vous cette thèse n'aurait pas été la même. Merci pour tous ces chaleureux moments !!!

Merci à tous les camerounais de l'ACI de Grenoble que j'ai pu côtoyer lors de diverses activités, et avec qui j'ai partagé de bons moments. Un remerciement particulier au président Simon Ngono dont j'ai bénéficié d'un soutien franc et constant en toute circonstance, durant ces mois passés à Grenoble. Merci également à Mme. Genet pour sa gentillesse et son accueil chaleureux lors de mon arrivée à Grenoble. Vous êtes une femme de valeurs !

Merci aux camerounais de Lille, aux membres du GECLI, pour leur agréable et joyeuse compagnie, entre autres mes jumelles Ingrid et Audrey, Stéphanie, Stéphane, Barbara, Noelle, Césaire, Billy, Atawa, Parfait, Dan, etc. Merci aussi aux footeux du samedi aprem avec qui j'ai souvent déstressé le WE après une semaine chargée, notamment Zeine, Christian, Claude, etc.

A ces aînés passés avant nous, et dont nous avons pu profiter de la lumière: Dr. Thierry Ottou, Dr. Achille Melingui et Dr. Emmanuel Mengue, merci !

Il y'a des personnes pour qui le mot "extraordinaire" est utilisé à bon escient ou juste pour flatter l'égo. Il y'a d'autres pour qui il est utilisé par défaut, parce qu'on ne trouve pas mieux. Je vais lister ici quatre personnes qui rentrent dans la dernière catégorie. Ils ont été présents au quotidien. La solution à mes problèmes, mes envies, les bonificateurs de mauvaises et bonnes périodes. Quoiqu'il arrivait, ils étaient là. Chacun d'eux sait au fond de lui à quel point il m'a été précieux. Gaelle Sando et Ingrid Eyango vous avez été mes plus belles découvertes, (Dr) Philemon Nogning et (Dr) Yvan Ngassa mes plus belles confirmations. Gue pin, Na som, ..., Me lapte !

Je finirai cette liste non exhaustive de remerciements par ma famille. Elle a toujours été

[1] La demoiselle qui loue mon bureau gratuitement.

mon moteur en toute circonstance.

Un merci à ceux de mes oncles et tantes, cousins et cousines, qui de près ou de loin m'ont soutenu chacun à leur manière.

A ces êtres exceptionnels avec qui je suis né et avec qui j'ai grandi : ma soeur Sandrine Avoa et mes frères, Fernand Essomba et Arnaud Atangana. Avec eux j'ai cheminé au quotidien, et j'ai toujours bénéficié de leur soutien et leur aide. Ensemble nous avons galéré, ensemble nous avons jubilé. Cette thèse, c'est notre réussite à tous. Merci ! Un merci spécial à mes fils Arthur, Sven, Alonzo pour les photos insolites et amusantes !

A ces deux êtres chers de qui je suis né et que je ne remercierai jamais assez. Ils m'ont inculqué les bonnes valeurs, notamment l'amour du travail bien fait et le sens des responsabilités. Ils m'ont toujours soutenu dans mes choix, et oeuvré pour que je réussisse à mes études. Sans eux, je ne serai jamais arrivé ici. Toute réussite associée à ce travail est plus leur mérite que le mien. Papa, maman, merci pour tout !

Même maladroitement, je n'aurai pu clore ce travail sans adresser ma profonde reconnaissance à la meilleure tante qui existe sur cette planète : tantine Marlyse ! J'aurais aimé rédiger une autre thèse pour te remercier comme tu le mérites, mais je n'ai pas assez de temps. Pour ta bonne humeur, tes coups de folies, ton incontestable gentillesse, ta disponibilité, ton affection dont tu as toujours fait preuve depuis ma naissance, et que tu as reproduit durant ces trois années de ma vie, merci du fond du coeur !

List of Figures

List of Tables

General Introduction

"*Les hommes d'habitude voient les choses telles qu'elles sont et disent « pourquoi ? »*
Je rêve de choses qui ne sont pas et je me demande « pourquoi pas ? »"

Georges Bernard Shaw

A General context

Most pharmaceutical active ingredients are currently formulated in the solid form. They are, for example, tablets, powders for inhalation or lyophilisates. These solids may be crystalline or amorphous [1]. The crystalline solids are characterised by a long-range periodic structural organisation of the molecules, a high cohesive energy and a low entropy. This gives them a very high physical stability. Conversely, in amorphous solids, molecules do not adopt any long-range order and are less cohesive. Their structure is in fact identical to that of liquids, although they have the rigidity of a solid. The amorphous form is inherently unstable physically. These differences between crystalline and amorphous forms have a strong effect on their physical properties such as, for example, their solubility, their dissolution rate, their stability [2–6] and their molecular mobility. The chemical stability [7–9] itself can also be affected by physical instability [5]. Awareness of the specificities of the amorphous state and its potential interests to improve the performance of pharmaceutical products is becoming increasingly evident [10]. The annual publications on this subject have, for example, been multiplied by ten during the last twenty years. From a practical point of view, amorphous materials have both advantages and disadvantages for the pharmaceutical formulation.

Disadvantages: Partial or total amorphisation of an active pharmaceutical ingredient can be induced unexpectedly by several processes frequently used in industrial manufacturing processes of tablets [4]. This is the case, for example, of milling, compression and drying. These amorphisations must be avoided because they decrease the physical and chemical stability of the materials, which does not guarantee their therapeutic efficacy during prolonged storage. Moreover, the kinetic of chemical modifications is generally the fastest in the amorphous state. In particular, the surface effects such as oxidations and hygroscopicity are amplified. In this case, it is extremely important to understand the amorphisation mechanisms associated with different industrial processes in order to better control and avoid them.

Advantages: The therapeutic efficacy of the pharmaceutical active ingredients is often better when they are formulated in the amorphous state [2, 7, 11, 12]. In particular, their

solubility in human body fluids is much higher than that of the corresponding crystalline forms. Consequently, amorphous forms are particularly attractive for improving the solubility of poorly water soluble pharmaceutical active ingredients [13], the number of which has increased exponentially in recent years. In practice, the use of the active principles in amorphous form requires improving their physical stability [14–17]. This is generally achieved by mixing them homogeneously with biocompatible polymers having a high glass transition temperature (T_g) [18]. This induces an anti-plasticisation of the active principle (increase of T_g), i.e. a reduction of the molecular mobility essential for recrystallisation. Amorphous excipients also have the property of preserving fragile biological molecules from the stresses undergone during the formulation stages. They are in particular used for the formulation of proteins [19] and of vaccines by lyophilisation. These excipients are mainly sugars and polyols with well-known lyoprotectant properties.

There are currently many amorphisation techniques. These techniques can be classified into three main categories that are distinguished by the different fundamental physical mechanisms they involve:

- **The mechanical route** [13, 20, 21]. This route consists in the progressive mechanical destruction of the crystalline order until an amorphous disordered solid is obtained. The mechanical action can be static as in the case of compression, or dynamic as in the case of mechanical milling [22–24]. Dehydration of a hydrated crystalline form also falls into this category [25, 26]. The main advantage of the mechanical route is that the amorphisation takes place directly in the solid state, i.e. without having to heat the material above its melting point [27]. This amorphisation route therefore generally allows amorphisation without chemical modification of the material [27–29]. However, it is essential to carry out the milling below the glass transition temperature of the material [30]. This requires the use of cryomilling when the T_g of the material is below ambient temperature, in order to avoid recrystallisation issues.

- **The thermal route.** This is the most classical route. It consists in melting the crystal to obtain a liquid, and then cooling the liquid sufficiently rapidly to avoid its crystallisation and to a sufficiently low temperature (below T_g) so that it has the viscosity of a solid [31, 32]. This route has two intrinsic difficulties. On the one hand, it is not always possible to reach the cooling rate that will allow avoiding the recrystallisation of the liquid. On the other hand, obtaining the liquid phase often causes uncontrolled and undesirable chemical modifications (degradation or mutarotation, for example). In practice, on an industrial scale, the thermal pathway is often coupled with techniques using mechanical action such as extrusion [33]. So both thermal and mechanical routes are combined. This makes possible to heat less the materials and avoid chemical degradation.

- **Concentration of a diluted form without crystallisation.** The diluted form may be a gas (condensation of a vapour on a cold surface) or a liquid (concentration of a solute in a solution). In the latter case, the most commonly used methods are freeze-drying (lyophilisation) and spray-drying [34]. Freeze-drying consists in freezing a solution and then sublimating the solvent by applying very low pressures. An amorphous matrix is then obtained. It has a high porosity which is generally very useful for accelerating the re-dissolution of the active principle when the drug is administrated. Spray-drying [34] consists in spraying the solution into fine droplets which are subsequently

suddenly dried in a hot gas [35]. The drying speed makes it possible to avoid crystallisation and to recover an amorphous and fine powder. This is a simple and fast method allowing the generation of large quantities of amorphous material [36]. It is therefore widely used in the pharmaceutical industry. However, it has the disadvantage, as the freeze-drying, to use solvents which may remain in the final product with toxic or plasticising effects. Moreover, there are a lot of poorly water soluble drugs for which it is not always possible to find an appropriate solvent.

Given the wide variety of amorphisation techniques and knowing the existence of polyamorphism situations (HDA and LDA water [37, 38]) or possible polyamorphism situations (mannitol [39, 40], TPP [41–43]), it is legitimate to ask whether amorphous products produced by different techniques have the same physical and chemical properties. In particular, we can wonder whether they have exactly the same structure, the same molecular mobility, the same physical stability and the same chemical structure. These properties are indeed crucial for optimising the therapeutic efficacy of a drug and guaranteeing its storage stability. The general objective of the thesis will then be to seek and identify structural, dynamic and chemical differences that potentially exist between amorphous forms of the same material obtained by different amorphisation routes. The achievement of this objective will in parallel allow to address fundamental questions of condensed matter physics such as: physical mechanisms involved in the different amorphisation routes, states far from equilibrium, glass transition, phase transformations and polyamorphism. In particular, we will improve our understanding of the transformation mechanisms induced by non-classical methods (milling, freeze-drying, spray-drying) used for altering the physical states of solid materials, and predict these changes (amorphisation or polymorphic transformations). Phase transformations induced by nonequilibrium perturbations of various types (variations of temperature or pressure, dehydration, etc) will be also investigated.

B Main objectives

Our goal is to determine the impact of an amorphisation method on the physico-chemical properties of the amorphous compound obtained. A great deal of research has been carried out in this direction - especially in our laboratory for many years [13, 25, 27, 30, 44–47] - and it mainly concerned milling and melt-quenching techniques. In particular the mechanism and physical parameters governing amorphisation under milling were studied. In this thesis, we will extend these investigations to spray-drying and freeze-drying amorphisation methods, and use new tools (neutron scattering and molecular dynamics (MD) simulations). Our specific objectives will thus be:

- To determine the energy, structural and dynamic changes induced by the four amorphisation methods, and their effect on the properties of the resulting glasses.

- To focus on the structural and thermodynamic changes taking place during the amorphisation under milling.

Our investigations will mainly be carried out on a model molecule: lactulose. It is a sugar (disaccharide) widely used in the pharmaceutical and food industries. After having performed some preliminary tests, we have chosen this material because it meets some required conditions for our study: ease to amorphise, high glass transition temperature (so that it is

stable during transportation for experiments on large instruments), reasonable price, non-toxic, not yet deeply studied in the literature.

To date, only amorphous lactulose obtained by melt-quenching has been studied. Its glass transition temperature T_g is not clearly defined, since different values ranging between 79 °C and 94 °C have been reported in the literature [48–50]. In a first step, we will therefore produce amorphous lactulose by melt-quenching, and we will try to explain these differences. Afterwards, we will produce amorphous lactulose by the three other techniques: milling, spray-drying and freeze-drying. These amorphous compounds will be first characterised by DSC, TGA and NMR.

A striking feature of lactulose is the possibility to exist in five different tautomeric forms, which can interconvert by a mutarotation mechanism [51]. We will thus study the influence of the different tautomers on the physical properties of the amorphous samples. Differences between the amorphous samples due to chemical changes will be clarified aiming to unravel the true impact of the amorphisation mechanism itself.

After having characterised the different amorphous lactulose on a macroscopic scale (DSC, TGA), they will then be analysed on a nanoscopic scale by neutron scattering and MD simulations. Thanks to the high neutrons sensitivity to hydrogen, neutron scattering represents the ideal probe for investigating either the structure or the dynamics of hydrogenous materials [52]. From the neutron scattering and MD simulations, a comprehensive picture of the hydrogen bonds (HBs) network of the compounds can be retrieved. The importance of HBs on the physico-chemical properties of molecular compounds is no longer to be demonstrated [53, 54]. Neutron diffraction will allow to determine the structure of the different amorphous compounds. Since the molecular vibrations are sensitive to the local environment, inelastic neutron scattering will further indirectly provide support and complement structural information on the compounds at a local scale. All the experimental data obtained will be always analysed and discussed on the basis of the results of molecular modelling (DFT calculations and MD simulations).

C Organisation of the thesis

This thesis is divided into five chapters.

The first chapter presents the concepts and approaches of condensed matter physics required for understanding our work. They concern in particular the crystalline state and the amorphous state. The general notions of structure and dynamics in amorphous compounds are especially developed. The four main amorphisation methods used during this thesis are also presented.

The second chapter is devoted to the known physico-chemical properties of lactulose. This chapter also presents the experimental details of the different amorphisation techniques, as well as the different numerical and experimental techniques used during this thesis to probe properties of compounds. For the sake of clarity, all activities related to neutron scattering are presented in chapter five only.

The third chapter is devoted to the study of the amorphous samples obtained by the four main amorphisation techniques used in this thesis. A thorough study of the physico-chemical properties of the four amorphous samples is done by DSC, X-Ray, NMR and MD

simulations in particular. The effect of tautomerisation and thermal degradation on the glass transition and the physical stability are discussed.

The fourth chapter is specifically dedicated to the study of transformations under milling of crystalline anhydrous lactulose. We especially determine the amorphisation kinetic of the anhydrous crystal during milling by an original method of isothermal calorimetry of dissolution.

The fifth chapter is a study by neutron scattering of the different amorphous compounds. A theoretical reminder on the neutron scattering is first presented. We then show the results of the diffraction and spectroscopic experiments that have been carried out on various instruments. These different results are mainly analysed using MD simulations.

Chapter 1

General concepts and theory

"The deepest and most interesting unsolved problem in solid state theory is probably the theory of the nature of glass and the glass transition. The solution of the (...) important and puzzling glass problem may also have a substantial intellectual spin-off. Whether or not it will help make better glass is questionable."

P. W. Anderson

Contents

This chapter aims to give the background needed to understand the results and interpretations that will be presented in the subsequent chapters (chapter 3 to chapter 5). In the first section, we will remind generalities on physical states, stability and transformations in condensed matter. In the second section, we will give an overview of the structure, dynamics and thermodynamics of glasses. In the third section, we will present the different methods that have been used in this work to amorphise compounds, with current theoretical knowledge. Special attention will be paid to the amorphisation by milling.

1.1 Generalities on physical states, stability and transformations

1.1.1 Physical states

The matter states can be classified in three categories: solid, liquid and gas (see figure 1.1). They differ in terms of their structures, dynamics and thermodynamics. In the ideal gas state, particles do not interact with each other because the density is very low. Their positions and orientations are therefore completely uncorrelated. Liquids and solids belong to the condensed matter states category. The difference between both of them lies in how they respond to the application of a shear stress.

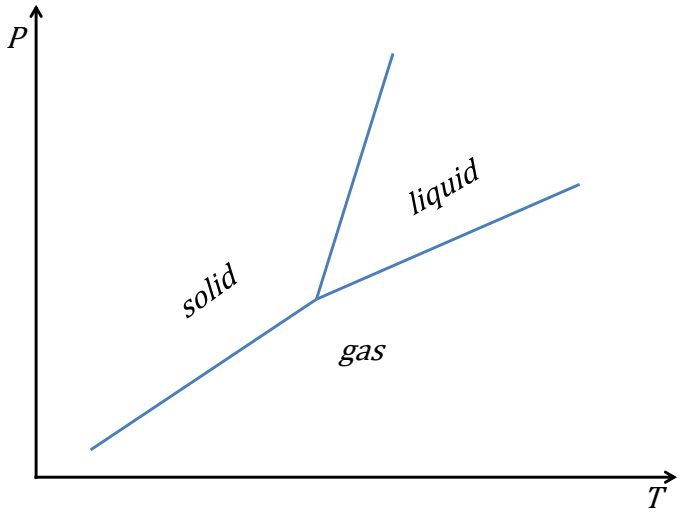

Figure 1.1 – Physical states in matter.

A liquid is a fluid, and deforms continuously when it is subjected to a stress shear. On the opposite, a solid can support a shear stress without flowing. Solids can be classified in two categories regarding their structure:

- Crystalline solids: in crystalline solids, a repeating pattern (which can be an atom, an ion, a molecule, a group of atoms ...) periodically extends in a three dimensional lattice over very long distances. Because it is ordered, a crystalline solid (crystal) is generally non-isotropic. Some materials can exhibit polymorphism. This means that they are able to exist in more than one crystalline structure. This is the case for example of water, for which more than eleven polymorphs have been reported [55, 56]. The ROY molecular crystal also has several polymorphs, differing by their colour (red, orange,

yellow, ...) [57]. Some materials can exhibit pseudo-polymorphism. This means that they can form hydrated crystalline form with solvent molecules. This is for example the case of trehalose [58].

- Amorphous solids: in amorphous solids, in contrast to crystalline solids, there is no long-range repeated pattern. Because of its disordered nature, an amorphous solid is generally isotropic. Some materials have been proposed to exhibit polyamorphism, meaning that they are able to exist in different disordered forms. For instance, water exhibits different glassy forms such as low density amorphous form, and high density amorphous form [37, 38, 59].

Figure 1.2 shows a schematic representation in 2D of a crystalline solid (left) and an amorphous solid (right).

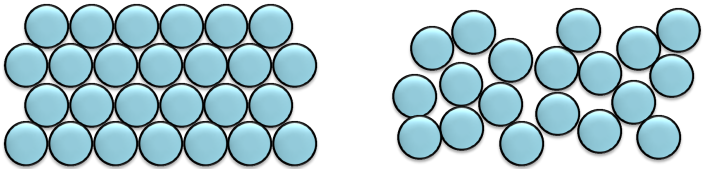

Figure 1.2 – Schematic representation in 2D of an ordered system (left) and a disordered system (right). The terms order/disorder used here refer to the position of the molecules.

1.1.2 Stability

The stability of a given form at a given temperature and pressure is determined by its Gibbs free energy G:

$$G = H - TS \tag{1.1}$$

where:

- H is the enthalpy, which measures the heat content of the system.
- T is the temperature.
- S is the entropy, which measures the level of molecular disorder.

Figure 1.3 represents the evolution of the Gibbs energy with respect to the volume at a given temperature and pressure. Three specific points can be seen:

- The point A represents a stable equilibrium point. It is the point having the lowest Gibbs energy. The system does not evolve when being at this configuration state.
- The point B represents a metastable equilibrium point. It is an equilibrium point which does not have the lowest Gibbs energy. For this reason, the system does not evolve when being in this configuration state, until some fluctuations give it the energy required to cross the energy barrier (ΔG_0 on the picture) and reach the stable equilibrium point.
- The point C represents an out of equilibrium point. When the system is at this configuration state, any fluctuation leads it towards the closest equilibrium point.

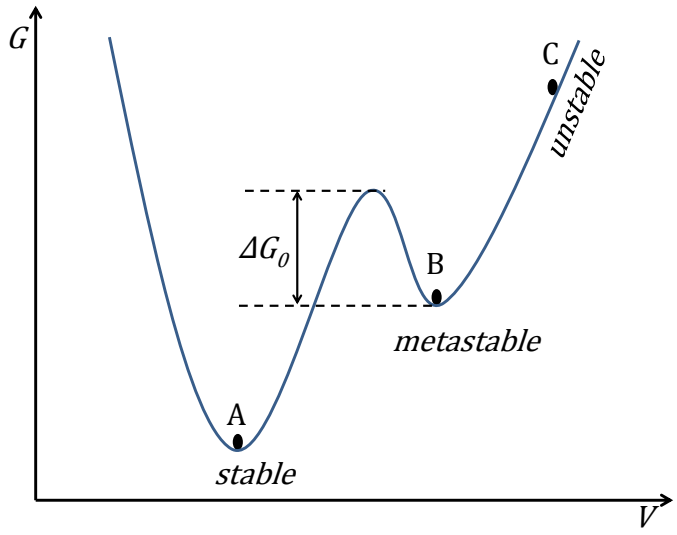

Figure 1.3 – Evolution of the Gibbs energy with the volume.

1.1.3 Thermodynamic changes occurring upon cooling a liquid

Assuming the previous figure (figure 1.3) is represented in the liquid state, the stable equilibrium point A corresponds to the liquid, and the metastable equilibrium point B to the crystal [1]. The evolutions of the Gibbs energy of those two equilibrium points (the crystal: black line, and the liquid: blue line) with respect to the temperature are represented in figure 1.4a. The two different paths (red lines) that can be followed by the system upon cooling from the liquid state are also represented. Figure 1.4b represents a time-temperature-transformation diagram. It is a diagram giving the time needed for the crystallisation of a given fraction of the compound at a given temperature. It shows a « nose » corresponding to the rate of the maximum of crystallisation. Two different paths (red lines) that can be followed by the system upon cooling from the liquid state are represented.

When cooling down the liquid, its evolution below the melting temperature (T_m) depends on the cooling rate:

- If the cooling rate is fast enough to avoid the crystallisation of the liquid (path n°2 in figure 1.4a), the liquid stays liquid (path n°2 in figure 1.4b).
- If not (path n°1 in figure 1.4a), the liquid crystallises, and a stable or metastable crystalline polymorph is produced (path n°1 in figure 1.4b)

Path n°1: crystallisation

When the cooling rate is slow enough such that the time scale associated to the cooling rate allows the system to reorganise and to have a Gibbs energy corresponding to this of the crystal, the liquid will crystallise below T_m.
The crystallisation of a liquid is generally described in the frame of the classical nucleation [60–62] and growth theory:

- **Nucleation:** appearance of a crystalline germ (assumed spherical) in the liquid. It is the result of the competition between an energy lost due to the formation of liquid/-crystal interface, and gained during the formation of the crystal. The Gibbs energy

[1] This is opposite in the crystal.

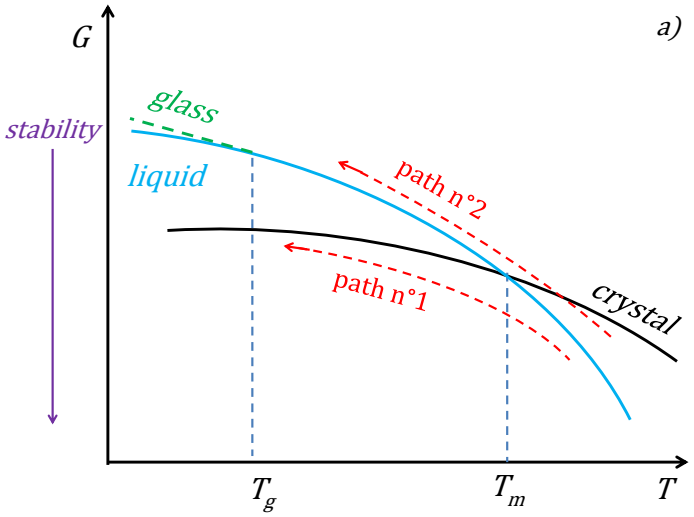

(a) Evolution of the Gibbs energy with temperature. The equilibrium lines of the liquid (blue line) and the crystal (black line) are represented, as well as the out of equilibrium line of the glass (green line). The two different paths (red lines) that can be followed by the system upon cooling the liquid state are also drawn.

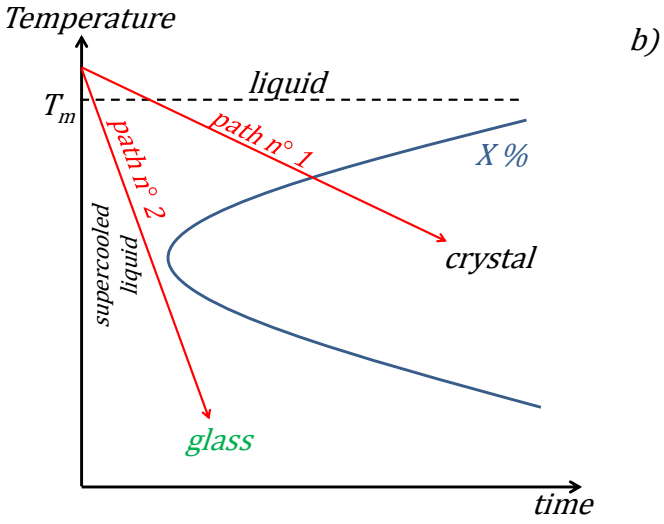

(b) Time-temperature-transformation diagram. The blue line represents the time needed for the crystallisation of a given fraction of the compound with respect to the temperature. The two different paths (red lines) that can be followed by the system upon cooling the liquid state are also drawn.

Figure 1.4 – Changes occurring upon cooling a liquid.

difference between the liquid and the crystal is then given by:

$$\Delta G = 4\pi r^2 \gamma - \frac{4}{3}\pi r^3 \Delta G_v \tag{1.2}$$

Where:

- γ is the interfacial free energy between the liquid and the crystal.
- r is the radius of the germ.
- ΔG_v is the Gibbs energy volume difference between the liquid and the crystal.

The germ that appears will:

- Either become stable if it reaches a certain critical radius of nucleation r*. This situation occurs when the fluctuations of the system produce an energy allowing crossing the nucleation barrier [63].
- Or disappear if not.

- **Growth:** the stable germ ($r > r^*$) already formed grows up by aggregation of the new molecules. The interface growth rate is mainly governed by the diffusion of the molecules, and can be given by the semi-phenomenological expression of Turnbull [64]:

$$G(T) = r\,p \exp(-\frac{A}{kT}) \exp(-\frac{V\Delta G_v}{kT}) \tag{1.3}$$

Where:

- r is the radius of the germ.
- p is the probability that a molecular jump contribute to the growth.
- A is the energy barrier involved in the mechanism of diffusion.
- V is the molecular volume.

Path n°2: the supercooled liquid and vitrification

When the time scale associated to the cooling rate is shorter than the time needed by the liquid to adopt the configuration of the crystal, it will not crystallise below T_m. A metastable liquid is thus obtained (see figure 1.4b), and is named supercooled liquid.

Upon further cooling, the system will follow the liquid equilibrium line until a certain temperature T_g where it will no longer be able to accommodate the structure of the liquid at the ongoing temperature. This is due to the fact that the time scale given by the cooling rate becomes shorter than the structural relaxation time (time needed by the system to adopt the more stable configuration) at the ongoing temperature. The supercooled liquid thus freezes and falls out of equilibrium: it is the calorimetric glass transition. This vitrification is the consequence of a sudden drop down of the mobility of the molecules. The slope of the plot describing the evolution of the enthalpy or the volume of the system decreases (see figure 1.5a) and there is a discontinuity of the specific heat or the thermal expansion coefficient (see figure 1.5b).

The temperature T_g is called the glass transition temperature.

A glass can then be viewed as a liquid in which an important slowing down of its diffusive motions prevents it to flow on the experimental time scale. Conventionally, a supercooled liquid is called glass at the temperature from which no translational motion occurs within a time scale of 100 s. This happens for liquids with viscosity of 10^{12} Pa-s or greater. The freezing of the motions when crossing the glass transition temperature gives rise to a drop of specific heat C_p in a Differential Scanning Calorimetry (DSC) curve (see figure 1.5b).
The glass transition temperature observed in a laboratory is a kinetic transition (and not thermodynamic), since it is given by a competition between the experimental time scale given by the cooling rate and the structural relaxation time of the system. The faster the cooling rate, the higher the T_g.

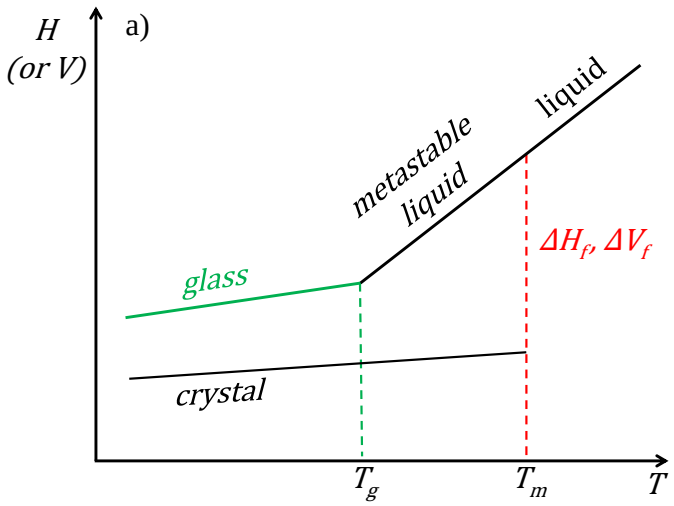

(a) Variation of the enthalpy H (or the specific volume V) with respect to the temperature.

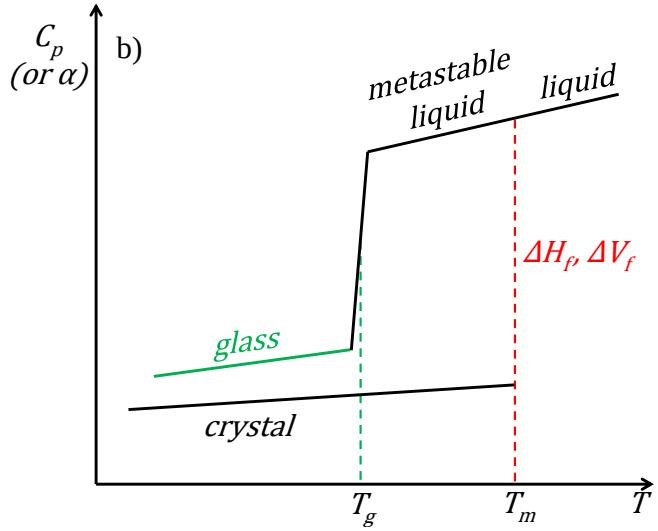

(b) Variation of the derived quantities: specific heat C_p (or thermal expansion coefficient α).

Figure 1.5 – Thermodynamic characterisation of the vitreous transition.

1.2 Disordered states: liquids, supercooled liquids and glassy states

1.2.1 Structure

The determination of the structure of a system is an important step when studying its physical properties. It is important information to have for a good understanding of the general behaviour of a system. When the system is ordered, an ordering rule helps to predict the positions of all elements of the compound. For disordered system, it is not the case, and the structural information measured is less precise than in ordered systems.

How to probe the structure of a system?

X-ray and neutron diffractions are the experimental techniques allowing to directly probing the microscopic structure of systems. When doing a diffraction experiment, the measured si-

gnal always allows to get the total scattering function S(Q) (more details are given in chapter 5) of the sample under study. For ordered systems, S(Q) contains Bragg peaks. The position of the Bragg peaks gives access to the structure, and by analysing the shape of the peaks, one can retrieve sample microstructure (presence of micro-strains, size of the structurally coherent domains ...) [65–67]. For disordered systems, such a detailed structural and microstructural analysis is difficult to perform on S(Q), because the pattern obtained is a « hump » (no more Bragg peaks). The pattern is useful to inform if the sample is « X-ray (neutron) » amorphous, i.e. does not have long-range correlations. However, the hump obtained is the proof of the existence of a certain ordered range (short or medium) in the system. This local order is difficult to assess on the total scattering function S(Q). By Fourier transforming S(Q), it is possible to obtain the Pair Distribution Function [68].

The most used tools to describe microscopic features of disordered systems are probability distribution functions. The most straightforward and simple is the pair distribution function g(r) [68]. It is a two-point correlation function that can be assessed by simulations and experiments, since as it has been previously mentioned, its reciprocal-space counterpart S(Q) is experimentally measurable. This function statistically describes the distances between pair of atoms (molecules ...) and gives the probability of finding an atom at a distance r from another. The position of the peaks depends on the average distances between pair of atoms. The width of the peaks depends on the distribution of the distances around their average value, either due to thermal vibrations or the inherent disorder of the system. This function is generally used to investigate ordered or disordered systems [69–71].

The g(r) function in the case of ordered systems is represented in figure 1.6 (a) and (b). Figure 1.6 (c) shows a representation of g(r) in the case of disordered systems. The broadening of the peaks gives information on the order level, and the area under the peaks give the number of neighbours at the corresponding correlation shell. As r values become large, the system looks more homogeneous and, g(r) has more broad peaks. It finally becomes completely flat at very high r values.

There are also other probability distribution functions such as the radial distribution function [72] which can give complementary information (the integration of the radial distribution function will directly yield the number of atoms within a coordination shell).

Structural description can also be done by numerical functions. An important numerical tool sometimes used is the Voronoi polyhedron. This is the equivalent of the Wigner-Seitz cell of the crystals. A statistical analysis of the distribution of volumes, shapes of those polyhedrons provide very precise information on the local structure of the system. The main limitation of the Voronoi polyhedron is that it is difficult to connect the information obtained with measurable physical quantities [73, 74].

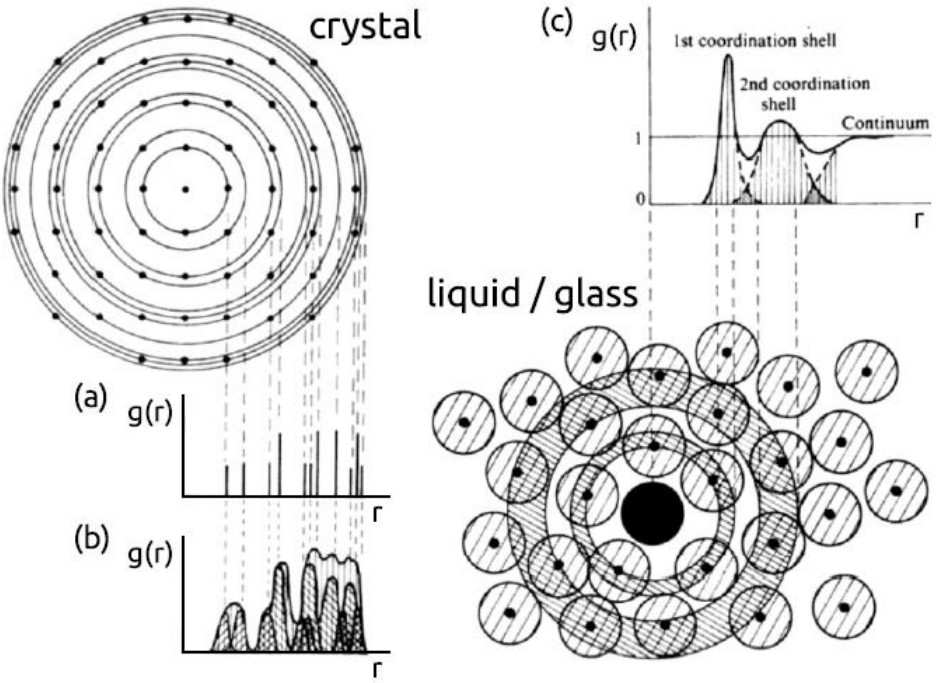

Figure 1.6 – Pair correlation function. (a) In the ideal case of a perfect crystal, molecules are perfectly ordered, so they appear as delta functions. (b) In real crystals the particles vibrate about their equilibrium positions and a certain probability distribution of finding the neighbour particle around each distance is obtained. (c) In a disordered material, such as a liquid or a structural glass, a distribution of distances is inherent to the variability of possible local arrangements of the system, so the peaks largely overlap, quickly becoming a uniform function at distances where their short range order is lost. Modified from [73].

1.2.2 Dynamic

There are several kinds of motion that take place in an amorphous solid. They can be classified in two categories, depending on their frequency:

- Vibrations, including high frequency (individual) and low frequency (collective) vibrations.
- Relaxations (very low frequency motions), as structural relaxations (α-relaxations).

All those motions are described in the following.

1.2.2.a) Vibrations

High frequency vibrations The modes between 200-4000 cm^{-1} (equivalent to 25-500 meV) are generally intramolecular motions. Intramolecular motions are motions involving atoms belonging to the same molecule, such as vibrations. Among them, one can mention stretching and bending:

- Stretching: vibration changing the bond length. There are two types of stretching vibration: the symmetric stretching (two bonds vibrate in and out together) and the asymmetric stretching (a bond is getting shorter while another is getting longer).

- Bending (scissoring): vibration changing the bond angle.

There are also rocking, wagging and twisting (see [75] for videos).

How to probe intramolecular vibrations of a disordered system? The techniques allowing probing intramolecular vibrations in a disordered system are the same than those used for an ordered system. Among them, we can mention inelastic neutron scattering (INS) [76], Raman spectroscopy [77] and infrared (IR) spectroscopy [78]. The interaction mode of all those techniques with the matter is different. Each of them is thus more or less adapted to detect a certain kind of vibration. When a vibration can be measured by IR, Raman and INS spectroscopy, only its measured intensity can change from one technique to another (see figure 1.7).

Vibrational motions can be identified and studied by simulations, doing Density Functional Theory (DFT) calculations in particular, and Molecular Dynamics (MD) simulations.

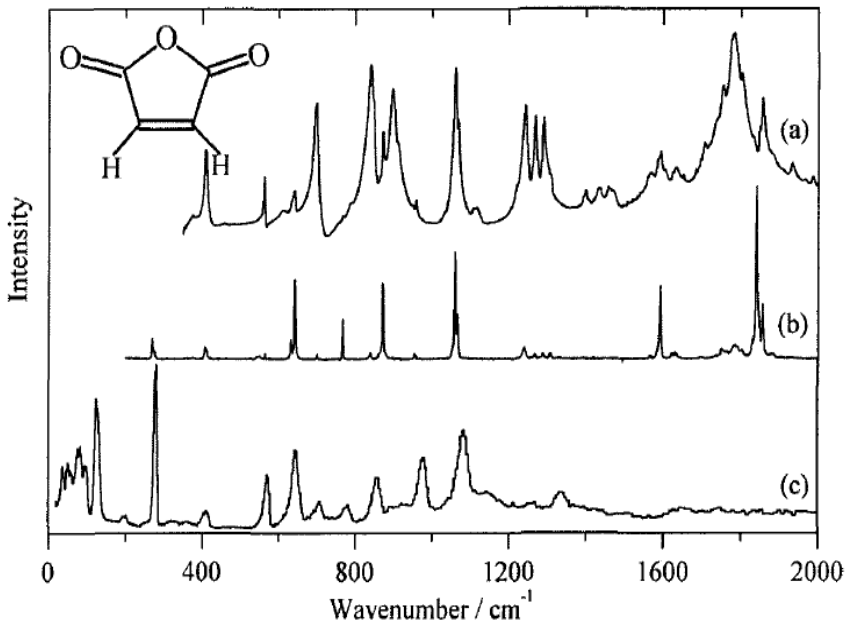

Figure 1.7 – Vibrational spectra of maleic anhydride: (a) IR spectrum, (b) Raman spectrum, (c) INS spectrum. The three methods are complementary: modes that are strong in one form of spectroscopy are weak or absent in the others. Taken from [79].

Low frequency vibrations The modes between 10-200 cm^{-1} (equivalent to 1-25 meV) are generally lattice modes. Lattice dynamics are collective excitations (intermolecular motions), and thus involve atoms not belonging to the same molecule. This includes phonons and magnons (case of magnetic systems) [80].

The Boson peak One of the most known characteristic of amorphous compounds is to exhibit in their vibrational density of states an « anomaly » called the « Boson peak » (BP). This is an excess of vibrational modes observed at low frequency values compared to the vibrational modes of an elastic crystal calculated using the Debye model [81–84].

$$g(\omega) = \frac{\omega^2}{2\pi\rho v^3} \tag{1.4}$$

Where:

- g(ω) is the density of states (DOS).
- ρ is the weight density.
- v is the sound velocity.

The BP can manifests experimentally by several ways:

- Maximum in the specific calorific energy at low temperature (10-30K) in contradiction with the Debye model.
- Peak in the energy range [20-60] cm^{-1} in the reduced DOS spectra measured by INS [82, 83, 85] and Raman spectroscopy [86, 87].

When the BP was discovered, little was known about its features besides its bosonic character (the temperature dependence of its intensity follows that of a harmonic oscillator characterised by the Bose-Einstein factor). The BP exhibits a lot of characteristics experimentally found. For instance, one can mention that:

- It appears in similar energy range for several amorphous solids with different local structures and bonding energies [88].
- It is more pronounced in stronger glass formers [87, 89, 90].
- Its intensity becomes weaker while increasing the temperature or the pressure [91, 92].

Nowadays, the origin of the BP and its microscopic mechanism is still disputed and some theories/models have tried to explain it. The validity of a model is tested by its ability to explain the characteristics of the BP listed above. Several studies on amorphous materials have found that the BP energy does not depend on the momentum transfer Q. This indicates that the BP is due to the local or quasi-local (non-propagating) vibrational modes [93, 94].

Taraskin and Elliot [95] suggested that the BP is due to the quasi-localisation of the acoustic phonons caused by the coupling between acoustic phonons and low optic phonons.

Using a two-order-parameter model of a liquid based on the assumption that a liquid can be view as having locally favoured structures (characterised by a particular spatial symmetry which is not consistent with the symmetry of the « equilibrium » crystal) randomly distributed in a sea of « normal-liquid structures », Tanaka [96] showed that a locally favoured structure (LFS) and its cluster are responsible for the BP. The BP is thus not just due to disorder, since it is a consequence of an order surrounded by disorder. This has been confirmed by an experimental observation of the BP in a disordered colloidal crystal [97]. The characteristic size of the LFS gives an indication on the BP energy (the larger the LFS, the smaller the BP energy). Since the LFS could exist also in the liquid state, a liquid can also exhibit a BP. Tanaka also suggested a connection between the BP and the glassy transition, by showing that those LFS are also responsible for the vitrification.

Several works [98–100] have shown that low-frequency transverse phonons contribute the most to the BP intensity in the range of wave numbers where both the longitudinal and transverse phonons show a solid-like response over large length scales, suggesting thus a direct link between transverse modes and the BP.

Recently, Chumakov et al. [101] have presented results suggesting that at high pressure, the BP becomes equivalent to the van Hove singularity. This means that there is no excess in the actual number of states at the BP and hence no additional modes compared to the crystal. According to their work, the BP is thus just related to the transverse acoustic singularity of the underlying crystal structure.

How to probe lattice dynamics of a disordered system? In the case of crystalline states, a straightforward study of the phonon is possible since they exhibit long range order and symmetry. Notions such as Brillouin zones, Bloch functions, electronic band structure, and phonon dispersion curves are theoretically well defined and allow a thorough investigation of the dynamic in a crystal [80]. However, all those notions are less well defined when losing the long-range order as in the case of amorphous solids. A theoretical interpretation of lattice dynamics in amorphous solids is thus difficult [102, 103]. Nevertheless, phonons can be investigated similarly to the case of crystals. In particular, the density of states function g(ω) giving the number of modes with an angular frequency ω provides information on the vibrational modes in the system. As in the case of crystals, there are a lot of experimental techniques to probe low vibrational dynamics in disordered systems. Among them, one can mention INS, Raman spectroscopy and IR spectroscopy. Lattice dynamics can also be assessed by MD simulations.

1.2.2.b) Relaxational dynamics (the 3 nons: non exponential, non Arrhenius, non linear)

Relaxational dynamics come from very slow motions belonging to the range 10^{-1} - 10^{-9} THz (equivalent to 10^{-8} to 1 meV). In this section, we will discuss how the structural relaxation motions, responsible of the vitrification of a glass, can impact the properties of the system.

Non exponential time dependence of the relaxations At a given temperature, the temporal response function of a supercooled liquid subjected to an external perturbation (as a temperature variation) can be expressed by the Kohlraush-Williams-Watts (K.W.W) function (stretched exponential):

$$\phi(t) = \exp\left[(\frac{-t}{\tau_{KWW}})^{\beta}\right] \tag{1.5}$$

Where β is a parameter within 0 and 1, and τ_{KWW} is the relaxation time.

For β equal to 1, this expression corresponds to the Debye theory. The exponential time dependence of the response function $\phi(t)$ is observed in equilibrium liquids, or in strong glasses (to be defined later) such as SiO_2.

When β is different to 1, the system exhibits a distribution of characteristic time of the relaxation (the system has dynamic heterogeneities). It has been observed that fragile glasses (to be defined later) have lower β values [104].

Non Arrhenius temperature dependence of the relaxations The logarithm of the shear viscosity η or the relaxation time τ_α of liquids may increase linearly or no with the inverse of the temperature (see figure 1.8). Angell thus proposed to classify liquid forming glasses regarding the linear behaviour or no of their mobility. This classification is done thanks to a parameter m which allows quantifying the evolution of the mobility when reaching the glass transition temperature T_g. This parameter, called « fragility » index, is given by the slope of the shear viscosity at T_g:

$$m = \left.\frac{d\log\tau_\alpha}{d(T_g/T)}\right|_{T=T_g} \tag{1.6}$$

Glass forming liquids having a small value of m (m ≈ 16) are said to be « strong ». The evolution of their structural relaxation time with respect to the temperature follows an Arrhenius law:

$$\tau_\alpha(T) = \tau_0 \exp\left[(\frac{C}{T})\right] \tag{1.7}$$

Where τ_0 is the characteristic time of the vibrational modes, C is a constant representing the energy barrier involved in the mechanism of structural rearrangement, and T is the temperature.

Oxide glasses (SiO_2 for example) belong to the category of strong glasses. Such systems exhibit short and strong interatomic interactions, like covalent bonding. Their bonding energy is of the order of magnitude of the activation energy of the relaxations.

Glass forming liquids having higher value of m are said to be « fragile ». The evolution of their structural relaxation time with respect to the temperature is not Arrhenius. Approaching T_g, their shear viscosity increases suddenly by several orders of magnitude when increasing the temperature just by 2-4 °C [32] (see figure 1.8). An incredible increase of the transport coefficients is thus observed, and seems to diverge at a certain temperature T_0. In that case, the evolution of the structural relaxation time with respect to the temperature can be expressed by an empirical law such as the Vogel-Fulcher-Tamman (V.F.T) law:

$$\tau_\alpha(T) = \tau_0 \exp\left[\left(\frac{B}{T - T_0}\right)\right] \tag{1.8}$$

Where τ_0 is the characteristic time of the vibrational modes, B is a constant, and T_0 is the temperature where the relaxation time diverges. It has been observed that this empirical law is not able to precisely describe the dynamic of glass forming liquid over a large temperature range, from high temperature (melting) to the glass transition temperature T_g.

NB: This non Arrhenius temperature dependence of the structural relaxation time could be related to the non-exponential time dependence of the relaxation processes [105].

Polymers and molecular (organic) systems belong to the category of fragile glasses. The molecular interactions in such systems (hydrogen bonds, van der Waals) are less energetic than in the case of strong glasses, and non-directional. The activation energy in such systems is higher than the intermolecular energy bonding. This means that there are large cooperative regions in the system, regions where rearrangements take place. Their size increases when the temperature decreases, and they are the main responsible of the non Arrhenius behaviour of structural relaxation.

Non linearity of relaxations, following large temperature jump The non-linearity derives from the fact that the relaxation time of an out-of-equilibrium liquid (a glass) depends not only on temperature, but also on the so-called fictive temperature [106–108]. Going from T_g+2 °C to T_g, the fictive temperature starts at T_g+2 °C and ends up at T_g, which implies a faster relaxation than when the fictive temperature starts at T_g-2 °C to end up at T_g.

One proof of the non-linearity of relaxations can be seen in figure 1.8. In the case of organic compounds, around the glass transition temperature T_g, there is an increase of the shear viscosity of more than one order of magnitude 2 °C above T_g, and this increase is higher than the increase of the shear viscosity from T_g-2 °C to T_g. A non-linear behaviour is also observed with the relaxations (faster below T_g than above T_g).

How to probe relaxation dynamic of a disordered system? Relaxations can be probed in a direct manner, by Quasi-Elastic Neutron Scattering, Neutron Spin Echo, Dielectric Relaxation Spectroscopy, and Nuclear Magnetic Resonance (NMR) for example. Those techniques allow measuring the motions driving the relaxations.

Relaxations can also be probed in an indirect way, by seing their impact on a « non spectroscopic » technique. For instance, the C_p jump seen at the glass transition temperature

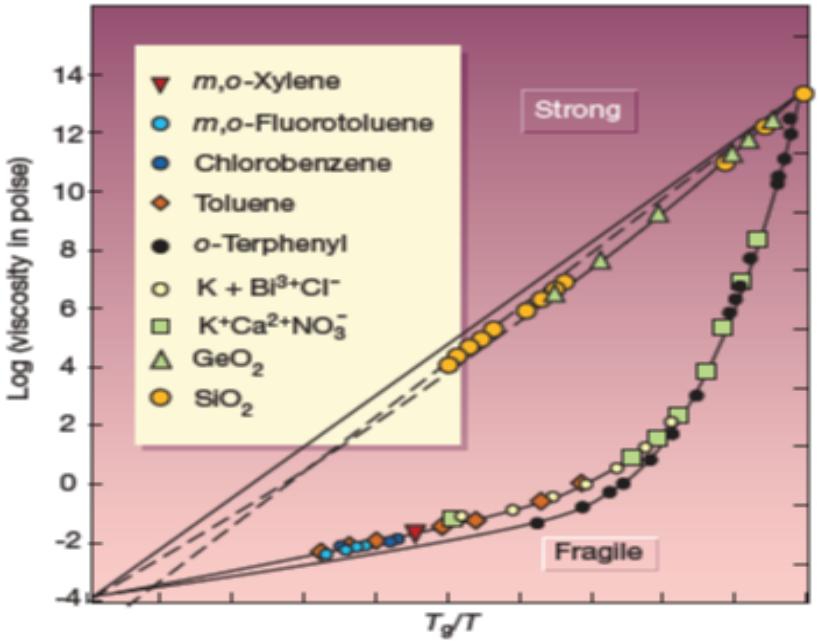

Figure 1.8 – Evolution of the shear viscosity of various liquid systems with respect to the inverse of the temperature (normalised by T_g). Systems showing an Arrhenius behaviour belong to the strong glasses category (SiO_2, GeO_2). Systems showing a strong deviation from the Arrhenius behaviour belong to the fragile glasses category (orthoterphenyl).

in a Differential Scanning Calorimetry (DSC) curve indicates that α relaxations have been unfrozen.

1.2.3 Thermodynamic

1.2.3.a) Physical stability

Since the glass is an out of equilibrium state, it naturally relaxes toward the closest equilibrium state (stable or metastable). This process is called the aging (physical aging). The glass will reach the closest equilibrium state more or less quickly, depending on the mobility of its molecules, and its temperature history.

The aging level reached by the glass can be detected in a DSC scan, as seen in figure 1.9. The existence of an endothermic peak just after the specific heat jump is characteristic of the aging. The area of this peak becomes higher the more the glass ages. This area will stop evolving if the system reaches the equilibrium line of the liquid. This means that the aging is finished, the system has already adopted the configuration that allows it to have the enthalpy of the liquid at the corresponding temperature. The system can further crystallise by nucleation/growth if fluctuations give the energy required to form a stable nucleus.

Structural (α) relaxations are usually the main relaxations driving the physical aging [109, 110]. For that reason, the lower the aging temperature, the slower the relaxations. However, some recent results also showed the important role of the secondary relaxation during physical aging [111].

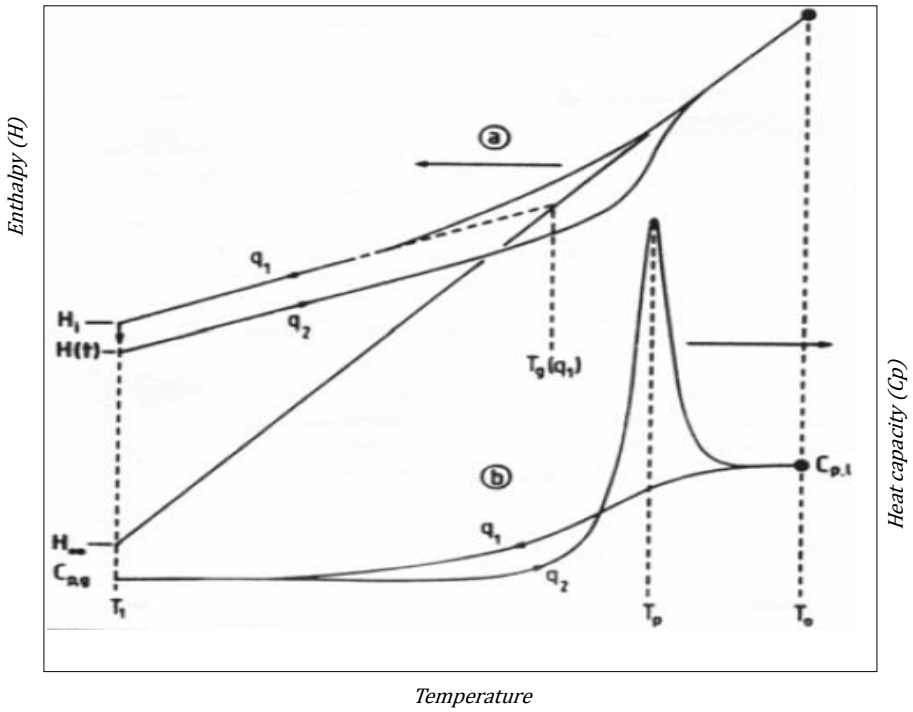

Figure 1.9 – Evolution with respect to the temperature of the enthalpy (a) and of the heat capacity of a liquid upon cooling (q1) and heating after an aging time t below T_g (q2). In the vitreous region, the system relaxes toward its equilibrium state, and the enthalpy tends to reach the level of the supercooled liquid. Upon heating, this evolution of the enthalpy expresses by the presence of an endotherm just after the jump of specific heat at T_g. It corresponds to the catching-up of the enthalpy relaxed during aging below T_g, the slope of the enthalpy curve becoming more high at T_g. Taken from [112].

1.2.3.b) Entropy below Tg: the Kauzmann paradox

The entropy formula given by Boltzmann established a link between the microscopic and the macroscopic properties of the matter:

$$S(N,V,E) = k_B \ln(\Omega) \tag{1.9}$$

In Eq. 1.9, Ω is the number of configurations sampled by the system. This number is low for ordered systems such as crystals. A crystal has a unique configuration ($\Omega = 1$) at T = 0 K. Having a null entropy above T = 0 K is then impossible.

Figure 1.10 gives a schematic representation of the evolution of the entropy of a crystal, and a glass forming liquid. Since the specific heat of the liquid is higher than that of the crystal, the entropy of the liquid decreases faster than this of the crystal upon cooling. As a consequence, the extrapolation into the vitreous region of the curve representing the entropy of the liquid allows defining a temperature T_K (Kauzmann temperature), below which the entropy of the liquid (disordered system) becomes lower than that of the crystal (ordered system). Moreover, following this extrapolated curve, the entropy of the liquid could become null and even negative above T = 0 K. This is in violation with the statistic expression of Boltzmann, and is called entropy crisis. Kauzmann was one of the first physicists to point out this paradoxical situation in 1948 [113].

Several scenarios have been proposed in order to solve this crisis. Kauzmann [113] for example suggested that a thorough cooling will leads to a cancellation of the barrier of crystallisation (energy) due to the diminution of the critical radius of nucleation. In that sense, even if one succeeds to avoid vitrification of the liquid upon cooling it very slowly, it would ineluctably crystallise above the T_K temperature. The Kauzmann temperature T_K can thus be considered as a metastability limit temperature, under which the liquid will always become crystal. Some others works suggested a change of the slope of liquid-equilibrium line at low temperature, in such a way that it will never be below this of the crystal.

So far, the glass transition always happens in all studied systems (when they do not crystallise), and this crisis has never been observed experimentally.

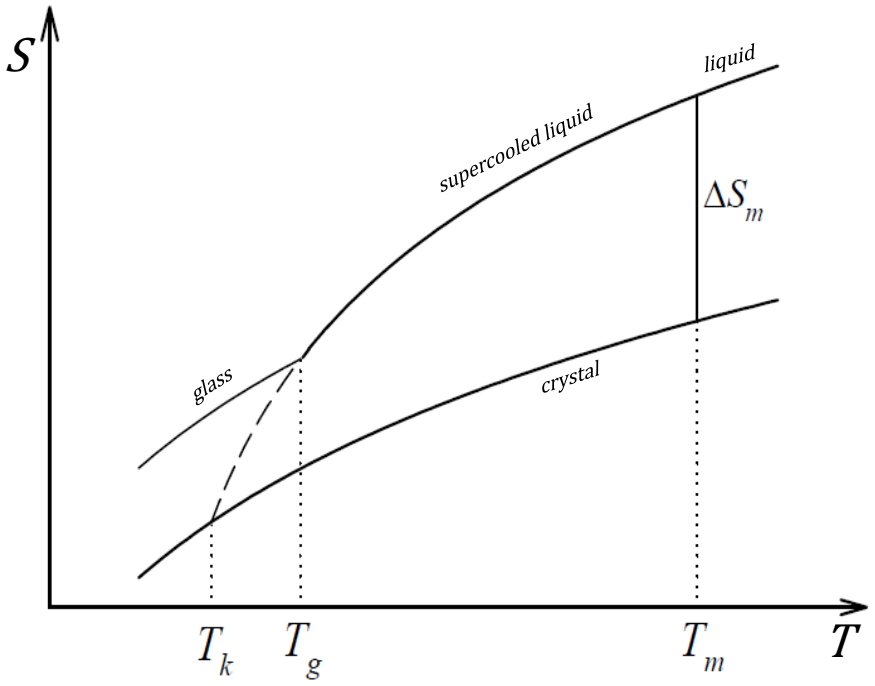

Figure 1.10 – Schematic representation of the entropy evolution of a liquid and a crystal with respect to the temperature. ΔS_m represents the melting entropy. When extrapolating the entropy curve of the supercooled liquid below T_g, it intersects that of the crystal at the Kauzmann temperature T_K.

How to probe the thermodynamic properties of a disordered system?

By determining some thermodynamic functions such as the enthalpy, the entropy and the Gibbs energy, it is possible to study the thermodynamic features of a system. Those thermodynamic functions can be measured by different methods, such as DSC experiments.

1.3 Other amorphisation routes

Besides the quenching of the liquid described in the previous sections, there are a lot of ways to amorphise a sample. Among them, we can list the high energy ball milling of a crystal

[13, 114], the irradiation of crystals with heavy particles [115], the freeze-drying [116], the spray-drying [116], the dehydration of crystalline hydrates [13, 116], the extrusion [117], the electrospinning [118], electrospray [119], etc. We give therefore a brief state of the art of the three other amorphisation routes (i.e. besides the quenching of the liquid) that have been used in this thesis: the milling, the spray-drying and the freeze-drying. Experimental details used to amorphise compounds by these routes are given in chapter 2.

1.3.1 Milling

A lot of compounds have already been shown to undergo a direct crystal to glass transformation upon high energy milling: trehalose [120], glucose [27], griseofulvin [121], linaprazan [45] ... As an example, figure 1.11 shows a heating (5 °C/min) DSC curve of a trehalose sample recorded after 30 hours milling of the crystalline trehalose (run 3). It clearly shows a C_p jump at T_g = 118.5 °C characteristic of the glass transition of this compound. This jump proves that the crystalline trehalose has been amorphised and then vitrified during the milling.

The amorphisation by milling is expected to result from a competition between a disordering process due to mechanical shocks and a subsequent structural reordering process which is thermally activated. This is why a complete amorphisation upon milling can generally only be observed when materials are milled far enough below their glass transition temperature [45, 120, 121]. In that case, the lack of molecular mobility prevents the structural reordering of amorphised fractions at the time scale of the milling process. A very important point concerning the amorphisation induced by milling is that it occurs directly in the solid state. This means that the amorphisation does not require heating the sample or dissolving it into solvents. As a result, the milling can generally amorphise materials without any chemical change [27, 44].

Several theories have already been elaborated to explain the phase transformations under milling. However, none of them is able to explain the whole transformations observed under milling. Among those theories, one can mention:

- The Lindemann generalised criteria.
- The Fecht model.
- The theory of forced alloys.

We present them in the following.

Lindemann generalised criteria

Lindemann has proposed a model related to the atomic vibrations $\langle \mu^2_{vib} \rangle$ in the system [122]. In the crystal, atoms vibrate around their equilibrium positions. The higher the temperature, the larger the amplitude of the vibrations. According to Lindemann, the system melts when the vibrational amplitude becomes larger than the half of the interatomic spacing. It thus exists a critical mean square displacement $\langle \mu^2_{cri} \rangle$ above which the system melts:

$$\langle \mu^2_{cri} \rangle = \langle \mu^2_{vib} \rangle \tag{1.10}$$

Generalising this criterion by including the atomic motion due to the static disorder $\langle \mu^2_{sta} \rangle$ (dislocations, vacancies ...) induced by the milling, we have:

$$\langle \mu^2_{cri} \rangle = \langle \mu^2_{vib} \rangle + \langle \mu^2_{sta} \rangle \tag{1.11}$$

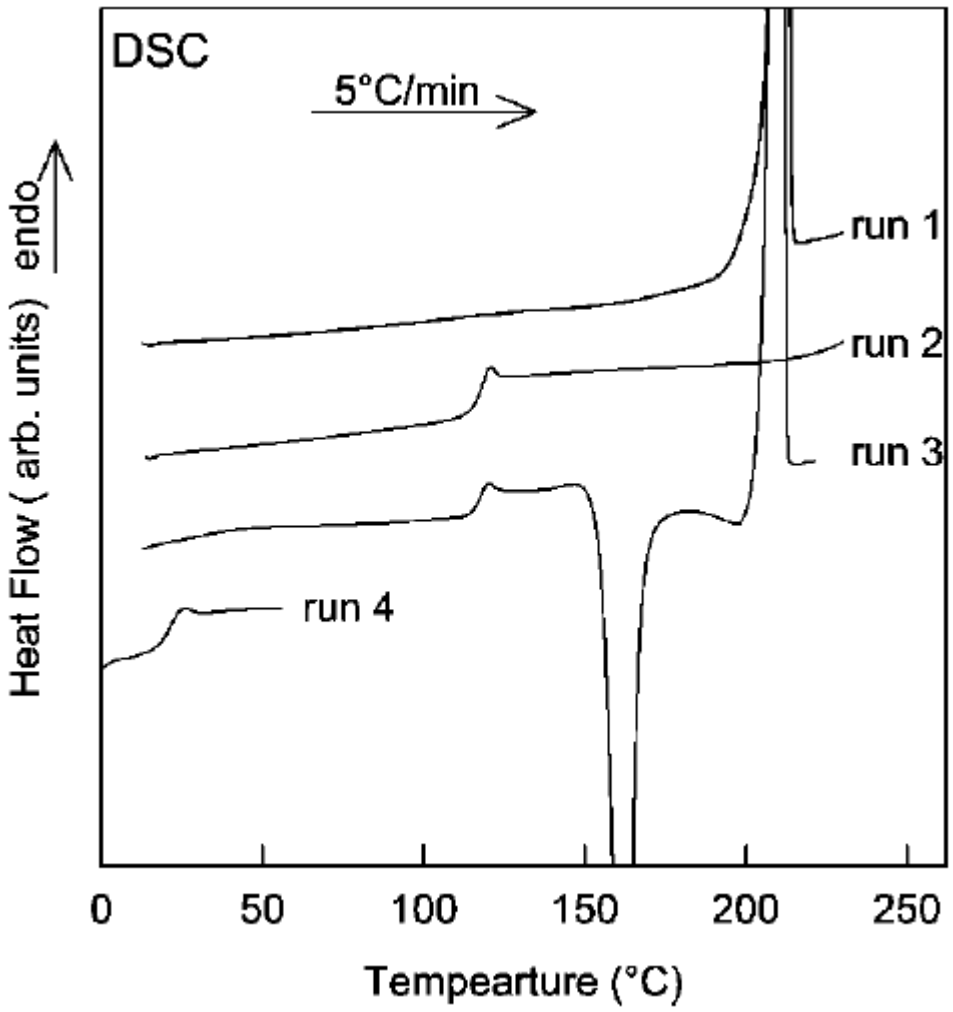

Figure 1.11 – DSC scans recorded upon heating (5 °C/min). Run 1: nonmilled form β. Run 2: quenched liquid trehalose. Run 3: form β after a 30 h milling process. Run 4: T_{2H_2O} melted and quenched in a hermetic pan. A C_p jump characteristic of vitreous transition is clearly visible at T = 118.5°C in run 3. Taken from [13].

This model thus predicts that the melting of the crystalline form could happen by two processes:

- either by heating the crystal (increasing then $\langle \mu^2_{vib} \rangle$) up to T_m ;
- or by putting enough defects in the crystal (increasing then $\langle \mu^2_{sta} \rangle$) even below the melting temperature T_m.

During the milling, there is an increase of the amount of defects and thus the statistic displacement $\langle \mu^2_{sta} \rangle$ is important. The crystal melts under milling when the atomic displacement becomes larger than $\langle \mu^2_{cri} \rangle$. The main limitation of this model is that it is not able to explain the polymorphic conversions that are sometimes observed when milling a crystal.

Thermodynamic approach: the Fecht model

The Fecht approach [123] is based on thermodynamic equilibrium, and assumes that the defects introduced by milling are part of the structure.

For a crystal without any defects, the thermodynamic criterion giving the condition of melting is:

$$\Delta G = G_{liq} - G_{cry} = 0 \tag{1.12}$$

Where G_{liq} is the Gibbs free energy of the liquid phase and G_{cry} is the Gibbs free energy of the crystal phase. If one takes into account the defects, this criterion becomes:

$$\Delta G^* = \Delta G - \Delta G^d = 0 \tag{1.13}$$

ΔG^d is the Gibbs free energy variation due to defects, and is given by the following expression:

$$\Delta G^d = C(\Delta H^d - T\Delta S^d) + kT(C\ln C + (1-C)\ln(1-C)) \tag{1.14}$$

Where C is the concentration of defects, ΔH^d is the variation of enthalpy due to defects, and ΔS^d is the variation of entropy due to defects.

The temperature T at which the defective crystal melts is the temperature at which $\Delta G^* = 0$. Figure 1.12 illustrates this condition. It shows that the more the concentration of defects is large, the lower the crystal → liquid transition temperature. For a limiting concentration of defects (C2), the Gibbs free energy of the defective crystal becomes tangent to that of the liquid. The highly defective crystal is then in a thermodynamic situation that "pushes" it to switch to the liquid phase. At this point, the transition is without latent heat and isentropic (second-order transition). If the temperature of the system is lower than the glass transition temperature, there is a direct crystal → glass transition.

The main limitation of this model is that it is not able to predict polymorphic conversions.

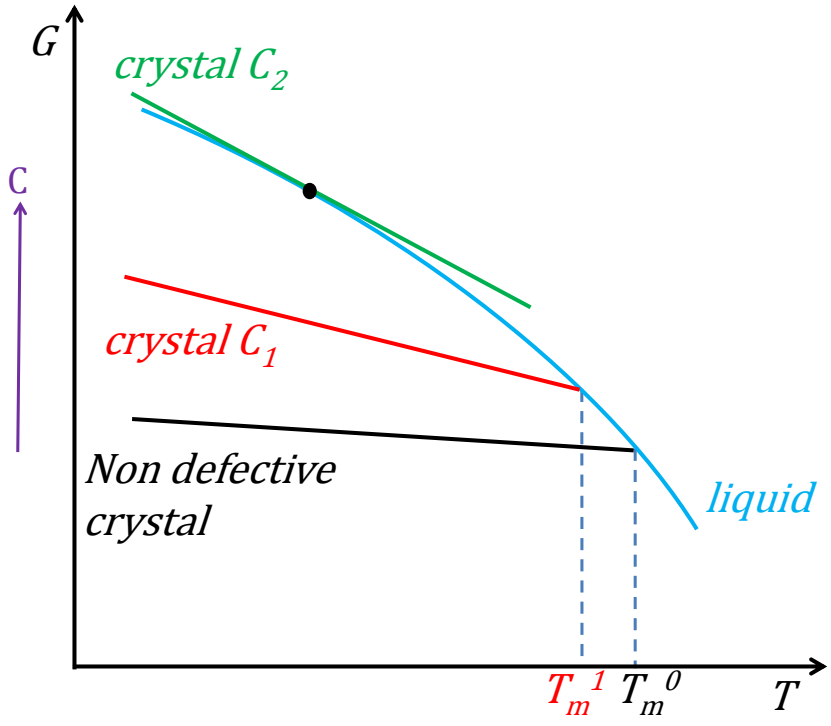

Figure 1.12 – Schematic representation of the Gibbs diagram of a perfect crystal (C = 0), a crystal containing a concentration C1 of defects, and a crystal containing a concentration C2 (C2 > C1) of defects according to the Fecht theory.

Theory of driven alloys: out of equilibrium view

The theory of driven alloys developed by Martin and Bellon aimed to model the behaviour of metallic alloys under irradiation [124]. It has been extended afterwards to the case of mechanical milling [125].

In normal thermodynamic conditions and without any external solicitation, an alloy explores its configuration space in such a way that it will frequently explore the most stable state (the state having the lowest Gibbs free energy). This exploration is made by thermally activated jumps of molecules. The frequency of the jumps depends on the environment of the atoms which is also changed by the atomic motions [126]. It is thus possible to describe the equilibrium configuration by a concentration profile corresponding to the stationary solution of the appropriate diffusion equation of the system [124].

In the theory of driven alloys, the idea is to assume that under external solicitations, the system explores the same configuration space than without solicitations, but in a different way. This exploration is governed by two mechanisms acting simultaneously: the jump of atoms thermally activated and the « ballistic jumps » due to external solicitations. In contrast to the « thermal jumps » which depend on the temperature, the « ballistic jumps » essentially depend on the intensity of the solicitation and are highly correlated in space and time. The equilibrium state reached under forcing corresponds to the more visited part of the configuration space. It is a dynamical state which is generally different of the thermodynamic equilibrium state.

The theory also introduces the notion of effective temperature under perturbation (T_{eff}). It is such that the state of the system, which is milled at a temperature T, is in fact that which would be observed, in absence of milling, at the effective temperature:

$$T_{eff} = T(1 + \frac{D_{Bal}}{D_{Th}}) \tag{1.15}$$

D_{Th} is the rate of thermal jumps which is temperature dependent. This rate can be enhanced by the fact that forcing can amplify the noise level and can thus create extra defects. D_{Bal} is the ballistic jump frequency, which only depends on the milling intensity (which increases with rotation speed in the experiments described above) but does not depend on temperature.

The competition of both effects clearly appears in the expression of T_{eff}. The model is able to reproduce, in a consistent way, the tendencies observed experimentally concerning the nature of the final states which are reached under perturbations, namely: amorphisation (equivalence of a melting) at high enough milling intensity or (and) low enough temperature (see figure 1.13).

1.3.2 Spray-drying

The spray-drying is an alternative method for achieving the amorphous state of pharmaceutical compounds [34, 127]. The starting compound (compound to amorphise by spray-drying) has to be first dissolved in a solvent. Afterwards, the obtained liquid solution is spray-dried.

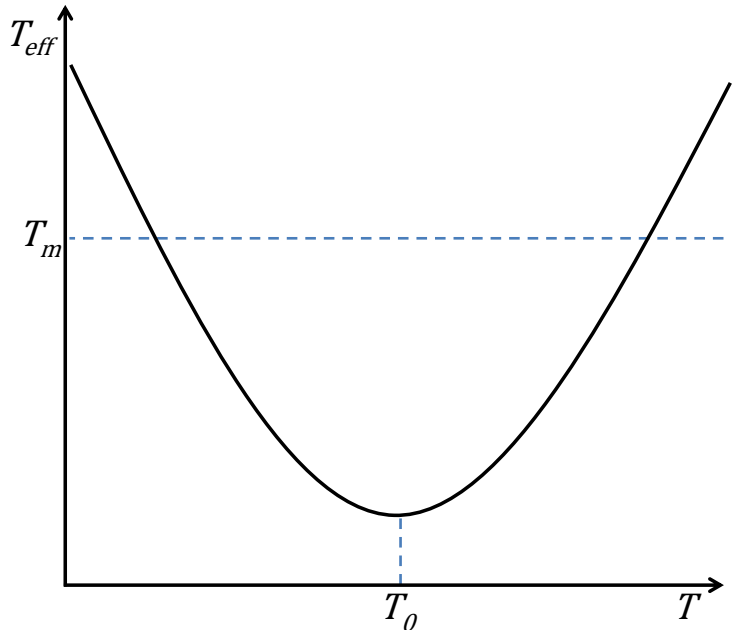

Figure 1.13 – Evolution of the effective temperature with respect to the temperature. At high temperatures (above T_0), the thermal effect is more important than the ballistic effect, and the effective temperature corresponds to the real one. At low temperatures (below T_0), the ballistic effect becomes more important than the thermal one, and the effective temperature becomes higher than the real one. It can even become higher than the melting temperature of the system, for very low temperature values.

The spray-drying process can be divided into two stages, namely the atomisation and the drying stages:

- The atomisation stage produces droplets of the starting solution. The kind of atomiser (rotary for example) directly impacts on the size of the droplets to be dried (spherical particles with a consistent size distribution, from sub-micron to micron diameter) [128]. The droplet size can also be influenced by the feed concentration and solution viscosity of the starting solution. This stage is less likely to influence the final state obtained compared to the drying stage.

- The drying stage is a complex transformation process from droplet to dry particles involving both heat and mass transport in a timescale of milliseconds [129]. During this stage, there are rapid and significant changes at the surfaces of the droplets in terms of distribution and movement of the components [129, 130].

There are some compounds that have been amorphised by spray-drying. As an example, figure 1.14 shows DSC curve of a lactose sample obtained by spray-drying (plot C), recorded upon heating. It shows a specific heat jump around 100 °C characteristic of a glass transition. This indicates that the spray-dried sample is a glass.

To the best of our knowledge, there is almost no theory explaining the physical mechanisms governing the transformations under spray-drying as in the case of the milling. It shall however be specified that there are several experimental parameters that can impact the properties (physical state, moisture content, particles size and morphology...) of the

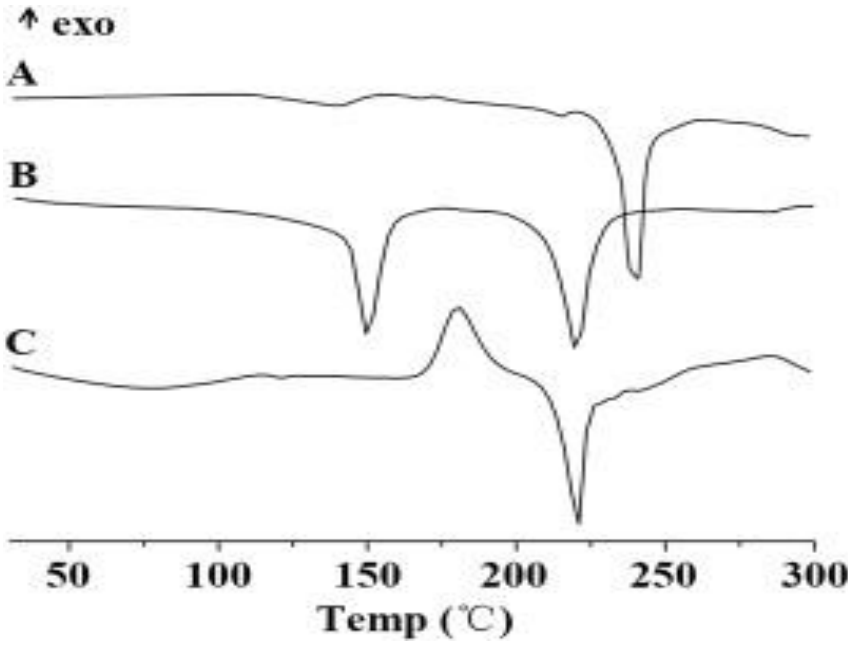

Figure 1.14 – DSC curves of different forms of lactose. (A: anhydrous lactose; B: lactose monohydrate; C: spray-dried lactose). Taken from [131].

spray-dried powder [132, 133]. Among them, one can mention the nature of the solvent (organic or water), the inlet temperature, the outlet temperature, the feed rate and the atomising gas flow. In particular, the physical state of the spray-dried compound is governed by the molecular mobility of the solute. Whether the drying process leads to crystallisation or amorphisation highly depends on the glass transition temperature in relation to the drying outlet temperature and the crystallisation kinetics of the material. As an example, low glass transition temperature compound does not generally allow obtaining a stable amorphous sample. This is due to the fact that the outlet temperature (T_{out}) of the dryer is higher than T_g. The sample produced will then recrystallise (to the initial form or not) if $T_{out} < T_m$ (melting temperature of the crystalline form of the compound), and liquefies if $T_{out} > T_m$.

Spray-drying is a fast method for obtaining substances in powder form. It can operate even with a laboratory setup. Spray-drying is used in different fields where the production of a free-flowing powder is required. This includes in particular the pharmaceutical, food and cosmetic industries. In food industry, it is also used for powder milk, powder coffee, etc. One main advantage of spray-drying is the possibility to dry a large range of compounds without major detrimental effects. The advantages of the spray-drying compared with freeze-drying (see next section) are the greater throughput rate and the short process times.

1.3.3 Freeze-drying

The freeze-drying (lyophilisation) is another method used to amorphise pharmaceutical compounds [134]. The starting compound (compound to amorphise by freeze-drying) has to be first dissolved in a solvent. Afterwards, the obtained liquid solution is freeze-dried.

Freeze-drying is a two steps experiment:

- Freezing step: firstly, the liquid solution (solvent plus solute) is frozen at low tempe-

rature. During this step, the solvent is separated from the solute to form crystals of solvent. This leads to solute molecules concentration separated by crystals of solvent. This formation of phase-separated, concentrated domains and solvent crystals, may initiate the formation of disordered phases.

- Drying step: secondly, solvent crystals are removed by sublimation under high vacuum. A second drying step is generally necessary to remove any residual moisture. This second drying is generally performed at higher temperature (20-60 °C).

The powder produced is generally an amorphous powder made of a lot of small voids.

There are some compounds that have been amorphised by freeze-drying. For example, figure 1.15 shows DSC curve of a trehalose sample obtained by freeze-drying, recorded upon heating (5 °C/min). It has a specific heat jump around 118 °C characteristic of a glass transition. This indicates that the freeze-dried sample is a glass.

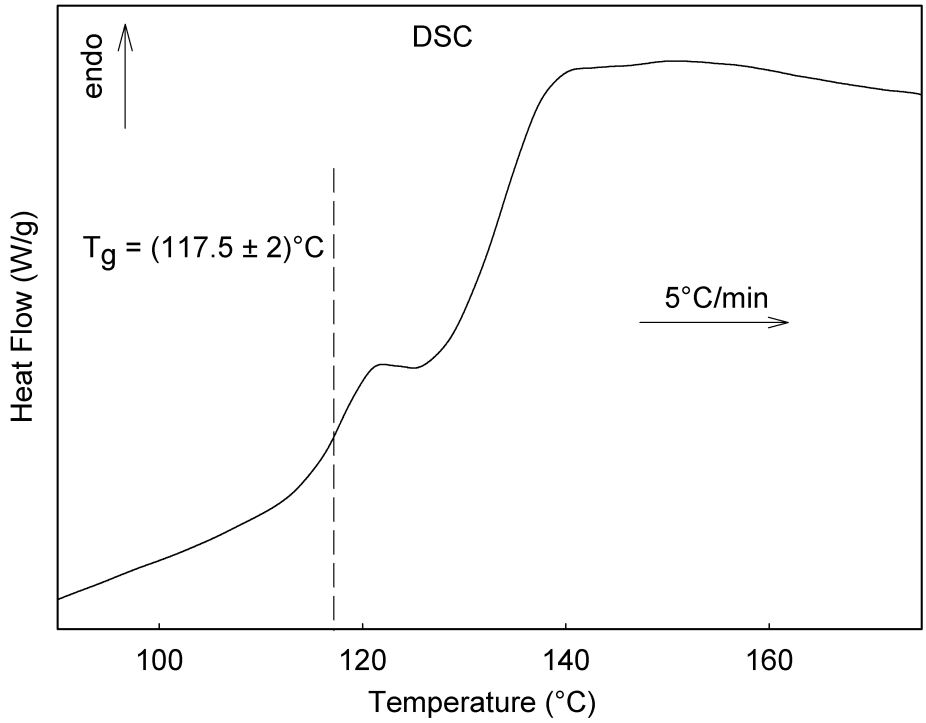

Figure 1.15 – Heating (5 °C/min) DSC curve of freeze-dried trehalose. Taken from [46].

To the best of our knowledge, there is almost no theory explaining the physical mechanisms governing the transformations under freeze-drying as in the case of the milling. Nevertheless, if the molecular mobility of the compound is not high enough to recrystallise during the freezing step, the sample produced will always be amorphous. This is why freeze-drying operations almost always lead to amorphous sample. It shall however be mentioned that the nature of the solvent, the number of desiccation cycles can impact the properties (moisture content, texture...) of the freeze-dried powder [35, 135, 136].

Freeze-drying has been used since 1250 B.C. as a method for conserving food. Since this time, its application in various fields has increased, particularly in the health care and food industries. In pharmacy, it raises a growing interest since it produces an amorphous powder having a very fast dissolution rate. The application of freeze-drying has been significantly expanded to include manufacturing orally disintegrating tablets, inhalable powders, etc. Many of the recent applications of freeze-drying are related to its ability to produce low-density and highly porous material.

The main difference between spray-drying and freeze-drying methods lies in how water is removed (see figure 1.16). For the spray-drying method, water is removed at the liquid state, by a sudden drying of the droplets. For the freeze-drying, water is removed at the solid state, by sublimation of ice crystals. We will see the importance of this difference in chapter 5.

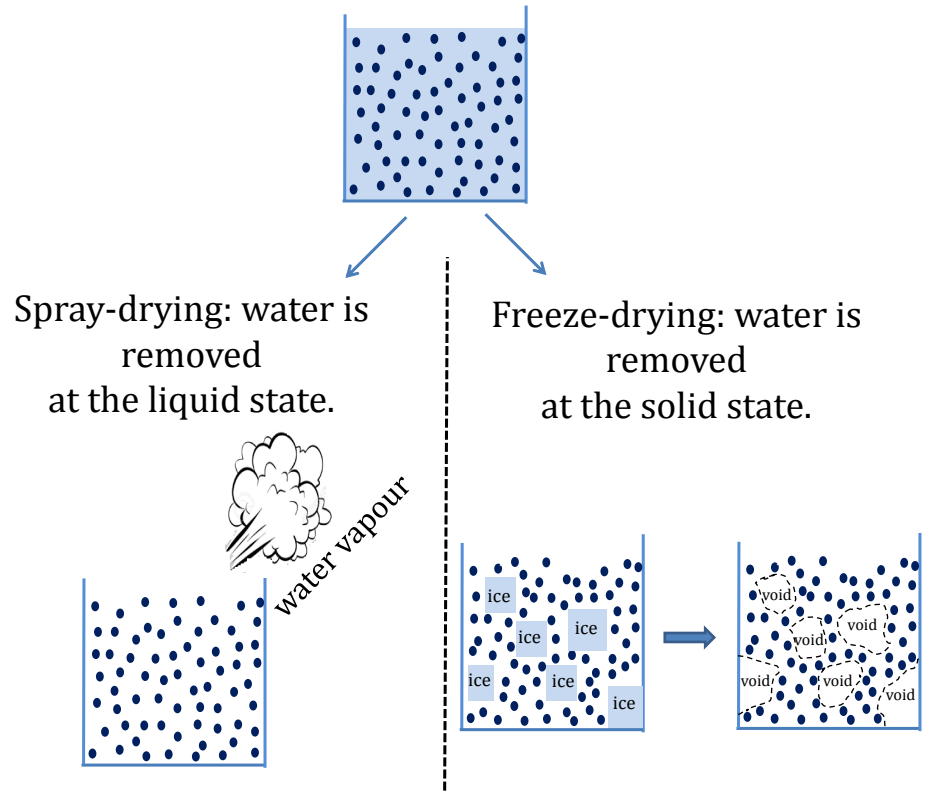

Figure 1.16 – Schematic representation of the differences between spray-drying and freeze-drying amorphisation methods.

Chapter 2

Presentation of lactulose - Experimental and simulation methods

Contents

This chapter is divided into four sections. In the first section, we will present general interests of lactulose in pharmaceutical and agrochemical applications. Then, physical and chemical properties of lactulose will be detailed with a special attention to its mutarotation properties. In the second section, experimental details about the amorphisation techniques used in this work will be given. The third section aims to give some experimental details about the characterisation techniques used in this thesis (besides the neutron scattering technique). For each of those techniques, the working principle will be presented beforehand. The fourth section will be dedicated to the simulation performed during this work. It will present both theoretical background and simulation details.

2.1 Properties of lactulose

2.1.1 Lactulose in pharmaceutical and agrochemical applications

Lactulose is a synthetic disaccharide that can be obtained from lactose by different synthesis methods. Chemical methods are based on the isomerisation of lactose in the presence of basic catalysts [137], and enzymatic methods use lactose as a galactose donor and fructose as a galactose acceptor [138]. The prebiotic properties of lactulose have been known for more than fifty years, and several studies have confirmed health benefits of lactulose as a food ingredient. Lactulose is thus widely used in food and pharmaceutical industry:

- In pharmacy, lactulose is commonly used as a laxative (for treatment of constipation) [139], in oral or rectal administration. It is also used for the improvement of calcium absorption, for selective stimulation of intestinal flora. Lactulose is useful in treating hyperammonemia (high blood ammonia), which can lead to hepatic encephalopathy [140]. It can be also used as a test of small intestine bacterial overgrowth (SIBO), for the treatment of diseases such as inflammatory bowel disease, reducing blood ammonia levels, colon carcinogenesis, tumor prevention and immunology [139]. It is also sometimes used as an excipient.

- In food industry, the use of lactulose in fermented milk manufacture may reduce the incubation period and favour the growth of Bifidobacterium. It is used as a sweetener in special dietary foods. With the growing interest in functional foods, the use of no digestible oligosaccharides such as prebiotic ingredients has increased during last decade. In this context, lactulose as a well-known prebiotic offers excellent possibilities to develop new functional foods. It can thus be used as a food additive in several cases [139, 141].

2.1.2 Chemical properties

Lactulose is a disaccharide belonging to the class of organic compounds known as o-glycosyl compounds: these are glycoside in which a sugar group is bonded through one carbon to another group via an O-glycosidic bond. At room temperature, it appears as a white powder and has a sweet flavour. Its chemical formula is $C_{12}H_{22}O_{11}$, for a molecular weight of 342.28 g/mol. As many other sugars (glucose [142], lactose [143], galactose [144], fructose [142] ...) lactulose exhibits a rich tautomerism and is prone to mutarotation.

The difference between tautomers and anomers should be specified here:

- Tautomers are constitutional isomers of organic compounds that are in dynamic equilibrium due to the migration of protons. A reaction involving simple proton transfer between different polar atoms in an intramolecular fashion is called a tautomerisation.
- Anomers are sub-category of tautomers that only differ in the position of the hydroxyl group –OH with respect to the $–CH_2OH$ group, around the carbon cycle.

A striking feature of lactulose is that it refers to not less than five tautomers [1] as seen in figure 2.1:

1) The galactosyl β-furanose tautomer having one cycle of five carbon atoms, and one of six carbon atoms.

2) The galactosyl α-furanose tautomer also having one cycle of five carbon atoms, and one of six carbon atoms. It differs to the galactosyl β-furanose tautomer in the orientation of the group -OH-CH_2OH presents in the cycle of five carbon atoms.

3) The galactosyl β-pyranose tautomer having two cycles of six carbon atoms.

4) The galactosyl α-pyranose tautomer having also two cycles of six carbon atoms. It differs to the galactosyl β-pyranose tautomer in the orientation of the group -OH-CH_2OH presents in one of their cycle of six carbon atoms.

5) The fifth tautomer is a partially open-chain molecule (molecule in the middle of figure 2.1).

In 1938, H. S. Isbell and W. W. Pigman [145] have established that the mutarotation in lactulose (4-galactosido-fructose, probably the galactosyl β-furanose tautomer) consists in a partial conversion of a furanose to a pyranose. More recently, Jeffrey et al. [51] established that the mutarotation of the lactulose in solution could be a conversion from one of the four first molecules mentioned above to another one, by going through the open-chain molecule (the fifth one) as it can be seen in figure 2.1. The interconversion probabilities in solution are different from one pair of tautomers to another. The concentrations at equilibrium are thus different for the different tautomers. For example, Jeffrey [146] has shown that a freeze-dried lactulose has 65 % of galactosyl β-pyranose (molecule n°3 in figure 2.1), 24% of galactosyl β-furanose (molecule n°1 in figure 2.1), and 11% of galactosyl α-furanose (molecule n°2 in figure 2.1). (See table 2.2)

As it can be noticed, this quantification indicates that there are only three tautomers in the freeze-dried lactulose. There was no evidence of the presence of the galactosyl α-pyranose tautomer (molecule n°4 in figure 2.1) or the open-chain molecule (molecule in the middle of figure 2.1) in the solid state.

Thereafter, we will only consider the following three tautomers:

- The galactosyl β-furanose (noted tautomer A in figure 2.1)
- The galactosyl α-furanose (noted tautomer B in figure 2.1)
- The galactosyl β-pyranose (noted tautomer C in figure 2.1)

In the following, they will be named tautomer A, B and C, respectively.

[1] In reality, the open-chain molecule in figure 2.1 is an epimer of the other four, and all the molecules should then be named “epimers”. However, for reasons of simplicity, we have named all of them “tautomers”.

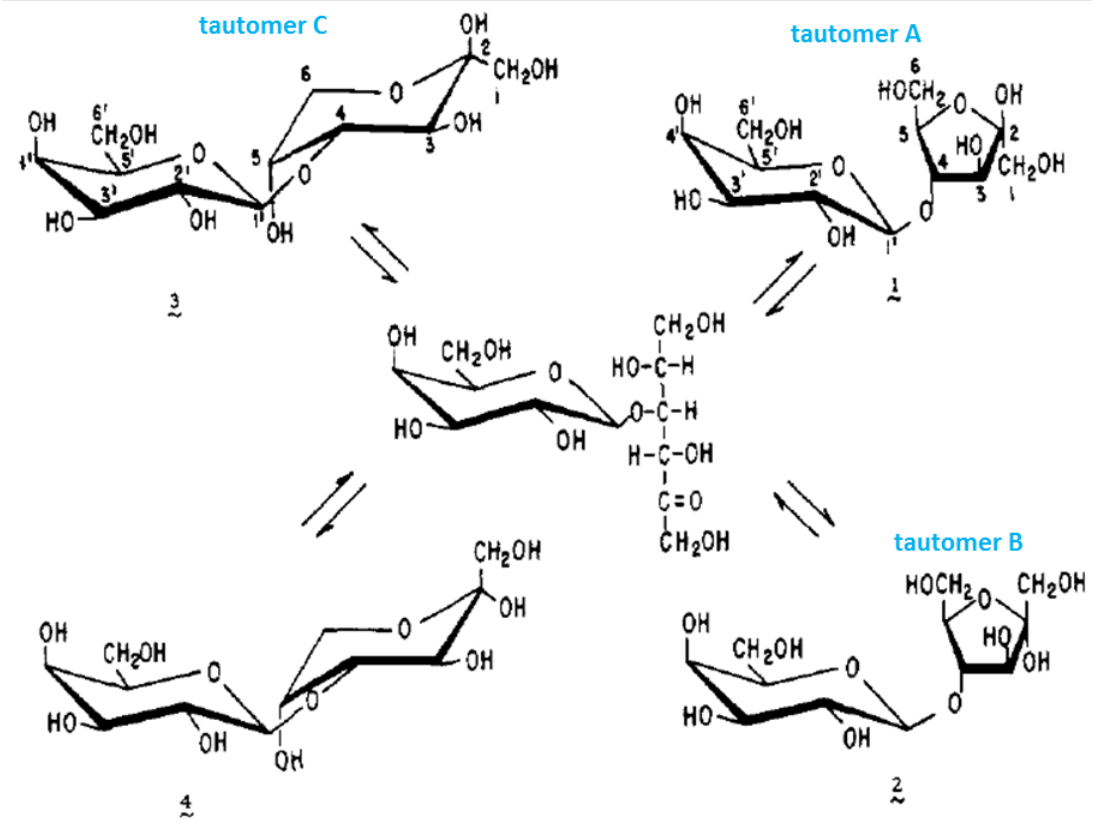

Figure 2.1 – Tautomers of lactulose in equilibrium in aqueous solution. Taken from [51].

2.1.3 Physical properties

We present here the main physical properties of the three solid forms of lactulose, which have been reported up to now:

- The anhydrous crystalline form.
- The trihydrate crystalline form.
- The amorphous form.

2.1.3.a) The anhydrous crystalline form

Anhydrous crystalline lactulose is not "tautomerically" pure. NMR analysis performed by Jeffrey et al. [51] indicated the presence of tautomers A, B and C in the anhydrous crystalline lactulose in the ratio 74.5%, 10.0% and 15.5%, respectively (see table 2.2). They also determined the crystal structure of the anhydrous crystalline form by X-ray diffraction [51]. The structure was determined assuming that the majority tautomer (tautomer A in figure 2.1) was the only one in the crystal. In this assumption, the structure was found to be monoclinic with a space group $P2_1$, and a multiplicity Z = 2. The cell parameters are the following:

$$a = 7.420(3)\ \text{Å}, b = 19.257(6)\ \text{Å}, c = 5.355(2)\ \text{Å}, \beta = 103.88(3)°, \alpha = \gamma = 90°$$

It must be mentioned that a detailed diffraction analysis of the anhydrous crystalline lactulose considering the three tautomers has never been done.

The melting temperature of the anhydrous crystalline lactulose has been estimated at T_m = 169 °C by Miller et al. [48]. The heat of solution at infinite dilution of the crystalline sample at 25 °C is 2 kJ/mol [48]. This value is really small compared to the value of similar disaccharides. Indeed, for trehalose and lactose, the heat of solution at infinite dilution of the crystal is 20 kJ/mol [48].

2.1.3.b) The trihydrate crystalline form

The tautomeric composition and the crystalline structure of lactulose trihydrate were determined by Jeffrey et al [146]. Crystals of lactulose trihydrate were obtained from a 70% aqueous solution of lactulose that was kept at 4 °C for several months. More crystals were obtained by using these initial trihydrate crystals to seed a solution prepared by dissolving the anhydrous lactulose into a small amount of water with gentle warming, then cooling to room temperature. NMR analyses of the trihydrate crystalline lactulose [146] have shown that it only contains the tautomer A, which is the main tautomer in the anhydrous form (see table 2.2). The crystal structure refinement of X-ray diffraction data of the sample established that the trihydrate form is orthorhombic, with a space group $P2_12_12_1$, and a multiplicity Z = 4. The cell parameters are as follows:

$$a = 9.6251(3)\ \text{Å}, b = 12.8096(3)\ \text{Å}, c = 17.7563(4)\ \text{Å}, \alpha = \beta = \gamma = 90°$$

Crystallographic parameters of the two known crystalline forms of lactulose are reported in table 2.1.

Table 2.1 – Crystallographic parameters of the two known crystalline forms of lactulose.

Properties	Anhydrous crystal	Trihydrate crystal
Space group	$P2_1$ (Monoclinic)	$P2_12_12_1$ (Orthorhombic)
a(Å)	7.420	9.6251
b(Å)	19.257	12.8096
c(Å)	5.355	17.7563
α(°)	90	90
β(°)	103.88	90
γ(°)	90	90

It is worth mentioning that what is generally called “lactulose” refers to a single molecule (the tautomer A), although in reality, lactulose can be just the tautomer A (as in the trihydrate crystal) or a mixture of three different molecules (the tautomers A, B and C – as in the anhydrous crystal) in different proportions. The absence of individual properties of tautomers B and C such as X-ray diffraction patterns indicates that there is no crystalline form only composed of the tautomer B or only composed of the tautomer C.

2.1.3.c) The amorphous form

Amorphous glassy lactulose can be easily obtained by melt quenching of the anhydrous crystal form. Several groups have determined the lactulose glass transition temperature T_g. The measured T_g range between 79 °C and 94 °C [48–50]. The fragility index of amorphous lactulose has been estimated to be m = 134±20 by Kaminski et al. [49]. The heat of solution at infinite dilution of amorphous lactulose at 25 °C is equal to -25.5 kJ/mol [48].

Table 2.2 – Tautomeric composition of different lactulose forms obtained by Jeffrey [51, 146].

Samples	Tautomer A (%)	Tautomer B (%)	Tautomer C (%)
Anhydrous lactulose (crystal)	74.5	10.0	15.5
Trihydrate lactulose (crystal)	100.0	0.0	0.0
Dehydrated lactulose trihydrate	40.8	21.7	37.5
Water “equilibrated” lactulose	24.0	11.0	65.0

2.2 Amorphisation techniques used in this thesis

This section gives the experimental details of the techniques used to prepare the different amorphous samples of lactulose. For all those techniques, the starting compound was the anhydrous crystalline lactulose purchased from Sigma Aldrich. It was more than 98% pure and has been used without further purification.

NB: There is no available description of the experimental protocol used by the Sigma Aldrich Company to produce lactulose.

2.2.1 Quenching from the melt

Amorphous lactulose was produced by heating the crystalline lactulose powder just above the melting temperature, and subsequently cooling the obtained liquid at room temperature. This operation was done directly inside the DSC calorimeter or using an external furnace when a large amount of amorphous material was required. In the latter case, 1 g of lactulose was melt in a furnace and then quenched at room temperature. The quenched liquid was then powdered by a slight crushing.

2.2.2 Milling

Amorphisation by milling was performed using a high-energy planetary mill « Pulverisette 7 » commercialised by Fritsch [147]. It consists of a solar disk on which two milling bowls of 45 ml are fixed (see figure 2.2). Each milling bowl contained seven grinding balls in zirconium oxide (see figure 2.2), material known for its high resistance to collisions.

The working principle of this ball miller can be seen in figure 2.3.

The comminution of the sample to be milled takes place primarily through the high-energy impact of milling balls. For this purpose, the milling bowl, containing the material to be milled and milling balls, rotates around its own axis on the solar disk whilst rotating rapidly in the opposite direction (rotation speed can reach 800 rpm). This creates antagonist centrifugal forces. The milling balls then cross the bowl at high speed and further mill the sample material by impacts against the opposite bowl wall. In addition, impacts between the balls themselves on the sample material add to the size reduction process.

Figure 2.2 – (left) Planetary mill, Pulverisette 7 of Fritsch.
(right) Grinding bowl, containing seven balls, used in the planetary ball miller.

For the reproducibility of the milling operations, the following parameters have been systematically used:

- The crystalline powder was dried at 50 °C during 30 min, before milling.
- The rotation speed of the milling bowls was set to 400 rpm.
- 1.1 gram of powder was put into a milling bowl having 7 balls.
- Milling periods (15 min) were alternated with pause periods (15 min) to avoid any local heating of the powder induced by the mechanical shocks.
- The samples were milled at room temperature, and at ambient humidity.

Crystalline samples were milled during periods varying from 0 to 8 hours.

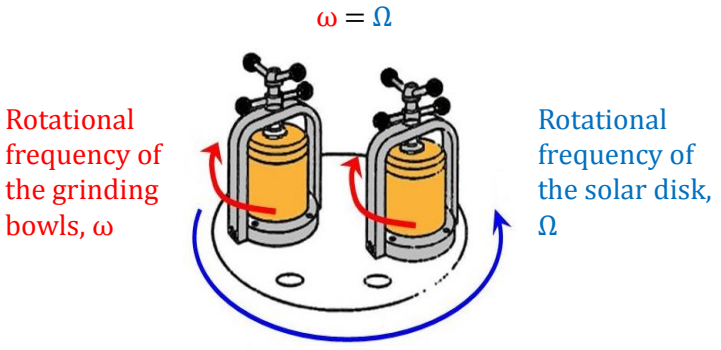

Figure 2.3 – Schematic representation of the working principle of the Pulverisette 7 ball miller.

2.2.3 Spray-drying

Amorphisation by spray-drying[2] was done using a B-290 mini spray-dryer, commercialised by Buchi [148]. A representation of the spray-dryer can be seen in figure 2.4.

To produce an amorphous powder by spray-drying, the initial lactulose powder is put into solution. The solution is then injected in a spraying nozzle where it is sprayed in a box heated at a high temperature (inlet temperature). Afterwards, the product is expelled to a second region (at an outlet temperature) colder than the box. The final product is then collected.

Figure 2.4 – B-290 mini spray-dryer of Buchi.

For the reproducibility of the spray-drying operations, the following parameters were always used:

- 5 g of lactulose were dissolved into 50 ml of water.
- The solution was injected into a 0.7 mm nozzle, at a feed rate of 5 ml/min, with an air flow rate of 601 l/h.

[2] All the spray-drying operations performed in this thesis have been done in INSERM research group heads by Prof Jurgen Siepmann (Univ. Lille 2). We thank very much Dr Mounira Hamoudi for all her help and support in spray-drying operations.

- The inlet temperature was set to 120 °C.

- The outlet temperature was set to 70 ± 5 °C.

2.2.4 Freeze-drying

Amorphisation by freeze-drying[3] was done using the Epsilon 2-4 LSC freeze-dryer, commercialised by Christ [149]. A representation of Epsilon 2-4 LSC can be seen in figure 2.5.

To produce an amorphous material, the initial crystalline powder is dissolved into aqueous solution. The solution is then frozen directly in the freeze-dryer. Then after, the main drying phase starts. The vacuum pump is turned on, the pressure inside the drying chamber is lowered to a value that corresponds to the freezing temperature (according to the phase diagram of ice), and thus the sublimation of the ice starts. The freezing step has to be not too fast to avoid the formation of small ice crystals, which have a negative effect on the duration of the drying process. A last drying step is done to have a product with minimal residual moisture. This step is optional, and is performed under the lowest possible pressure (according to the phase diagram of ice, with respect to the drying temperature). The vacuum pump is then switched off, the drying chamber aerated with ambient air, and the product is taken away.

Figure 2.5 – Epsilon 2-4 LSC freeze-dryer of Christ.

[3] All the freeze-drying operations performed in this thesis have been done in INSERM research group heads by Prof Jurgen Siepmann (Univ. Lille 2). We thank very much Dr Mounira Hamoudi for all her help and support in freeze-drying operations.

For the reproducibility of the freeze-drying operations, the following parameters were always used:

- 5 g of lactulose were dissolved into 50 ml of water.
- The solution was then frozen at -45 °C during 4 hours.
- This frozen solution was then sublimated at -20 °C during 30 hours under a pressure of 0.07 mbar.
- The second desiccation step was done at 35 °C during 40 hours under a pressure of 0.0014 mbar for removing the remaining water.

2.3 Experimental characterisation

We present here all the characterisation methods used in this thesis to investigate the physical properties of amorphous lactulose, except neutron scattering. The latter will be presented in chapter 5.

2.3.1 X-ray diffraction

2.3.1.a) General principle

X-ray diffraction is a common technique used to determine the structure and microstructure of a sample.

Its principle is the following: an X-ray beam is directed toward the sample. The interaction of the incident beam with the sample (precisely the electrons of the sample) produces waves that can interfer constructively or not [4]. In the case of a crystalline structure, constructive interferences are obtained when the Bragg law is satisfied: $n\lambda = 2d_{hkl}\sin\theta$, where θ is the angle between the incident beam and the atomic plan (hkl), d_{hkl} is the distance between (hkl) planes, and λ the wavelength of the X-ray beam.

The X-ray intensity diffracted by the sample is then detected against the diffraction angle. By scanning the sample through a range of diffraction angles, all possible diffraction directions of the lattice are attained (in the case of a powdered material, due to the random orientation of the crystallites), and the full diffraction pattern of the sample is thus obtained. A layout illustrating the Bragg law is presented in figure 2.6.

There is a lot of information that can be retrieved from a powder diffraction pattern, as it is shown in figure 2.7.

It must be noted that, for the specific case of hydrogenous molecular systems, the analysis of the diffraction pattern obtained is tricky, since:

- The symmetry of those systems is generally low (monoclinic, triclinic). This gives rise to an important number of peaks, and then leads to an overlapping of some of them. The line profile analysis thus becomes difficult.

[4] Waves interfer only if the wavelength of the incident beam is of the order of magnitude of the atomic distances in the system. This condition is always satisfied with the X-ray produced.

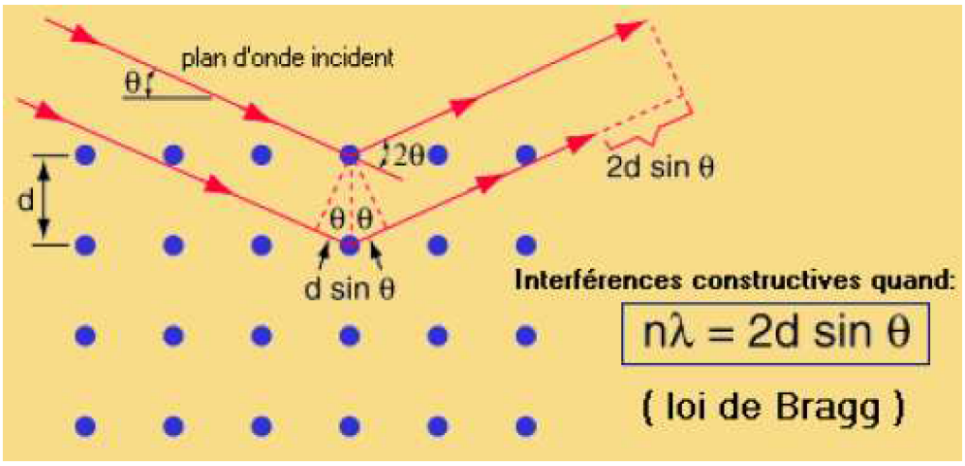

Figure 2.6 – Layout illustrating the Bragg law.

- X-ray are not very sensitive to H atoms because they have only one electron. The influence of hydrogen bonding, which generally determines the stability of the sample, is thus not well assessed.

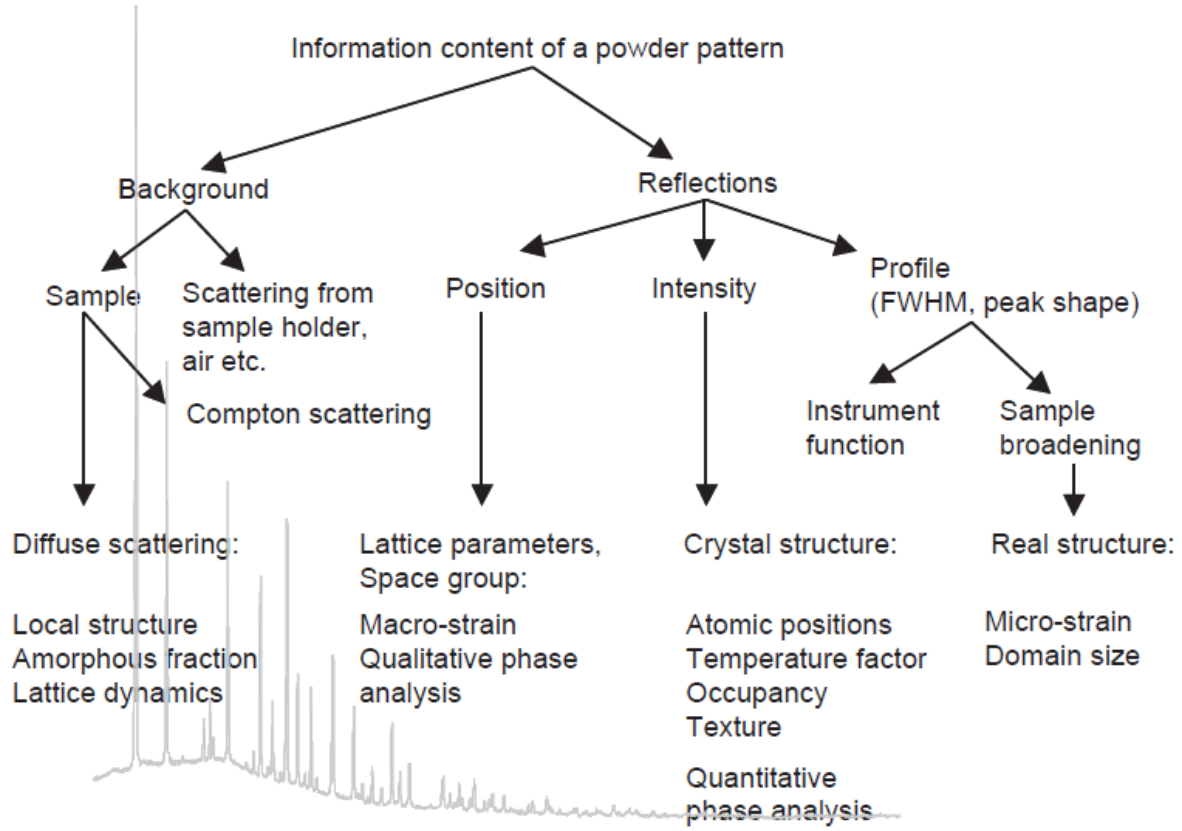

Figure 2.7 – Information content of a powder diffraction pattern. Taken from [150].

2.3.1.b) Experimental details

For all the X-ray diffraction experiments performed in this work, the X'Pert Pro diffractometer commercialised by Philips was used (see figure 2.8). The X-ray beam is produced by a Cu

anode tube (λ=1.54 Å), and is detected with an X'celerator detector [151].

Figure 2.8 – X'pert pro diffractometer of Philips.

In this thesis, X-ray diffraction (XRD) experiments have been done to characterise materials in a qualitative manner:

- To discriminate between crystalline vs amorphous phases.
- To detect the apparition of new phases after a mechanical or thermal treatment.

The diffractometer can be used in two different setups:

- One setup allowing studying samples fill in a capillary tube, which has the advantage of reducing preferred orientations.
- One setup allowing studying samples put on a flat plate, which has the advantage of being really easy to prepare.

Only the first setup was used in this thesis. The configuration generally used to measure samples in a capillary tube is a Debye-Scherrer setup mounted in transmission geometry [150, 152] (see figure 2.9). Some slits are put just after the anode to control the divergence of the beam. Afterwards, the divergent beam from the X-ray anode crossed a curved monochromator. This monochromator focusses the beam and absorbs Kβ radiation of Cu. The final beam (before the sample) thus contained $K\alpha_1$ (λ = 1.541 Å) and $K\alpha_2$ (λ=1.544 Å) radiations of Cu. The presence of $K\alpha_1$ and $K\alpha_2$ wavelengths leads to splitting of the peaks that are much more visible at higher 2θ angles.

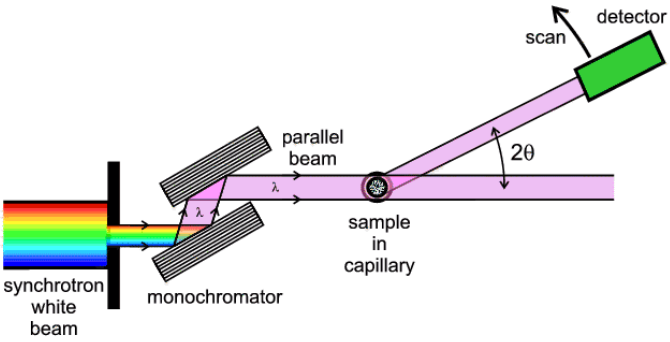

Figure 2.9 – Schematic representation of the Debye Scherrer geometry.

The samples were always filled into a Lindeman glass capillary of 0.7 mm diameter and spun during the scan in order to scale down effects of preferred orientations.

For all the diffraction patterns obtained during the different measurements, the Bragg angles are given with 0.1° of precision. Data were recorded from 5° to 60° by step of 0.0167° using a counting time of 50 s per step (which corresponds roughly to 22 min 30 s). The results were analysed using the FullProf software [153].

2.3.2 Thermogravimetric Analysis (TGA)

The TGA allows measuring the variations of the weight of the sample with respect to the temperature, or at a given temperature with respect to the time. This technique has been used in this work to detect moisture content and thermal degradation of the samples.

The instrument used is the Q500 (see figure 2.10) of TA Instruments [154]. For the reproducibility of the experiments, the following parameters were used:

- Around 5-8 mg were filled in a platinum boat.
- During the experiment, the sample was flushed with a dry nitrogen flux of 60 ml.

The temperature reading was calibrated using the Curie points of alumel and nickel, while the mass reading was calibrated using balance tare weights provided by TA Instruments.

The results were analysed using the Universal Analysis software of TA Instruments.

2.3.3 Differential Scanning Calorimetry (DSC)

2.3.3.a) General principle

The DSC is an analysis method that allows following the evolution of the thermodynamic state of a sample during heating, cooling or isothermal treatments.

A DSC experiment can be basically explained as follows: a reference and a sample are placed onto, respectively, the reference platform and the sample platform that are into a common furnace. Each platform is connected to a thermocouple. The heat flow absorbed or emitted by the sample is then measured by estimating the difference between the sample temperature and the reference temperature continuously measured by the thermocouples.

Figure 2.10 – Q500 of TA Instruments.

2.3.3.b) Experimental details

DSC and MDSC (Temperature Modulated DSC, see annex A) experiments have been performed using the DSC Q1000 and Q200 of TA Instruments (see figure 2.11) [155]. These calorimeters are equipped with an RCS (Refrigerated Cooling System), which allows covering a large temperature range, from -90 °C to 550 °C.

Small amounts of sample (3-5 mg) were placed into an aluminum DSC pan, so that they can be able to best follow the temperature variations commanded by the instrument. The samples were usually placed in open pans (pans without lid) to allow any water absorbed during the preparation process to evaporate upon heating. A continuous dry nitrogen flow crossing the container improves the heat transfers, the homogeneity of the temperature in the cell, and helps to evacuate all polluting elements (humidity, oxygen). A schematic representation of the DSC cell is shown in figure 2.12.

In general:

- DSC experiments were performed from 20 °C to 200 °C using a heating rate of 5 °C/min.
- MDSC experiments were performed from 20 °C to 200 °C, using a medium heating rate of 5°C/min, a modulation amplitude of 0.663 °C and a modulation period of 50 s. Those parameters correspond to conditions of “heat only”. This means that, despite the modulation, the sample is never cooled during the experiment.

Temperature and enthalpy readings were calibrated using pure indium at the same scan rates used in the experiment. The results were analysed using the Universal Analysis software of TA Instruments. The reference glass transition temperature of each sample was defined as the midpoint of the glass transition heat flow jump.

2.3.4 Isothermal calorimetry of dissolution

The isothermal calorimetry of dissolution allows measuring the dissolution enthalpy of a sample at a given temperature. In this thesis, we have used this technique to measure the

Figure 2.11 – DSC Q200 of TA Instruments.

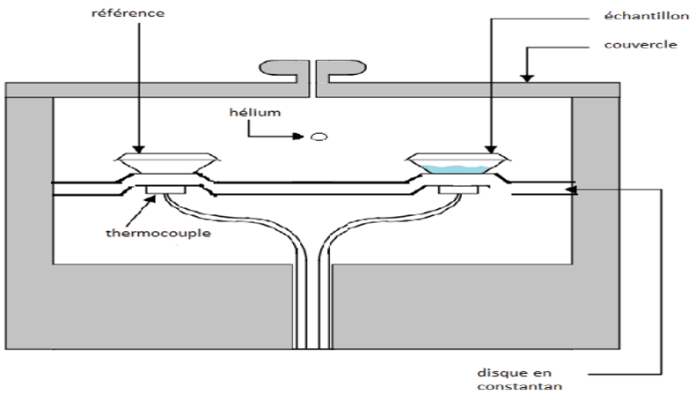

Figure 2.12 – Schematic representation of the DSC cell.

amorphous fraction of a material in the course of a milling process.

The instrument used is the C80 calorimeter of Setaram (see figure 2.13 (a)) [156]. It has a reversing cell, which allows mixing the solvent with the solute. For our measurements, we have used two reversal cells (see figure 2.13 (b)):

- One sample cell: having the sample in the bottom compartment and the solvent (water in our case) in the top compartment.
- One reference cell: having just the solvent in the above compartment, and in the same quantity than in the sample cell.

At the limit between both compartments, small amount of paraffin oil was put into the

cells to improve the tightness of the two compartments. Thermocouple sensors allowing measuring the heat emitted or absorbed during the dissolution surround each of those cells. The experiment proceeds in several steps. All those steps are described in more details in chapter 4. The results were analysed with the Calisto Precessing software.

Figure 2.13 – (a) Picture of C80 calorimeter of Setaram. (b) Picture of the reversal cells.

2.3.5 Nuclear Magnetic Resonance (NMR)

2.3.5.a) General principle

The NMR spectroscopy is based on the fact that nuclei of atoms have magnetic properties that can be used to yield chemical information. It is an analytical chemistry technique used for determining the content and purity of a sample, as well as its molecular structure [157].

Quantum mechanics subatomic particles (electrons, protons and neutrons) can be imagined as spinning on their axes. For some atoms (such as ^{12}C) these spins are paired against each other, such that the nucleus of the atom has no overall spin. However, for many others (such as ^{1}H and ^{13}C) the nucleus does possess an overall spin. For the latter, an NMR experiment is possible.

An NMR experiment can be basically explained as follows: an external magnetic field is applied to the system. An energy transfer is possible between the base energy and a higher energy level (generally a single energy gap). This energy transfer takes place at a wavelength that corresponds to radio frequencies. When the external field is interrupted, the nuclear spin returns to its base level, emitting the corresponding energy difference. The signal that matches this transfer is thus measured and processed in order to yield an NMR spectrum for the nucleus concerned.

The precise resonant frequency of the energy transition depends on the effective magnetic field at the nucleus. This field is affected by electron shielding which is in turn dependent

of the chemical environment. As a result, information about the nucleus chemical environment can be derived from its resonant frequency. In general, the more electronegative the local environment of the nucleus, the higher the resonant frequency (notion of "deshielding" [157]) is.

2.3.5.b) Experimental details

In this study we have used the NMR 400 MHz spectrometer commercialised by Bruker (see figure 2.14) [158].

It was used to determine tautomeric proportions in amorphous lactulose. The quantification process is easy to perform when there is a well-defined peak on the spectrum, characteristic of one tautomer in particular. Solid-state NMR on amorphous solids gives very broad peak difficult to exploit. We have thus chosen to do liquid-state NMR. Jeffrey [146] performed its experiment on ^{13}C, but we have done proton NMR since proton NMR spectrometers were easier to access, and measured proton NMR spectra can be used for tautomeric quantification. Indeed, there is almost always one H atom – named anomeric proton- close to oxygen atoms (thus around electro-attractive atoms), which has an NMR peak completely deshielded with respect to the other peaks (because its local environment is electronegative). This deshielded peak generally facilitates the tautomeric quantification [159, 160]. [5]

About 10 mg of sample were dissolved into 0.75 ml of DMSO. This solvent has been used for its ability to slow down the mutarotation in solution [146, 161]. The signal was collected at room temperature just after (3 min) the dissolution, in order to limit as much as possible the tautomerisation. A 5 mm TBI probe was used for all the experiments. This probe is known to be very suitable for the acquisition of the signal during proton NMR.

The results were analysed using the TopSpin 3.5pl5 software of Bruker.

[5] Indeed, in the measured spectra, most of the signals heavily overlap, but the resonances of the anomeric proton of each tautomer are well separated from the others, and the proportion of each tautomer can thus be measured.

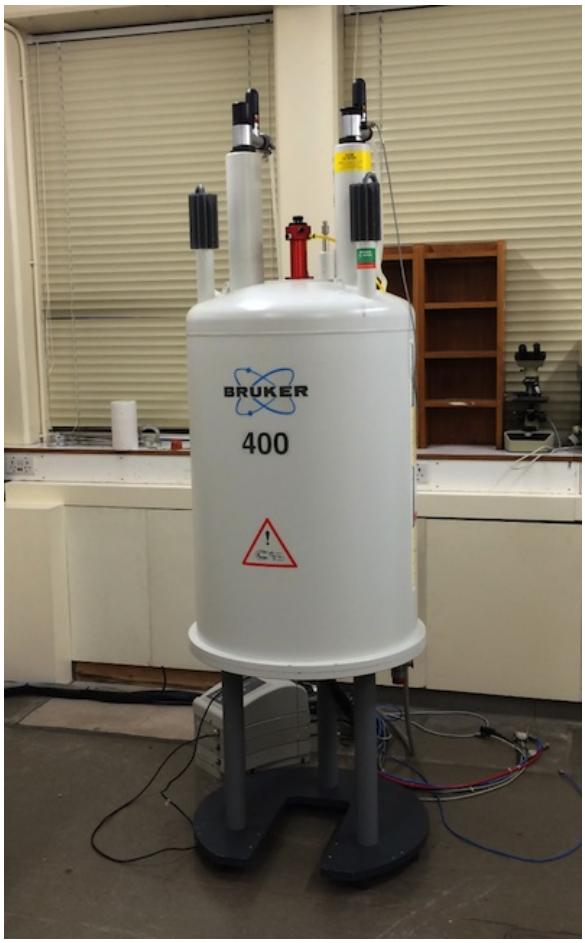

Figure 2.14 – NMR 400 spectrometer of Bruker.

2.4 Simulation methods

This section aims to give a brief understanding of the computational methods that have been used throughout this work as well as the computational and simulation details. Interested reader is referred to the excellent books of Allen and Tildesley [162], Haile [163], Rapaport [164], Frenkel and Smit [165] for a more comprehensive overview of Molecular Dynamics simulations. Books of Scholl [166], Dreizler [167], Parr [168] give a detailed presentation of the Density Functional Theory formalism.

The choice of the appropriate simulation method depends on the level of required accuracy, timescale, nature and size of the system. Quantum mechanical ab-initio methods such as Density Functional Theory (DFT) give the best level of realism on the calculated physical properties. However, they necessitate a significant computational power, which limits these techniques to the study of models made up of some hundreds of atoms at more, during a quite short timescale (1-100 ps in the case of Ab initio Molecular Dynamics simulations). For larger systems, empirical force fields (FF) methods such as Molecular Dynamics (MD) simulations have to be used, however giving less realistic results. Nevertheless, the goal of MD simulations is not to give a value close to the experimental one, but to reproduce (and therefore explain) the experimental tendencies. In general, MD simulations are employed to study physical or chemical phenomena that occur over a spatial scale between 0.1 nm and 100 nm, and a time scale between few fs and 100 ns.

As it will be continuously viewed along this thesis, a deep understanding of the complex features observed in the experimental data could not disregard the use of computational tools.

2.4.1 Ab initio methods

2.4.1.a) General principle

Background of ab initio methods: the quantum mechanics At the beginning of the 20th century, in order to explain fundamental physical phenomena where simple approaches using classical mechanic (of Newton) or statistical physics (of Boltzman) failed, physicists have developed a robust theory, without any approximation: the quantum mechanics. This theory was supposed to describe the matter at a subatomic scale.

Schrödinger suggested to describe the state of a particle by a wave function $\Psi(\vec{r}, t)$. The square modulus of this wave function gives the probability to find the particle at the position r at the time t. This function is the solution of the Schrödinger equation, equation describing the evolution in time of a non-relativist particle:

$$H\Psi(\vec{r}, t) = E\Psi(\vec{r}, t)$$

where H is the Hamiltonian of the system and E the energy of the particle. In the case of stationary states, the Schrödinger equation of the system is of the form:

$$H\Psi(\vec{r}) = E\Psi(\vec{r})$$

The Hamiltonian H of a molecular system constituted of M ions and N electrons in interaction is defined as the sum of their kinetic and potential energies. The potential energy comprises three Coulomb terms V_{ee}, V_{nn} and V_{en}, corresponding respectively to the electrostatic forces between electrons, between ions, and between electrons and ions. The kinetic energy is composed of two contributions T_e and T_n, corresponding respectively to the motions of the N electrons and to the M ions. Therefore:

$$H = T_n + T_e + V_{en} + V_{nn} + V_{ee}$$

The Schrödinger equation can be written as:

$$H\Psi(\vec{r}, \overrightarrow{R}) = E\Psi(\vec{r}, \overrightarrow{R}) \tag{2.1}$$

with $\vec{r} = \vec{r}_1, ..., \vec{r}_N$ and $\overrightarrow{R} = \overrightarrow{R}_1, ..., \overrightarrow{R}_M$ representing respectively all electrons and ions coordinates of the system. Ψ is the wave function associated to the stationary state with energy E. It depends on the 3N electron and 3M ion coordinates. By resolving Eq. 2.1, one obtains the wave function of the system and its associated energy E, giving thus access to all its physical and chemical properties. However, owing to the very large number of variables in this equation (3N+3M), it is impossible to solve it for systems in condensed matter. Therefore approximations were introduced, the so-called Born-Oppenheimer approximation being one of the most famous.

Born-Oppenheimer approximation and resolution of the Schrödinger equation The Born-Oppenheimer approximation stipulates the following: electrons move faster than nuclei in such a way that, for a given configuration of the nuclei, electronic positions are instantaneously adjusted to nuclear positions before nuclei move again.

It is therefore possible to write the wave function as a product of two functions, one depending only on the nuclear coordinates, and the other depending on the electronic coordinates, and in a parametric manner, to the nuclear coordinates:

$$\mathrm{H}\Psi(\vec{r},\overrightarrow{\mathrm{R}}) = \Psi_n(\overrightarrow{\mathrm{R}})\Psi_e(\vec{r},\overrightarrow{\mathrm{R}}) \tag{2.2}$$

After some simplifications and approximations judiciously chosen, introducing Eq. 2.2 in Eq. 2.1, one can obtain:

$$(\hat{\mathrm{T}}_e(\vec{r}) + \hat{\mathrm{V}}_{ee}(\vec{r}) + \hat{\mathrm{V}}_{en}(\vec{r},\overrightarrow{\mathrm{R}}))\Psi_e(\vec{r},\overrightarrow{\mathrm{R}}) = \mathrm{E}_e(\overrightarrow{\mathrm{R}})\Psi_e(\vec{r},\overrightarrow{\mathrm{R}}) \tag{2.3}$$

where,

$$\mathrm{E}_e(\overrightarrow{\mathrm{R}}) = \frac{(\hat{\mathrm{T}}_e(\vec{r}) + \hat{\mathrm{V}}_{ee}(\vec{r}) + \hat{\mathrm{V}}_{en}(\vec{r},\overrightarrow{\mathrm{R}}))\Psi_e(\vec{r},\overrightarrow{\mathrm{R}})}{\Psi_e(\vec{r},\overrightarrow{\mathrm{R}})}$$

Eq. 2.3 can be developed as:

$$\left[\frac{-\hbar^2}{2m_e}\sum_{i=1}^{\mathrm{N}}\nabla^2_{\vec{r}_i} + \frac{1}{2}\sum_{i\neq j=1}^{\mathrm{N}}\frac{1}{4\pi\varepsilon_0}\frac{e^2}{|\vec{r}_i-\vec{r}_j|} - \sum_{j=1}^{\mathrm{M}}\sum_{i=1}^{\mathrm{N}}\frac{1}{4\pi\varepsilon_0}\frac{\mathrm{Z}_j e^2}{|\overrightarrow{\mathrm{R}}_j-\vec{r}_i|}\right]\Psi_e(\vec{r},\overrightarrow{\mathrm{R}}) = \mathrm{E}_e(\overrightarrow{\mathrm{R}})\Psi_e(\vec{r},\overrightarrow{\mathrm{R}}) \tag{2.4}$$

It is important to notice that the dependence of $\Psi_e(\vec{r},\overrightarrow{\mathrm{R}})$ to nuclear coordinates is done only via the Coulombian interaction between nuclei and electrons. And, the potential generated by nuclei on an electron can be defined as:

$$\mathrm{V}(\vec{r}) = -\sum_{j=1}^{\mathrm{M}}\frac{1}{4\pi\varepsilon_0}\frac{\mathrm{Z}_j e^2}{|\overrightarrow{\mathrm{R}}_j-\vec{r}|}$$

In a nutshell, with the Born-Oppenheimer approximation, one assumes that electrons are under potential $\mathrm{V}(\vec{r})$ generated by nuclei. After the nuclear configuration is chosen, one solves the electronic Schrödinger equation (Eq. 2.4) and for this configuration calculated the total energy of the system:

$$\mathrm{E} = \frac{1}{2}\sum_{i\neq j=1}^{\mathrm{M}}\frac{1}{4\pi\varepsilon_0}\frac{\mathrm{Z}_i\mathrm{Z}_j e^2}{|\overrightarrow{\mathrm{R}}_i-\overrightarrow{\mathrm{R}}_j|} + \mathrm{E}_e(\overrightarrow{\mathrm{R}})$$

Thanks to the Born-Oppenheimer approximation, a [3N+3M] body problem has been reduced to a 3N body problem. However, the resolution of the electronic Schrödinger equation is still a complex many-body problem. The poly-electronic wave function depends on 3N variables. A numerical representation of such functions is almost impossible for big values of N. For this reason, methods for the calculation of electronic structure have approximations. Two different strategies can be adopted:

- Methods using wave function (Hartree, Hartree-Fock, Configuration Interaction, ...).
- Density Functionnal Theory (DFT).

Hartree-Fock and DFT approaches are briefly presented below.

Hartree-Fock method The goal of the Hartree-Fock (HF) method is to solve the many-body problem. To do so, Hartree made the following assumption: many-electron wave function is just a product of a set of single-electron wave functions:

$$\Psi(1,...,N) = \varphi_1(1)\varphi_2(2)...\varphi_N(N) \tag{2.5}$$

There are N time-independent equations for each of the N single electrons.

The HF approximation is an extension of the Hartree assumption, to include the permutation symmetry of the wave function. The Pauli exclusion principle states that the total wave function for the system must be antisymmetric under particle exchange. For example,

$$\Psi(1,2,...,N) = -\Psi(2,1,...,N)$$

In the HF approximation, instead of using the simple product of wave functions shown in Eq. 2.5, a Slater determinant function which satisfies antisymmetric condition is used.

This exchange (antisymmetric) condition leads to the exchange term in the one-electron equations of the single-electron wave functions. Therefore, HF method deals exactly with exchange. Exchange is the fact that different electrons, because of their quantum nature, cannot be differentiated from each other when they are close together, and their wave functions overlap.

Advantages of HF method:

- It gives, in an approximate way, information about orbitals which can be used as an input for more accurate methods, usually called post-HF methods.

- Electron exchange part of the Schrödinger equation is well defined.

Disadvantages of HF method:

- Electron correlation is missing.

- Not applicable to large systems.

DFT method Density Functional Theory is one of the most popular and successful quantum mechanical approaches to matter. Its high efficiency and good scaling with a relatively high accuracy are the main reasons for its important and still growing success. The main idea behind DFT is that the electronic density n(r) is used as the basic variable of the problem and that all the properties can be calculated from it. The use of the density (which has just 3 variables) as the basic variable, instead of the many-body wave function is a great advantage. This renders the electronic problem solvable for systems containing more atoms (several hundred). This method is based on theorems (Hohenberg-Kohn, etc.), choices (Kohn and Sham method, etc.) and approximations (LDA, etc.).

- **Hohenberg-Kohn theorems**

  L. Thomas and E. Fermi put the basis of DFT already in 1928, and later P. Hohenberg and W. Kohn gave a robust formalism in 1964, by introducing approximations to model the interactions between the electrons. The Hohenberg and Kohn (HK) theorems are the following [169]:

i) First HK theorem: *the external potential v is uniquely determined by the electronic charge density n($\vec{r}$).*

This means that every ground-state property, and in particular the ground-state energy, is a functional of the electron density:

$$E[n] = F[n] + \int n(\vec{r})\, v\, d\vec{r}$$

with F[n] = T_e[n] + V_{ee}[n], the universal (do not depend to the system) HK functional, and the second term depends on the system.

NB: This external potential is the one created by the nuclei (plus an eventual applied field).

ii) Second HK theorem: *the ground state energy can be obtained variationally: the density that minimises the total energy is the exact ground state density.*

- **Kohn and Sham approach**

Kohn and Sham (KS) proposed to replace the fully interacting many-body system by an ensemble of independent fictitious particles in a modified external potential having the same density as that of the real electronic [170]. In the Kohn-Sham approach, the total energy functional can be written as:

$$E[n] = T_s[n] + V_{ext}[n] + E_H[n] + E_{XC}[n]$$

where T_s[n] is the non-interacting kinetic energy, V_{ext}[n] is the external potential, E_H[n] is the Hartree energy and represents the classical Coulomb interaction of an interacting charge density , E_{XC}[n] = (T_e[n] - T_s[n]) + (V_{ee}[n] - E_H[n]) is the exchange-correlation energy. The exact ground state and energy could be obtained in principle by finding n($\vec{r}$) such that:

$$\frac{\delta(E[n])}{\delta n} = 0$$

By developing this equation, it is possible to reach the Kohn-Sham equations [170], which can be solved by an iterative self-consistent procedure. At this level, DFT is an exact theory. The remaining problem is that the exact expression of the exchange-correlation functional E_{XC}[n] is unknown. This term has to be approximated.

- **Approximations**

Numerical result depends on the choice of exchange-correlation functional. There are several approximations used for the exchange-correlation functional. Among them, one can mention the:

  - LDA (local density approximation) [170, 171]
  - GGA (generalized gradient approximation) [172, 173]
  - Hybrid methods (LSDA, B3PW91, B3LYP, etc.) [174–178]

Nowadays, DFT theory implemented in different software thus reflects brilliant ideas of HK and KS.

2.4.1.b) Simulation details

Optimisation of the structure is necessary before the determination of the vibrational spectrum. It was performed on molecules whose initial coordinates were taken from the crystal structure, or from MD simulations boxes. The vibrational spectrum was then calculated on the optimised molecules. Both geometry optimisation and frequency calculation of the molecules were performed using DMol3 modulus [179] of Material Studio. The calculations were done using the B3LYP functional and 6-31G* basis set, which has been proved to be very well adapted to optimise disaccharides [180, 181]. For DFT calculations on small amorphous phases (having five molecules), the molecules were always put in an amorphous cell (with symmetry P1) at a density of 1.4 g/cm^3, and the GGA-PBE functional used instead. This is because B3LYP functional cannot be used on systems having certain symmetry. Moreover, the GGA-PBE is known to provide a fairly accurate description of hydrogen bonds, and for this reason, it is commonly used to compute vibrational modes of disaccharides [182, 183]. The DNP (Double Numerical plus Polarisation) basis set was used for all calculations, with fine convergence criteria (dE < 10^{-5} Ha, Max. force on atoms = 0.002 Ha/Å, max. displacement of atoms = 0.005 Å). All those parameters have been chosen after having done several tests.

In the case of single molecule calculation, the geometry optimisation and frequency calculation typically cost less than 24 h on a 16 processors node.

Principle of vibrational frequencies calculation g(w) When a molecule or a cell is built or input to the software, it usually needs to be refined to bring it to a stable geometry. This is done during a geometry equilibration step, consisting in slightly moving atoms such a way to find a relative minimum on the energy hypersurface. It is done using a smart procedure, combination of Steepest descent, Conjugated Gradients and Newton-Raphson methods. Thereafter, the stable molecule is used to compute vibrational frequencies. To do so, DMol3 computes the 3N*3N (N being the total number of atoms in the structure) Hessian matrix, by finite differences of analytic first derivatives. This means that each atom is slightly displaced in the three Cartesian directions (including positive and negative direction), and the new values of energy are used to construct the Hessian matrix. This matrix is diagonalised afterwards, and the eigenvalues and eigenvectors are obtained. From these values the atomic displacements and their amplitude in real space can be expressed in terms of normal modes coordinates. Therefore, the frequencies of the normal modes can be calculated, and performing a summation over all modes the density of states, g(w), can be obtained.

2.4.2 Molecular Dynamics (MD) simulations

In this section, we will first explain the principle of MD simulations. After that, some tricks commonly employed to implement a MD simulations code will be presented. In the last part, the simulation parameters used during this thesis will be given.

2.4.2.a) General principle and some important background

Principle In order to follow time evolution of atoms and molecules, molecular dynamic adopts the Born-Oppenheimer approximation: since electrons move faster than nuclei, one can assume that those two motions are uncoupled. In MD, this approximation means that the effect of electrons can be average, and the atoms are thus only reflected by their nuclei.

These latter are treated as point masses, and therefore obey to classical equations of motion, Newton equations for example:

$$\overrightarrow{\mathrm{F}}_i = m_i \vec{a}_i \tag{2.6}$$

Where $\overrightarrow{\mathrm{F}}_i$ stands for the force acting on the atom (nucleus) i, m_i its mass and $\vec{a}_i$ its acceleration.

The force $\overrightarrow{\mathrm{F}}_i$ is obtained by derivating the force field U:

$$\overrightarrow{\mathrm{F}}_i = -\frac{\partial \mathrm{U}}{\partial \vec{r}_i} \tag{2.7}$$

where $\mathrm{U}(\vec{r}_1, \vec{r}_2, \ldots, \vec{r}_\mathrm{N})$ is an empirical function that approximates potential energy E, and $\vec{r}_1, \vec{r}_2, \ldots, \vec{r}_\mathrm{N}$ are the positions of atoms 1, 2, ... N.

The achievement of MD simulations firstly requires to choose a force field. Afterwards, one needs to numerically solve the equations of motion, in order to get the different dynamical parameters (position, velocity and acceleration) of the atom of mass m_i. The accuracy of MD simulations is based on a judicious exploitation of those parameters.

MD simulations in practice In the previous section we have briefly introduced the physical concepts behind MD simulations. Their numerical implementation is quite complex, and usually requires some tips. A MD simulation aims to produce a dynamical trajectory of a system composed of N particles, by integrating Newton equations of motion. To do so, one initially needs:

- a set of initial conditions (positions and velocities of each particle);
- a good model to represent the forces acting between the particles (either from electronic structure calculations or using an empirical force field as it will be presented after);
- to choose the thermodynamic ensemble in which simulations will be performed;
- to define the boundary conditions to be employed. This step is not mandatory, but it is usual to perform MD simulations using periodic boundary conditions.

i) Initial conditions

In the case of a crystal, the position of each particle can be typically available in the form of a crystallographic file and it is possible to construct a supercell combining several unit cells. For a disordered system, the position of each particle is usually generated randomly or by melting an ordered structure. In both cases (ordered and disordered systems), the generated structure is not always physically acceptable. A geometry optimisation step is thus almost always necessary. During this step, the geometry of the system is optimised by minimising its potential energy, in order to reach the most stable possible configuration. Among geometry optimisation methods, there are the Steepest descent method [184–186], the Conjugated Gradients method [186–188], and the Newton-Raphson method [186, 189].

The velocity of each particle is attributed randomly from a Maxwellian distribution centered on the desired temperature and then they are adjusted in order to zero the angular momentum and the center of mass velocity of the total system.

ii) Force field

MD simulations consist in calculating the time evolution of the positions, velocities and accelerations of particles in a system. The force field is the key element of this calculation, the heart of MD simulations. A force field is a mathematical expression describing the dependence of the potential energy of a system on the coordinates of its particles. A bad model of the different interactions acting between particles could lead to bad results. In its simplest form, a force field is as follows:

$$U = U_{bonded} + U_{nonbonded}$$

with:

- $U_{bonded} = U_{bond} + U_{angle} + U_{dihedral}$ including intramolecular interactions between atoms separated by one, two or three covalent bonds.

  U_{bond}: model of the covalent bond between two atoms.

  U_{angle}: model of the valence angle between three atoms.

  $U_{dihedral}$: model of the dihedral angle between four atoms.

- $U_{nonbonded} = U_{vdW} + U_{electrostatic}$ including interactions between atoms of different molecules, or belonging to the same molecule but separated by more than three covalent bonds.

  U_{vdW}: model of the van der Waals interaction between two atoms (Lennard-Jones potential).

  $U_{electrostatic}$: model of the electrostatic interaction between two atoms (Coulomb potential).

Parameters of the force fields are obtained by empirical approaches: they are adjusted with experimental values, or with values obtained by theoretical calculations. Among famous force fields, one can mention CHARMM [190], AMBER [191], GROMOS [192, 193], OPLS [194], COMPASS [195].

iii) Thermostats and barostats

Any MD simulation is done in a statistical ensemble generally chosen according to the properties to investigate. Although the NVE ensemble is the natural thermodynamic ensemble of simulations (since the energy E, number of particles N and volume V are constant), it generally exists reasons why one needs to do a simulation in NPT (P: pressure) or NVT (T: temperature) ensemble. In those cases, the system is "plunged" into a thermostat or barostat, so that the temperature or the pressure will be kept constant respectively. In practice, this means to add an extra non-conservative force f in the Eq. 2.6. This force creates fluctuations of the energy, but those fluctuations remain weak when the system has been well equilibrated, and do not affect the simulation results.

Among thermostats and barostats, we can mention the Berendsen algorithm [196] and the Nose-Hoover algorithm [197–199]. In the Berendsen algorithm, the instantaneous temperature is pushed towards the desired temperature by scaling the velocities at each step. For the Berendsen barostat, the size and shape of the simulation cell are dynamically adjusted in order to obtain the desired average pressure P_{ext}.

iv) Periodic boundary conditions

Because of a limited computational power, it is not yet possible to perform simulations on boxes having the size of a real system, i.e. containing around $N_A = 6.02\ 10^{23}$ (Avogadro number) atoms. One can then think that the results obtained are biased because of the small size of the box compared to the experimental dimensions. Fortunately this is not the case, because in general the size effects are scaled down by applying periodic boundary conditions [162, 164]. This trick improves considerably the final results by reducing surface effects. On another hand, in most cases, we are looking for bulk properties (of liquid or solid systems). We thus need to impose some boundary conditions to have a real system with a large amount of bulk and a small amount of surfaces.

It must be underlined that with periodic boundary conditions, the real system being simulated consists of the primitive box and all its replicas (see figure 2.15). When simulating disordered systems, this introduces an artificial periodicity. If the size of the simulation box is sufficiently large, the effects are normally not important, but it is important to be careful when considering any property that depends on long-range correlations. This issue does not arise for a crystal.

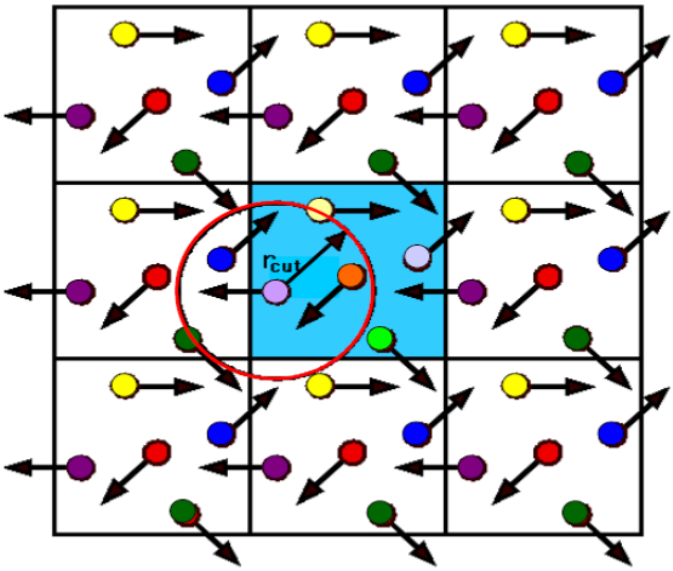

Figure 2.15 – Schematic representation of periodic boundary conditions in a 2D system. The "real" box is represented in blue. The pseudo-infinity character of the system thus generated forces to make certain approximations, concerning the treatment of interactions between molecules. In particular, the so-called "minimum image convention" [162, 200] assumes that each particle of the central cell interacts with the closest image of all the other particles.

v) Resolution of the Newton equation

Having a force field, one can get the force F acting on each atom and then numerically solve Eq. 2.6. There are several numerical algorithms to solve it, the Verlet algorithm [201], the leapfrog algorithm [202] and the velocity Verlet algorithm [203] for instance. The velocity Verlet algorithm is presented below.

All numerical expressions for integrating Newton equations are based on Taylor series:

$$r(t+\Delta t) = r(t) + v(t)\Delta t + \frac{1}{2}a(t)\Delta t^2 + \ldots \tag{2.8}$$

with r(t), v(t) and a(t) the position, velocity and acceleration at time t respectively, and Δt the time step.

After some developments, one can get the following expressions:

$$r(t+\Delta t) = 2r(t) - r(t-\Delta t) + a(t)\Delta t^2 + 0(\Delta t^4) \tag{2.9}$$

$$v(t+\frac{1}{2}\Delta t) = v(t) + \frac{1}{2}a(t)\Delta t + 0(\Delta t^3) \tag{2.10}$$

$$v(t+\Delta t) = v(t) + \frac{1}{2}\left(a(t) + a(t+\Delta t)\right)\Delta t + 0(\Delta t^3) \tag{2.11}$$

$$v(t+\Delta t) = v(t+\frac{1}{2}\Delta t) + \frac{1}{2}a(t+\Delta t)\Delta t + 0(\Delta t^3) \tag{2.12}$$

The new positions are determined using Eq. 2.9, knowing the position, velocity and acceleration at the current moment. After that, velocities are determined at $t+\frac{1}{2}\Delta t$ using Eq. 2.10. Finally, new velocities and accelerations are determined using Eq. 2.11 and Eq. 2.12. This algorithm has a precision of $0(\Delta t^4)$ on the positions, and of $0(\Delta t^3)$ on the velocities.

2.4.2.b) Simulation details

We have used the DL_POLY (classic and 4.7 versions) software [204–207]. It is a free (for academics) and open source classical MD simulations software, implemented in Fortran 90. The OPLS all-atom force field (a second generation force field, see annex C) has been used during simulations. The parameters of this force field were fitted to reproduce results from ab initio calculations on sugars (glucopyranose, galactopyranose), and therefore, it reproduces very well sugar properties [208, 209]. Newton equations are integrated using two versions of the Verlet algorithm. The first is the Verlet leapfrog algorithm [162] and the second is the velocity Verlet algorithm. The structures were optimised using the Conjugate Gradients minimisation method [210] and/or doing a 'zero K' temperature molecular dynamics. The latter is actually a real MD simulation conducted at 1 K, where dynamics have been modified so that the velocities of the atoms are always directed along the force vectors. Thus the dynamics follows the steepest descent to the local minimum. The time step is generally chosen in such a way that at least 10 «photos » of the progression of the fastest vibration in the system are taken (that typically means it should be at more 10 times less than the fastest vibration in the system). In our system, at 300 K, the fastest vibration (the OH stretching) has a frequency of 470 meV, and thus occurs over 9 fs. A time step of 1 fs was then generally used. However, in order to increase the simulation time step (up to 2 fs), the SHAKE algorithm [211, 212] was sometimes used. It constraints some fast and non-relevant vibrations. Berendsen thermostat and barostat were always used, with relaxation times of 0.2 ps and 2.0 ps, respectively. This has been decided after testing some other thermostats and barostats. Interatomic electrostatic forces were calculated using a shifted Coulombian potential. A r_{cut} of 10 Å was used for interatomic interactions. All those parameters have been chosen after having done several tests. Periodic boundary conditions were applied in all directions.

After an equilibration run, a production run was always done in order to extract and analyse simulation data. Analysis in MD simulations is done by following the evolution of structural, dynamic of thermodynamic parameters of the system with respect to the time. This gives some useful information on the system. In particular, auto-correlation functions are usually calculated to assess specific physical quantities.

All the calculations have been performed at the University of Lille (cluster Zeus, cluster thot, local desktop) or on the cluster of ILL, Grenoble. For illustrative purposes, a 20.000 steps simulation performed with 1 fs time step, and using 8 processors on a box having 2880 atoms took 24 min.

Chapter 3

Presentation of crystalline and amorphous lactulose obtained by different amorphisation routes

"Savoir s'étonner à propos est le premier pas fait sur la route de la découverte."

Louis Pasteur

Contents

The aim of this chapter is to present the physico-chemical properties of crystalline and amorphous lactulose compounds. In the first part, the anhydrous crystalline lactulose is presented, with an emphasis on the tautomerisation happening in this system. Thereafter, trihydrate crystalline lactulose will be presented. The next parts will be devoted to the amorphous samples obtained by four different methods:

- Quenching from the melt of the anhydrous crystal (QFTM);
- Milling of the anhydrous crystal (MIL);
- Spray-drying of an aqueous solution of lactulose (SD);
- Freeze-drying of an aqueous solution of lactulose (FD).

The properties of amorphous lactulose obtained from the four different amorphisation routes will be progressively presented and compared to the previous ones.

It is worth mentioning that the results presented here were obtained by conventional powder X-Ray Diffraction (XRD), Differential Scanning Calorimetry (DSC), Thermogravimetric Analysis (TGA), Nuclear Magnetic Resonance (NMR) and Molecular Dynamics (MD) simulations. Furthermore, the different compounds have also been analysed by neutron scattering, and the corresponding results will be presented in chapter 5.

In the previous chapter the three main tautomers that characterise lactulose, namely, galactosyl β-furanose, galactosyl α-furanose, and galactosyl β-pyranose were presented. As a reminder, they will be respectively named tautomer A, tautomer B and tautomer C throughout this manuscript.

3.1 Crystalline lactulose

3.1.1 Anhydous lactulose (commercial form)

Commercial lactulose (98% purity) was purchased from Sigma Aldrich, and used without further treatment.

3.1.1.a) Characterisation by XRD, TGA and DSC experiments

Figure 3.1 shows a XRD pattern of commercial lactulose recorded at ambient temperature in a spinning capillary, between 5° and 40° in 2θ (black line). The diffraction pattern of an empty capillary is also reported (blue line).

The black line contains Bragg peaks characteristic of a crystalline state. The analysis of this XRD pattern made with the FullProf software [153] indicates that the system is monoclinic, with cell parameters compatible with those previously obtained by Jeffrey et al. on anhydrous crystalline lactulose [51]:

$$a = 7.420(3)\ \text{Å}, b = 19.257(6)\ \text{Å}, c = 5.355(2)\ \text{Å}, \beta = 103.88(3)°, \alpha = \gamma = 90°$$

A small diffusion halo appears between 17° and 28° on this XRD pattern. This halo is similar to the XRD pattern of the empty capillary (blue line). It is therefore attributed to

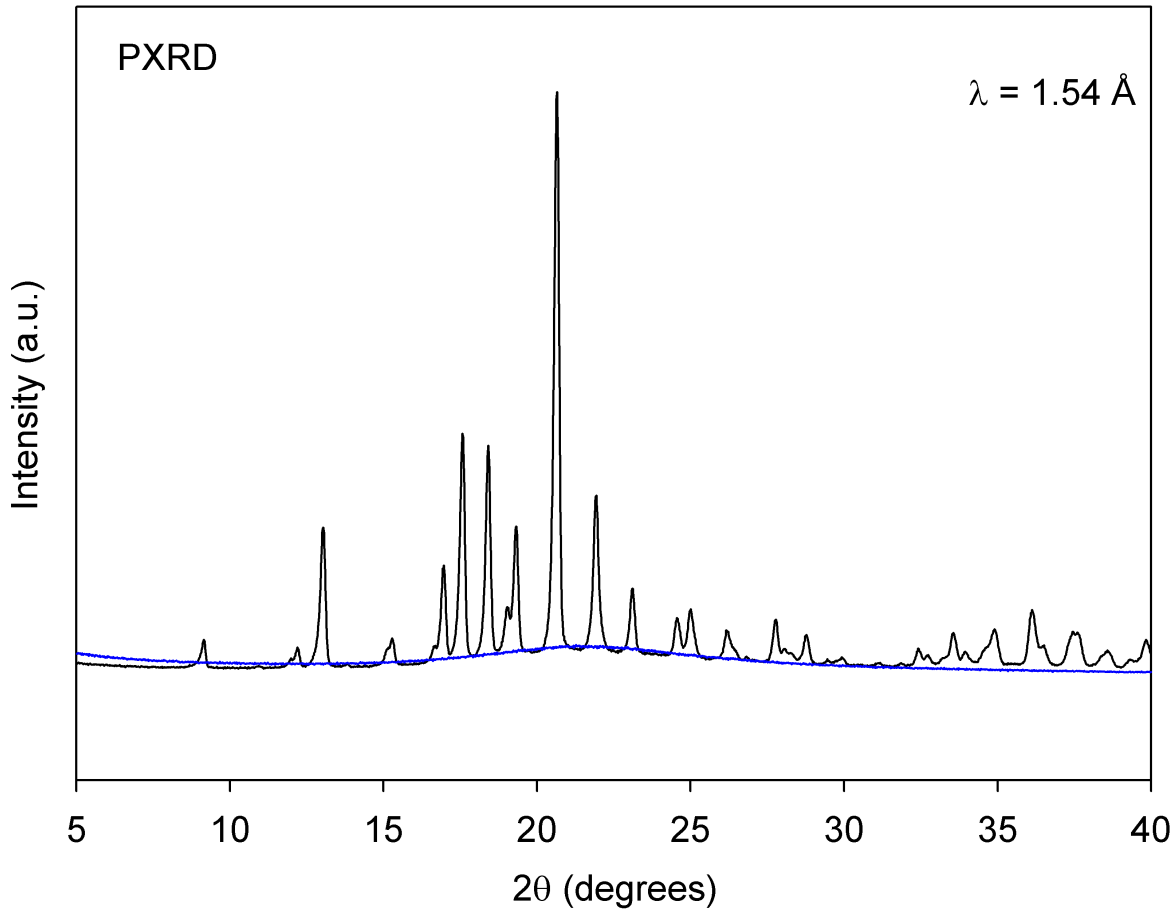

Figure 3.1 – XRD patterns of commercial form of lactulose (black line) and empty capillary (blue line) recorded at room temperature.

the scattering of the X-ray beam by the capillary, and by the air in the illuminated volume surrounding the sample.

Figure 3.2 b) shows the TGA curve of the anhydrous crystalline lactulose recorded upon heating (5 °C/min) between 30 °C and 180 °C (black line), as well as the derivative signal with respect to the temperature (blue line). They reveal three mass losses:

- The first one, of about 0.5%, is at 60 °C. XRD experiments performed on the compound before and after this mass loss did not show any structural changes. This mass loss is therefore assignable to a departure of free water.

- The second one, wider, spreads between 120 °C and 160 °C. The experiment that will be presented in section 3.2.2 shows that this mass loss corresponds to a departure of the water inclusions present in the commercial form. This water has probably been trapped in the crystalline matrix during the manufacture of the anhydrous lactulose.

- The third one begins after 160 °C. It corresponds to the thermal degradation of lactulose. Above this temperature, the compound colour changes from white to brown, proving that it has caramelised.

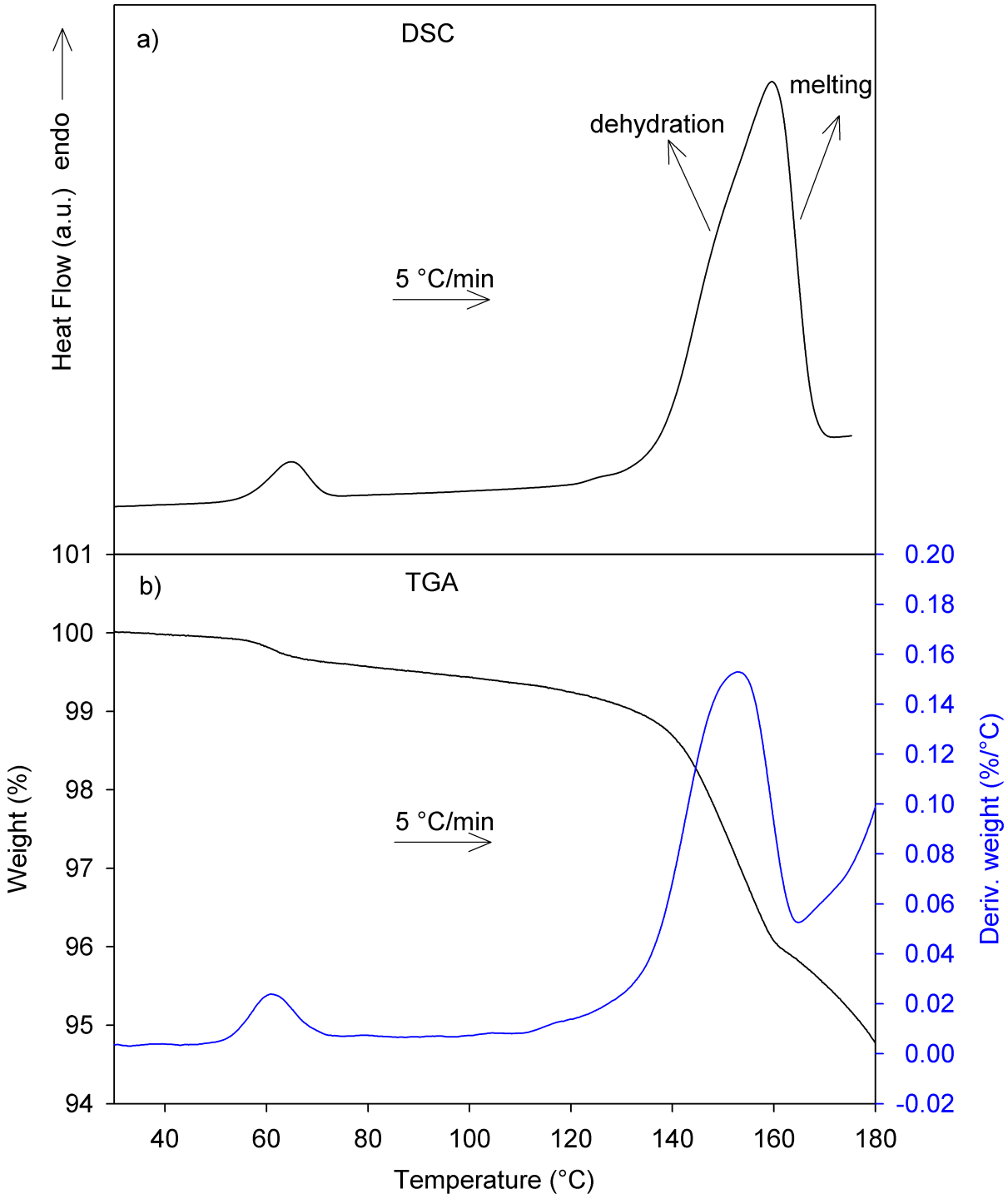

Figure 3.2 – a) DSC curve of the anhydrous crystalline lactulose (5°C/min)
b) TGA curve and derivative TGA curve of the anhydrous crystalline lactulose (5°C/min)

Figure 3.2 a) shows a DSC curve of the same crystal recorded in the same conditions (heating at 5 °C/min between 30 °C and 180 °C). There are two endotherms in the figure:

- The first one, around 60 °C, corresponds to the departure of the free water, as pre-

viously seen by TGA.

- The second one, wider, ranges from 120 °C to 165 °C. It consists of a shoulder at about 145 °C, temperature where the second mass loss has been seen in the TGA curve (see figure 3.2 b)). It therefore corresponds to the departure of the water inclusions. The rest of the endotherm consists mainly of the endothermic signal due to the melting of the crystal. In addition, a small endothermic contribution due to the thermal degradation of the sample (seen in TGA, figure 3.2 b)) and beginning above 160 °C is present in this endotherm. It is therefore a complex **dehydration-melting-degradation** endotherm.

The endotherms due to the thermal degradation of lactulose and the departure of water inclusions are superimposed on that of the melting. A precise determination of the melting enthalpy and the melting temperature on the thermogram present in figure 3.2 a) is therefore not possible. However, it has been possible to measure the melting enthalpy of the crystal on a compound which was weakly ground (to break the crystallites in which the water is trapped), aged and then dried. The obtained results are presented in the following paragraph.

Estimation of the melting enthalpy of the anhydrous crystal Several DSC experiments were carried out on crystalline lactulose weakly ground and then dried, but none of the obtained results showed an enough sharp melting endotherm. This is mainly due to the fact that the weak grinding combined with the diffusion of the water during drying, partially degrades the crystallinity. Thus, an experiment where the crystal was weakly ground and then aged at ambient temperature was carried out. This favours the reconstitution of the crystallites.

Figure 3.3 presents a thermogram of a crystalline lactulose sample obtained upon heating (5 °C/min). This sample has been previously slightly crushed (during 5 min), aged during 3 months, and dried at 60 °C during 15 min. The thermogram does not show any C_p jump nor exothermic recrystallisation which indicates that the crushing has not induced any partial amorphisation of the material. It only shows the melting endotherm. This melting endotherm is much sharper and occurs at a slightly higher temperature than the one observed in the commercial lactulose as received. These differences are due to the crushing stage which has allowed the removal of water inclusions upon drying. This endotherm is thus the genuine melting peak of lactulose from which an accurate melting temperature T_m= (162.5±1) °C and melting enthalpy ΔH_m= (125.7±1) J/g can be derived.

3.1.1.b) Tautomeric composition of crystalline lactulose: Investigations by NMR experiments

This part aims to show the possibility of determining the tautomeric composition of lactulose samples using liquid-state proton NMR. To do so, the lactulose solid samples were previously dissolved into Dimethyl Sulfoxide (DMSO). This solvent is expected to strongly slow down the tautomerisation processes in the solution [146, 161]. A rapid measurement just after dissolution could thus provide the real tautomeric composition of the initial crystalline sample.

Figure 3.5 a) shows simulated NMR spectra of tautomers A (red line), B (blue line) and C (green line), represented between 4.5 and 5.7 ppm. The simulations were performed with the ACD/NMR Predictors software of ACD/Labs company [213]. This software uses an experimental knowledgebase containing the chemical shifts, in a DMSO environment, of all the

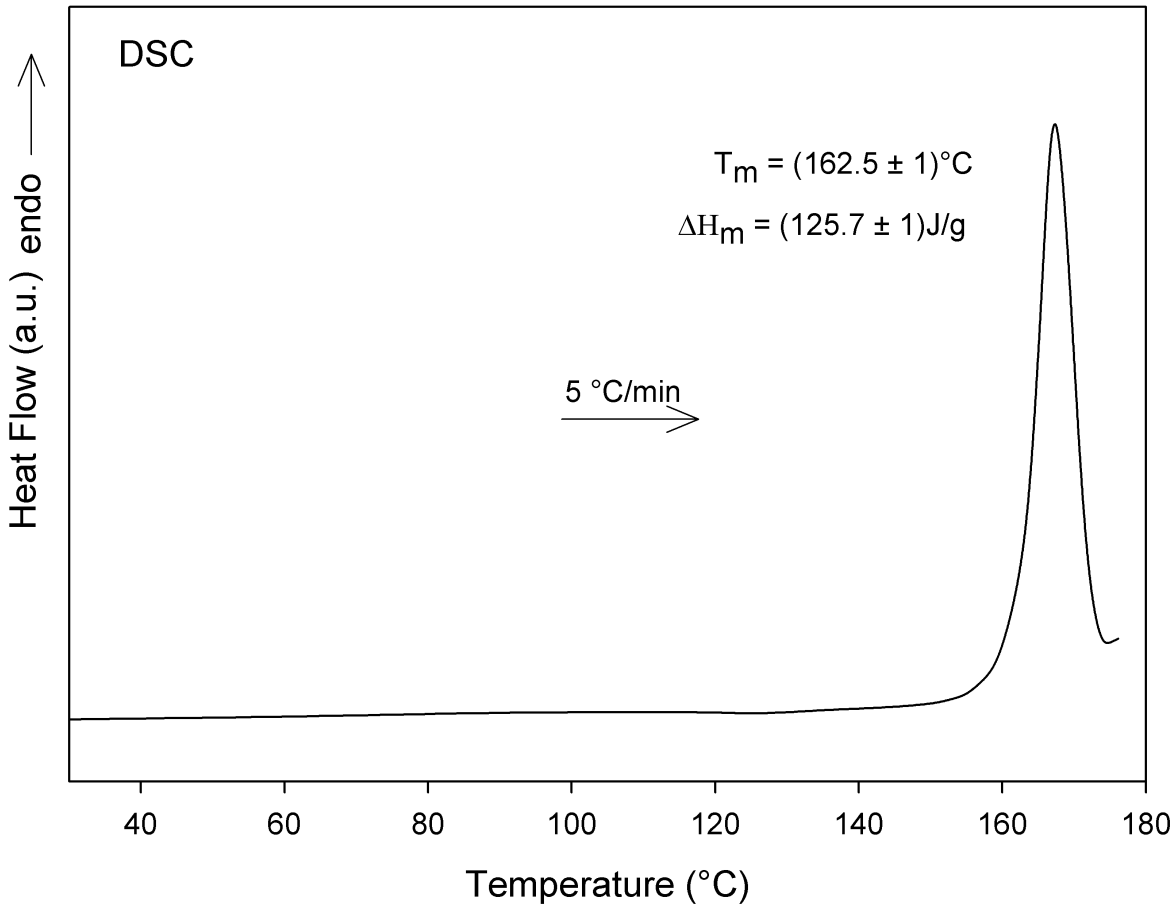

Figure 3.3 – DSC curve of commercial anhydrous crystalline lactulose recorded at 5 °C/min after slight crushing (during 5 min), 3 months aging at room temperature, and 15 min drying at 60 °C

H atoms present in the different tautomers. These chemical shifts change with respect to the chemical group of each H atom and its local environment, as experimentally. The simulations are therefore non ab-initio calculations.

It is important to precise that the position of all atoms in tautomer A has already been well determined by XRD [51]. But in the case of tautomers B and C, the position of most of the H atoms is unknown [51]. We have thus performed structure minimisation thanks to DFT calculations, in order to predict the position of the undetermined H atoms. Therefore, for the ACD/NMR simulations performed, the structure of tautomer A comes from the litterature, and those of tautomers B and C come from DFT calculations.

In figure 3.5 a), it can be noticed that above 4.5 ppm, each tautomer has a characteristic peak at a specific chemical shift:

- The peak at 4.7 ppm corresponds to tautomer B;
- The peak at 4.9 ppm corresponds to tautomer A;
- The peak at 5.2 ppm corresponds to tautomer C.

A thorough analysis of the simulation results showed that these characteristic chemical shifts come from the same hydrogen atom in the three tautomers. It is the hydrogen atom present between the two cycles (named anomeric proton), and having two oxygen atoms in its vicinity (see figure 3.4). The presence of a deshielded peak due to the anomeric proton has already been observed on other sugars [214].

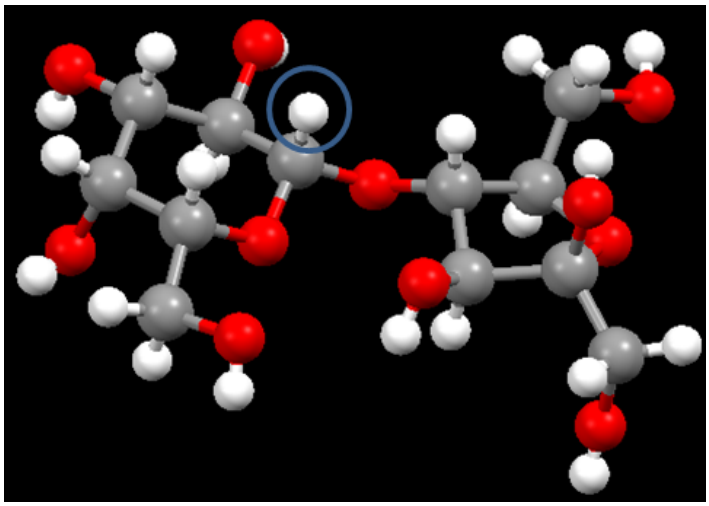

Figure 3.4 – Tautomer A molecule. The anomeric proton is encircled in blue.

Figure 3.5 b) represents the experimental NMR spectrum of anhydrous crystalline lactulose measured at room temperature, 3 min after dissolution in DMSO (black line). It shows the three characteristic peaks of the three tautomers. The position of these peaks, however, does not correspond to that of the peaks obtained by simulation. This is due to the fact that experimental parameters that can influence the position of the peaks - such as the lactulose concentration in DMSO - are not taken into account in the simulation. In addition, the simulation uses « empirical » chemical shift values, which do not necessarily correspond to those of lactulose tautomers.

The NMR spectrum shown in figure 3.5 b) enables to assess the sample tautomeric composition, 3 min after dissolution in DMSO. No trace of tautomers no. 4 and no. 5 presented in chapter 2 (section 2.1.2) was detected in the DMSO solution. Consequently, they will be considered as negligible. The fraction of a given tautomer will thus be obtained by dividing the area of the corresponding characteristic peak by the sum of the areas of the characteristic peaks of each of the three tautomers. This calculation performed on the spectrum of the anhydrous crystalline lactulose (figure 3.5 b)) indicates that it consists of 79.3% of tautomer A, 10.3% of tautomer B and 10.4% of tautomer C.

In order to evaluate the ability of DMSO to block the mutarotation of lactulose, and to have an indication of the tautomerisation kinetic in this solvent, the time evolution of the tautomeric composition after dissolution was followed.

Figures 3.6a, 3.6b and 3.6c show the time evolution of the NMR peaks characteristic of tautomers A, B and C after dissolution of crystalline lactulose in DMSO, respectively. A decrease of the peak area associated with tautomer A can be seen, as well as an increase of the peak area associated with tautomers B and C. The integration of these peaks allows retrieving the time evolution of the tautomeric composition in the DMSO solution. The results

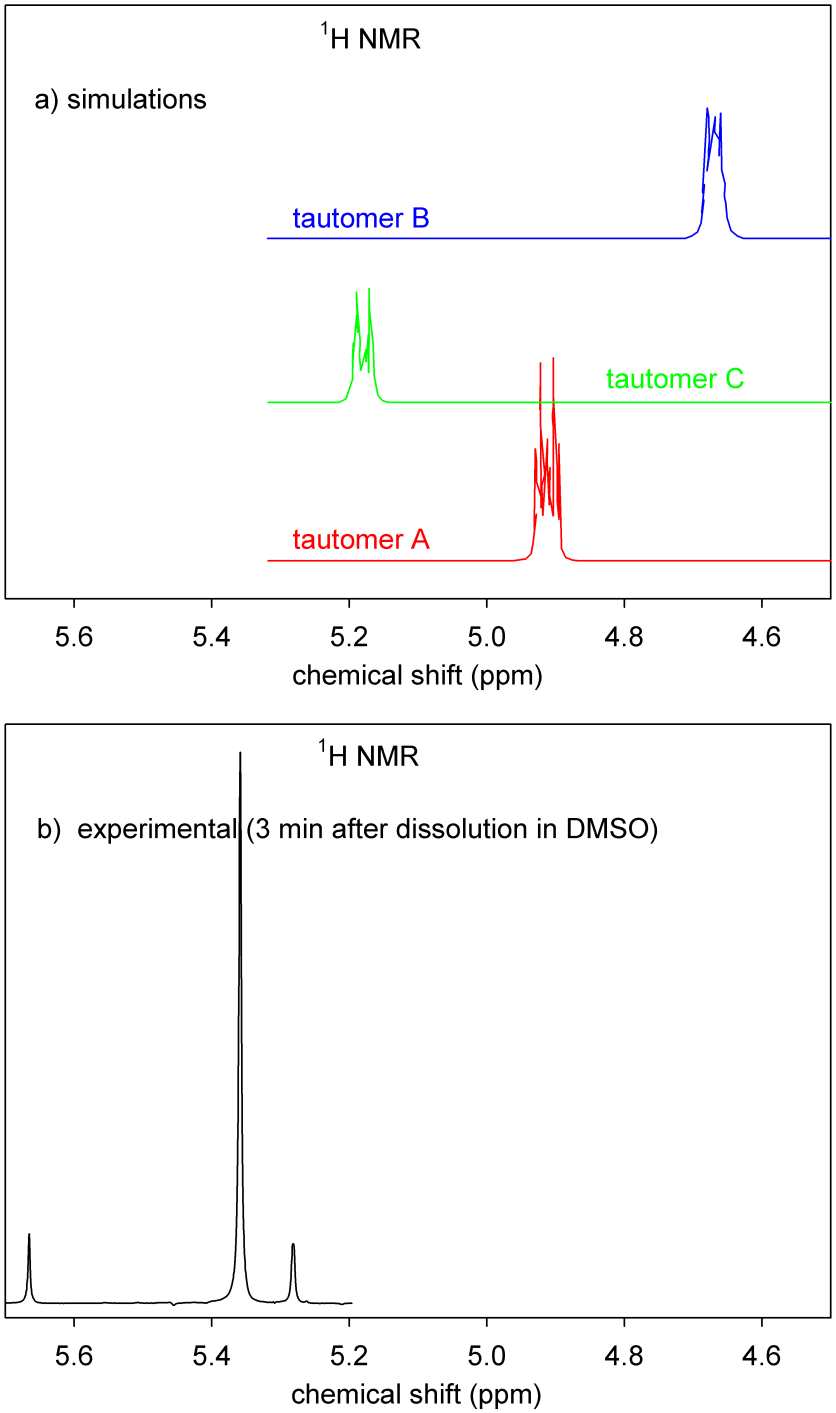

Figure 3.5 – a) NMR simulated spectra of tautomer A (red line), tautomer B (blue line) and tautomer C (green line) of lactulose in DMSO.
b) NMR spectrum of the anhydrous lactulose (black line) recorded 3 min after dissolution in DMSO.

obtained are reported in table 3.1, and the time evolution is shown in figure 3.7. We can note a strong decrease in the proportion of tautomer A, as well as a strong increase in the proportion of tautomer C, and a moderate one in the proportion of tautomer B.

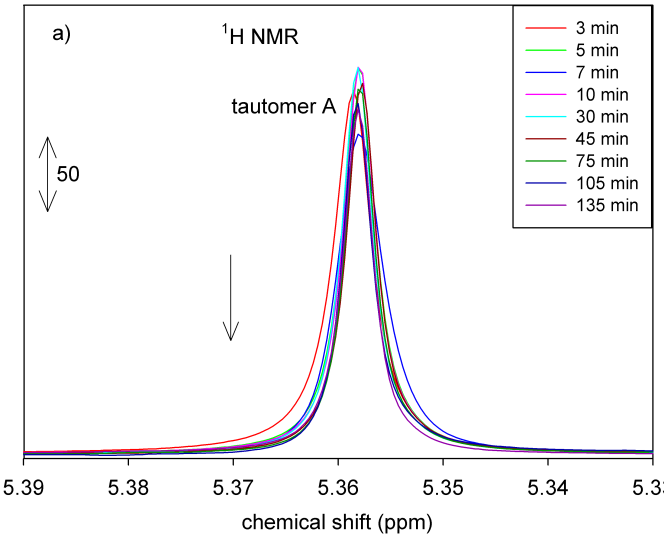

(a) Case of tautomer A.

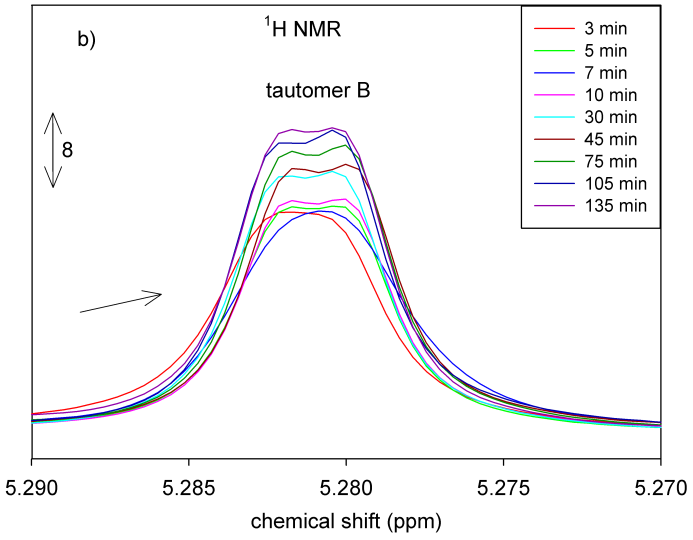

(b) Case of tautomer B.

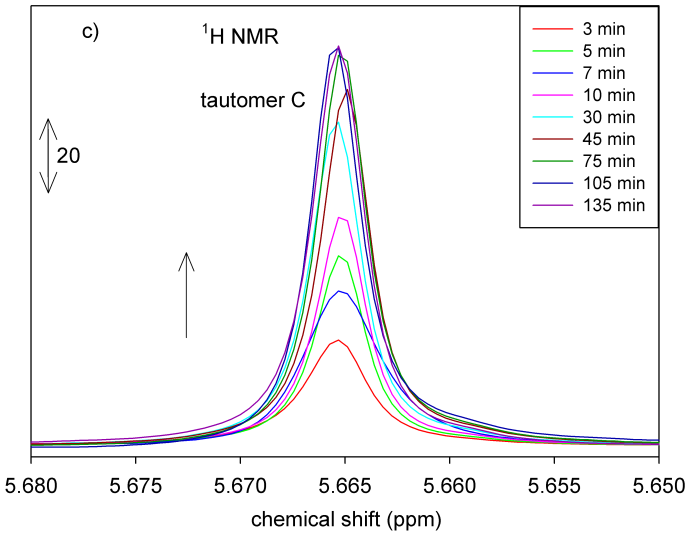

(c) Case of tautomer C.

Figure 3.6 – Time evolution of the tautomeric fractions in DMSO.

The solid lines in figure 3.7 represent the best fit of the data using an exponential relaxation law. The evolutions of the tautomeric proportions have been extrapolated to t=0 in order to best estimate the tautomeric proportions in the crystal before dissolution. The following values were obtained: 79.9% of tautomer A, 10.5% of tautomer B and 9.6% of tautomer C. These values have been reported in table 3.1 (values highlighted in grey). It can be noticed that they are not very different from those determined 3 min after dissolution. The differences observed enable to estimate the error made by approximating the composition of the compound in the solid state with that measured 3 min after its dissolution in DMSO.

The dashed lines in figure 3.7 represent the values of the tautomeric fractions two weeks after dissolution in DMSO: 45.6% of tautomer A, 34.2% of tautomer B and 20.2% of tautomer

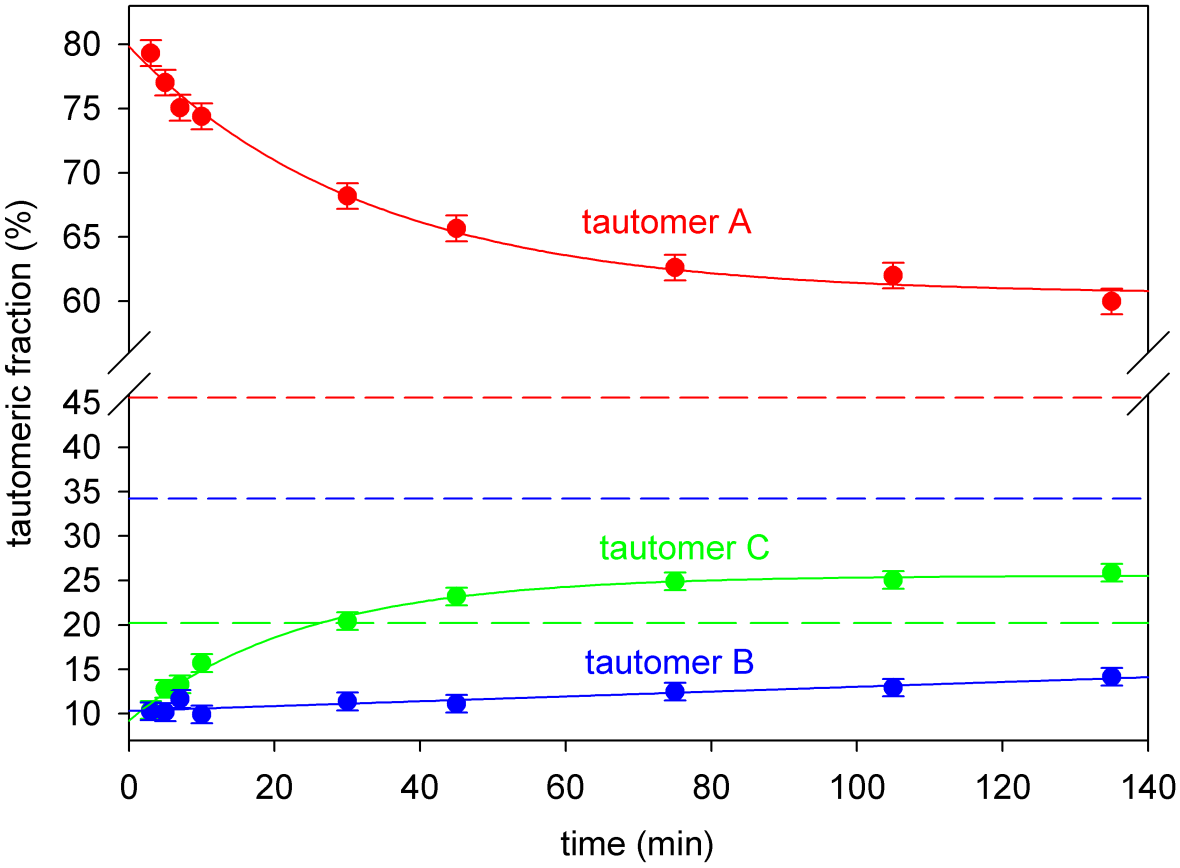

Figure 3.7 – Time evolution of the fraction of tautomers A (red points), B (blue points) and C (green points) after dissolving the crystalline lactulose in DMSO. The solid lines represent the best fit of the data using an exponential relaxation law. The dashed lines represent the values of the tautomeric fractions two weeks after dissolution in DMSO.

Table 3.1 – Time evolution of the fraction of tautomers A, B and C in DMSO. The values highlighted in grey correspond to the extrapolation of the experimental values (i.e. from t= 3min) to t=0 min using an exponential relaxation law.

Time (min)	% of tautomer A (±2)	% of tautomer B (±2)	% of tautomer C (±2)
0	79.9	10.5	9.6
3	79.3	10.3	10.4
5	77.0	10.2	12.8
7	75.1	11.6	13.3
10	74.4	09.9	15.7
30	68.2	11.4	20.4
45	65.7	11.1	23.2
75	62.6	12.5	24.9
105	62.0	12.9	25.1
135	60.0	14.2	25.8

C. Those values are different from that measured 135 min after dissolution. This means that the equilibrium was not yet reached 135 min after dissolution, and the tautomeric propor-

tions measured two weeks after dissolution are closer to the equilibrium one.

Moreover, from 0 to 2h after dissolution, the results presented in figure 3.7 show a very small evolution of the amount of tautomer B. A similar behaviour has already been observed when dissolving glucose in DMSO [47]. Since the conversion from α to β glucose is similar to that from tautomer A to tautomer B (pure anomerisation), it can be assumed that, conversion from tautomer A to tautomer B is nearly "blocked" (slowed down) by DMSO. On the other hand, the conversion from A to C (pure tautomerisation) is different, and appears to be less strongly "blocked" by DMSO.

The previous results indicate that the tautomerisation is not totally blocked by the DMSO. However the kinetic of tautomerisation appears to be slow enough to get a realistic estimation of the tautomeric composition in the initial crystal if the NMR measurements are performed immediately and rapidly after the dissolution. In the remainder of this manuscript, the determination of the tautomeric compositions of the various compounds studied will thus be carried out systematically by analysing the NMR spectra of the compounds recorded 3 min after their dissolution in DMSO.

Therefore, the tautomeric proportions in anhydrous crystalline lactulose are (79.3 ± 4[1])% of tautomer A, (10.3 ± 2)% of tautomer B and (10.4 ± 4)% of tautomer C. This is slightly different from the results obtained by Jeffrey [51]: 74.5% of tautomer A, 10.0% of tautomer B and 15.5% of tautomer C. Nevertheless, it is important to precise that several tests have been carried out on different crystalline lactulose samples coming from different commercial batches. These tests showed that the fraction of tautomer B is always the same (between 9% and 10%) but those of tautomers A and C vary from one batch to another: between 74% and 79% for tautomer A, and between 10% and 16% for tautomer C.

3.1.2 Trihydrate lactulose

To the best of our knowledge, there is no commercial trihydrate lactulose available. Trihydrate lactulose crystals have been produced by Jeffrey et al. [146], from a 70% aqueous solution of anhydrous lactulose kept at 4 °C for several months. This method has the disadvantage of being long (more than one year is necessary to obtain crystallites).

We will here produce trihydrate lactulose by an innovative method: **the co-milling of anhydrous crystalline lactulose with water**. 1.1 g of anhydrous crystalline lactulose were co-milled with 180 mg of pure water, which typically corresponds to one molecule of lactulose for three molecules of water. The mixture was co-milled during 50 min, alternating milling periods (10 min) and break periods (10 min).

3.1.2.a) Characterisation by XRD and DSC experiments

Figure 3.8 shows a XRD pattern of a mixture "crystalline lactulose / water" in the molar ratio [1:3] which has been co-milled during 50 minutes (blue line). The XRD pattern of the anhydrous crystalline lactulose (black line) is also reported for comparison. Both patterns were

[1] there is an error due to the integration of the peaks area, and an error due to the 3 min spent before the measurement.

recorded at room temperature.

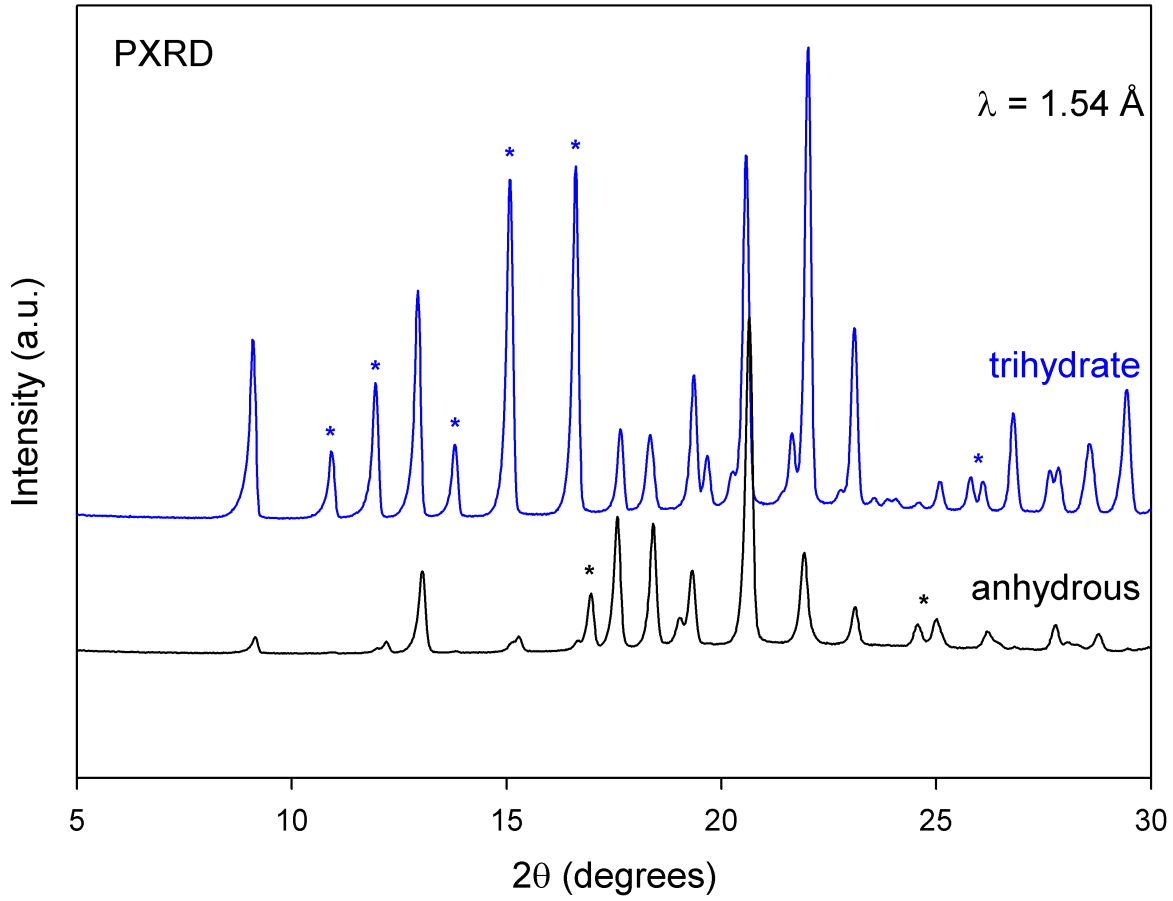

Figure 3.8 – XRD pattern of a mixture "crystalline lactulose / water" in the molar ratio [1:3] after a 50 minutes co-milling (blue line). The pattern of anhydrous lactulose (black line) is reported for comparison.

The blue line shows Bragg peaks characteristic of a crystalline state. The pattern is however partly different from that of the anhydrous crystal. It shows, in particular, characteristic Bragg peaks at 10.9°, 11.9°, 13.8°, 15.1°, 16.6° and 25.8° which are not present in the anhydrous crystal pattern. Moreover, the Bragg peak at 17.0°, present in the anhydrous crystal pattern, is absent in that of the co-milled mixture. These differences indicate that structural changes occurred during the co-milling of the anhydrous crystal with water. The analysis of the XRD pattern - of the compound obtained after co-milling the anhydrous crystalline lactulose with three water molecules - made with the FullProf software [153] indicates that it crystallises in an orthorhombic system, having the following cell parameters:

$$a = 9.6251(3)\ \text{Å}, b = 12.8096(3)\ \text{Å}, c = 17.7563(4)\ \text{Å}, \alpha = \beta = \gamma = 90°$$

Those cell parameters are identical to the ones obtained by Jeffrey et al. [146] for the trihydrate crystalline lactulose. The compound obtained after co-milling the anhydrous crystalline lactulose with water in the ratio [1:3] is thus the trihydrate crystalline lactulose.

DSC curves of trihydrate crystalline lactulose recorded at 5 °C/min in an open pan are depicted in figure 3.9.

Run 1 corresponds to the first heating run, from 20 °C to 120 °C. It shows one broad endotherm which mainly corresponds to the dehydration of the trihydrate crystal. A XRD pattern recorded at room temperature after the dehydration stage shows small Bragg peaks characteristic of the anhydrous form. This indicates that the dehydration of the trihydrate form leads, at least partly, to the anhydrous form.

Run 2 corresponds to the re-heating (5 °C/min) of the sample rapidly cooled down to 20 °C at the end of run 1. It shows:

- A specific heat (C_p) jump at T_g= 88 °C characteristic of a glass transition. It indicates that an amorphous fraction has been formed during the dehydration stage of lactulose trihydrate (which occurred during run 1);

- An endotherm corresponding to the melting of the anhydrous crystal. The enthalpy associated to this melting endotherm is ΔH = 42 J/g. Comparing it to the melting enthalpy of the anhydrous crystal (ΔH_m = 125.7 J/g), it can be deduced that the fraction of anhydrous crystal produced during the dehydration stage (i.e. at the end of run 1) is 0.33, while the fraction of amorphous lactulose produced is 0.67.

The formation of a crystal/amorphous phase mixture during the dehydration of a hydrate has already been observed on trehalose [25]. It has been shown that the relative proportions of crystal and amorphous phases depend on the dehydration rate. A slow dehydration favours the formation of the crystalline anhydrous form, while a rapid dehydration promotes the formation of the amorphous phase. The dehydration of lactulose trihydrate probably follows the same behaviour. A detailed study of this phenomenon, similar to that carried out on trehalose dihydrate, is beyond the scope of this work. It would however be an interesting extension.

3.1.2.b) Tautomeric composition of the trihydrate crystal

Figure 3.10 shows the NMR spectra of the trihydrate crystal (cyan line) and the anhydrous crystal (black line), both measured at room temperature 3 min after dissolution in DMSO. For this experiment, trihydrate crystal was obtained by co-milling the anhydrous lactulose with heavy water (D_2O) in order to avoid disturbance of the NMR signal by the H atoms present in light water (H_2O). By XRD, we have checked that this compound has the same structure than the trihydrate crystal obtained by co-milling the anhydrous lactulose with light water.

On the figure, it can be seen that for the trihydrate crystal, the characteristic peaks of tautomers A, B and C are slightly moved towards large chemical shifts, compared to those of the anhydrous crystal. This comes from the pH difference between the two solutions (the one containing the trihydrate lactulose being more basic because of the presence of water).

The tautomeric proportions deduced from the NMR spectra (figure 3.10) are shown in table 3.2. They indicates that fraction of tautomer A is much higher in the trihydrate lactulose than in the anhydrous sample. This result is in line with the results of Jeffrey et al. [146], which show that the trihydrate crystal obtained by crystallisation in solution is only

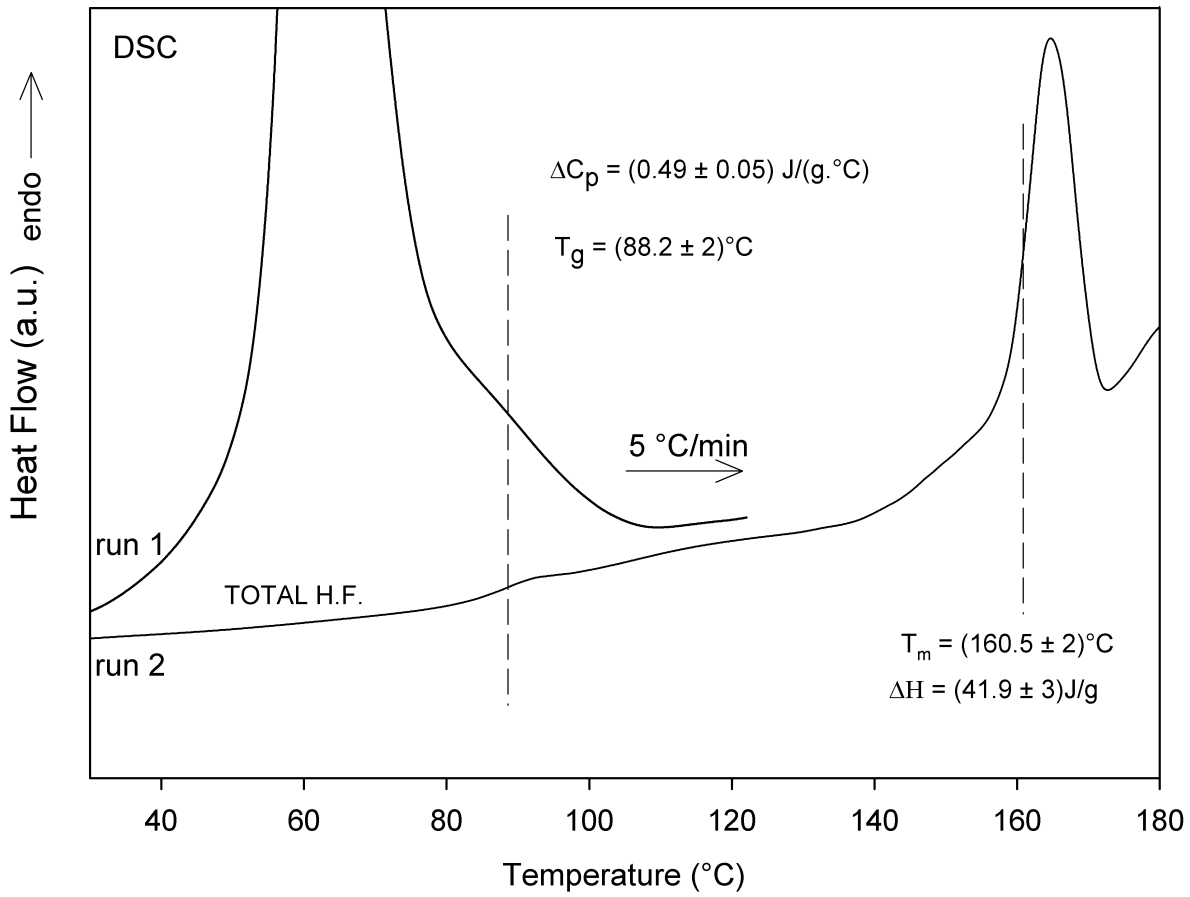

Figure 3.9 – DSC curves of trihydrate crystalline lactulose (5°C/min)
run 1: heating (up to 120 °C) of the trihydrate lactulose obtained by co-milling.
run 2: Rescan of the trihydrate lactulose after run 1.

composed of tautomer A. The slight differences between the results obtained here and those obtained by Jeffrey et al. are mainly due to two factors:

- Since the fraction of tautomer A is greater in the trihydrate crystal than in the anhydrous one, the systematic conversion of tautomer A toward tautomers B and C during the first 3 min after dissolution in DMSO is inevitably greater. The fraction of tautomer A in the trihydrate crystal 3 min after dissolution in DMSO is thus more underestimated than in the anhydrous crystal (from the kinetic of mutarotation A → B/C in DMSO determined in section 3.1.1.b), the underestimation of tautomer A is expected to be about 0.6% for a sample with 80% of tautomer A).

- The excess or the lack of water used during the co-milling with anhydrous crystal, to reach molar proportions [1:3], may modify the global tautomeric composition of the sample. In particular, it can generate a small amorphous fraction or a small anhydrous crystal fraction in the co-milled sample, both of which are characterised by a fraction of tautomer A smaller than 1.

Complementary experiments have shown that the tautomeric composition strongly depends on the dehydration rate. In particular, the proportion of tautomer A is greater as the

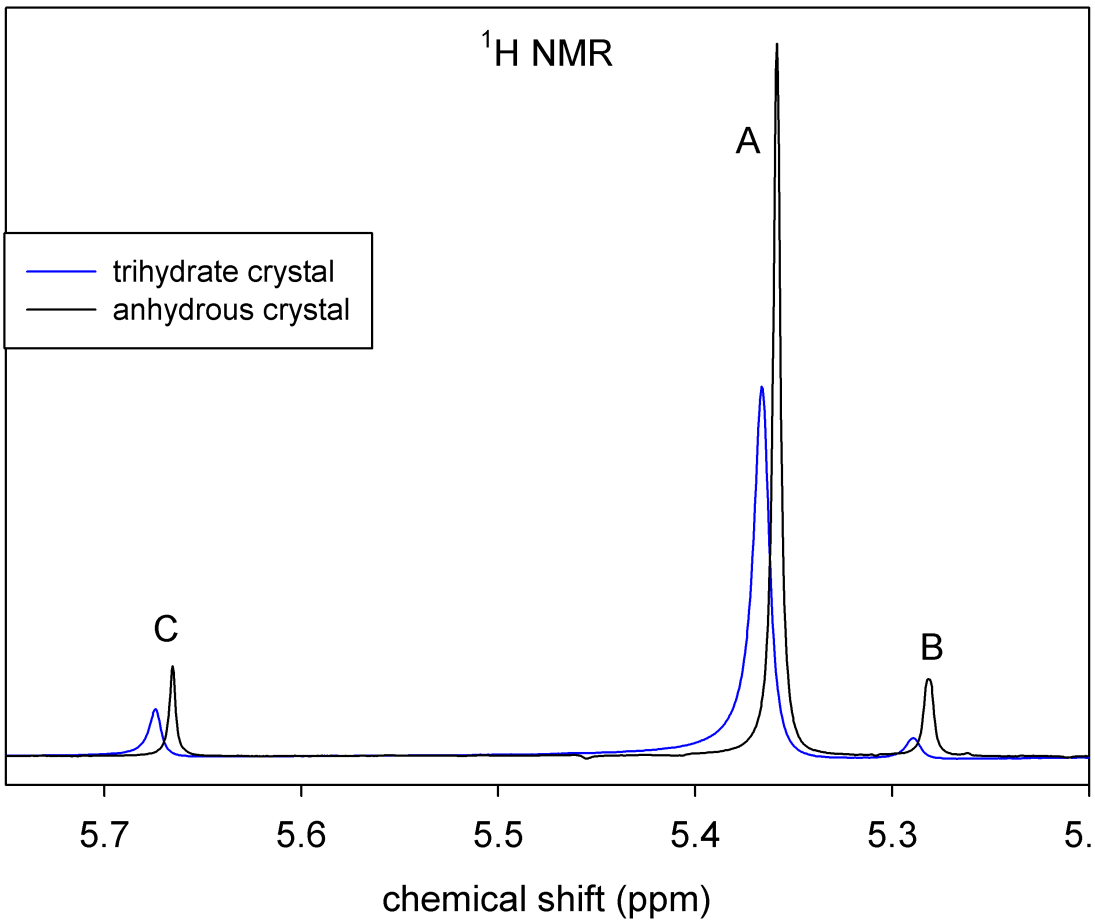

Figure 3.10 – NMR spectra of trihydrate (blue line) and anhydrous (black line) crystalline forms of lactulose, recorded at room temperature 3 min after dissolution in DMSO.

Table 3.2 – Tautomeric proportions of trihydrate and anhydrous crystalline forms of lactulose.

Samples	% of tautomer A (±4)	% of tautomer B (±2)	% of tautomer C (±2)
Trihydrate crystal	88.8	2.7	8.5
Anhydrous crystal	79.3	10.3	10.4

dehydration rate is slow. **It was however not possible to obtain the anhydrous crystal just having tautomer A, by dehydration, even at slow rate, of the trihydrate crystal.**

3.2 Amorphous lactulose obtained by quenching the melted lactulose

The physical properties of the amorphous lactulose obtained by quenching the melted lactulose are presented in this section.

3.2.1 Characterisation by XRD and DSC experiments

Figure 3.11 shows a XRD pattern (green line) of a lactulose sample which has been quenched from the melt (QFTM). The starting crystal was initially dried (isotherm of 30 min at 50 °C) before melting. The QFTM sample was obtained by melting at 180 °C (5 °C/min) the anhydrous crystal, and subsequently suddenly quenching the melt at room temperature. The absence of Bragg peaks in this XRD pattern strongly suggests that the material is amorphous, so that it has been successfully undercooled. This XRD pattern shows a main diffusion halo centered on the XRD pattern region of the anhydrous crystal (black line) where the Bragg peaks are the most intense.

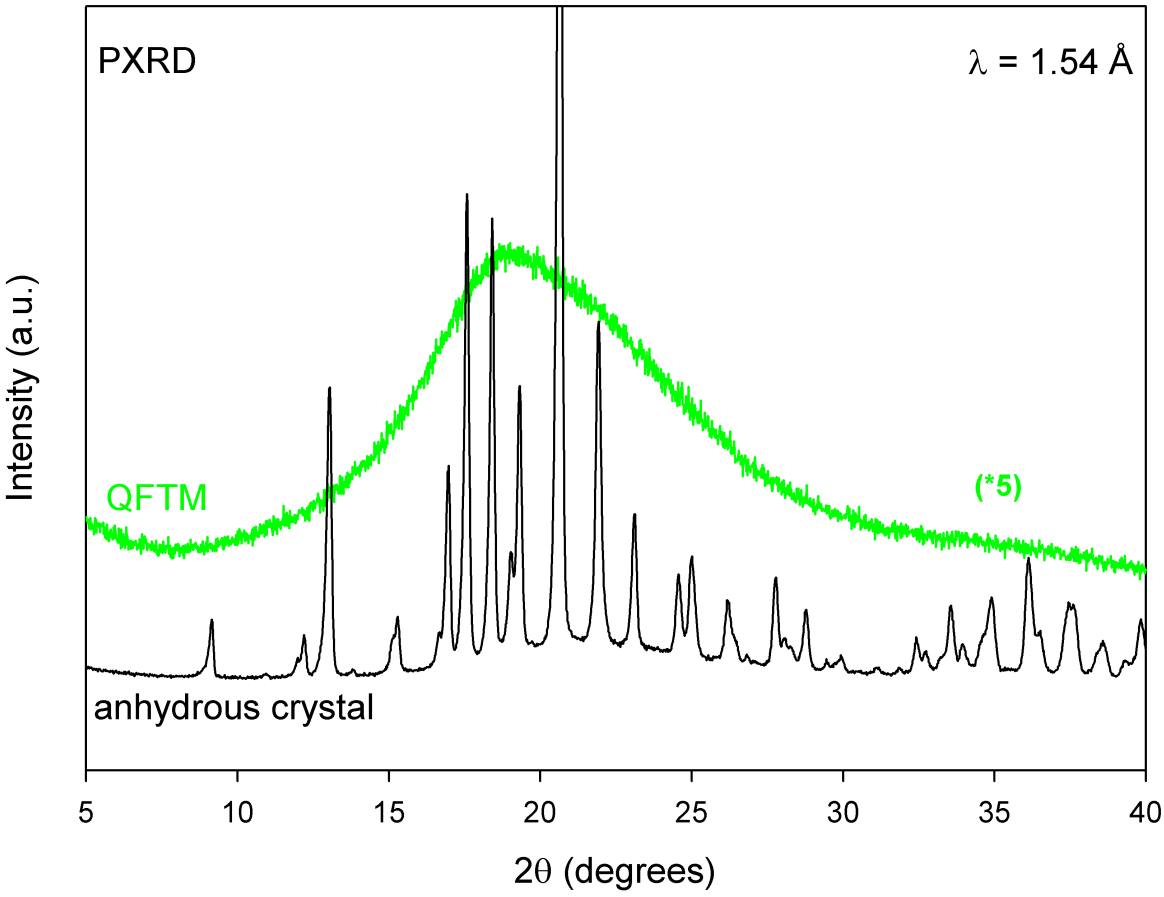

Figure 3.11 – XRD pattern of the QFTM lactulose (green line). The XRD pattern of the anhydrous crystalline lactulose (black line) is also reported for comparison.

DSC curves of lactulose samples recorded between 20 °C and 175 °C are depicted in figure 3.12.

Run 1 corresponds to the heating (5 °C/min) of the anhydrous crystal. It shows one endotherm occurring around T = 155 °C. This endotherm corresponds to the dehydration-melting-degradation endotherm as explained in section 3.1.1.a).

Run 2 corresponds to the cooling (5 °C/min) of the melt down to 20 °C. No sign of exothermic crystallisation can be detected, which means that the liquid can be easily undercooled using a moderate cooling rate.

Run 3 corresponds to the re-heating (5 °C/min) of the quenched liquid. It clearly shows a specific heat jump (ΔC_p = 0.64 J/(g.°C)) characteristic of a glass transition at T_g= 94.7 °C. This C_p jump indicates the vitrification of the lactulose obtained by quenching the liquid. The value of the glass transition temperature obtained here corresponds to the experimental value obtained by Miller et al. [48].

Above T_g, no calorimetric accident is observed. In particular, no recrystallisation exotherm is detected. This indicates that **lactulose is a good glass former.**

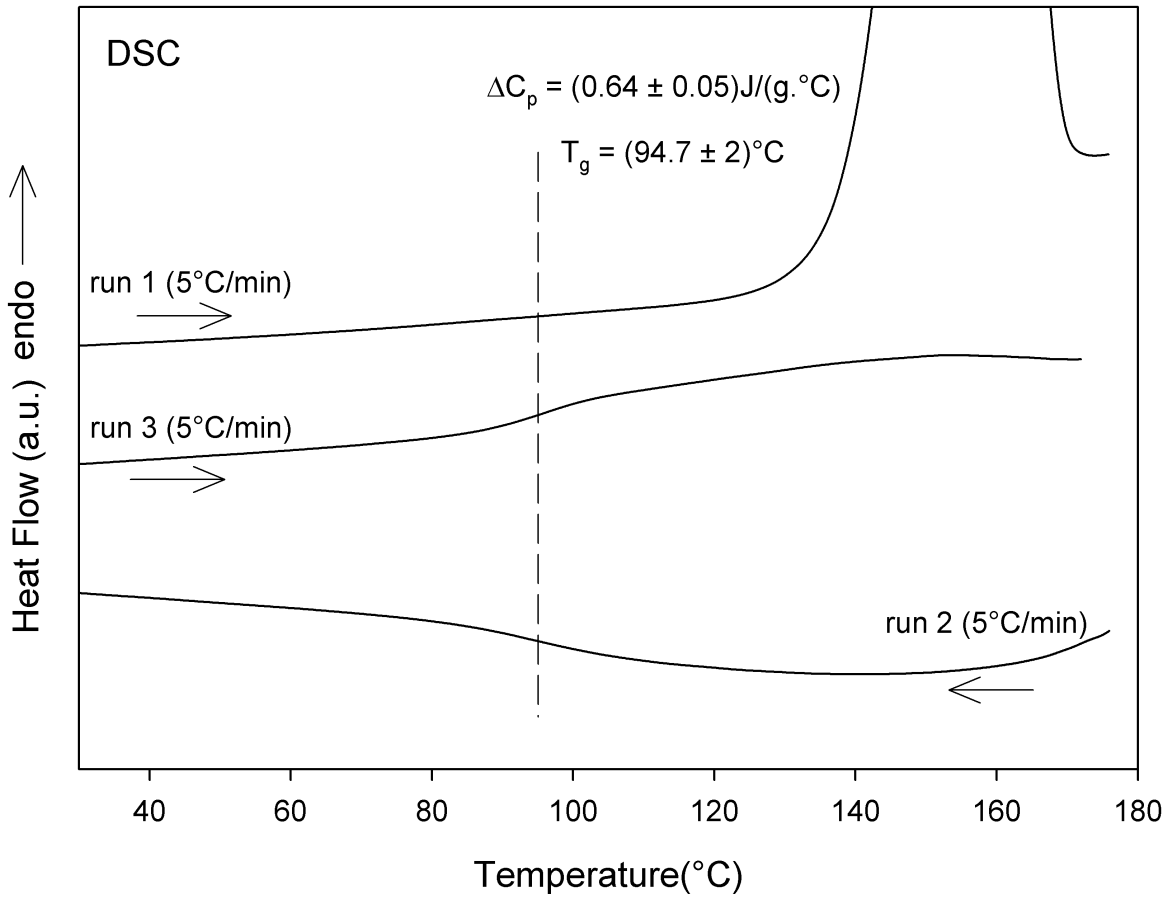

Figure 3.12 – DSC curves (5 °C/min) of lactulose:
run 1: heating of the anhydrous crystalline form.
run 2: cooling of the melt.
run 3: heating of the undercooled liquid.

3.2.2 Evidence of water inclusions in the commercial lactulose

The analysis of the results obtained on anhydrous crystalline lactulose by DSC and TGA showed that:

- the melting temperature range is wide;
- several mass losses occur in the melting temperature range.

A serie of DSC experiments aiming to better understand the different mechanisms that accompany the melting of the anhydrous crystalline lactulose are presented here.

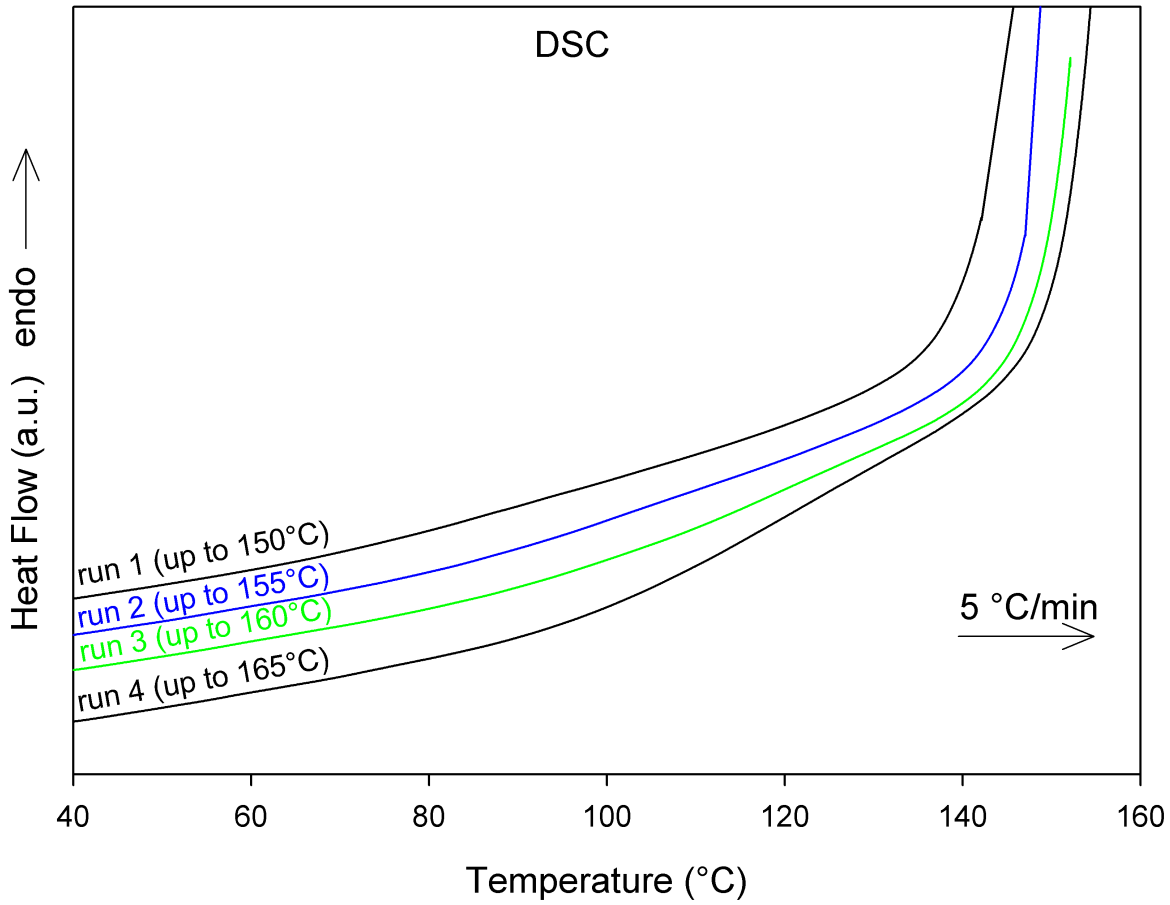

Figure 3.13 – Repeated DSC scans (5 °C/min) of a crystalline lactulose sample performed for increasing final temperatures ranging from 150 °C to 165 °C. The initial sample was previously dried at 120 °C during 20 min.
run 1: heating from 20 °C to 150 °C.
run 2: heating from 20 °C to 155 °C.
run 3: heating from 20 °C to 160 °C.
run 4: heating from 20 °C to 165 °C

An anhydrous crystalline lactulose sample was first dried at 120 °C during 20 min in order to remove the free water. The sample was then submitted to several DSC scans (5 °C/min) performed for increasing final temperatures ranging from 150 °C to 165 °C. These scans are

reported in figure 3.13.

Run 1 corresponds to a heating up to 150 °C. It shows an endotherm starting at 135 °C.

Run 2 corresponds to a heating up to 155 °C. It shows an endotherm starting at 140 °C. The absence of specific heat (C_p) jump in the glass transition temperature region means that no amorphous phase was created during run 1. Thus, the incipient endotherm detected at the end of run 1 does not correspond to the melting. It probably corresponds to the release of water inclusions present in the compound. This departure of water is at the origin of the second mass loss (from 130 °C to 160 °C) previously detected by TGA (see figure 3.2 b)).

Run 3 corresponds to a heating up to 160 °C. It shows an endotherm which starts at 143 °C. This endotherm is preceded by a weak C_p jump, which spreads between 105 °C and 120 °C. This jump is characteristic of a glass transition. It indicates the presence of an amorphous fraction which is likely to come from a partial melting of the material during run 2. This indicates that the melting of the compound starts between 155 °C and 160 °C. However, the water release can also be partly at the origin of this amorphisation.

Run 4 corresponds to a heating up to 165 °C. It shows a larger C_p jump revealing the presence of a higher amorphous fraction. This C_p jump is followed by an endotherm which begins at the same temperature than the one seen in run 3. This well-defined temperature suggests that this endotherm now corresponds to a pure melting process.

The above results indicate that the endotherm at high temperature is the consequence of two different mechanisms occurring in neighbouring temperature ranges. The first one is a release mechanism of water molecules strongly imprisoned in the crystal in the form of inclusions. This phenomenon does not create significant amorphous phase as it does not give signs of glass transition during the following scans. Moreover, removing the remaining water inclusions requires heating the sample at higher temperatures during the next scan. This is the reason why the part of the endotherm associated with the water release shifts towards higher temperatures during the following scans. The second mechanism is the melting itself. This melting creates a valuable amorphous fraction which is detected during the following scans by a C_p jump. Since melting takes place at a well-defined temperature, the endotherm due to the melting does not shift towards higher temperatures.

It should also be noted that the glass transition temperature detected in runs 3 and 4 is located at T_g = 110 °C. It is therefore 15 °C higher than that of the QFTM lactulose. Furthermore, the associated C_p jump is very wide. These effects are the consequence of the thermal degradation due to the extended time spent at high temperature in the course of the cycling experiment. This point will be developed in more details in section 3.3.4.

3.2.3 Tautomeric composition of the QFTM lactulose

Figure 3.14 shows the NMR spectra of QFTM lactulose and anhydrous crystalline lactulose samples. These spectra were recorded at room temperature, 3 min after dissolution in DMSO. Analysis of the NMR spectra enables to determine the tautomeric compositions of these different samples. The results obtained are reported in table 3.3.

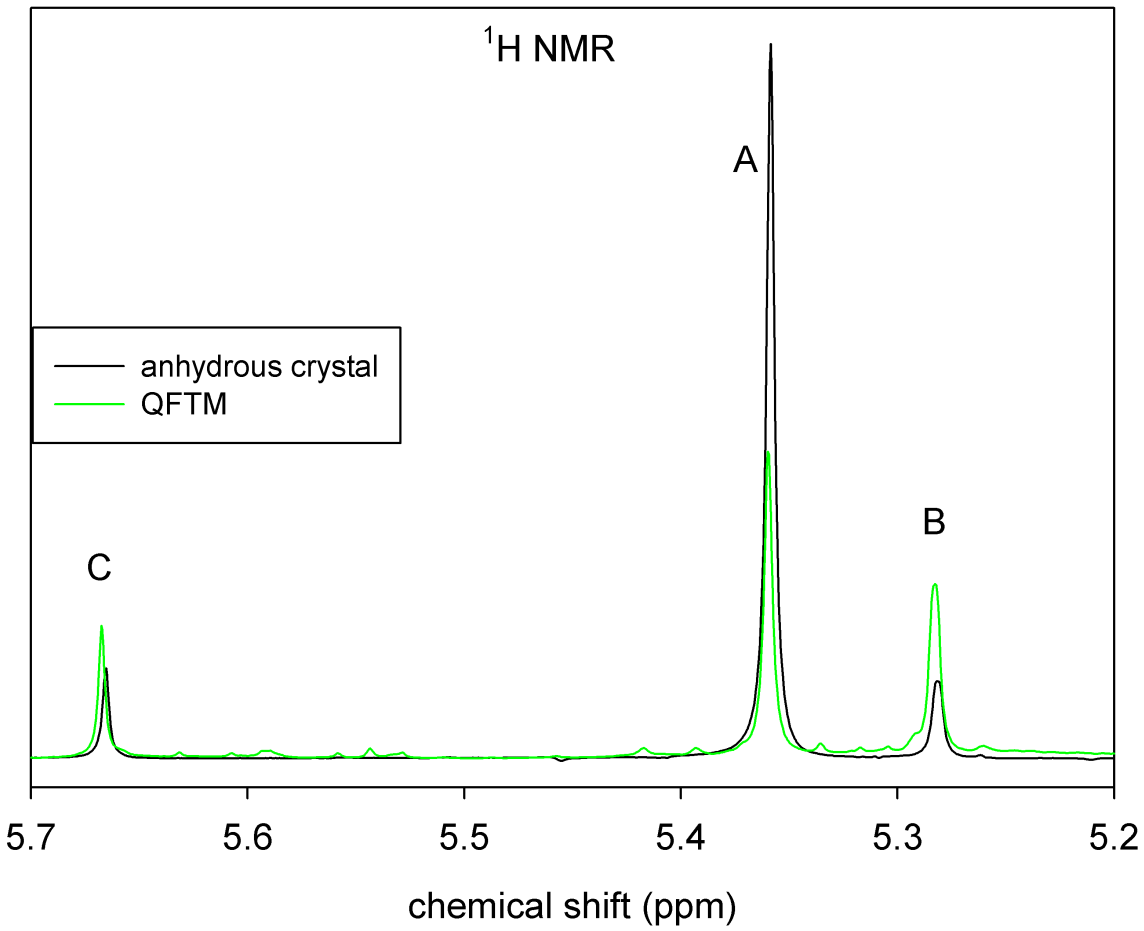

Figure 3.14 – NMR spectra of two lactulose samples: QFTM (green line) and anhydrous crystal (black line). Both spectra were recorded at room temperature 3 min after dissolution in DMSO.

It is found that the tautomeric compositions of the anhydrous crystal and the QFTM samples are notably different. In particular the fraction of tautomer A has strongly decreased to the benefit of tautomers B and C. Moreover, the QFTM spectrum contains some additional small peaks which could be signs of degradation. Possible small molecules (monosaccharides, etc.) present in the system and resulting from the thermal degradation of the compound may give rise to such peaks.

Table 3.3 – Tautomeric composition of the QFTM lactulose. The anhydrous crystalline lactulose is reported for comparison.

Samples	% of tautomer A (±4)	% of tautomer B (±2)	% of tautomer C (±4)
QFTM	48.9	33.6	17.5
Anhydrous crystal	79.3	10.3	10.4

3.3 Amorphous lactulose obtained by milling the crystal

This section aims to study the effects of milling on the physical state of anhydrous crystalline lactulose. To this end, anhydrous crystalline lactulose was milled during 8 h using a planetary mill, alternating milling phases (15 min) with pause phases (15 min) in order to avoid any local heating of the sample induced by the mechanical chocks. The physical state of the milled material was then analysed by XRD, TGA, DSC and NMR as presented below.

3.3.1 Characterisation by XRD experiments

Figure 3.15 shows the diffraction patterns of anhydrous crystalline lactulose before (black line) and after 8 h of milling (red line), recorded at room temperature between 5° and 40° in 2θ. The diffraction pattern of the QFTM lactulose (green line) is also shown for comparison.

The diffraction pattern of the anhydrous crystalline lactulose milled 8 h does not show Bragg peaks. This strongly suggests that it is an amorphous compound. This diffraction pattern is similar to that of the QFTM lactulose: both of them have a diffusion halo centred at 18° (2θ).

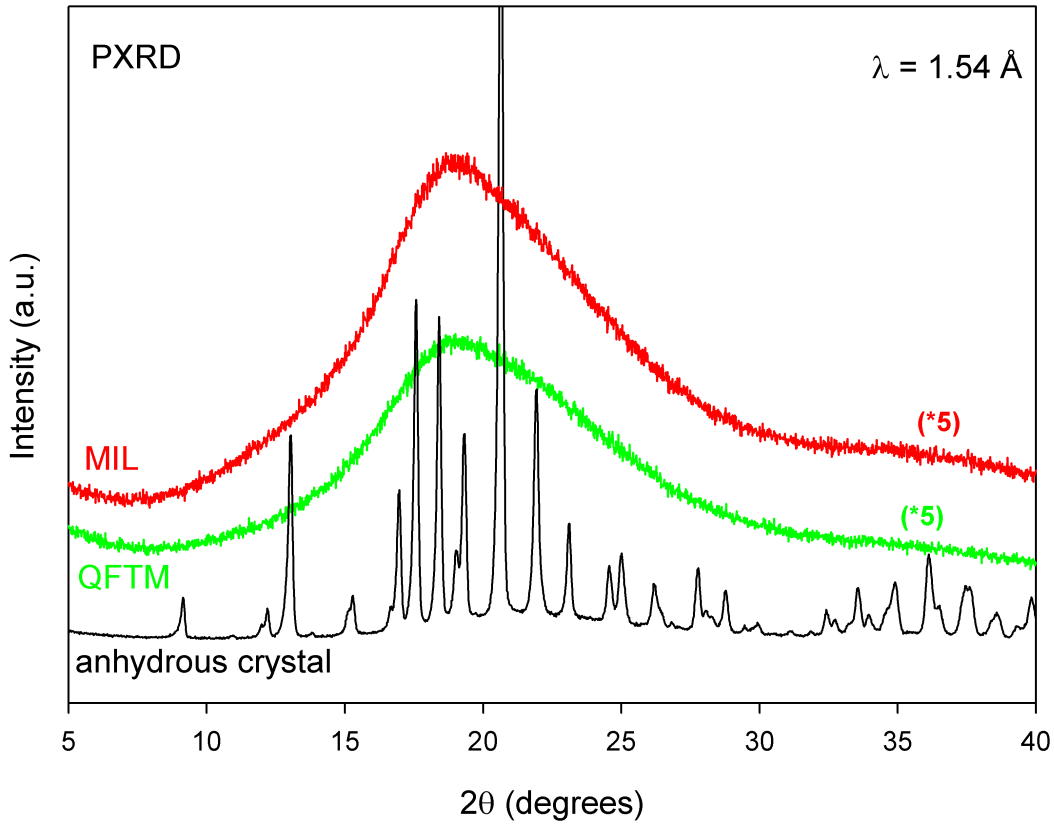

Figure 3.15 – XRD patterns of crystalline lactulose before (black line) and after 8h of milling (red line). The XRD pattern of the QFTM lactulose (green line) is also reported for comparison.

3.3.2 Tautomeric composition of the MIL lactulose

Figure 3.16 shows NMR spectra of lactulose samples obtained after milling the anhydrous crystal under two different relative humidity conditions:

- In a first case, the lactulose crystal was milled during 8 h at room temperature and ambient humidity, and the starting crystalline powder was used as received (red line).
- In a second case, the lactulose crystal was first dried (2 h at 45 °C) and then milled under very low relative humidity (RH # 0%), at -10 °C (blue line).

In both cases the milled sample has been found amorphous from XRD analysis.
The NMR spectrum of the anhydrous crystal (black line) is also reported for comparison. All these spectra were recorded at room temperature 3 min after dissolution in DMSO. The tautomeric compositions of the different samples derived from the analysis of the NMR spectra are reported in table 3.4.

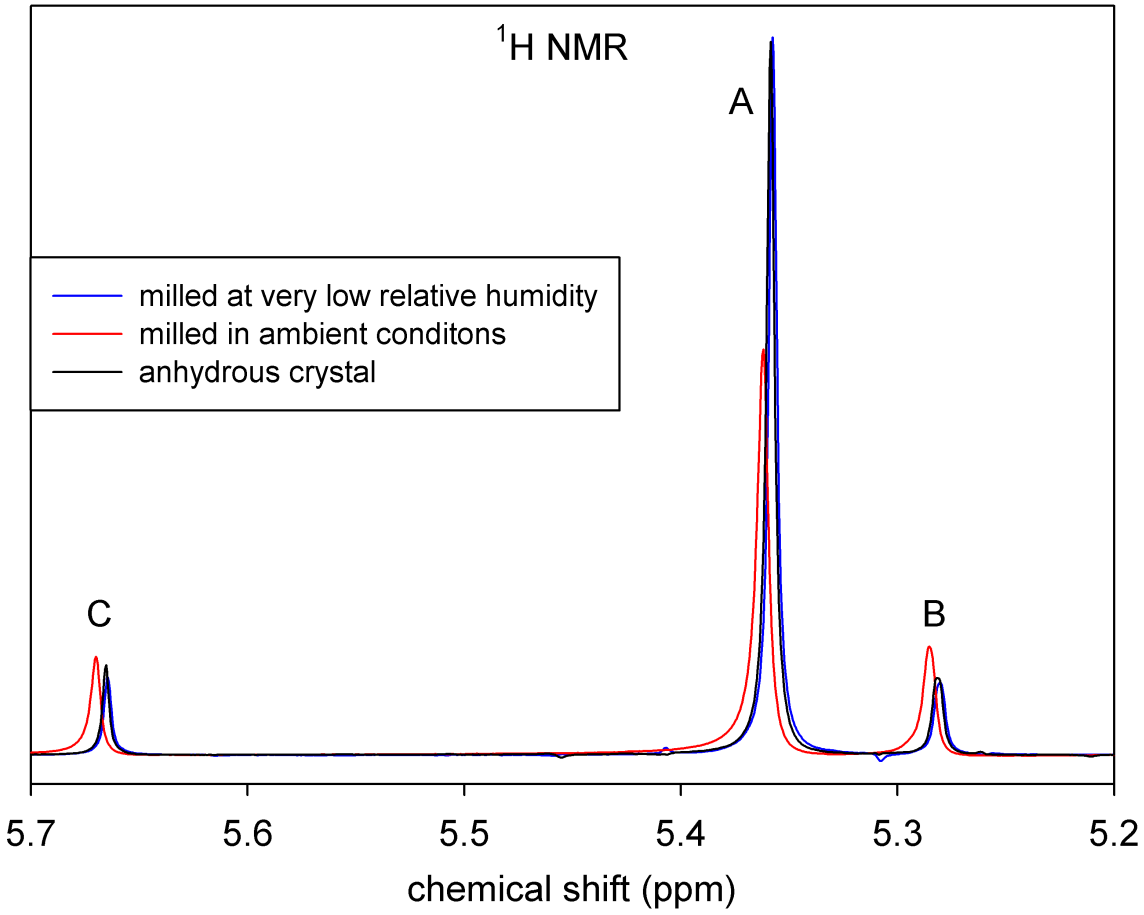

Figure 3.16 – NMR spectra of anhydrous crystalline lactulose: non-milled (black line), milled 8 hours at ambient humidity (red line) and milled 8 hours at very low relative humidity (blue line). All spectra have been recorded at room temperature 3 min after dissolution in DMSO.

Table 3.4 – Tautomeric proportion of crystalline lactulose before and after 8h of milling in two different conditions.

Samples	% of tautomer A (±4)	% of tautomer B (±2)	% of tautomer C (±4)
Milled in ambient conditions	70.1	14.9	15.0
Milled at RH # 0%	81.7	10.1	8.2
Anhydrous crystal	79.3	10.3	10.4

It is found that the tautomeric proportions in the anhydrous crystal and in the anhydrous crystal milled 8 h at very low relative humidity are close. This shows that milling changes the structure of the lactulose (as seen in figure 3.15) without altering its chemical state and in particular without inducing tautomerisation. On the other hand, the tautomeric proportions are substantially modified during milling at ambient humidity. This shows that mutarotation under milling is favoured by the presence of free water caught during milling. Furthermore, the absence of mutarotation during milling under dry conditions proves that the sample does not reach the melting temperature during milling, even locally. Indeed, such a melting would inevitably lead to a strong mutarotation as shown in section 3.2.3 of the QFTM. The sample does not even reach the glass transition temperature during milling, because, as it will be seen later, the mutarotation can occur in the MIL lactulose just above T_g. This behaviour - no local heating of the sample during milling - is identical to that observed for the mutarotation of lactose under milling [215].

Moreover, no signs of degradation are visible on the spectra of the milled compounds (no peaks indicating the presence of possible fragments of molecules in the system). This means that, contrary to the quenching of the melt, **the milling does not degrade the sample**.

3.3.3 Characterisation by TGA and DSC experiments: glass transition and tautomerisation effect

Figure 3.17 shows the TGA and MDSC scans (5 °C/min) of the anhydrous crystalline lactulose milled during 8 h (MIL lactulose). The sample was dried before milling (isotherm of 30 min at 50 °C) and after milling (isotherm of 10 min at 55 °C).The milling was performed at room temperature and ambient humidity.

The TGA curve (figure 3.17 b)) shows a mass loss beginning at about 150 °C and corresponding to the thermal degradation of the compound, as already seen on the crystalline sample (see figure 3.2 b)).

The reversible signal (cyan line in figure 3.17 a)) derived from the MDSC scan (modulation amplitude of 0.663 °C, and a modulation period of 50s) shows two successive specific heat (C_p) jumps:

- The first one, located at T_g = 88.6 °C, corresponds to the glass transition of the sample. This C_p jump shows that the crystal has been amorphised during the 8 hours milling, and that the amorphous compound obtained is a glass.

- The second jump is an artefact due to an apparent increase in the specific heat of the material. It usually follows the glass transition of finely divided amorphous material.

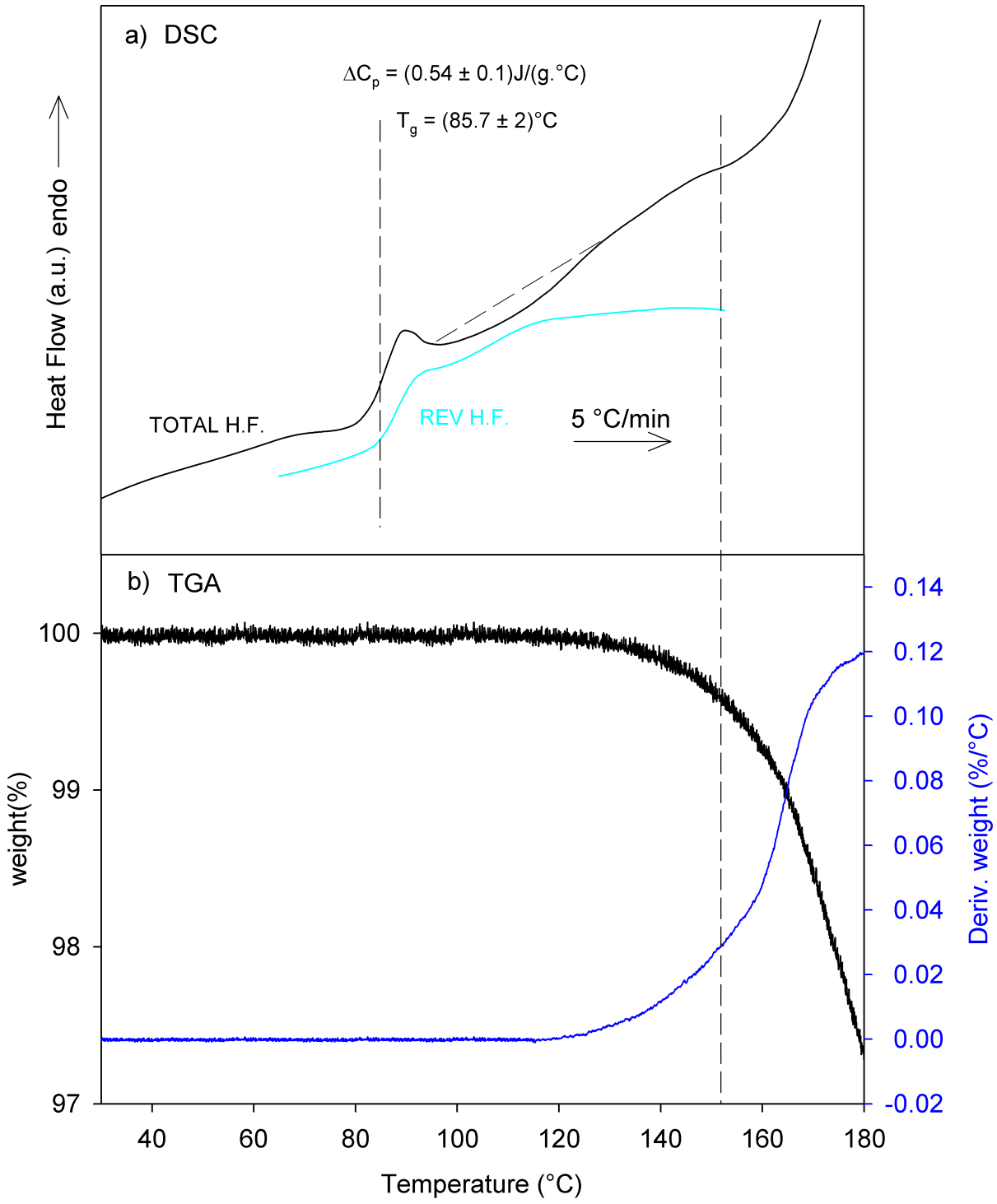

Figure 3.17 – a) DSC curves (reversible and total heat flow) and b) TGA curves of the anhydrous crystalline lactulose milled 8h (5 °C/min).

This effect is due to an increase in the thermal conductivity of the sample which passes from a very fine amorphous powder below T_g to a very dense liquid droplet above T_g. Detailed information on this effect can be found in another thesis [46].

On the total heat flow (black line in figure 3.17 a)), it can be seen:

- a C_p jump at T_g = 85.7 °C. This glass transition temperature is slightly lower (about 3 °C) than that detected on the reversible signal. This is a known effect, due to the fact that the two signals probe the sample with different time scales. For the total heat flow, the time scale is given by the average heating rate (5 °C/min). For the reversible heat flow, it is given by the modulation period (50 s). The amplitude of the C_p jump is ΔC_p = 0.54 J/(g°C). It should be noted that the overlapping of an endotherm and an exotherm located on either side of the C_p jump complicates the determination of the C_p jump amplitude.
  It should also be noted that the glass transition temperature of the MIL lactulose is located 8 °C below that of the QFTM lactulose. The higher T_g of the QFTM lactulose is expected to be due to the degradation that occurs when melting the crystal. This point will be addressed in more details in the next section.

- a small exotherm located just below the C_p jump. Such an exotherm is characteristic of annealed hyper-quenched liquids [216]. It is due to the particular enthalpic catch up of high-energy glasses. It corresponds to a non-reversible phenomenon which does not therefore appear on the reversible signal. This exotherm will be investigated in more details in section 3.6.

- an endotherm located at the end of the C_p jump. It is due to the aging of the glass.

- an exotherm just above the glass transition starting after the previous endotherm. Its amplitude is attenuated by the C_p jump artefact seen in the reversible signal. This exotherm, not visible on the reversible signal, corresponds to a non-reversible phenomenon. However, XRD experiments have shown that the amorphous sample does not undergo partial recrystallisation in this temperature range upon heating at 5 °C/min. Figure 3.18 shows the NMR spectra of milled lactulose recorded just after the milling process and after heating (5 °C/min) to 130 °C. The two spectra are clearly different which indicates a change in the tautomeric composition of the amorphous material upon heating at 5 °C/min. The analysis of the NMR spectrum indicates that the tautomeric composition changes as follows:
  tautomer A: 81.7% → 57.9%
  tautomer B : 10.1% → 25.9%
  tautomer C : 8.2% → 16.2%
  The tautomeric composition at 130 °C is very close to that of the quenched liquid. This tautomerisation is expected to mainly develop just above the glass transition temperature as it has already been shown for some other sugars (lactose [215] and glucose [29]).
  DFT calculations were carried out on single molecule of tautomers A, B and C in order to determine the energy of each of these tautomers. Each of the molecules was initially geometrically optimised. Thereafter, their total energy has been calculated at 0K, with the zero of energy taken as being the infinite separation of all electrons and nuclei. This total energy is thus generally negative, corresponding to a bound state, and can be taken as the energy of the ground state. The results obtained are:
  E_C = -3.602011*10^6 kJ/mol, E_B = -3.602003*10^6 kJ/mol and E_A = -3.601965*10^6 kJ/mol.
  Thus, $E_C < E_B < E_A$. This explains why the tautomeric equilibrium which occurs above T_g gives an exothermic peak.

- finally, an endotherm follows the exothermic tautomerisation process. This endotherm corresponds to the thermal degradation, as seen in figure 3.17 b).

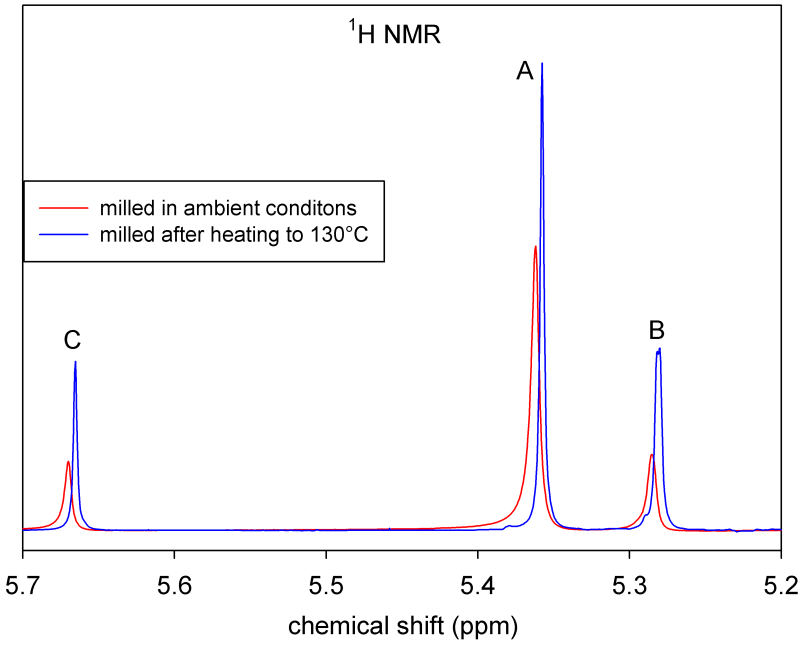

Figure 3.18 – NMR spectra of milled lactulose recorded just after the milling process and after heating (5 °C/min) to 130 °C.

It is important to note that the thermogram of the MIL lactulose shows no signs of recrystallisation. **The amorphous compound obtained by milling is therefore stable upon heating at 5 °C/min**. This stability is quite exceptional, because amorphous compounds obtained by milling almost always recrystallise during heating at 5 °C/min [27, 45, 120].

3.3.4 Effect of tautomerisation and degradation on the glass transition temperature

This section aims to study the influence of thermal degradation on the glass transition temperature. To this end, an amorphous lactulose sample obtained by milling was repeatedly scanned (5 °C/min) by DSC for increasing final temperature. For each new scan, the final temperature is increased by 10 °C compared to the previous scan. Figure 3.19 b) shows a schematic illustration of this thermal treatment, and figure 3.19 a) shows the DSC curves obtained for final temperature varying between 125 °C and 185 °C.

The analysis of the thermograms shown in figure 3.19 a) indicates that their evolution can be split into two stages:

- The first stage corresponds to runs 1 and 2. It shows no evolution of the glass transition temperature, whose value remains around (85 ± 2) °C.

- The second stage corresponds to the last five thermograms (runs 3 to 7). A considerable shift of the glass transition temperature towards high temperatures is observed. Indeed, the glass transition temperature increases by 20 °C when the maximum temperature explored by the sample varies from 145 °C to 175 °C. Moreover, this evolution is accompanied by a strong spreading of the associated C_p jump and a slight decrease

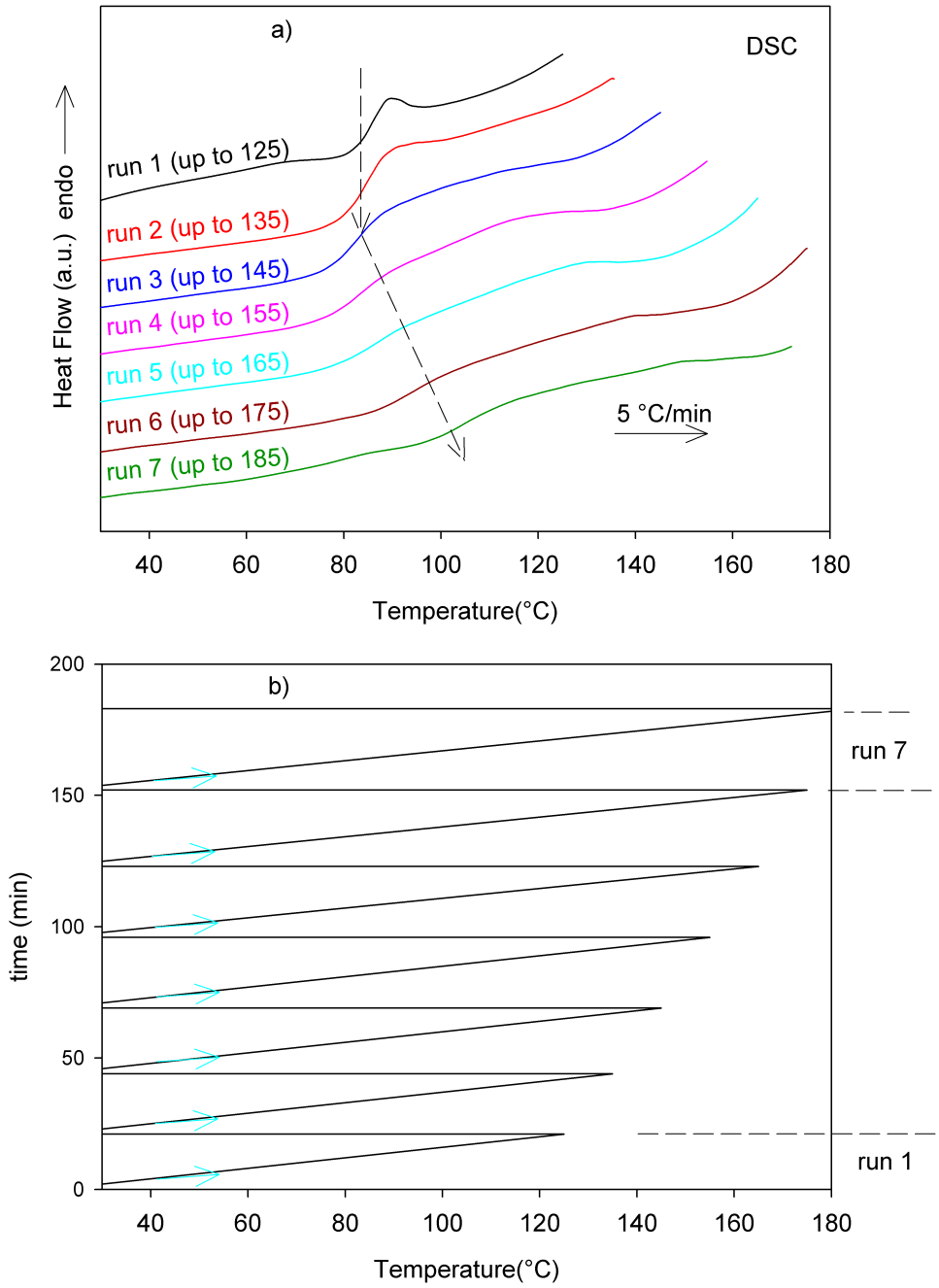

Figure 3.19 – a) Repeated DSC scans (5 °C/min) of crystalline lactulose milled 8 h. For each run, the end temperature is increased by 10 °C compared to the previous one. At the end of each run the sample has been rapidly cooled to 20 °C.
b) Schematic illustration of the thermal treatment used to perform the DSC scan from run 1 to run 7.

of its amplitude. It is also noted that the end of each scan is marked by the development of an endothermic signal. This endothermic signal corresponds to the thermal degradation of lactulose, as previously presented.

NMR experiments performed just before the run 1, run 2 and run 7 are reported in figure 3.20. The tautomeric compositions of the samples deduced from these spectra are reported

in table 3.5. It appears that the tautomeric composition of the samples change noticeably between run 1 and run 2 while T_g is almost constant. The tautomerisation occurring upon heating the amorphous milled lactulose has thus only a little effect on the glass transition of the material.

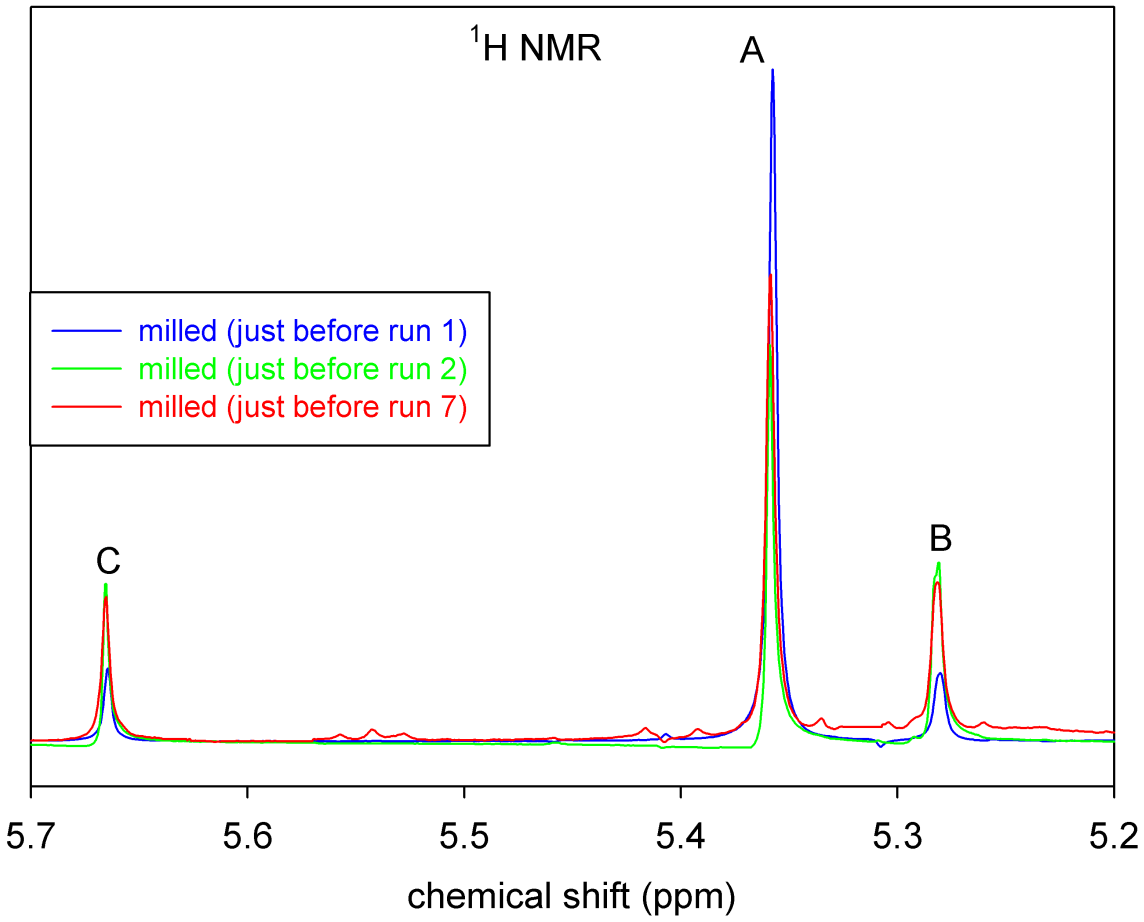

Figure 3.20 – NMR spectra amorphous lactulose recorded just before run 1 (blue line), run 2 (green line) and run 7 (red line) of figure 3.19. All spectra have been recorded at room temperature 3 min after dissolution in DMSO.

Table 3.5 – Tautomeric proportions of amorphous lactulose measured just before run 1, run 2 and run 7. These results are derived from the NMR spectra presented in figure 3.20.

Samples	% of tautomer A (±4)	% of tautomer B (±2)	% of tautomer C (±4)
Milled (just before run 1)	81.7	10.1	8.2
Milled (just before run 2)	53.1	28.8	18.1
Milled (just before run 7)	54.7	26.3	19.0

On the contrary the tautomeric composition of the samples nearly does not change between run 3 and run 7 while T_g strongly increases. This increase must thus not be ascribed to a change of the tautomeric composition. Therefore, it is clearly the thermal degradation,

which goes crescendo with the maximum temperature reached by the sample, which is responsible for the shift of the glass transition temperature seen in runs 3 to 7.

Thermal degradation of lactulose compounds thus appears to have a strong anti-plasticising effect. This anti-plasticising effect explains the high values of the glass transition temperature determined for the QFTM lactulose (compared to the MIL lactulose), which requires heating the crystalline sample beyond its melting temperature, and then above the beginning of thermal degradation.

In the previous section, it has been shown that the MIL lactulose does not recrystallise upon heating, and does not degrade during milling. This gives the opportunity to form a non-degraded quenched liquid, by heating the MIL lactulose just above T_g (so that it softens) without reaching the temperature at which degradation starts, and then cooling the undercooled liquid obtained. It is thus possible to compare the « conventional » quenched liquid (which has undergone thermal degradation) with a non-degraded quenched liquid. The compound at the beginning of run2 (figure 3.19 a)) is precisely a non-degraded quenched liquid obtained by softening the MIL lactulose, and then quenching the undercooled liquid obtained. It has a glass transition temperature equal to that of the MIL lactulose: T_g = 85 °C. This temperature is noticeably smaller than that of the quenched liquid obtained in the « conventional » manner: T_g = 94.7 ° C.

Moreover, as shown by NMR results, the MIL lactulose (compound at the beginning of run 1 in figure 3.19 a)) and the non-degraded quenched liquid (compound at the beginning of run 2 in figure 3.19 a)) have different tautomeric proportions (see table 3.5). **This means that the small differences in tautomeric composition between these two amorphous materials do not strongly influence their glass transition temperature**. However, as it will be seen later, larger tautomeric differences may have an influence on the glass transition temperature.

3.4 Amorphous lactulose obtained by spray-drying and freeze-drying

This section is dedicated to the investigation of physico-chemical properties of lactulose compounds obtained by spray-drying and freeze-drying. These two preparation methods have been enforced following the protocols described in chapter 2. The results obtained by XRD, DSC and NMR are presented below.

3.4.1 Characterisation by XRD

Figure 3.21 shows the XRD patterns of lactulose samples obtained by spray-drying (SD lactulose, pink line) and freeze-drying (FD lactulose, blue line), recorded at room temperature between 5° and 40° in 2θ. The XRD patterns of the QFTM lactulose (green line) and the MIL lactulose (red line) are also reported for comparison.

No Bragg peaks can be seen on the XRD patterns of the SD and FD lactulose. This strongly suggests that they are amorphous compounds. These XRD patterns are similar to those of the QFTM and MIL lactulose: all four have a diffusion halo centred at 18° (2θ) approxima-

tely. This means that the compounds obtained by the four different techniques have similar structures. These structures will be more deeply analysed by neutron scattering experiments in chapter 5.

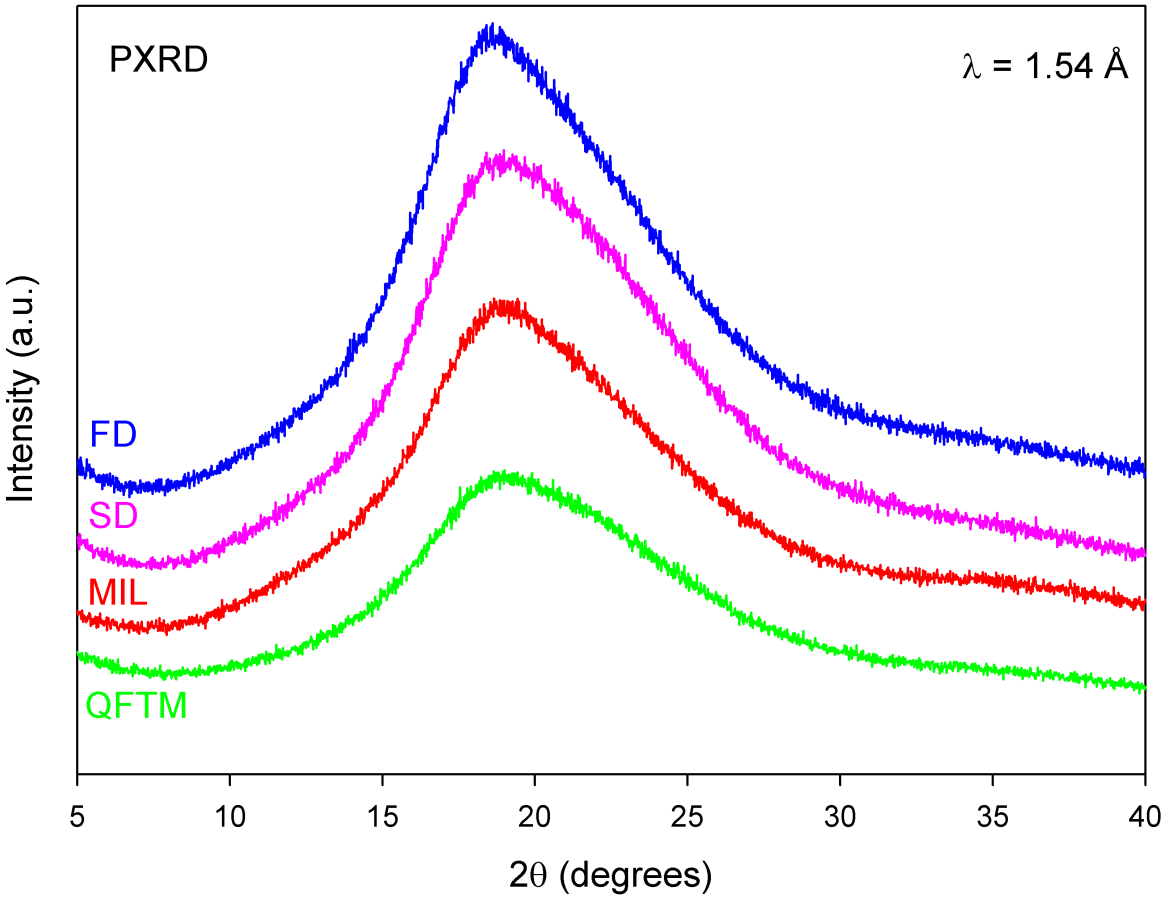

Figure 3.21 – XRD patterns of the SD (pink line), FD (blue line), QFTM (green line) and MIL lactulose (red line).

3.4.2 Characterisation by NMR spectroscopy

Figure 3.22 shows NMR spectra of:

- the SD lactulose (pink line)
- the quenched from the “softened spray-dried” lactulose (QFTSSD), obtained after quenching at room temperature the liquid lactulose coming from the softening (heating at 5°C/min up to 150 °C) of the SD lactulose (red line)
- the FD lactulose (blue line)
- the quenched from the “softened freeze-dried” lactulose (QFTSFD), obtained after quenching at room temperature the liquid lactulose coming from the softening (heating at 5 °C/min up to 150 °C) of the FD lactulose (cyan line).

- the MIL lactulose (black line) added for comparison.

All spectra have been recorded at room temperature 3 min after dissolution in DMSO.

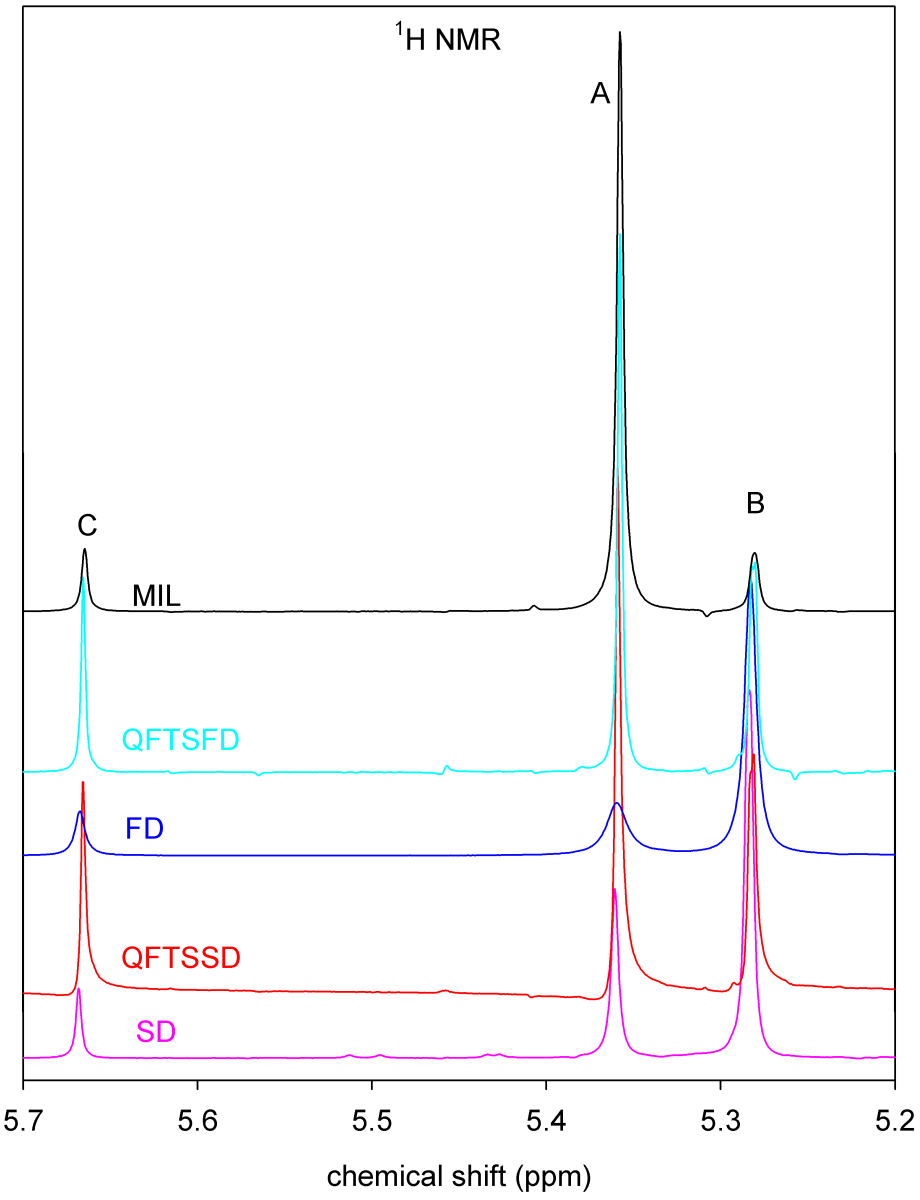

Figure 3.22 – NMR spectra of different amorphous lactulose samples:
SD (pink plot);
QFTSSD (red plot);
FD (blue plot);
QFTSFD (cyan plot);
MIL (black plot).

The tautomeric compositions of the samples, deduced from each of these spectra are reported in table 3.6. It can be seen that the tautomer B predominates in the amorphous samples obtained by spray-drying and freeze-drying. This is not the case in the MIL sample,

where tautomer A predominates. These differences of tautomeric compositions between the MIL sample on the one hand, and the SD and FD samples on the other hand, are due to the mutarotation which took place when the crystalline lactulose was in solution (during the spray-drying and freeze-drying operations).

One can also notice that, after being softened and subsequently quenched (QFTSSD and QFTSFD), the tautomeric compositions of the SD and FD samples completely change, and the tautomer A becomes the majority one.

Table 3.6 – Tautomeric proportions of different amorphous samples of lactulose: the SD, the FD, the QFTSSD, the QFTSFD, and the MIL.

Samples	% of tautomer A (±4)	% of tautomer B (±4)	% of tautomer C (±4)
SD	29.4	61.8	8.8
FD	23.4	68.4	8.2
QFTSSD	50.0	31.9	18.1
QFTSFD	51.2	31.0	17.8
MIL (milled at RH # 0%)	81.7	10.1	8.2

3.4.3 DSC analysis of the SD and FD lactulose

3.4.3.a) Case of the SD sample

Figure 3.23 shows the results of a MDSC experiment performed on SD lactulose. The SD lactulose sample was initially dried during a heating ramp (5 °C/min) from 20 °C to 65 °C. It was then analysed by MDSC, using an average heating rate of 5 °C/min, a modulation amplitude of 0.663 °C, and a modulation period of 50 s. The signals corresponding to the total heat flow (black line) and the reversible heat flow (blue line) are shown in the figure.

The reversible heat flow (blue line) shows two successive specific heat (C_p) jumps:

- The first one, located at T_g = 98.8 °C corresponds to the glass transition of the SD lactulose. This C_p jump attests that the lactulose has been amorphised by spray-drying, and that the amorphous sample obtained is a glass.

- The second one, located immediately after the first one spreads from 101 °C to 122 °C. This jump is an artefact frequently observed in amorphous materials with large specific surface areas (see [46]).

The total heat flow (black line) shows:

- An endotherm centred at 80 °C corresponding to the release of free water remaining in the sample. TGA experiment on the SD lactulose has confirmed this point. Such free water in SD amorphous materials is quite usual as spray-drying technique requires to first dissolve the material in water.

- A C_p jump at T_g = 95.6 °C. This value is nearly 10 °C higher than that of the MIL lactulose. Such a difference is likely to be due to the different tautomeric compositions of the two amorphous materials reported previously (see table 3.6).

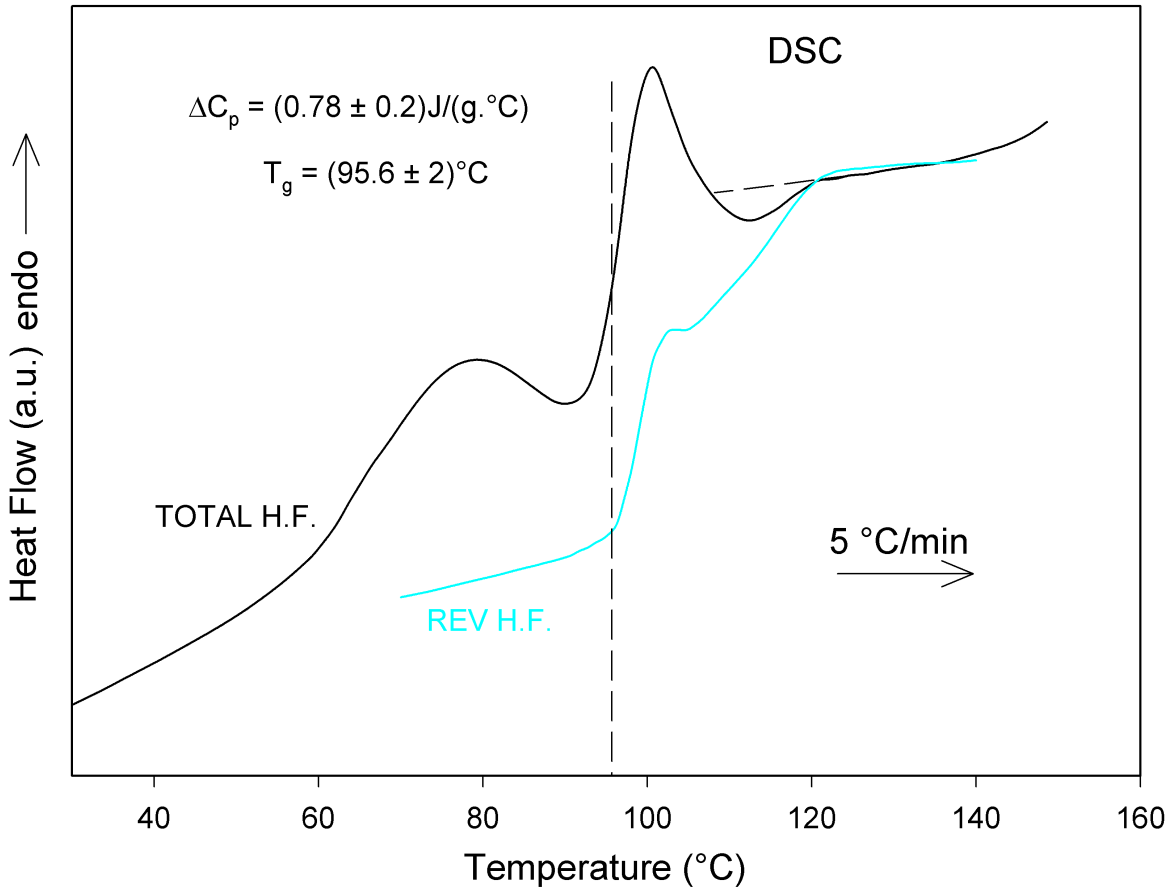

Figure 3.23 – DSC curves (reversible and total heat flow) of the SD lactulose recorded upon heating (5 °C/min) from 20 °C to 150 °C.

- An endotherm, located just after the C_p jump. This endotherm results mainly from the recovery of the enthalpy lost during the aging of the glass which has occurred during the scan itself and during the initial drying stage. It gives rise to a relaxation endotherm. Its amplitude is however much larger than that of the MIL lactulose (see figure 3.17). This is due to the fact that the T_g of the initial spray-dried sample is strongly depressed by the free water. The annealing stage used for drying the sample is thus performed at a temperature which is close to the effective T_g of the plasticised material. This makes the relaxation faster and deeper.
  Before the endotherm is completed, the heat flow increases, because of the artefact previously mentioned in the reversible signal. This gives rise to a fictive exotherm on the thermogram, ranging from 105 °C to about 118 °C. The equilibrium line of the liquid is then caught-up from 120 °C.

- Above 145 °C, an endotherm which starts to develop. This endotherm corresponds to thermal degradation. This was also observed in the case of the MIL lactulose.

As previously mentioned, mutarotation is "unblocked"[2] in the SD compound just above

[2]Normally mutarotation is allowed at any temperature. It is just a matter of kinetic. Depending on the mobility, it will be necessary to spend more or less time for the mutarotation to establish **so as to be perceptible**.The

T_g. It therefore evolves from the tautomeric composition of the SD sample (see table 3.6) to that of the undercooled liquid. But enthalpic signature (expected to be endothermic from DFT results presented in section 3.3.3) of this tautomerisation is embedded in the enthalpic events that happen in this temperature range (from T_g to T_g + 25 °C).

The previous sample (SD lactulose heated up to 150 °C) was then quenched at 20 °C and rescanned at 5 °C/min. In figure 3.24, this rescan (run 2) is compared to the first one.

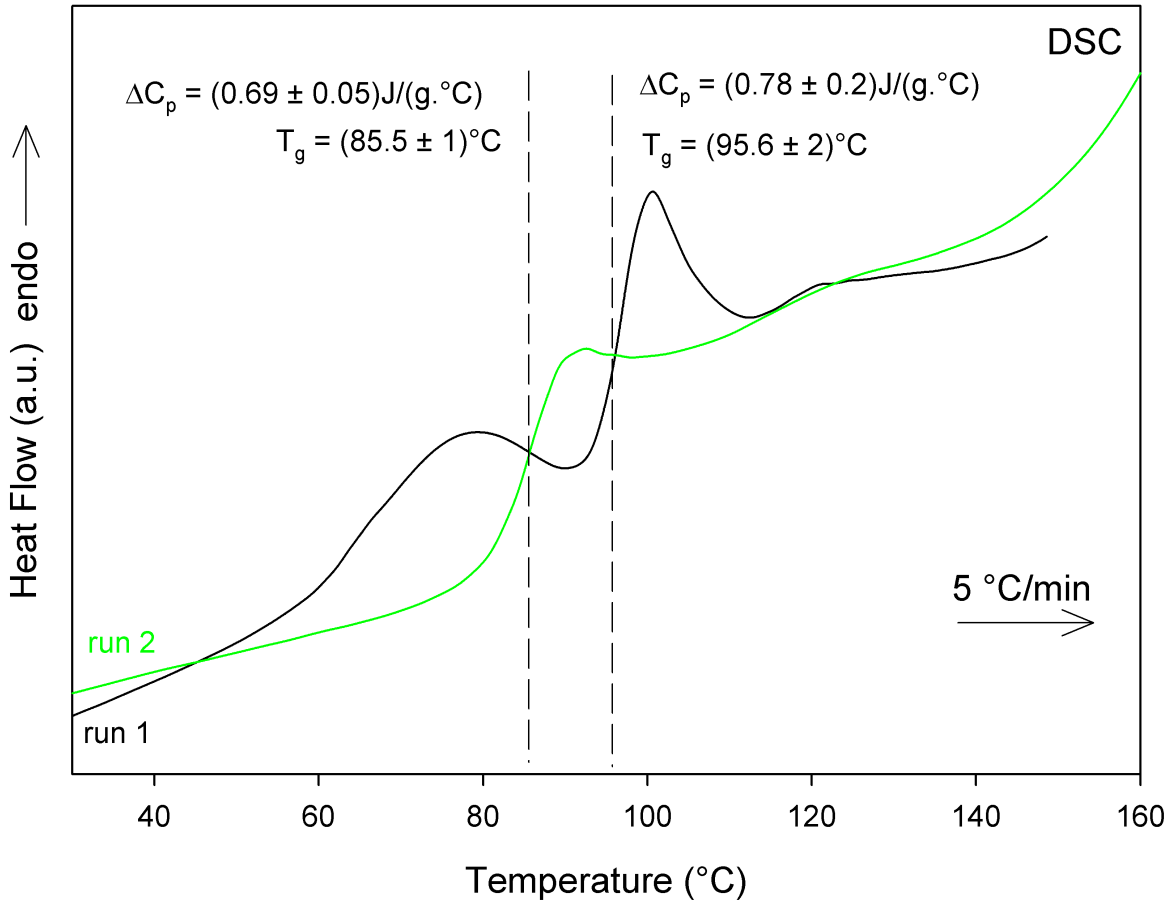

Figure 3.24 – DSC curves (5 °C/min) of lactulose:
run 1: heating of the SD sample (black line).
run 2: heating of the sample obtained by rapidly cooling down (to 20 °C) the liquid at the end of run 1 (green line).

Run 2 shows:

- No endotherm associated with the free water release.
- A C_p jump characteristic of the glass transition (T_g = 85.5 °C). This jump is shifted by 10 °C towards low temperatures compared to that seen on run 1, so that it is now identical to that of the MIL lactulose. The NMR spectrum of the material after the quench at 20 °C (i.e. just before run 2) is reported in figure 3.22 (named QFTSSD) and the

higher the mobility, the smaller this time will be.

corresponding tautomeric composition is reported in table 3.6 (named QFTSSD). This composition strongly differs from that determined just after spray-drying (i.e. just before run 1). In particular, tautomer A becomes the majority one in the QFTSFD sample, while tautomer B was the majority one in the initial SD sample. These results indicate that strong tautomerisation occurred during run 1, which is probably the cause of the T_g variation. This hypothesis will be numerically tested in section 3.7.

- A small endotherm around 120 °C. This endotherm has also been seen in compounds exhibiting mutarotation, such as fructose [217–219] and glucose [217]. So far, its origin is poorly understood. Its explanation is beyond the scope of this thesis.

3.4.3.b) Case of the FD sample

Figure 3.25 shows the results of a MDSC experiment performed on FD lactulose. The FD lactulose sample was initially dried during a heating ramp (5 °C/min) from 20 °C to 60 °C. It was then analysed by MDSC, using an average heating rate of 5 °C/min, a modulation amplitude of 0.663 °C, and a modulation period of 50 s. The signals corresponding to the total heat flow (black line) and the reversible heat flow (blue line) are reported in the figure.

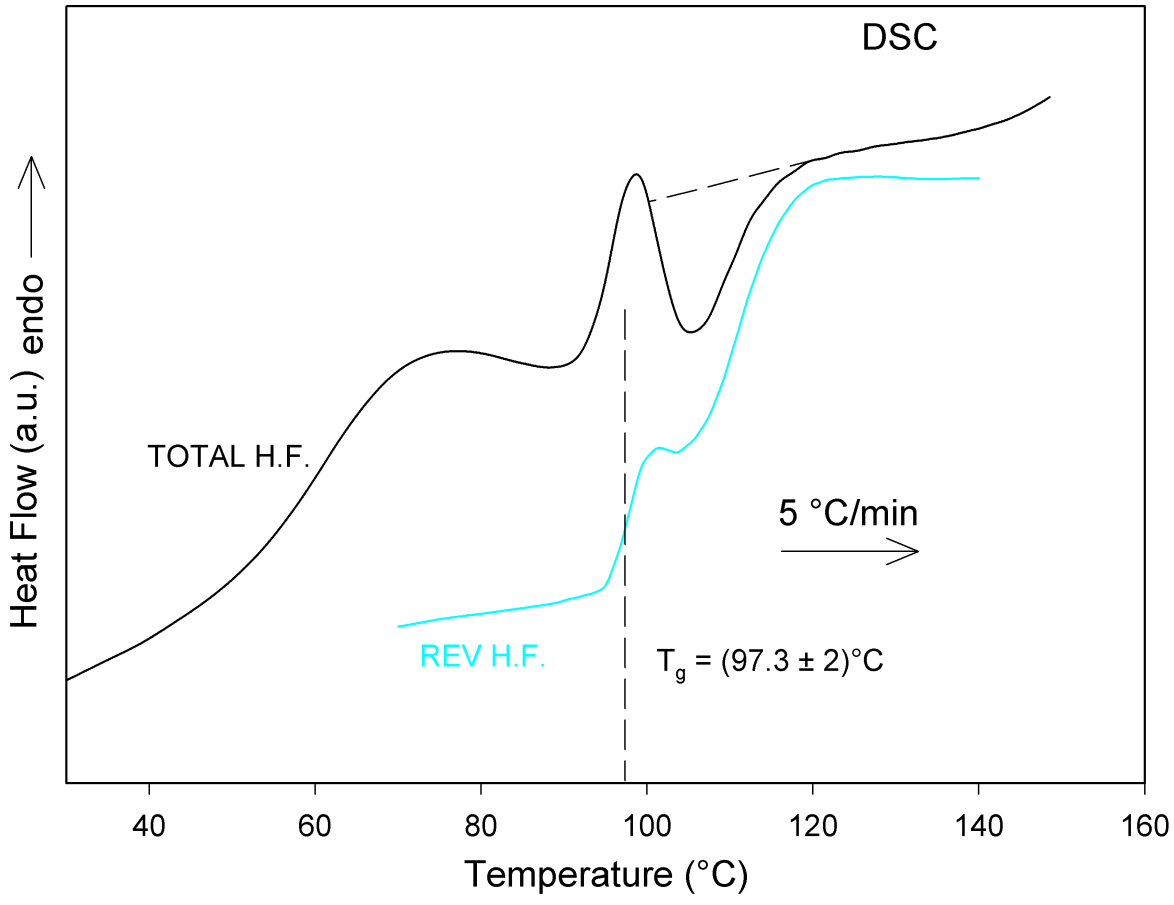

Figure 3.25 – DSC curves (reversible and total heat flow) of the FD lactulose recorded upon heating (5 °C/min) from 20 °C to 150 °C.

The reversible heat flow (blue line) shows two successive specific heat (C_p) jumps:

- The first one, located at T_g = 97.3 ° C corresponds to the glass transition of the FD lactulose. This C_p jump attests that the lactulose has been amorphised by freeze-drying, and that the amorphous sample obtained is a glass.

- The second one, located immediately after the first one spreads from 104 °C to 122 °C. This jump is an artefact frequently observed in amorphous materials with large specific surface areas (see [46]).

The total heat flow (black line) shows:

- An endotherm centred at 75 °C corresponding to the release of free water remaining in the sample. TGA experiment on the FD lactulose has confirmed this point. Such free water in FD amorphous materials is quite usual as freeze-drying technique requires to first dissolve the material in water.

- **No clear C_p jump**.

- A second endotherm just after the previous one. This endotherm results mainly from the recovery of the enthalpy lost during the aging of the glass which has occurred during the scan itself and during the initial drying stage. It gives rise to a relaxation endotherm. Its amplitude is however much larger than that of the MIL lactulose (see figure 3.17). This is due to the fact that the T_g of the initial freeze-dried sample is strongly depressed by the free water. The annealing stage used for drying the sample is thus performed at a temperature which is close to the effective T_g of the plasticised material. This makes the relaxation faster and deeper.
  Before the endotherm is completed, the heat flow increases, because of the artefact previously mentioned in the reversible signal. This gives rise to a fictive exotherm on the thermogram, ranging from 100 °C to about 120 °C. The equilibrium line of the liquid is then caught-up from 120 °C.

- Above 143 °C, an endotherm which starts to develop. This endotherm corresponds to thermal degradation. This was also observed in the case of the MIL lactulose.

The enthalpic events occurring in the temperature region where the glass transition is expected prevent its clear visualisation. However, based on the glass transition temperature measured on the reversible heat flow, one can estimate that on the total heat flow, T_g = 94.3 °C. The glass transition temperature of the FD lactulose is then nearly 9°C higher than that of the MIL lactulose.

As previously mentioned, mutarotation is “unblocked” in the FD compound just above T_g. It therefore evolves from the tautomeric composition of the FD sample (see table 3.6) to that of the undercooled liquid. But enthalpic signature (expected to be endothermic from DFT results presented in section 3.3.3) of this tautomerisation is embedded in the enthalpic events that happen in this temperature range (from T_g to T_g + 25 °C).

The previous sample (FD lactulose heated up to 150 °C) was then quenched at 20 °C and rescanned at 5 °C/min. In figure 3.26, this rescan (run 2) is compared to the first one.

Run 2 shows:

- No endotherm associated with the free water release.

- A C_p jump characteristic of the glass transition (T_g = 85.2 °C). This jump is shifted by 9 °C towards low temperatures compared to that seen on run 1, so that it is now identical to that of the MIL lactulose. The NMR spectrum of the material after the quench at 20 °C (i.e. just before run 2) is reported in figure 3.22 (named QFTSFD) and the corresponding tautomeric composition is reported in table 3.6 (named QFTSFD). This composition strongly differs from that determined just after freeze-drying (i.e. just before run 1). In particular, tautomer A becomes the majority one in the QFTSFD sample, while tautomer B was the majority one in the initial FD sample. These results indicate that strong tautomerisation occurred during run 1, which is probably the cause of the T_g variation. This hypothesis will be numerically tested in section 3.7.

- A small endotherm around 120 °C. This endotherm is similar to that observed on the SD sample, and its explanation is beyond the scope of this thesis.

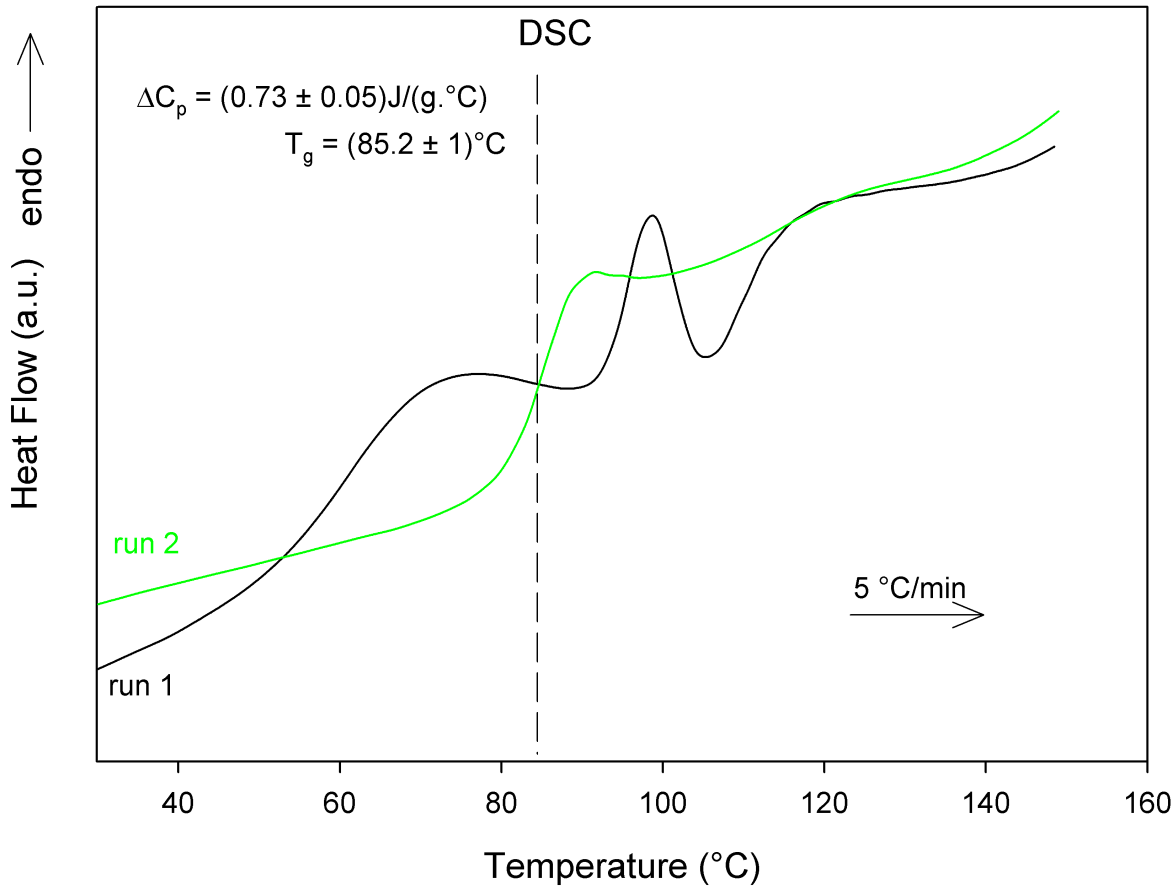

Figure 3.26 – DSC curves (5 °C/min) of lactulose:
run 1: heating of the FD sample (black line).
run 2: heating of the sample obtained by rapidly cooling down (to 20 °C) the liquid at the end of run 1 (green line).

3.5 Physical stability

During this thesis, all laboratory experiments on amorphous lactulose were performed just after the sample preparation to avoid, as much as possible, any evolution of the material between its preparation and its analysis. Such a precaution was not applicable for experiments performed on large instruments (ILL, PSI, ISIS). In that case, amorphous samples were generally prepared a few days before their analysis. It was therefore found necessary to test the physical stability of these amorphous materials over the time period between their preparation and their measurement on large instruments. MIL lactulose, SD lactulose and FD lactulose samples were annealed at room temperature and ambient humidity for several days in order to test their physical stability with regard to recrystallisation.

Figures 3.27b and 3.27c show XRD patterns of the SD lactulose and FD lactulose samples respectively, recorded immediately after their preparation (black lines) and after eight months storage at room temperature and humidity (green lines). It is found that no Bragg peak appears on the XRD patterns of both the fresh and annealed samples. This indicates that the samples are amorphous after the spray-drying and freeze-drying processes, and that they remain in this state at least eight months after their manufacturing. SD lactulose and FD lactulose samples are thus stable with respect to recrystallisation over a period of at least eight months. They can therefore be analysed safely a few days after their production, without a risk of being contaminated by even small crystallisation.

Figure 3.27a shows the XRD patterns of the MIL lactulose sample recorded:

- just after its preparation (black line)
- after a four months storage at room temperature and room humidity (green line)
- after a four months storage at room temperature under vacuum (red line).

The XRD pattern of the anhydrous crystal is also reported for comparison (dark cyan line). Just after milling no Bragg peak can be observed, indicating the amorphous character of the material. However, a tiny Bragg peak is found on the XRD pattern of the compound annealed four months in ambient humidity (green line). This peak is at the position of the most intense Bragg peak in the diffraction pattern of the anhydrous crystal. It reflects a beginning of recrystallisation of the MIL lactulose sample. The very low integrated intensity associated with this peak indicates that this recrystallisation is extremely weak. On the contrary, after four months of annealing in vacuum conditions, the MIL sample showed absolutely no signs of recrystallisation (red line). Therefore, the MIL lactulose was kept under vacuum until it was measured on the large scale facilities, in order to avoid recrystallisation problems.

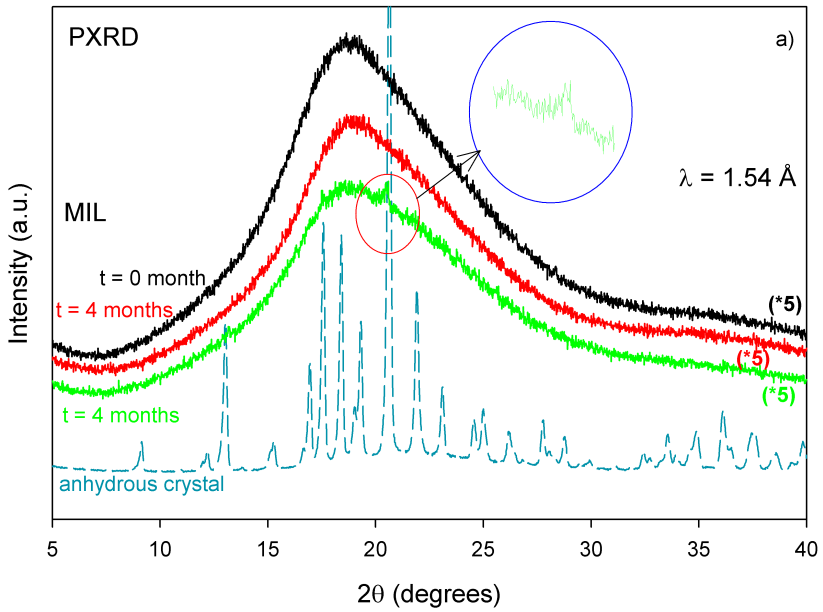

(a) XRD patterns of MIL lactulose recorded:
- just after milling (black line)
- after a four months storage at room temperature and room humidity (green line)
- after a four months storage at room temperature under vacuum (red line)
The XRD pattern of the anhydrous crystal is also reported (dark cyan line).

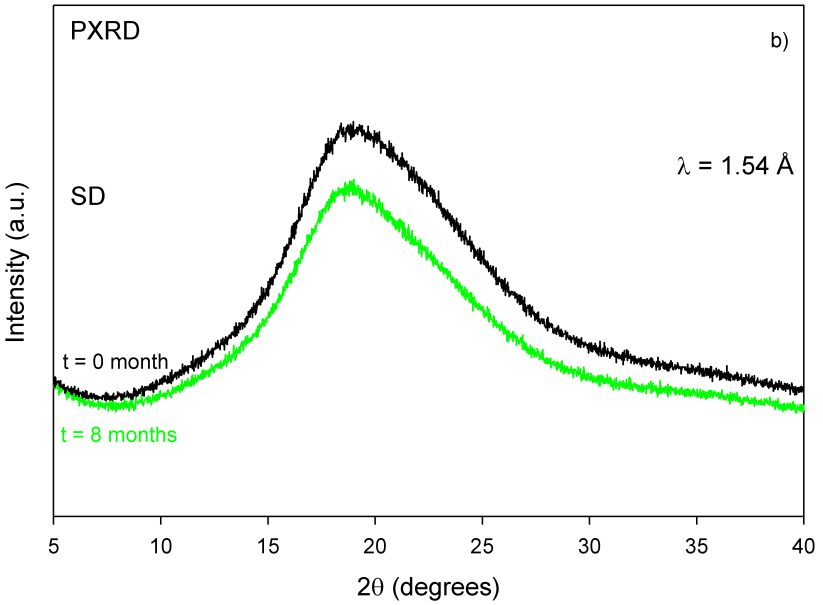

(b) XRD patterns of SD lactulose recorded just after spray-drying (black line) and after eight months storage at room temperature and humidity (green line).

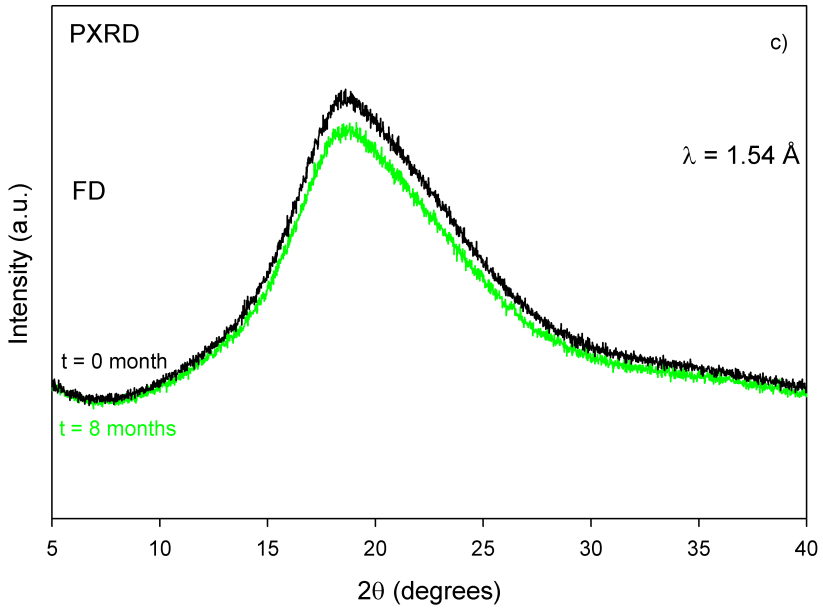

(c) XRD patterns of FD lactulose recorded just after freeze-drying (black line) and after eight months storage at room temperature and humidity (green line).

Figure 3.27 – XRD patterns of MIL, SD and FD lactulose. The patterns were recorded just after the amorphisation processes and also a few months (4 or 8) latter.

3.6 Hyper-quenched character of the MIL lactulose: endotherm and exotherm before the glass transition

The results presented in figure 3.17 show an exotherm just before the C_p jump on the DSC curve of the MIL lactulose. This exotherm is itself preceded by an endotherm of small amplitude. The purpose of this section is to explain the origin of those exotherm and endotherm preceding the C_p jump characteristic of the glass transition.

The endotherm and the exotherm preceding the C_p jump characteristic of the glass transition have often been observed on DSC curves of organic [220–223] and inorganic [216, 224] metallic glasses of high enthalpy, prepared by hyper-quenching a liquid. Recent examples of such behaviours have also been observed in an organic glass (trehalose) obtained by milling [225]. In those different systems, the existence of an endotherm (position and intensity) before the C_p jump is related to an aging effect of the glass initially in a high enthalpy situation. The presence of this thermodynamic signature on the thermogram of the MIL sample suggests that it is equivalent to that of a glass obtained by hyper-quench. Annealing experiments on the MIL lactulose sample were therefore performed in order to test this hypothesis.

The isothermal annealing step was carried out:

- At 45 °C (T_g - 40 °C). This temperature was chosen so as to be sure that the annealing

takes place below the effective glass transition temperature of the compound (decreased by the water present in the compound).

- In an open pan, in order to remove a part of the free water present in the compound.

After annealing, the sample pans were closed in order to avoid water re-adsorption at lower temperatures by the sample. The compounds were then analysed by MDSC upon heating (5 °C/min) from 20 °C to 160 °C. Figure 3.28 shows total (figure 3.28 c)), reversible (figure 3.28 b)), and non-reversible (figure 3.28 a)) heat flows recorded on three compounds differing in their annealing time at 45 °C: 1 h, 2 h and 70 h respectively.

The reversible heat flow (figure 3.28 b)) of the three different samples shows one specific heat (C_p) jump at T_g = 80 °C corresponding to the glass transition of the samples. This C_p jump is 8 °C lower than the T_g of the MIL lactulose previously measured. This is due to the plasticisation of lactulose by some free water which was not removed during the annealing stage at 45 °C.

The total heat flow reveals three consecutive enthalpic events: an endotherm, an exotherm and a C_p jump at about 77 °C. The C_p jump corresponds to the glass transition of lactulose and is also found in the reversible signal. The endotherm and the exotherm are non-reversible phenomena only appearing in the corresponding signal.

It is found that the glass transition temperature does not vary much with the annealing time. On the other hand, the endotherm below T_g develops and shifts towards high temperatures when the annealing time increases. The effect is such that, after 70 h of annealing, the endotherm is partially superimposed on the C_p jump occurring at T_g. The exotherm however seems to be gradually masked by the development and the shift of the previous endotherm, so that after 70 h of annealing it is no longer visible.

Those results, obtained on an annealed MIL sample, are similar to that of a hyper-quenched glass having undergone an annealing. Therefore, **the milling is an amorphisation process which leads to high enthalpy glasses** similar to those obtained by hyper-quenching a liquid [216, 224].

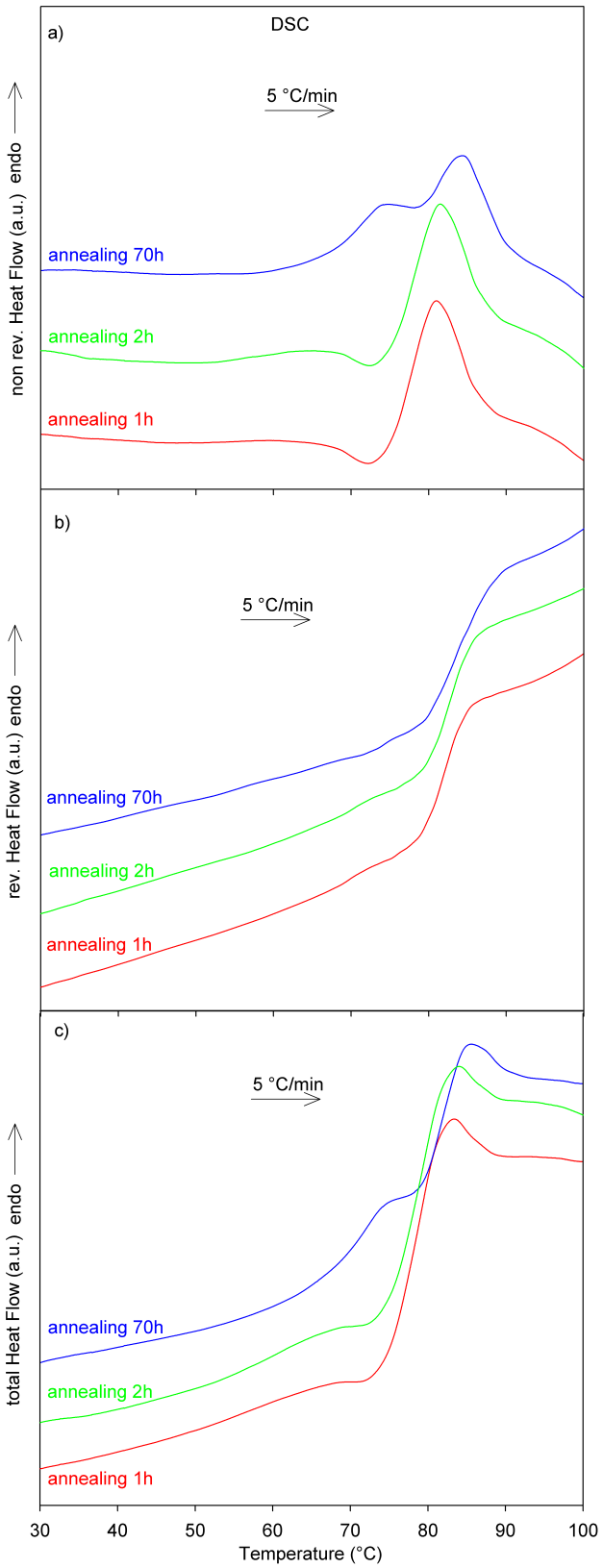

Figure 3.28 – DSC curves of three MIL lactulose samples annealed during 1 h (red line), 2 h (green line) and 70 h (blue line) at 45 °C.
a) Non reversible heat flow signals.
b) Reversible heat flow signals.
c) Total heat flow signals.

3.7 Determination of the mobility of tautomers A and B by MD simulations

A combined analysis of the values of the experimental glass transition temperature of the different amorphous lactulose compounds and their tautomeric composition suggests that the proportion of tautomer A and tautomer B in a compound has a strong impact on its glass transition temperature. It would be ideally necessary to determine the glass transition temperature of a compound just composed of tautomer A, or tautomer B. However, to the best of our knowledge and unlike to the case of lactose or glucose [29, 44, 143], lactulose amorphous compounds just made of tautomer A or tautomer B have not yet been produced. Several experiments were performed in this work, such as the dehydration of lactulose trihydrate, in order to obtain amorphous samples having just one tautomer. None of them gave satisfactory results. The reasons for such failure come from the ease of lactulose to mutarotate [146].

One of the big advantages of numerical simulations is precisely that they can be freed from such experimental limitations. Molecular mobility of amorphous compounds composed only of tautomer A, and only of tautomer B has been thus determined by MD simulations.

The glass transition temperature can be determined by MD simulations for example by plotting the evolution of the volume with respect to the temperature [226]. The intersection of the low temperature out of equilibrium line and the high temperature equilibrium line may be used to estimate the glass transition temperature (T_g). However, the determination of the glass transition temperature by MD simulations is a tricky calculation, mainly because of two factors:

- The calculated T_g depends strongly on the potential well in which the energy configuration of the system is trapped. Several calculations would have to be made to better estimate the uncertainty on the result obtained.

- The calculated T_g obtained is usually much higher than the one obtained from experimental studies. Differences of the order of 100 K can be found. This behaviour stems from the extremely high quenching rate used in simulation (K/ps) comparatively to the experimental one (K/s). Therefore, a correction of the raw T_g value obtained from MD simulations should be applied, which is far from being obvious [227–229].

Instead of calculating T_g, the molecular mobility of tautomers A and B was studied by means of their coherent intermediate scattering function S(Q,t). This allows comparing the collective dynamic of tautomers A and B. The number of intermolecular hydrogen bonds (HBs) developed by each of the tautomers has been also calculated. The results obtained are presented below.

Simulation details Two systems each composed of only tautomer A and only tautomer B were generated by placing 64 molecules in a pseudo crystal. The systems were then melted at 700 K during 2 ns in NPT (P = 1 atm) to eliminate any orientational or translational order, and to obtain a liquid. These equilibrated liquids have been later hyper-quenched (from 700 K to 500 K) at 20K/200ps. The obtained boxes were further equilibrated at 500 K, during 3 ns (including 2 ns in NPT (P = 1 atm) followed by 1 ns in NVT) for the box composed of tautomer A, and 4 ns (including 3 ns in NPT (P = 1 atm) followed by 1 ns in NVT) for the box

composed of tautomer B. A production run of 5 ns with frames saved every 0.1 ps succeeded this equilibration step. The MD trajectory generated during this production run has been used for the calculations presented below.

3.7.1 Neutron coherent intermediate scattering function

Figure 3.29 shows the time evolution of the neutron coherent intermediate scattering functions S(Q,t) calculated in the lactulose boxes having only tautomer A (green line) and only tautomer B (blue line). Those functions are correlation functions allowing studying collective dynamics in the system. The functions were calculated at Q = 1.3 $Å^{-1}$ and Q = 2.0 $Å^{-1}$. These two Q points have been chosen because they correspond to the points on the first diffraction peak where the S(Q) is maximum and minimum respectively (see figure 5.7 in chapter 5). These points Q are therefore the points where the relaxation time is maximal and minimal [230, 231].

The S(Q,t) function was calculated using the following formula:

$$S(Q,t) = \sum_{j \neq j'} b_j b_{j'} < \exp(iQ(r_j(t) - r_{j'}(0))) > \tag{3.1}$$

It can be clearly seen in this figure that the curve of the system composed only of tautomer A decreases more rapidly than the one of the system composed only of tautomer B. This means that the collective dynamics of the system composed only of tautomer A decorelates much more rapidly than that of the system composed only of tautomer B. This effect is more marked at low Q (which corresponds to a greater distance in real space). This result indicates that the molecular mobility of tautomer A is higher than that of tautomer B, and thus $T_g^A < T_g^B$. Therefore, a mixture composed of a higher proportion of tautomer B, as found for the SD lactulose (% A = 29.4,% B = 61.8) and the FD lactulose (% A = 23.4, % B = 68.4), could be expected to have a higher T_g than a mixture composed of a higher proportion of tautomer A, as found for the MIL lactulose (%A= 81.7, %B= 10.1).

3.7.2 Hydrogen bonds (HBs) network

The lactulose molecule ($C_{12}H_{22}O_{11}$) can form many HBs. As seen in the case of trehalose ($C_{12}H_{22}O_{11}$), the dynamic is strongly governed by the HBs [54]. In order to understand the differences previously seen in the dynamic of the two tautomers, the number of HBs they form was calculated.

The HBs network of lactulose may be described by the populations of lactulose molecules that form HBs with their neighbouring lactulose molecules. In the present study, two lactulose molecules are considered to be H-bonded if the oxygen–oxygen distance d(O-O) is less than 3.4 Å and the O-H...O angle larger than 120.0°. This geometric criterion included quite deformed and weaker HBs. Attempts to compute distribution of HBs with a more stringent criterion (O-H...O angle > 150.0°) including only well-formed and strong HBs, have given similar (but more noisy) results, and are thus not presented here.

The distribution of HBs between lactulose molecules has been calculated from the same production runs used for the calculation of S(Q,t).

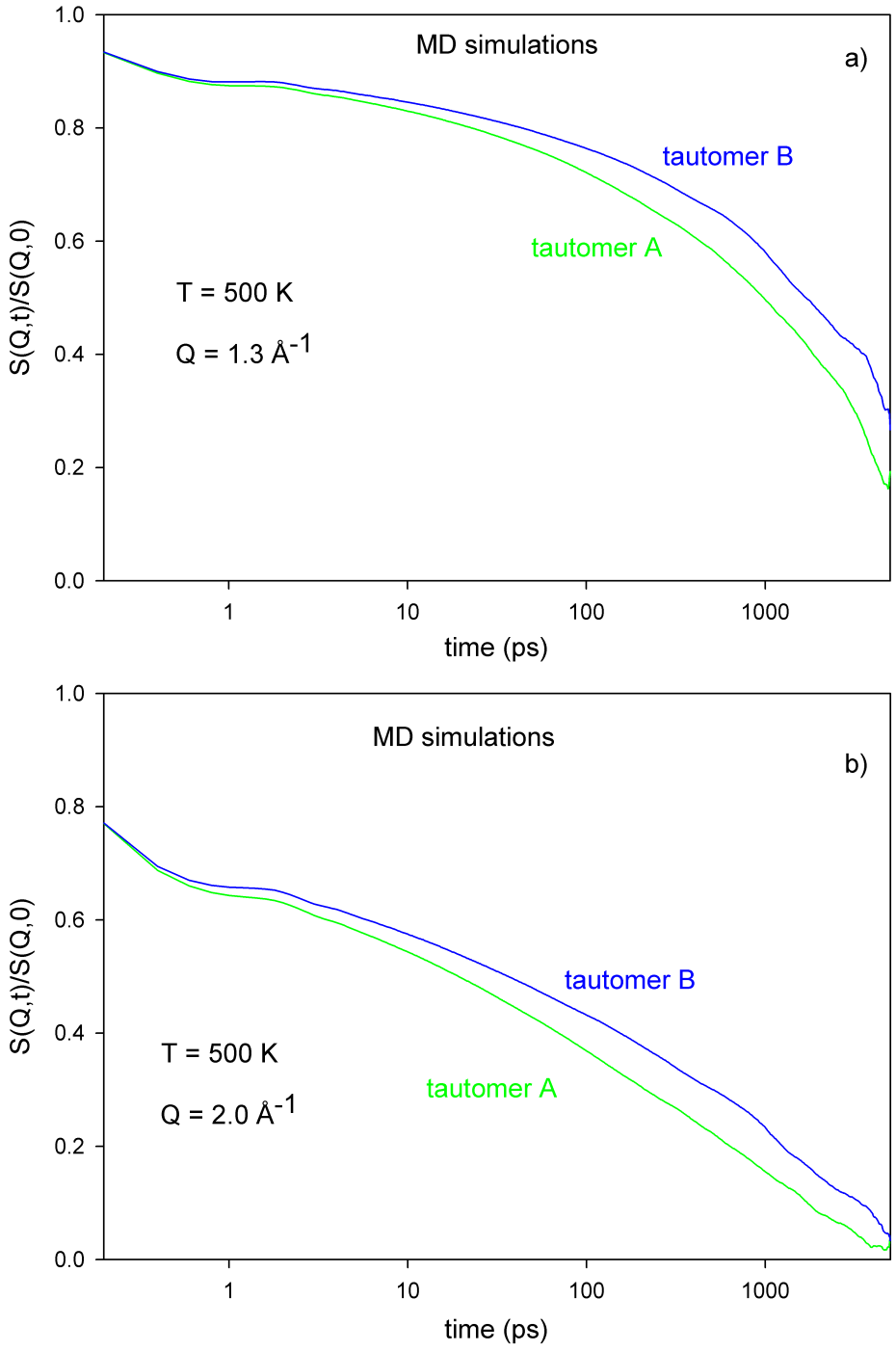

Figure 3.29 – Dynamical scattering function S(Q,t)/S(Q,t=0) at T=500 K calculated at two different Q values using MD trajectories of 5 ns:
a) Calculations performed at Q = 1.3 Å^{-1}.
b) Calculations performed at Q = 2.0 Å^{-1}.

The results obtained are represented in figure 3.30 which shows the distribution of intermolecular HBs for a system exclusively composed of either tautomers A (green line) or tautomers B (blue line). As it can be seen, the distribution is quite broad as a consequence of thermal disorder and small local rearrangements. Nevertheless, tautomer B develops 6.09

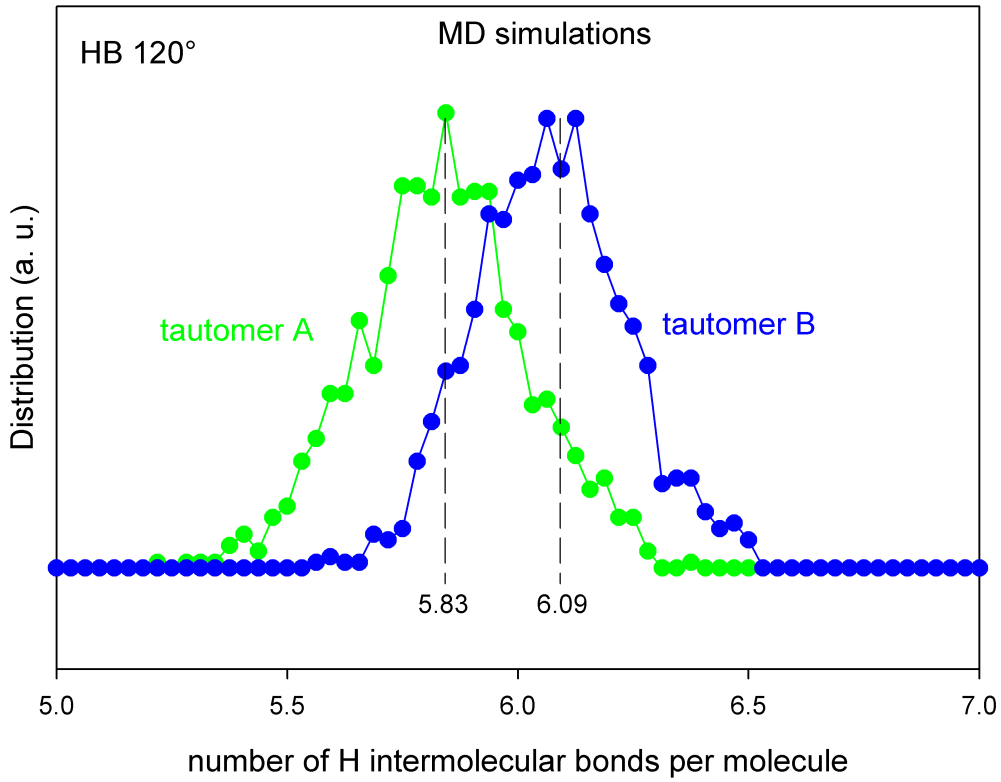

Figure 3.30 – Distribution of intermolecular HBs of tautomer A (green line) and tautomer B (blue line).

HBs in average, and tautomer A develops 5.83 HBs in average. Tautomer B thus develops more intermolecular HBs than tautomer A. This behaviour is well in line with the results obtained with the dynamic correlation functions S(Q,t) (see previous section), for which tautomer B has a molecular mobility smaller than that of tautomer A.

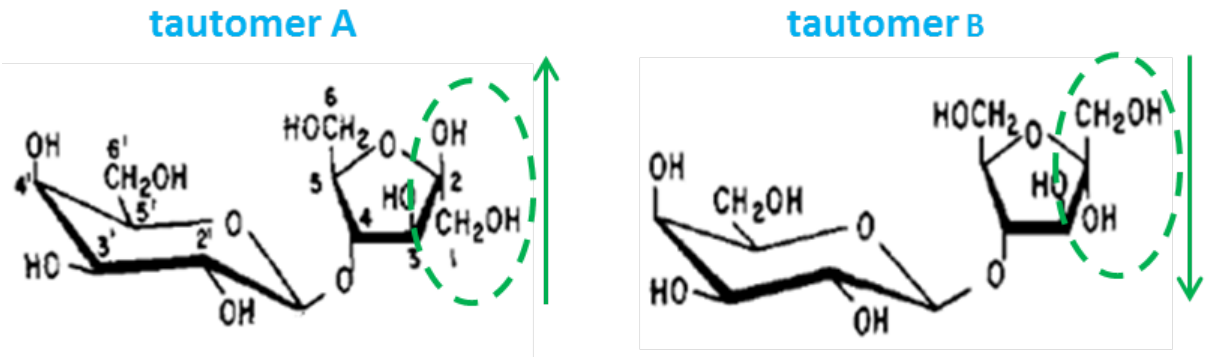

Figure 3.31 – Representation of tautomers A and B. The two tautomers differ in the orientation of the OH-C-CH_2OH group at the end of the 5-C cycle (see atoms encircled in green).

This difference in the number of intermolecular HBs developed by the two tautomers is due to their different topology (see figure 3.31), the orientation of the OH-C-CH_2OH group being different in the two molecules. DFT calculations carried out on the two tautomers

made it possible to determine their dipolar moment: $\mu_A = 4.36$ D, $\mu_B = 5.0$ D. The tautomer B is thus more polar than the tautomer A, and therefore develops more HBs than the tautomer A. Those results are in agreement with molecular mobility obtained from MD simulations.

Summary

In this chapter, we have studied the physico-chemical properties of crystalline forms (anhydrous and trihydrate), and amorphous forms of lactulose. In the latter case, the influence of the amorphisation method on the properties of the amorphous compound was studied in detail. The different amorphous compounds are distinguished essentially by their tautomeric composition and its impact on the glass transition temperature of the compound.

Crystalline forms
The anhydrous crystalline form (commercial form) is characterised by a monoclinic structure involving three of the five tautomers of lactulose (see table 3.7). The trihydrate crystalline form is characterised by an orthorhombic structure, and tends to be "tautomerically" pure. These results are in agreement with those previously reported by Jeffrey et al. [146]. The originality of our work lies in the fact that the trihydrate crystalline form has been obtained here by co-milling anhydrous crystalline lactulose with water in the molar ratio [1:3]. This method has the advantage of being much faster than the crystallisation in solution used by Jeffrey [146], since a few minutes of co-milling are sufficient to form the trihydrate. In addition, it is quite remarkable that the tautomeric purity of a compound can be improved, in the solid state, by mechanical milling.

Amorphous forms
We have shown the possibility of amorphising lactulose by four totally independent methods: liquid-quenching, high energy crystal milling, spray-drying and freeze-drying. NMR analyses revealed that the tautomeric composition of the amorphous compounds obtained strongly depends on the amorphisation method used. These compositions are summarized in table 3.7. It appears that:

- The amorphous compound obtained directly in the solid state by mechanical milling keeps the tautomeric composition of the starting crystal. This indicates that this amorphisation method does not lead to tautomerisation. This behaviour corresponds to that of lactose [215] and glucose [47] studied in previous theses.

- The quenched liquid, on the other hand, has a very different tautomeric composition from that of the starting crystal. This is due to a strong and inevitable tautomerisation occurring during the melting.

- Both the spray- dried and freeze-dried compounds have the same tautomeric composition, which is very different from that of the previous two amorphous compounds. This composition is in fact very similar to that of lactulose in water solution. This shows that spray-drying and freeze drying processes do not cause by themselves any tautomerisation.

These differences in tautomeric composition lead to a large variation in the glass transition temperature, which ranges from 85.7 °C for the amorphous compound obtained by milling, to 95.6 °C for the amorphous compound obtained by spray-drying. The fact that lactulose involves at least three tautomers makes it difficult to establish an unambiguous relationship between the tautomeric concentrations and the T_g of the amorphous compound. **However, the set of experimental results clearly indicates that the tautomers A and B have respectively plasticiser and anti-plasticiser roles**. This has been confirmed by MD simulations. It is linked to the different capabilities of tautomers A and B to form intermolecular

HBs due to different conformation of their 5 C cycle.

The quenched liquid, however, shows an additional complexity linked to the thermal degradation that occurs during melting. We have shown that the products of this degradation have an anti-plasticising effect which interferes with the changes in tautomeric composition which also accompany the melting. These effects could be demonstrated by comparing the quenched liquid obtained in a conventional manner by melt-quenching, with equivalent systems, non-degraded, obtained by heating (between T_g and T_m) and then cooling the safely amorphised compounds obtained by milling, spray-drying and freeze-drying.

The amorphous compounds obtained by milling, spray-drying and freeze-drying have a tautomeric composition which reflects that of the starting system: the crystal in the case of milling, and the aqueous solution in the cases of spray-drying and freeze-drying. Consequently, these amorphous compounds undergo strong tautomerisations upon heating, so as to join the equilibrium tautomeric composition corresponding to that of the quenched liquid. These tautomeric re-equilibrations have been detected by calorimetry. They occur systematically and massively just above the glass transition temperature. As in the case of glucose, this behaviour suggests a strong coupling between the slow relaxations that freeze at T_g (intermolecular cooperative mechanism) and the tautomerisation mechanism (intramolecular mechanism).

Table 3.7 – Summary of the glass transition temperatures (T_g) and the tautomeric compositions of the different lactulose compounds: anhydrous crystal, trihydrate crystal, milled crystal (MIL), quenched from the melt (QFTM), spray-dried (SD), freeze-dried (FD), quenched from the softened spray-dried (QFTSSD), quenched from the softened freeze-dried (QFTSFD).

Samples	T_g (°C)	% of tautomer A (±4)	% of tautomer B (±4)	% of tautomer C (±4)
Anhydrous crystal	-	79.3	10.3	10.4
Trihydrate crystal	-	88.8	2.7	8.5
MIL	85.7	81.7	10.1	8.2
QFTM	94.7	48.9	33.6	17.5
SD	95.6	29.4	61.8	8.8
FD	94.3	23.4	68.4	8.2
QFTSSD	85.5	50.0	31.9	18.1
QFTSFD	85.2	51.2	31.0	17.8

Chapter 4

Structural and thermodynamic evolutions of lactulose under milling

Contents

In the previous chapter, we have shown that crystalline lactulose reaches an amorphous and vitreous state during long-term milling (8 h) at 25 °C. In this new chapter, we will study in detail how this transformation occurs during the milling itself. This transformation will be followed by the usual X-Ray Diffraction (XRD) and Differential Scanning Calorimetry (DSC) techniques. Moreover, the amorphisation kinetic under milling will be determined by an original technique of isothermal calorimetry of dissolution whose principle will be presented beforehand.

From a practical point of view, the anhydrous crystalline lactulose was milled at high energy in a planetary mill, for milling times varying from 0 to 8 h. A fresh sample was used for each milling time. The rotation speed of the jars, maintained constant during the experiment, is 400 rpm. To avoid overheating of the sample during long milling (> 15 min), pause periods (15 min) were alternated with milling periods (15 min). The characterisation of milled sample was carried out immediately after the milling operations to avoid, as best as possible, any evolution of the material which would not be due to the milling itself.

4.1 XRD analysis

Figure 4.1 shows the XRD patterns of anhydrous crystalline lactulose, recorded after different milling times varying from 0 to 8 h. The XRD pattern of the QFTM is also reported for comparison. All patterns were recorded at room temperature.

They show a progressive decrease in the intensity of the Bragg peaks as well as the development of an underlying diffusion halo for increasing milling times. This reflects the development of an amorphous fraction during milling. The evolution is also marked by a widening of the Bragg peaks. This widening reflects a reduction in the size of the lactulose crystallites not yet amorphised, as well as the appearance of defects and micro strains. It can be noted that these evolutions occur rapidly. They are already perceptible after 5 min of milling, and the Bragg peaks have almost disappeared after 1 h of milling, where only the diffusion halo remains. After 1 h of milling, the sample is "X-ray amorphous" and no further evolutions of the XRD patterns can be discerned for longer milling time.

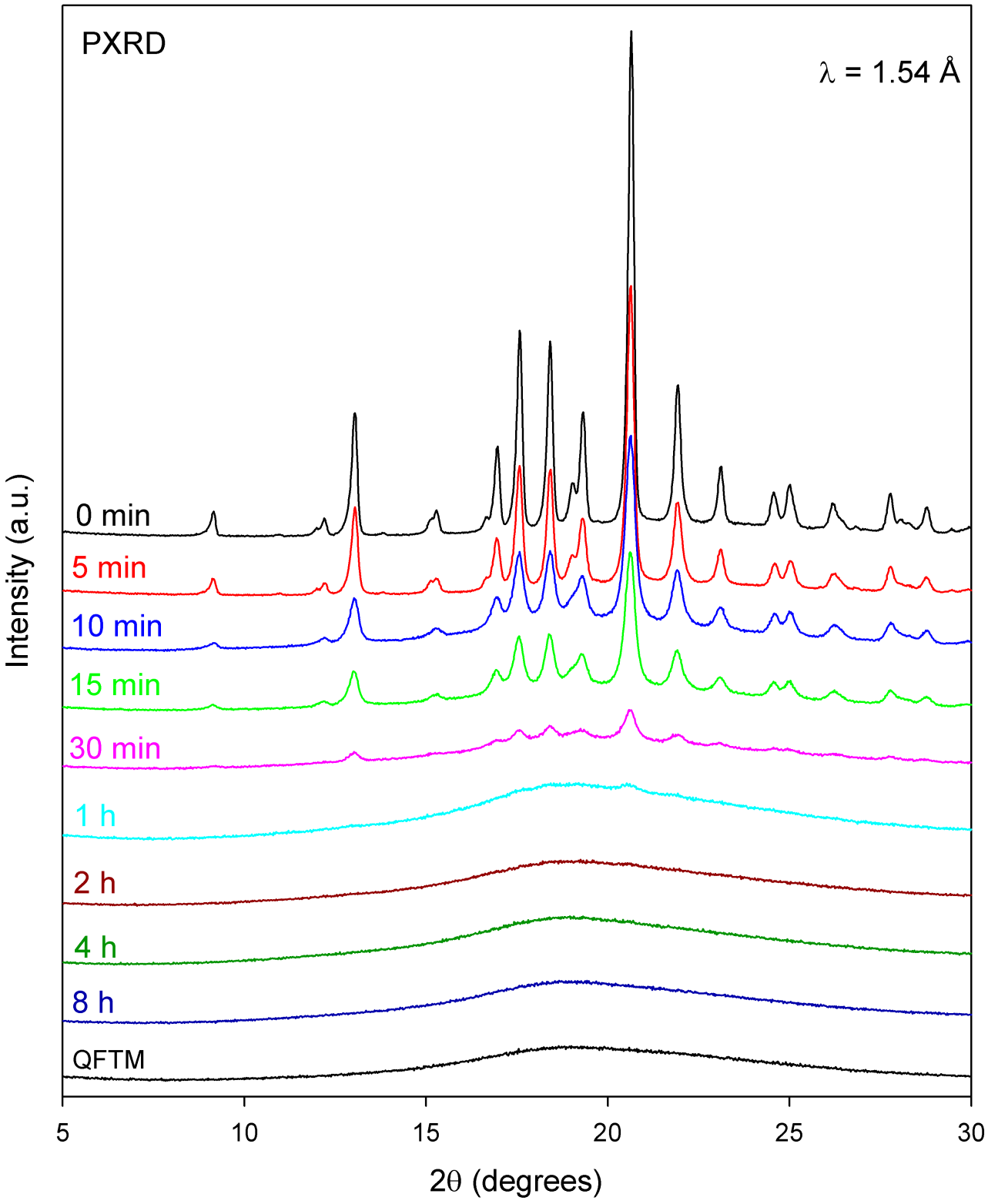

Figure 4.1 – XRD patterns of anhydrous crystalline lactulose recorded after different milling times ranging from 0 to 8 h. The XRD pattern of the QFTM is reported for comparison. All patterns were recorded at room temperature.

4.2 DSC analysis: recrystallisation and glass transition

Figure 4.2 shows DSC curves (total heat flows) of crystalline lactulose recorded after different milling times ranging from 0 to 8 h. These thermograms were recorded upon heating (5 °C/min) after having dried the sample during 10 min at 60 °C. It can be noted the presence of three enthalpic events:

- **A specific heat (C_p) jump** at T_g = 85.5 ° C. This jump is detectable from 5 min of milling on the reversible heat flow signal. The amplitude of this jump increases progressively up to 1 h of milling where it is maximum. This indicates that a total crystal-to-glass conversion under milling occurs in less than 1 h. Beyond 1 h of milling, the amplitude of the jump remains unchanged. However, one can see a small exotherm just below T_g. This exotherm has been attributed in section 3.6 of chapter 3 to the fact that the milling leads to a vitreous state of high enthalpy similar to that of a hyper-quenched glass.

- **A crystallisation exotherm** already detectable after 5 min of milling. XRD experiments performed after this recrystallisation show that the milled material recrystallises towards the initial anhydrous crystal (see figure 4.3). It can be seen that this recrystallisation occurs around 120 °C during the first 30 min of milling, and then shifts towards high temperatures. This shift is frequently observed in compounds amorphising under milling. It is generally attributed to a decrease in the crystalline fraction not yet amorphised which can serve as potential nuclei for the recrystallisation of the amorphous fraction. It is also noted that the shift is accompanied by a reduction of the recrystallisation enthalpy, which even becomes zero after 8 h of milling. This indicates that an increasing fraction of the amorphous phase generated during milling no longer recrystallises upon heating. However, a fine analysis of the evolution of the recrystallisation enthalpy is difficult, since the recrystallisation exotherm is more or less superimposed on the melting endotherm which follows it. This endotherm is described below.

- **A melting endotherm** which presents a complex evolution with the milling time. After only 5 min of milling, the melting endotherm is very different from that of the non-milled sample. In particular, the onset of melting seems to be offset by 10 °C towards high temperatures compared to that of the non-milled sample, while the temperature marking the end of the melting is identical in both samples. As a result, the melting endotherm appears much sharper after 5 min of milling. This effect has already been noted in section 3.2.2 of chapter 3. It is due to the fact that the commercial crystalline lactulose contains water inclusions whose release upon heating takes place just before the melting. The milling of the crystal, even if slight, allows the water previously included in the crystal to release during the prior drying step at 60 °C. There is thus no more water loss so that the melting endotherm appears sharper.

Between 5 and 30 min of milling, a widening and a shift towards low temperatures of the melting endotherm are observed. This behaviour is frequently observed in milled compounds. It is generally attributed to both the creation of defects in the crystallites and the strong crystallite size reduction ("Gibbs Thompson effect" [232, 233]) induced by milling. Moreover, the melting depression leads to an overlapping of the melting and recrystallisation peaks which complicates the determination of the enthalpy related to these two events.

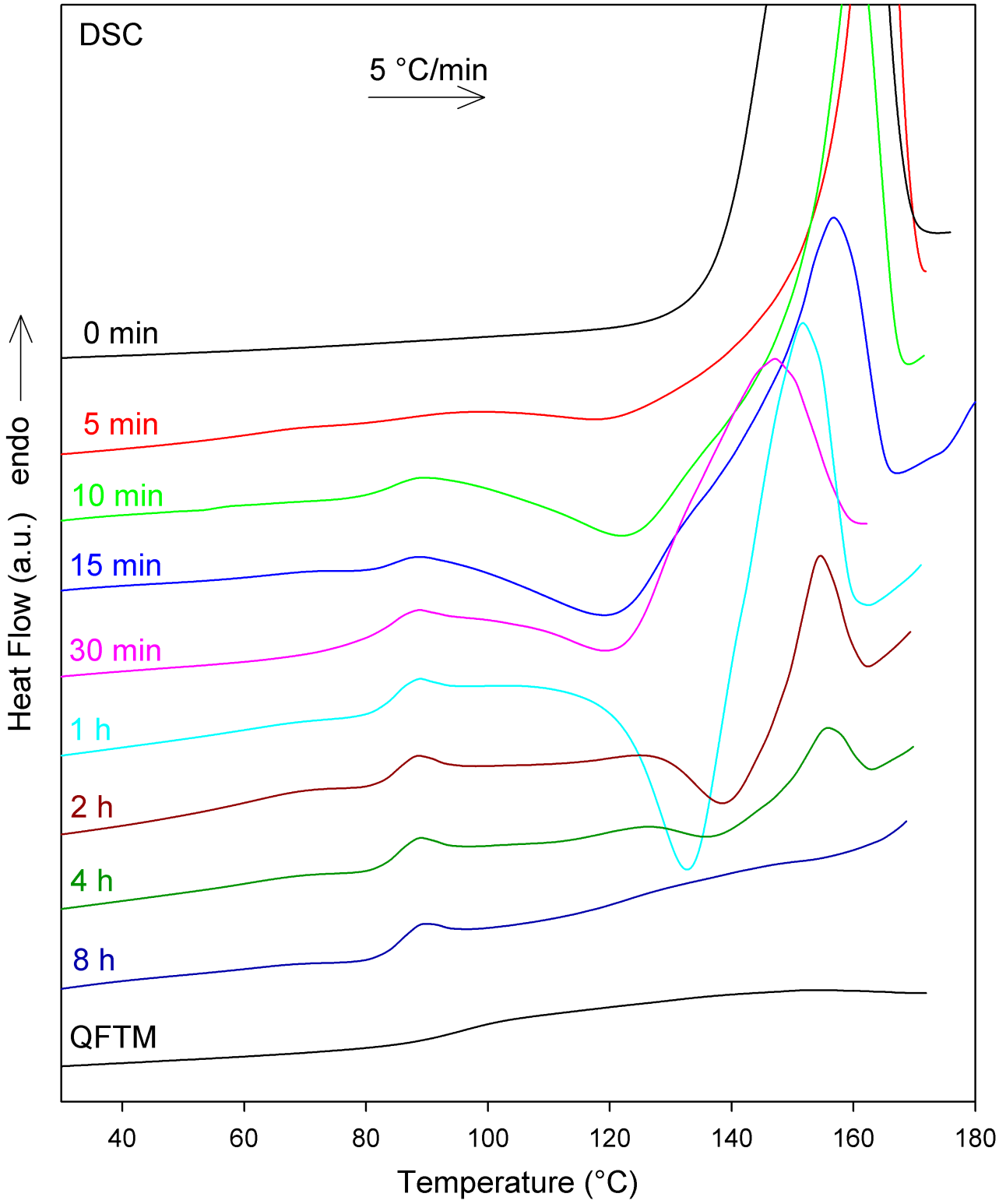

Figure 4.2 – Heating DSC curves (5 °C/min) of crystalline lactulose samples recorded after different milling times ranging from 0 to 8 h.

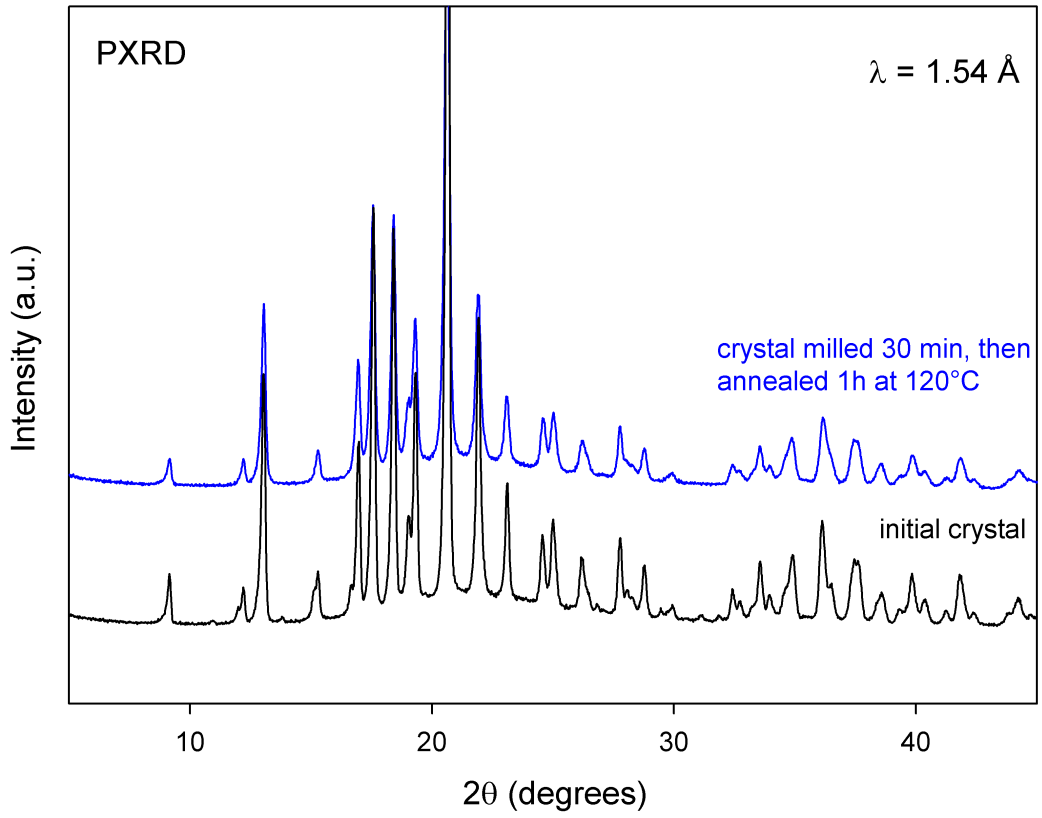

Figure 4.3 – XRD patterns recorded at room temperature: anhydrous crystal (black line), and the anhydrous crystal milled 30 min and subsequently annealed 1 h at 120 °C (blue line).

After 30 min of milling, the previous behaviour inverses and the melting endotherm shifts towards high temperatures. This indicates that the observed melting now concerns mostly crystallites coming from the recrystallisation of the amorphous phase obtained under milling, rather than crystallites not yet amorphised as it was the case at the very beginning of the milling. The crystallites resulting from the recrystallisation upon heating were not milled, and their melting is therefore not depressed by a size effect (i.e. a Gibbs Thomson effect) or a high defect concentration. Furthermore, the melting enthalpy decreases and becomes zero after 8 h of milling. This behaviour is consistent with those of the C_p jump at T_g and the recrystallisation. It indicates that the lactulose amorphises totally upon milling and that an increasing part of the amorphised fraction loses its propensity to recrystallise under the heating conditions used (5 °C/min) when the milling time increases.

Origin of the recrystallisation

The previous results show that the recrystallisation propensity of amorphous lactulose obtained by milling decreases when the remaining crystalline fraction decreases. It disappears progressively once no more crystallites are detected by XRD. This behaviour can have two origins:

- either there is residual crystalline fraction (not detected with X-ray for milling time

longer than 1 h, because the fraction becomes too small) acting as nuclei which trigger the recrystallisation of the amorphous faction during heating. This residual crystalline fraction decreases as the milling time increases, and becomes zero for more than 8 h of milling.

- or the structure (local order) of the amorphous phase evolves upon milling and modifies the nucleation and growth rates that drive the recrystallisation.

To better understand the origin of this recrystallisation, we studied the recrystallisation of an amorphous lactulose sample seeded by lactulose crystallites. This heterogeneous compound was obtained by quenching liquid lactulose at 170 °C, introducing crystal seeds (4.5%) in the metastable liquid, and quenching the mixture at 20 °C. The thermogram of this sample recorded upon heating (5 °C/min) is shown in figure 4.4.

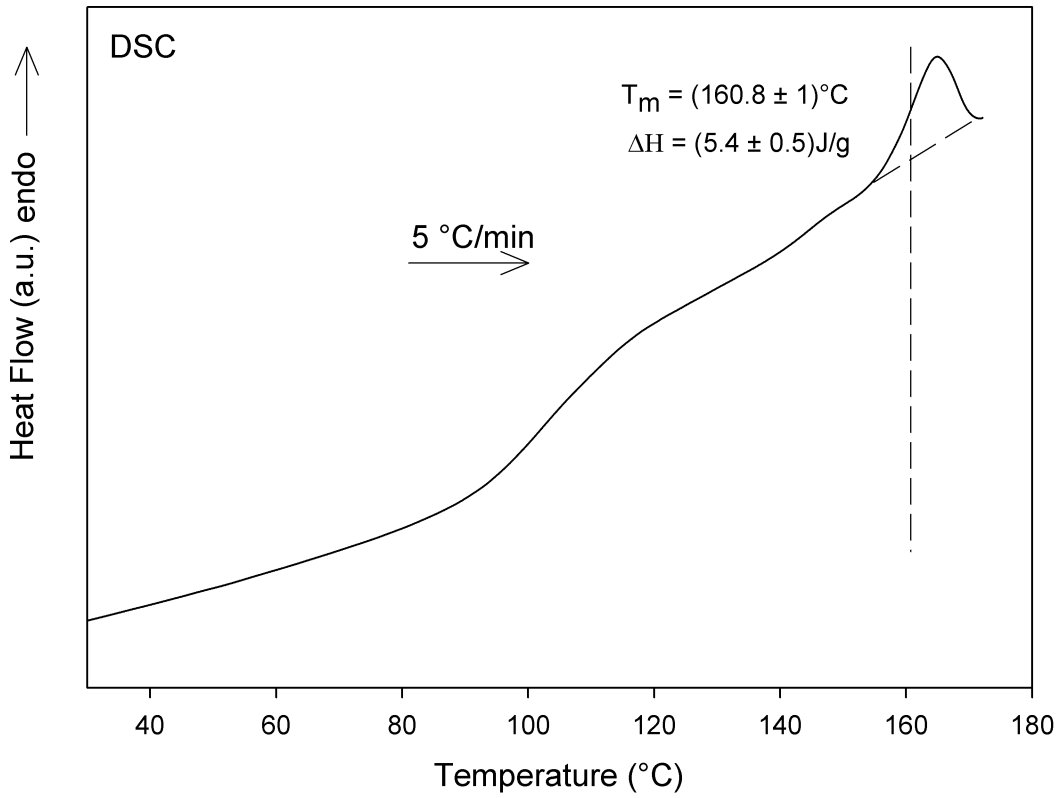

Figure 4.4 – Heating DSC curve (5 °C/min) of an amorphous lactulose sample (obtained by quenching the melt) seeded by 4.5% of crystal.

It shows a C_p jump at T_g = 102.4 °C arising from the glass transition of the QFTM lactulose, and a melting endotherm at 160.8 °C. No exotherm characteristic of a recrystallisation can be detected. Moreover, the melting enthalpy corresponds exactly to that expected for the melting of the seeds. The crystallites present in the sample have thus not induced any crystallisation of the amorphous phase. This means that the recrystallisation of lactulose upon heating, detected after different milling times ranging from 5 min to 4 h, is not due to the presence of residual crystallites not yet amorphised by milling. It is thus probably due to the specific nature (structure) of the amorphous lactulose at this stage of the milling process.

4.3 The dissolution

The previous investigations, by DSC and XRD, do not allow a precise determination of the amorphisation kinetic of crystalline lactulose under milling, i.e., the evolution of the amorphous fraction $X_{am}(t)$ as a function of the milling time t. Indeed:

- By DSC:
  - The evolution of the amplitude of the C_p jump with the milling time is difficult to estimate. At short milling times, the C_p jump is truncated by the recrystallisation exotherm of the amorphous fraction. For longer milling times, the endotherm and exotherm characteristic of high energy glasses also prevent an accurate determination of the amplitude of the C_p jump. Moreover, the "two steps" C_p jump at T_g characteristic of amorphous powders with large specific surface areas further complicates the analysis.
  - The evolution of the recrystallisation enthalpy with the milling time does not either allow to determine the amorphisation kinetic. On the one hand, there is often a strong overlapping of the recrystallisation exotherm with the C_p jump and with the melting endotherm. On the other hand, all the fraction amorphised during the milling does not systematically recrystallise upon heating at 5 °C/min. This is particularly obvious for the sample milled 8 h, which does not recrystallise at all whereas it is completely amorphous (see previous section).
- By XRD:
  The XRD patterns recorded after milling were obtained with samples regularly taken from the milling jar. These different samples do not, of course, have the same particle size. It is thus impossible to fill them into Lindemann capillaries with the same compactness. This precludes performing a precise quantitative analysis of the amorphous fraction. In addition, from 1 h of milling, the Bragg peaks become too weak (or even non-existent) to be analysed.

In view of the inefficiency of the "conventional" characterisation methods (DSC and XRD), the amorphisation kinetic of crystalline lactulose under milling was determined by dissolution calorimetry. This technique has the advantage of being quantitative, precise, and do not require to heat the sample.

In the following, we present the main mechanisms occurring during the dissolution of a solute into a solvent and the enthalpy changes induced by these mechanisms. We also give experimental details of isothermal calorimetry experiments we have performed to measure the dissolution enthalpy of lactulose. The amorphisation kinetic of lactulose upon milling deduced from the dissolution enthalpy measured for increasing milling times is then finally presented.

4.3.1 Origin of the dissolution enthalpy

The dissolution of a solute in a solvent implies the breaking and the formation of several intermolecular bonds, as sketched in figure 4.5. The bond breakings concern solute-solute bonds, and solvent-solvent bonds. These breakings require external energies (ΔH_1 and ΔH_2) so that they are endothermic. The bond formations concern solvent-solute bonds

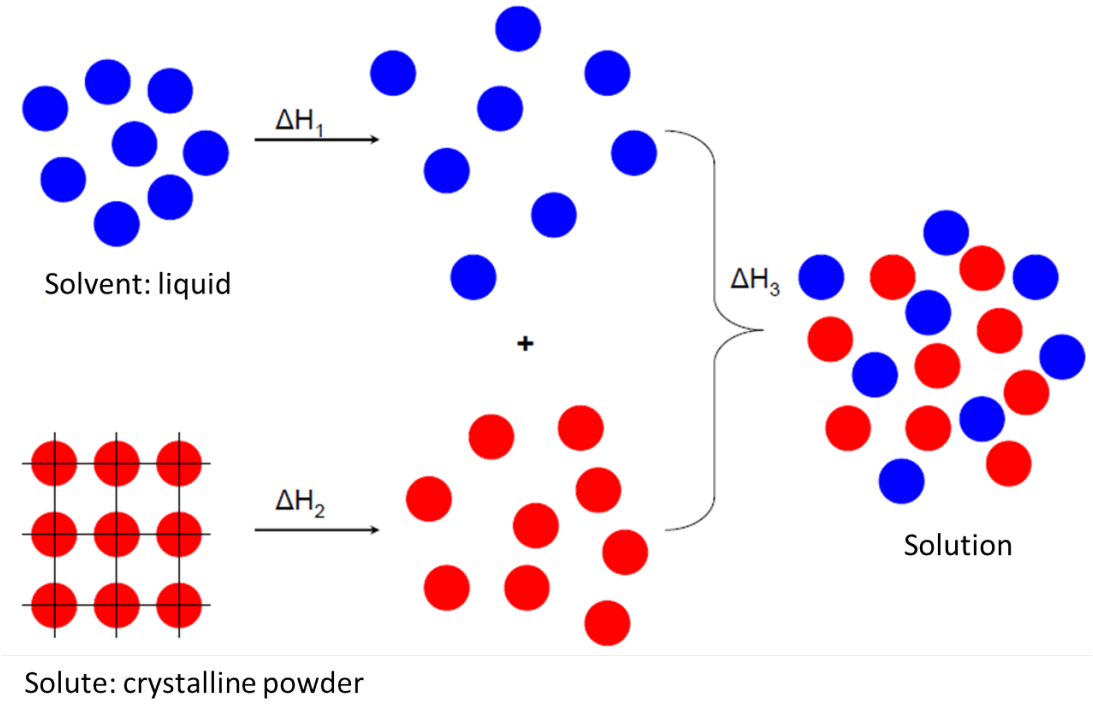

Figure 4.5 – Schematic representation of the different steps of the dissolution of a crystalline solute into a liquid solvent.

and are, on the contrary, exothermic processes (ΔH_3).

It is the competition between endothermic processes of bond breaking, and exothermic processes of bond formation which yields to the dissolution enthalpy. As sketched in figure 4.6 the dissolution enthalpy can be endothermic or exothermic:

- The dissolution enthalpy is endothermic when the energy required to break solute-solute and solvent-solvent bonds is higher than the energy required to form the new solute-solvent bonds (see figure 4.6 a)). This is generally the case for crystalline solids, since the destruction of the intermolecular bonds responsible of the cohesion of the crystal is highly endothermic (like a melting).

- On the contrary, the dissolution enthalpy is exothermic when the energy required to break solute-solute and solvent-solvent bonds is smaller than the energy needs to form the new solute-solvent bonds (see figure 4.6 b)). This is generally the case for amorphous solids for which the energy required to break solute-solute bonds is much smaller than that of corresponding crystals which are much more cohesive. In that case, the sample is said diluted (and not dissolved).

The different enthalpies presented in figure 4.6 a) and b) are:

- ΔH_1: enthalpy related to the breaking of solvent-solvent intermolecular bonds (endothermic process, $\Delta H_1 > 0$)

- ΔH_2: enthalpy related to the breaking of solute-solute intermolecular bonds (endothermic process, $\Delta H_2 > 0$)

- ΔH_3: enthalpy related to the formation of solute-solvent intermolecular bonds (exothermic process, $\Delta H_3 < 0$)

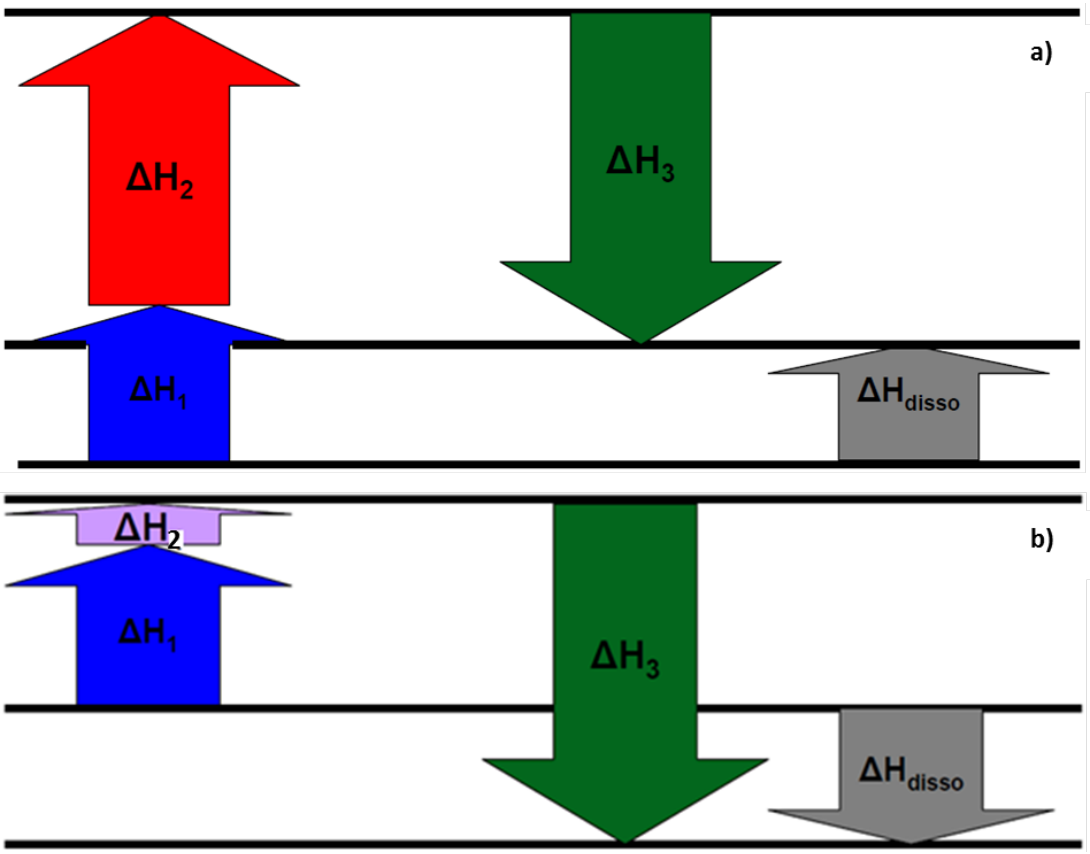

Figure 4.6 – a) Diagram illustrating the relative enthalpic contributions of the various molecular associations and dissociations during the dissolution of a solute into a solvent. The situation corresponds to the dissolution of a crystalline material presenting a strong cohesive energy, making the dissolution process globally endothermic ($\Delta H_{disso} > 0$). b) Diagram illustrating the relative enthalpic contributions of the various molecular associations and dissociations during the dissolution of a solute into a solvent. The situation corresponds to the dissolution of an amorphous material with low cohesive energy, making the dissolution process globally exothermic ($\Delta H_{disso} < 0$).

- ΔH_{disso}: dissolution enthalpy ($\Delta H_{disso} = \Delta H_1 + \Delta H_2 + \Delta H_3$). For a crystalline material, the dissolution is most often endothermic ($\Delta H_{disso} > 0$). In contrast, the dissolution of an amorphous material is most often exothermic ($\Delta H_{disso} < 0$).

It is worth noting that the dissolution enthalpy includes several other energetic contributions like: the wetting energy, the energy of mutarotation, and, in the case of amorphous materials, some differences of enthalpic level. However, all these enthalpic contributions are much smaller than that associated with the dissolution itself (enthalpies of bond breaking and bond formation). They have thus been neglected in this work.

The energy required to break solute-solute bonds highly depends on the structural state of the solute. This energy is high for a crystalline solute, since the breaking of intermolecular bonds responsible of the cohesion of the crystal is similar to the melting. The dissolution of a crystal is thus generally an endothermic process and fall within the situation reported in figure 4.6 a). In contrast, in the case of an amorphous solid, the energy required to break solute-solute bonds is much smaller. This is due to the fact that molecules in amorphous solids are in a mess like in liquids, and are thus linked by weak bonds. The dissolution of an

amorphous solid is thus generally an exothermic process and fall within the situation reported in figure 4.6 b).

It is also important to note that the driving force of dissolution of a solute in a solvent is not only governed by the enthalpy changes taking place during the dissolution. The dissolution is in fact governed by the changes in the Gibbs free energy (ΔG= ΔH-TΔS) that it induces. Both enthalpic and entropic effects thus govern the dissolution, and determine for example the solubility of the solute in the solvent.

4.3.2 Practical realisation of an experiment of isothermal calorimetry of dissolution

The dissolution enthalpy of milled lactulose samples were measured through isothermal calorimetry of dissolution experiments performed at 37 °C using the C80 isothermal calorimeter of Setaram. A typical experiment takes place in four steps:

4.3.2.a) Preparation of the sample and reference cells

Similarly to DSC experiments, isothermal calorimetry experiments consist in measuring the heat flow difference between a sample cell and a reference cell.

The sample cell is shown in figure 4.7. It is a cylindrical cell in hasteloy, having a bottom compartment and a top compartment separated by a removable cap. The solute (powder) is put into the bottom compartment and the solvent in the top compartment, the cap preventing the mixing of both compounds. 100 mg of solute were always used for the experiment. Since the water solubility of lactulose is 764 g/L at 30 °C [234], the amount of water (solvent) used in each experiment is 3.8 g (so we put thirty times more water than that required for the dissolution of the lactulose). This solute/solvent ratio assures a total dissolution of the solute during the experiment. This point is essential to be sure that the exact dissolution heat has been measured. Moreover, a large solute/solvent ratio leads to a fast dissolution, and thus a big dissolution heat flow. This increases the precision of the measurements. Furthermore, the same solute/solvent ratio was used during all the experiments, to ensure the reproducibility of the results.

The reference cell is identic to the sample cell. The bottom compartment is left empty, and the top compartment is filled with the same amount of solvent put into the sample cell, in order to reduce the difference of specific heat between both cells. A small amount of paraffin oil was always put around the cap so as to improve the sealing of bottom compartment. This oil has been checked to have no effect on the dissolution process.

4.3.2.b) Initialisation of the experiment

Reference and sample cells are then put into the two wells of the calorimeter which has been initially set at 37 °C. The insertion of those cells in the calorimeter sets at 37 °C creates an important unbalance of the heat flow difference of the sample cell and the reference cell. This important unbalance is due to the mass of the two cells (about 100 g for a C80 cell compared to 15 mg for a DSC pan). It is thus necessary to reach a new equilibrium of the calorimeter before starting the mixing of the solute and the solvent. In practice, roughly 1 h is needed to reach this new equilibrium.

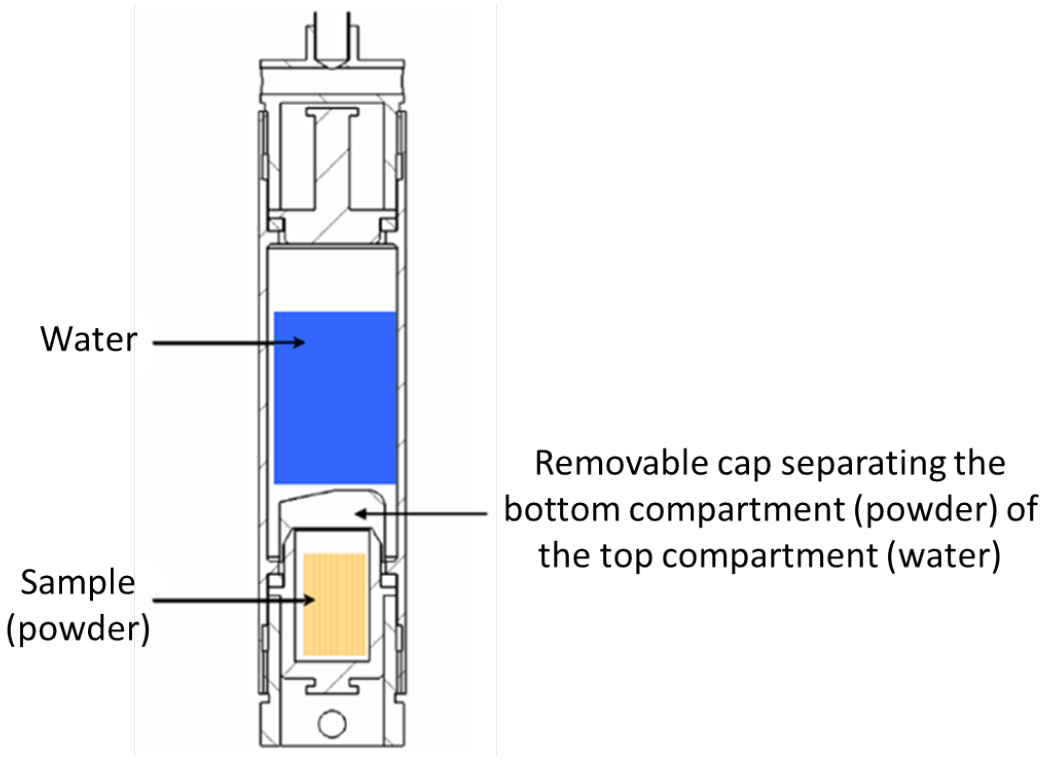

Figure 4.7 – Sketch of the sample cell used during the isothermal calorimetry of dissolution experiments performed with the C80 setaram calorimeter.

4.3.2.c) Launch of the dissolution

After the equilibration of the calorimeter, the mixing of the solute with the solvent is done by the rotation of the calorimeter itself. The first rotation removes the cap in the body of the cell, which allows the solute to mix with the solvent. The motions of the cap during next rotations allow homogenising the mixture.

4.3.2.d) Measurement of the dissolution enthalpy

When the rotation starts, the dissolution of the solute in the solvent is revealed by an important peak on the heat flow signal. This peak can be exothermic or endothermic, depending on the solute physical state. The dissolution enthalpy is then directly measured by integrating the heat flow peak. This integration requires adequately define the base line. For that purpose, it is important to note that:

- The heat flow suddenly increases when the dissolution starts, and then decreases more slowly to reach a level below that of the initial one. This change of level reflects the difference of specific heat between the initial binary system (solute + solvent) and the final binary and homogeneous mixture obtained after dissolution.

- The release of heat due the dissolution takes roughly 1 h. This is not compatible with the dissolution kinetic of sugars in water given in the literature. For example, Miller et al. [48] have measured a dissolution (in water) time of 30 sec for the case of crystalline trehalose. This value is much smaller than the time noted for C80 (1 h). This difference is due to two factors:

i) C80 uses a « Calvet » technology for heat detection [235, 236]. The heat absorbed or emitted by the sample is detected by a network of 38 thermocouples surrounding the sample cell.

ii) The mass of the empty cell (100 g) is very big compared to that used in DSC (15 mg). Hence, the emission of the heat due to the dissolution takes a long time to go through the walls of the cell and to reach the network of thermocouples. There is thus a long delay between the heat flow generated by the dissolution and the heat flow detected by the C80 captors. The C80 calorimeter does not thus allow obtaining the dissolution kinetic.

All the previous information indicates that the mixture of the solute and the solvent creates a difference of C_p, and that difference is already effective just 1 min after the beginning of the dissolution. We can then reasonably consider that the C_p of the sample during the heat release (1 h) is constant and equal to the C_p of the final homogeneous mixture. The base line chosen to integrate the dissolution peak has thus been obtained by horizontal extrapolation of the heat flow recovered after the end of the dissolution peak.

4.3.3 Determination of the amorphisation kinetic of lactulose upon milling, by isothermal calorimetry of dissolution

4.3.3.a) Calibration curve

The determination of the amorphous fraction X_{am} in a milled sample of lactulose from its dissolution enthalpy ΔH_{dissol} requires to establish a calibration curve, i.e. an univocal relation $\Delta H_{dissol} = f(X_{am})$ between ΔH_{dissol} and X_{am}. To do so, dissolution enthalpies of physical mixtures of crystalline lactulose and QFTM lactulose were measured. Five different concentrations of amorphous fraction (X_{am}) were chosen: X_{am} = 0.0, 0.25, 0.50, 0.75, and 1.0.

Figures 4.8 a) b) and c) show thermograms of lactulose samples recorded during their isothermal dissolution in water at 37 °C.

Figure 4.8 a) corresponds to totally amorphous lactulose (X_{am} = 1.0). It shows a broad, but well defined, exothermic peak as expected for amorphous materials. The peak integration leads to a dissolution enthalpy close to ΔH_{dissol} = 57.35 J/g. This value is compatible with that determined by Miller et al [48] at 25 °C (74 J/g). Indeed, Jasra [237] shows that the exothermic contribution of the dissolution decreases when increasing the temperature.

Figure 4.8 b) corresponds to crystalline lactulose (X_{am} = 0.0). It shows a quite sharp endotherm overlapping a broader exotherm. The resulting dissolution enthalpy determined by integration of the heat flow signal is ΔH_{dissol} = -2.17 J/g, in agreement with the value obtained by Miller et al. [48] at 25 °C (-7.11 J/g). This value is close to zero which means that the energy required to destroy the crystal lattice and that required to disperse the lactulose molecules in water, have the same order of magnitude. Moreover, the crystal destruction obviously precedes the molecular dispersion in water. The slight time shift between the two processes and their equivalent energy (while opposite) make possible the unusual detection of the two processes during the dissolution experiment.

Figure 4.8 c) corresponds to physical mixtures of crystalline and amorphous lactulose. Three amorphous fractions have been investigated: X_{am} = 0.25, X_{am} = 0.50 and X_{am} = 0.75.

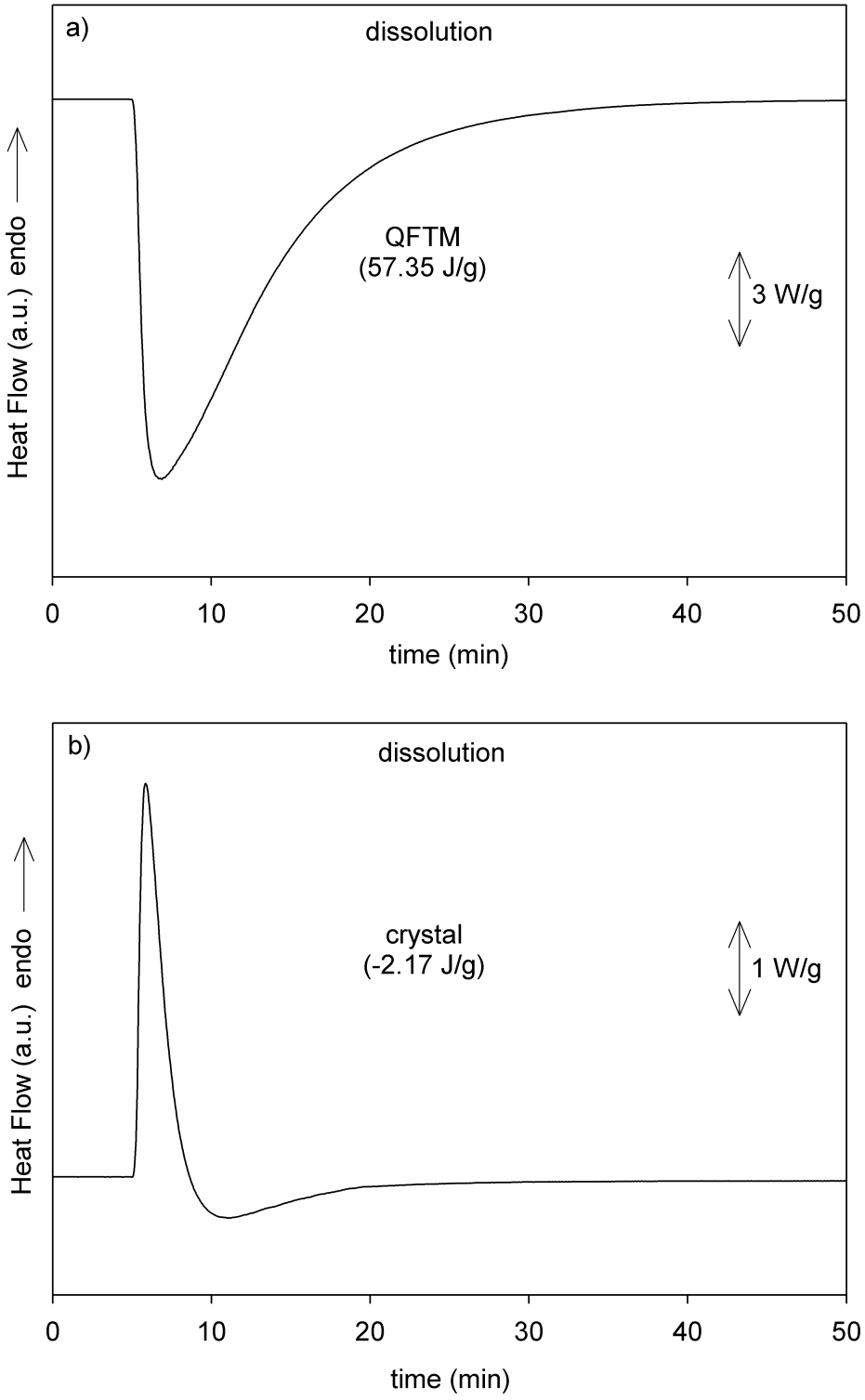

a) Thermogram recorded during the isothermal dissolution at 37 °C of the QFTM lactulose.
b) Thermogram recorded during the isothermal dissolution at 37 °C of crystalline lactulose.

Each thermogram shows a large exotherm whose amplitude increases for increasing amor-

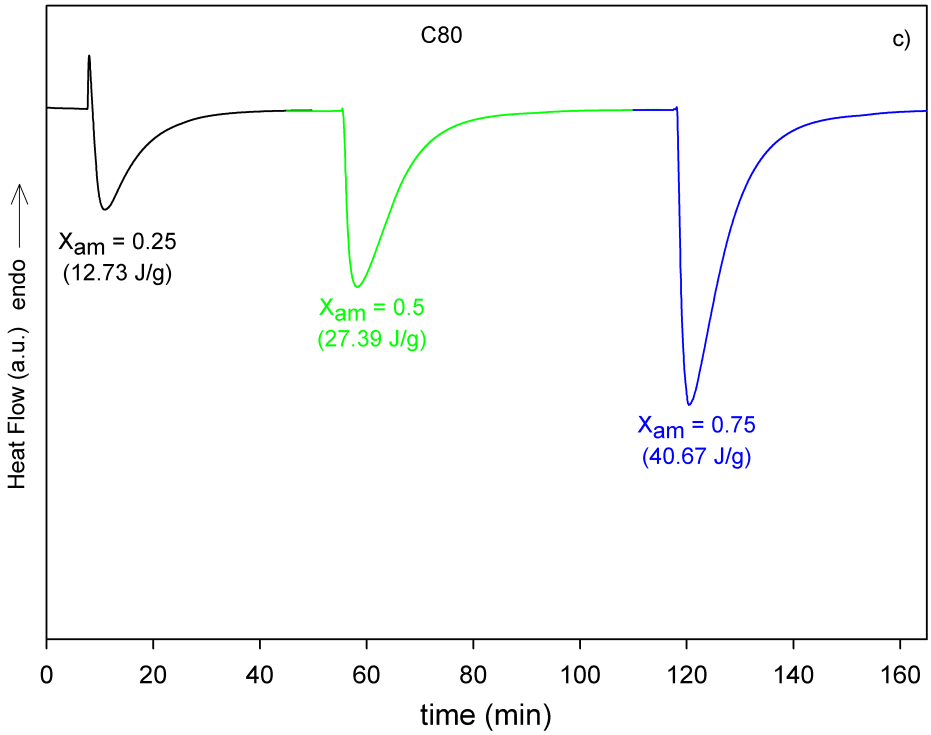

c) Thermograms recorded during the isothermal dissolution at 37 °C of three physical mixtures of amorphous and crystalline lactulose. The amorphous fractions are X_{am} = 0.25 (black line), 0.5 (green line) and 0.75 (blue line).

Figure 4.8 – Isothermal dissolution thermograms.

phous fraction. It can be noted that the thermogram of the mixture containing 25% of QFTM has, in addition, a weak and narrow endotherm at the very beginning of the dissolution process. This endotherm has the same origin as that observed during the dissolution of the pure crystal (see figure 4.8 b)). It corresponds to the destruction of the lattice of the crystalline fraction which slightly precedes the dispersion of the molecules in the solvent. The endotherm is, however, much weaker here because, on the one hand the crystalline fraction is smaller, and on the other hand the amorphous fraction gives rise to a larger exotherm which partially hides the endotherm. This effect is stronger when the amorphous fraction in the physical mixture increases so that the initial endotherm is no longer observed for X_{am} = 0.5 and X_{am} = 0.75. The dissolution enthalpies of the three physical mixtures were determined by integrating the dissolution peaks. The values obtained are given in table 4.1, and the evolution of the dissolution enthalpy as a function of the amorphous fraction is represented in figure 4.9. This evolution is clearly linear, which indicates that there is a proportionality between the amorphous fraction in the mixture and the dissolution enthalpy of the mixture. This evolution has been adjusted by a linear law:

$$\Delta H_{dissol} = \alpha X_{am} + \beta \tag{4.1}$$

The best fit was obtained for α = 58.79 J/g and β = -2.20 J/g. This equation will be later used to estimate the amorphous fraction present in milled crystalline lactulose samples, from their dissolution enthalpy.

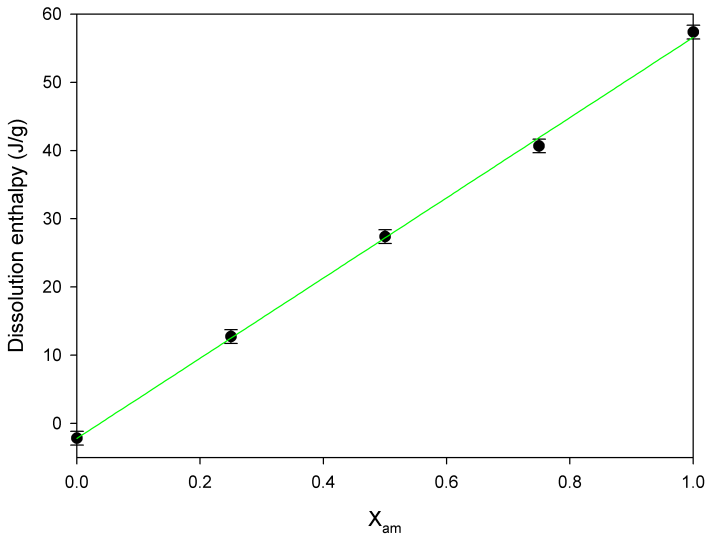

Figure 4.9 – Evolution of the dissolution enthalpy with respect to the amorphous fraction.

Table 4.1 – Dissolution enthalpy of different physical mixtures of QFTM and crystalline lactulose. A negative value corresponds to an endothermic process.

X_{am}	Dissolution enthalpy in J/g
0	-2.17
0.25	12.73
0.5	27.39
0.75	40.67
1.0	57.35

4.3.3.b) Amorphisation kinetic of lactulose upon milling derived from isothermal calorimetry of dissolution.

Figure 4.10 shows the thermograms recorded during the isothermal dissolution at 37 °C of crystalline lactulose samples having undergone milling operations of a duration varying from 3 min to 2 h. All the thermograms show an exotherm. This exotherm develops up to 1 h of milling and then becomes stationary for the higher milling times. This amplification of the exotherm reflects the presence of an increasing amorphous fraction during milling. It can also be noted that the thermogram recorded after 3 min of milling has a tiny endotherm at the very beginning of dissolution. This endotherm is similar to that already observed for the pure crystal and the physical mixture containing 25% of amorphous lactulose (see figure 4.8). It is due to the dissolution of the crystalline fraction which slightly precedes that of the amorphous fraction.

The dissolution enthalpies of the crystalline lactulose milled samples were determined by integrating the dissolution peaks and reported in table 4.2. Fractions amorphised by milling (X_{am}) were then estimated using the calibration curve (see figure 4.9 and Eq. 4.1). These amorphous fractions are shown in table 4.2 and their evolution with the milling time is illustrated in figure 4.11. This evolution corresponds to a monotonous increase of the amorphous fraction. The experimental points could be correctly fitted by a simple exponential relaxation law of the type:

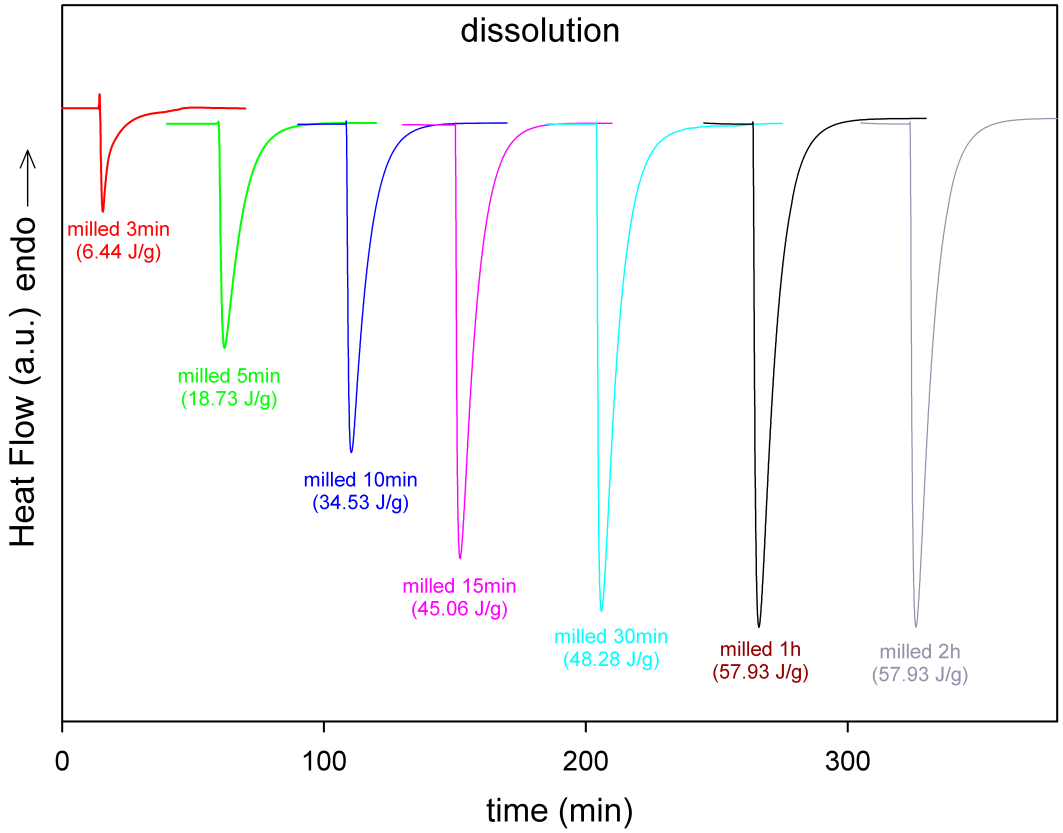

Figure 4.10 – Thermograms recorded during the isothermal dissolution at 37 °C of crystalline lactulose samples having undergone milling operations of a duration varying between 3 min and 2 h.

$$X_{am} = 1 - \exp(-\frac{t}{\tau}) \tag{4.2}$$

The best fit was obtained for a relaxation time $\tau = 11$ min. This time is considerably shorter than the relaxation time usually observed in molecular materials for identical milling conditions. For example: chlorhexidine [238], glucose [27], lactose [215] or dexamethazone [to be published] have relaxation times of about 1 h for identical milling conditions. **Lactulose therefore appears to be a material that amorphises particularly rapidly upon milling.** This point is consistent with the fact that the energy required to destroy the crystal lattice upon dissolution is quite weak.

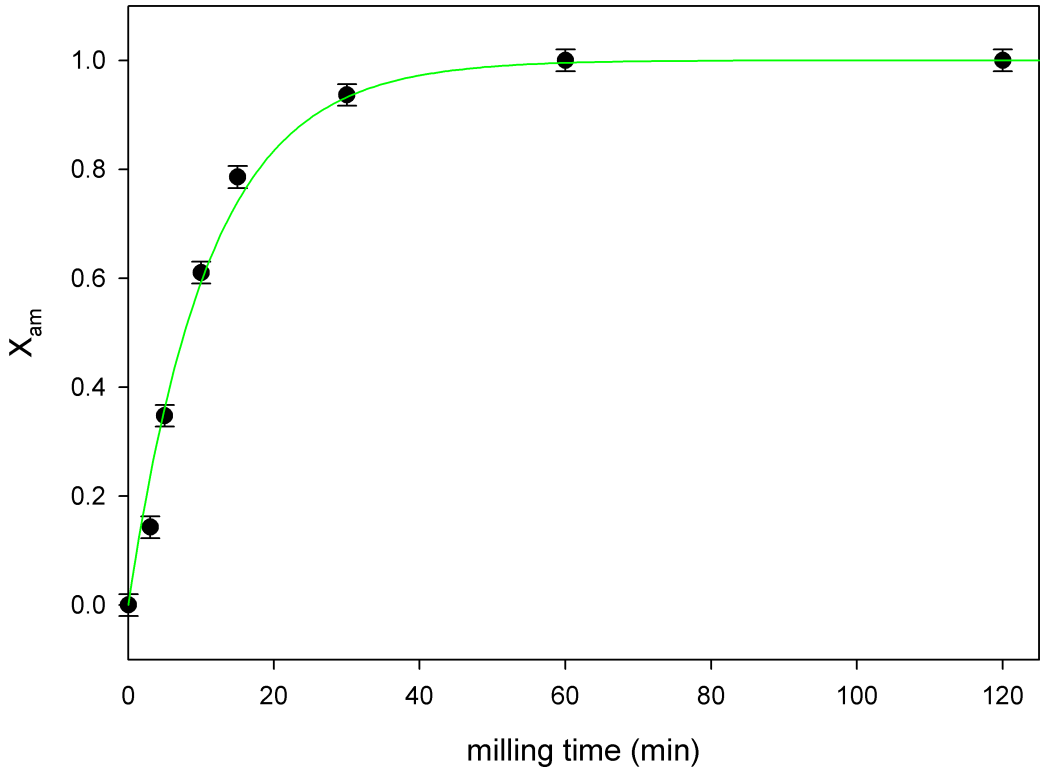

Figure 4.11 – Amorphisation kinetic of crystalline lactulose under milling. The green line represents the best fit of the evolution using an exponential law.

Table 4.2 – Dissolution enthalpy and amorphous fraction of initially crystalline lactulose samples determined after milling times varying from 0 to 2 h. The dissolution enthalpy of the QFTM lactulose is added for comparison.

Milling time (min)	Dissolution enthalpy in J/g	X_{am}
0	-2.17	0.00
3	6.44	0.14
5	18.73	0.35
10	34.53	0.61
15	45.06	0.79
30	48.28	0.94
60	57.93	1.00
120	57.93	1.00
QFTM	57.35	1.00

Summary

In this chapter, we have studied the structural and thermodynamic evolutions of a lactulose powder, initially crystalline, towards an amorphous and vitreous state during a mechanical milling operation.

The structural evolutions followed by XRD revealed a total disappearance of the Bragg peaks after only one hour of milling, suggesting a rapid and total amorphisation of the material. On the other hand, the analyses carried out by DSC revealed a strong evolution of the thermograms after one hour of milling. In particular, there is a complete disappearance of the recrystallisation exotherm indicating that the amorphous material obtained during the first milling hour progressively loses its propensity to recrystallise. After 8 h of milling, the sample no longer shows any sign of recrystallisation upon heating (at 5 °C/min). This behaviour is quite exceptional. Up to now, only trehalose has shown similar behaviour for milling operations of very long durations (100 h). The gradual disappearance of the recrystallisation may be due either to a gradual disappearance of residual crystal nuclei, which usually favour recrystallisation, or to a modification of the nature of the amorphous sample. However, seeding experiments on the QFTM (which does not recrystallise upon heating) have shown that the presence of crystallites does not induce its recrystallisation upon heating (at 5 °C/min). Therefore, the recrystallisation of the amorphous lactulose does not seem to depend very much on the presence of pre-existing crystal nuclei. Consequently, the disappearance of the recrystallisation abilities of lactulose during milling must be attributed to a change in the nature of the obtained amorphous sample. This could be for example an evolution of the associated local order characterising the amorphised material.

Conventional XRD and DSC techniques have proved ineffective in accurately determining the amorphisation kinetic ($X_{am}(t)$) under milling. For XRD, the problem is essentially due to the evolution of the granulometry during milling which prevents a reproducible filling of the Lindeman capillaries. For DSC, the problem arises from the important overlapping of the main enthalpic events (glass transition, recrystallisation and melting) as well as the progressive loss of recrystallisation of the amorphised fractions. We have been able to overcome these difficulties by carrying out original experiments of dissolution calorimetry, and by establishing a relation between the dissolution enthalpy of a sample and its amorphous rate. The obtained kinetic corresponds to a simple exponential relaxation with a relaxation time of 11 min. This characteristic time is much shorter than that measured for other materials (typically 1 h) with identical milling conditions. Lactulose thus appears as a material which amorphises easily and quickly under milling.

Chapter 5

Neutron diffraction and spectroscopy results

"Neutrons tell us where atoms are and how they move"

Clifford G. Shull

Contents

This chapter is mainly dedicated to neutron scattering results complemented with molecular dynamics and ab-initio simulations. Neutron scattering theory and concepts are preliminary given. The aim of the first section is thus to take the reader into the basic principles of neutron scattering, including the main formulas that have been explicitly and implicitly used for the completion of the experimental part of the chapter. In the second and third sections, neutron diffraction and neutron spectroscopy results are presented, respectively. Specific details about the neutron data treatment are given in annex B. It is important to remind that samples were prepared as explained in chapter 2. As seen in chapter 3, the quenched from the melt sample has undergone a thermal degradation, while the spray-dried and freeze-dried samples have undergone important tautomeric changes.

5.1 Neutron scattering

James Chadwick discovered the neutron in 1932. Fourteen years later, E.O. Wollan and C.G. Shull established the basic principles of neutron diffraction technique using the Graphite Reactor at the Oak Ridge National Laboratory, in USA. Some years later, thanks to the first three-axis spectrometers built at Chalk-River (Canada) in 1955, B.N. Brockhouse laid the foundations of neutron scattering spectroscopy as we know it today.

5.1.1 Generalities on the neutron

The neutron is a subatomic particle with zero charge, mass **m = 1.0087** atomic mass units, spin **1/2**, and magnetic moment, **urn= - 1.9132** nuclear magnetons. These four properties combine to make the neutron a highly effective probe of condensed matter.

There are several ways to produce neutrons. In neutron scattering facilities, neutrons are usually produced by two different procedures:

- By fission: In fission reaction, a thermal neutron is absorbed by a ^{235}U nucleus. The nucleus becomes highly excited and splits into fission fragments (medium-heavy elements) and 2 to 5 fast neutrons. On the average, each reaction gives 2.5 neutrons, of which some are needed to keep the chain reaction going. This method is used at nuclear reactor sources such as the Institut Laue-Langevin (Grenoble, France) for example.

- By spallation: It is a process where high-energy particles (typically 1 GeV) such as protons chop a heavy metal target. These collisions eject protons, pions, muons, neutrinos, and neutrons from the target. This method is used at ISIS (Oxford, UK) for instance.

Both methods lead to very hot neutrons, of about 1 MeV. With such very hot neutrons, interaction of neutrons with matter will lead to excitations of the internal nuclei levels and core electronic states of atoms in the compound under study. Such situation has to be avoided when studying excitations in condensed matter. To be useful for neutron scattering studies of condensed matter, neutrons have to be moderated into thermal neutrons, with energy of few meV and wavelength of few Å. To do so, neutrons are slowed down in a moderator, where they are brought into thermal equilibrium through inelastic collisions with light atoms such as H, D or Be.

Because of its very small dimension, neutron displays wave-particle duality. Whether to treat it as a particle or a wave depends on the observed phenomenon. Its wavelength fits perfectly interatomic distances in the matter. This insures that interference between waves (after interaction with the sample) is observable. For this reason, neutrons are well suited to investigate structure in condensed matter at an atomic level. Its energy, in the range 1 meV to 1 eV, matches elementary excitations energies in the condensed matter (phonon, molecular vibrations ...). For this reason, neutron is a particle of first interest to study excitations in condensed matter. Figure 5.1 shows the different timescales accessible by several neutron spectroscopy techniques.

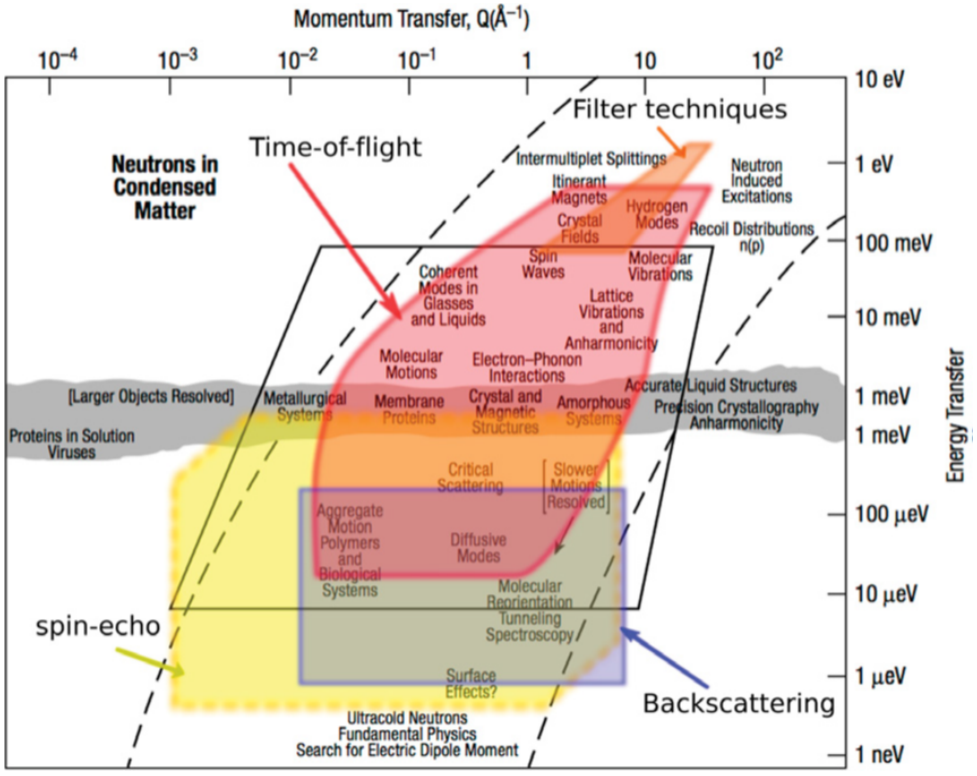

Figure 5.1 – Spatial (r[Å]= 2π/Q[Å^{-1}]) and time (t[ps]=0.658/ħω[meV]) scales associated to main physical phenomena potentially observable by inelastic neutron scattering (INS). Regions of space (Q,ω) accessible by the main family of instruments (spin-echo, backscattering, time of flight, filter techniques) are specified.

In a scattering experiment, the momentum and energy conservation are expressed by the equations:

$$\begin{cases} \mathbf{Q} = \mathbf{k} - \mathbf{k'} \\ \hbar\omega = E - E' \end{cases} \tag{5.1}$$

Where **Q** is the scattering vector, **k** and **k'** are the initial and final wave vectors of the neutron, $\hbar\omega$ is the energy exchange with the sample, E and E' are the initial and final energies of the neutron.
By using the de Broglie relation [1], the energy of a neutron can be expressed as:

[1] a particle having a mass and velocity can be expressed as a wave function whose momentum, **k**, can be expressed as $|p| = \frac{h}{\lambda} = \hbar|\mathbf{k}|$

$$E = \frac{h^2}{2m\lambda^2} = \frac{\hbar^2 k^2}{2m} = \frac{mv^2}{2} \tag{5.2}$$

Where m is the mass of the neutron, λ its wavelength.
After some developments, from Eqs. 5.1, the following kinematical law is obtained:

$$\frac{\hbar^2 Q^2}{2m} = 2E - \hbar\omega - 2\sqrt{E(E-\hbar\omega)}\cos 2\theta \tag{5.3}$$

Each neutron spectrometer covers a specific kinematical range. It can be determined using Eq. 5.3. This range depends both on the incident energy of the neutron, and also on the 2θ angles covered by the instrument detectors.

5.1.2 Why to use neutrons?

A high-flux reactor has about ϕ= 1.5*10^{21} thermal neutrons per m^2.s. Their density, with an average speed of v=2200 m/s is n =ϕ/v = 6.8*10^{17} neutrons per m^3. To get the same density of air, you have to pump to 10^{-7} mbar, which corresponds to a high vacuum. This means that neutrons are really scarce. They should always be used to supplement what you already know from others techniques (X-ray, IR ...), or to get new information that any other technique cannot give. Neutrons should always be used intelligently. Some characteristics making neutrons an unique tool for research in condensed matter are listed below:

- Neutrons interact with nuclei. The scattering length (it is the radius of the fictive volume around the nucleus in which nucleus is sensitive to the presence of neutrons) is thus not atomic number dependent. For this reason, neutron scattering is sensitive to the presence of light elements such as hydrogen. Moreover, adjacent elements in the periodic table are usually easily distinguished.

- The zero charge means that its interactions with matter are confined to the short-ranged nuclear and magnetic interactions. This means that the interaction probability is small, so the neutron can usually penetrate into the bulk of a sample of condensed matter, without destructing the sample. Inelastic neutron scattering (INS) results are thus naturally weighted to the measurement of bulk properties.

- The mass of the neutron is small (1 amu). When scattered, the neutron transfers momentum to the atom and INS measurements are not limited to observation at the Brillouin zone centre, as are photon techniques (like Raman spectroscopy). It is thus easy to measure dispersion curves. Moreover, in contrast to IR or Raman spectroscopies, all vibrations are active in INS and, in principle, measurable.

- The measured INS intensities are directly related to the atomic displacements of the scattering atom, which can often be obtained from simple classical dynamics. Any difficulties arising from the electro-optic parameters are avoided. Indeed the band positions and intensities of most molecular systems can be accurately calculated using modern ab initio simulations. INS spectra are thus accurately modelled.

It must however be pointed out that neutron scattering is a low flux technique, which is one of its most important limiting factors. As a consequence, the amount of sample required for neutron investigations is much larger than the other scattering techniques, and neutron scattering experiments are much longer than other scattering experiments. As commonly

stated, it is the complementarity of the different techniques (IR, Raman, X-Ray, NMR, neutrons ...) what allows retrieving a coherent and meaningful picture of the sample studied.

5.1.3 Basics of neutron scattering

In this section we provide the basics of neutron scattering useful for understanding neutron results presented in this chapter. The whole theory has been extensively developed elsewhere, and interested readers can read general textbooks of condensed matter physics and neutron scattering [76, 239–241]. This section has been mainly written with the help of the Squires book [239].

The principle of a scattering technique consists in measuring how a flux of known characteristics is changed when passing through the sample under investigation. This flux can be anything that displays interference properties (X-ray, neutrons, electrons ...).

In the case of neutron scattering for example, the incident neutron can be transmitted if it does not come close enough to the nuclei to interact with them, or interact with the nuclei if it does. This interaction can be classified in two categories:

- Absorption: the incident neutron may be absorbed by the nuclei of the sample, leading to a reaction in which the excited nucleus undergoes fission, or expels an α-particle, a proton, or most likely a γ radiation.
- Scattering: the incident neutron may be scattered by the nuclei of the sample, and changes both its direction and energy. It is the main event when neutrons interact with nuclei.

The intensity measured at the detectors is thus the summation of the transmitted intensity (due to neutrons that have not been scattered by the sample) and the scattered intensity. It is the observable when doing a neutron scattering experiment. The **scattered** intensity $I(2\theta,\omega)$ represents the number of neutrons scattered by the sample with an energy exchange $\hbar\omega$ at the scattering angle 2θ. It can be expressed as:

$$I(2\theta,\omega) = C\phi_0 \frac{d^2\sigma}{d\Omega dE'}(2\theta,\omega)\epsilon(k') \tag{5.4}$$

Where $C\phi_0$ represents the flux of incident neutrons, $\epsilon(k')$ the efficiency of the detection device and $\frac{d^2\sigma}{d\Omega dE'}$ the double differential scattering cross section.

5.1.3.a) Scattering cross section

In a scattering process, what is measured is the number of neutrons with an initial wave vector **k** and energy E, that are scattered by a target into a solid angle $d\Omega$ with a final wave vector **k'** and energy E'. Figure 5.2 summarises the scattering process using polar coordinates.

The scattering geometry in figure 5.2 assumes that the detector is very far from the target. The double differential cross section is defined as:

$$\frac{d^2\sigma}{d\Omega dE'} = \frac{\text{number of neutrons scattered per second into a small solid angle } d\Omega \text{ in the direction } (\theta,\phi) \text{ with final energy between E' and E'+dE', divided by the incoming intensity.}}{} \tag{5.5}$$

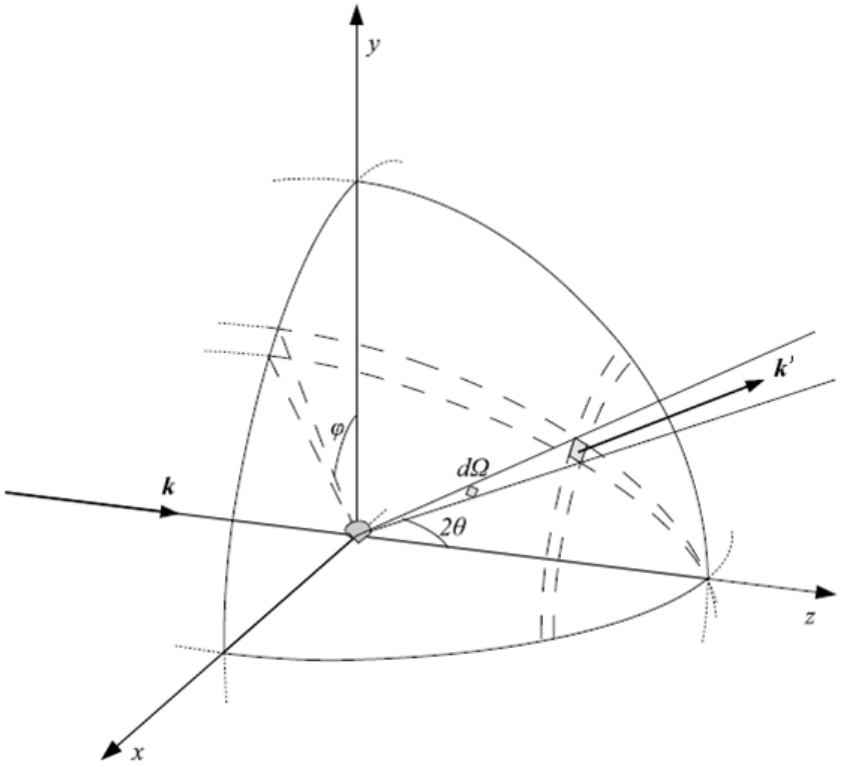

Figure 5.2 – Geometry for scattering experiment.

$\frac{d^2\sigma}{d\Omega dE'}$ has its unit in area divided by energy.

When the energy change is not analysed, the double differential scattering cross section is integrated with respect to the energy change $d\omega$, and one can define the differential scattering cross section as:

$$\frac{d\sigma}{d\Omega} = \int_0^{\infty} \left(\frac{d^2\sigma}{d\Omega dE'}\right) dE' \tag{5.6}$$
$$= \text{number of neutrons scattered per second into a small solid angle } d\Omega \text{ in the direction } (\theta,\phi), \text{ divided by the incoming intensity.}$$

$\frac{d\sigma}{d\Omega}$ has its unit in area.

When neither the energy change nor the direction of scattering is analysed, one can define the total scattering cross section as:

$$\sigma_{tot} = \int_{\text{all directions}} \left(\frac{d\sigma}{d\Omega}\right) d\Omega \tag{5.7}$$
$$= \text{total number of neutrons scattered per second, divided by the incident intensity.}$$

Consider the differential scattering cross section $\left(\frac{d\sigma}{d\Omega}\right)_{\lambda\to\lambda'}$ representing the sum of all processes in which the state of the scattering system changes from λ to λ', and the state of the neutron changes from **k** to **k'**. It can be expressed as:

$$\left(\frac{d\sigma}{d\Omega}\right)_{\lambda\to\lambda'} = \frac{1}{\phi}\frac{1}{d\Omega}\sum_{\mathbf{k'}\ in\ d\Omega} W_{\mathbf{k},\lambda\to\mathbf{k'},\lambda'} \tag{5.8}$$

Where $W_{\mathbf{k},\lambda\to\mathbf{k'},\lambda'}$ is the number of transitions per second from the state **k**, λ to the state **k'**, λ', and ϕ the flux of incident neutrons.

Since the wavelength of the neutron is of the order of 10^5 times bigger than the nuclear interaction range (fm), one can assume the nucleus to be a point-like scatterer. Therefore, when scattering from a single, fixed nucleus, the neutron experiences a point-like potential V(r), and thus the scattered wave is spherical, expressed as $\Psi(r) = -\frac{b}{r}e^{i\mathbf{k}r}$. The transition from an initial state **k**, λ to a final state **k'**, λ' (final sample state is fixed) will only occur for the values |**k'**| lying in the small solid angle. Within this scenario, Fermi golden rule (this rule is derived in quantum mechanics books, as [242] in chapter 18) can be used to evaluate the expression on the right-hand side of Eq. 5.9:

$$\sum_{\mathbf{k'}\ in\ d\Omega} W_{\mathbf{k},\lambda\to\mathbf{k'},\lambda'} = \frac{2\pi}{\hbar}\rho_{\mathbf{k'}}\left|\langle\mathbf{k'}\lambda'|V(r)|\mathbf{k}\lambda\rangle\right|^2 \tag{5.9}$$

In this expression, $\rho_{\mathbf{k'}}$ is the density of final states in $d\Omega$, and V(r) is called the Fermi pseudo-potential.

The expression on the right-hand side of Eq. 5.9 can be solved using the Born Approximation, based on the first order perturbation theory. This approximation can be used in the basis of two assumptions:

- the incident and scattered waves are considered plane waves
- the interaction between the neutron and nucleus is weak, given by the Fermi pseudo-potential.

Within the Born Approximation, the double differential scattering cross-section can be expressed as follows:

$$\left(\frac{d^2\sigma}{d\Omega dE'}\right)_{\lambda\to\lambda'} = \frac{k'}{k}\left(\frac{m}{2\pi\hbar^2}\right)^2\left|\langle\mathbf{k'}\lambda'|V(r)|\mathbf{k}\lambda\rangle\right|^2\delta\left(E_\lambda - E_{\lambda'} + E - E'\right) \tag{5.10}$$

V(r) is a short-range attractive/repulsive potential between a fixed nucleus and a neutron:

$$V(r) = \sum_j b_j\delta\left(r - R_j\right) \tag{5.11}$$

Where R_j is the position vector of each nucleus, r is the position vector of the neutron, and b_j is the scattering length of each nucleus.
The variable b is called scattering length. It is (θ,ϕ) independent, and for the majority of the elements b is also neutron energy independent. It is a complex quantity whose imaginary part is related to the absorption.

The final double differential cross-section for nuclear scattering can be obtained by applying the following steps (see Squires [239]): inserting Eq. 5.11 into 5.10, expressing the δ-function as a time integral by introducing the Heisenberg time-dependent operators, summing over all final states λ' for a fixed initial state λ and finally averaging over all λ [2]:

[2] In Eq. 5.12, $\mathbf{R}_j$ is a time-dependent Heisenberg operator.

$$\frac{d^2\sigma}{d\Omega dE'} = \frac{k'}{k}\frac{1}{2\pi\hbar}\sum_{jj'} b_j b_{j'} \int_{-\infty}^{\infty} \langle \exp\{-i\mathbf{Q}.\mathbf{R}_{j'}(0)\} \exp\{i\mathbf{Q}.\mathbf{R}_j(t)\}\rangle \exp(-i\omega t)\, dt \tag{5.12}$$

This finally leads to one of the most important expressions of the double differential scattering cross section, related to the dynamical structure factor $S(\mathbf{Q},\omega)$:

$$\frac{d^2\sigma}{d\Omega dE'} = N\frac{k'}{k}\frac{\sigma_{tot}}{4\pi} S(\mathbf{Q},\omega) \tag{5.13}$$

$S(\mathbf{Q},\omega)$ is the total dynamical structure factor, and contains the complete information of the sample state. The goal of any scattering experiment is to measure it.

5.1.3.b) Coherent and incoherent scattering cross sections

Notions of coherence and incoherence are the building blocks in neutron scattering theory. When the neutron is scattered by the nucleus, its energy and/or the trajectory can be influenced. The neutron-nucleus interaction is characterised by a scattering length b [239, 243], which varies from one chemical species to another, but also from one isotope to another within the same species. This interaction depends on the total spin state $\mathbf{J} = \mathbf{I} + \mathbf{S}$ of the neutron-nucleus system, with I the nucleus spin and S that of the neutron. For a given isotope i, the average value of the scattering length over all the spin states b_i is called the coherent scattering length. In general, the coherent part of the scattering approximates an ideal system where all isotopes i are in the same average spin state. The deviation of the actual system from this ideal one gives origin to the incoherent scattering. The scattering cross section measured can therefore be separated in to two terms, the coherent and incoherent scattering cross-sections:

$$\begin{aligned}\left(\frac{d^2\sigma}{d\Omega dE'}\right)_{coh} &= \frac{\sigma_{coh}}{4\pi}\frac{k'}{k}\frac{1}{2\pi\hbar}\sum_{jj'}\int_{-\infty}^{\infty} \langle \exp\{-i\mathbf{Q}.\mathbf{R}_{j'}(0)\} \exp\{i\mathbf{Q}.\mathbf{R}_j(t)\}\rangle \exp(-i\omega t)\, dt \\ &= \frac{\sigma_{coh}}{4\pi}\frac{k'}{k} S_{coh}(\mathbf{Q},\omega)\end{aligned} \tag{5.14}$$

$$\begin{aligned}\left(\frac{d^2\sigma}{d\Omega dE'}\right)_{inc} &= \frac{\sigma_{inc}}{4\pi}\frac{k'}{k}\frac{1}{2\pi\hbar}\sum_{j}\int_{-\infty}^{\infty} \langle \exp\{-i\mathbf{Q}.\mathbf{R}_{j}(0)\} \exp\{i\mathbf{Q}.\mathbf{R}_j(t)\}\rangle \exp(-i\omega t)\, dt \\ &= \frac{\sigma_{inc}}{4\pi}\frac{k'}{k} S_{inc}(\mathbf{Q},\omega)\end{aligned} \tag{5.15}$$

Where $S_{coh}(\mathbf{Q},\omega)$ and $S_{inc}(\mathbf{Q},\omega)$ are the coherent and incoherent dynamical structure factors, respectively. The coherent and incoherent cross sections are defined by $\sigma_{coh} = 4\pi(\overline{b})^2$ and $\sigma_{inc} = 4\pi\{\overline{b^2} - (\overline{b}^2)\}$.

Those expressions of the coherent and incoherent double differential scattering cross sections allow us understanding that the coherent scattering is qualitatively very different from the incoherent scattering. The coherent scattering describes correlation between the positions of the same nucleus at different times, and the correlation between the positions of different nuclei at different times. For this reason, from the coherent signal, information

such as the collective dynamics of nuclei, the structure, can be retrieved. On the other side, the incoherent scattering describes correlation between the positions of the same nucleus at different times. For this reason, the incoherent signal gives dynamics of individual particles (diffusive motions, internal dynamics, and molecular vibrations). No information about the structure can be retrieved from the incoherent scattering.

Coherent and incoherent scattering cross sections can both be separated into an elastic and inelastic part.

5.1.3.c) Elastic and inelastic scattering cross sections

The expressions of the coherent and incoherent structure factors for elastic and inelastic scattering have been developed elsewhere, and interested readers are referred to textbooks of neutron scattering [239, 240].

Elastic When there is no energy transfer between the neutron and the sample, the scattering is elastic. For such situation, $\omega = 0$, and the only relevant variable to consider is the scattering vector **Q** between the neutron wave and the sample.

- **The elastic coherent** scattering provides information on the atomic structure. For the case of an harmonic non-Bravais crystal (non-Bravais crystal means crystal having more than one atom per unit cell), Bragg peaks are obtained for directions of the scattering vector **Q** corresponding to the vectors of the reciprocal lattice.

- **The elastic incoherent** scattering appears in the intensity measured on a diffractometer as a background. The only dependence of this cross section on the scattering vector **Q** is in the Debye-Waller (DW) factor. At low temperature or low $|\mathbf{Q}|$, the DW factor is close to unity.

Inelastic By contrast to the elastic scattering, when the neutron gains or loses energy while interacting with the sample, the scattering is inelastic. Inelastic scattering intensities are well measured on spectrometers. They can be measured as a function of « coherent » **Q** (case of low energy transfer range, for spectrometers covering an enough large Q-range) or no (case of high energy transfer range).The resulting inelastic spectrum $S(Q, \omega)$ allows retrieving the generalised density of states $GDOS(\omega)$ of the sample under study.

The incoherent scattering is inclusive, and all vibrational modes are a priori present in the cross section. In contrast, the coherent scattering is selective, and a specific mode will only contribute to the cross section for specific lattice vectors [244]. For this reason, the incoherent scattering is generally employed to obtain a good estimation of the density of states.

5.2 Neutron diffraction: experiments and results

As previously mentioned, the scattering cross section can be separated into coherent and incoherent scattering cross sections, where only the coherent scattering gives the structural information of the sample.

$$\frac{d\sigma}{d\Omega} = \left(\frac{d\sigma}{d\Omega}\right)_{coh} + \left(\frac{d\sigma}{d\Omega}\right)_{inc} \tag{5.16}$$

The incoherent scattering in a diffraction experiment thus acts as a background, and should be as small as possible. This condition is satisfied for systems just having coherent scatterers such as C, or O. But in the case of strongly hydrogenated samples such as ours (lactulose, $C_{12}H_{22}O_{11}$), a huge incoherent scattering intensity is present in the measured signal. This incoherent scattering intensity comes from H atoms whose incoherent cross-section is huge (σ_{inc} = 80.27(6) barns), compared to the coherent cross-section σ_{coh} = 1.7523(10) barns [243]). This incoherent scattering signal may reach over 90% of the measured signal as seen in the case of light water H_2O [245, 246], and prevents to well visualise the structural information (i.e. the coherent scattering) of interest. Deuteration is usually used in order to reduce the incoherent scattering intensity, since D has a smaller incoherent scattering length compared to H (σ_{inc}(D) = 2.05(10), σ_{coh}(D) = 5.592(6)). But we did not deuterate our system, mainly because it can very easily degrade or mutarotate (see chapter 3). As a consequence, deuteration process could change system properties.

For isotopic ^{1}H hydrogen, the incoherent scattering is only due to the nuclear spins disorder (« spin-incoherent »). As it has been shown by Moon et al. [247], this scattering of the neutrons partially (2/3) reverses their polarisation ("spin-flip", SF), while coherent and isotope incoherent scattering do not ("non-spin-flip", NSF). As a result, the coherent and incoherent scattering cross sections are linear combinations of the spin-flip and non-spin-flip scattering cross sections. In the case of elastic one-scattering events, they are given as follows:

$$I_{coh}(Q) + I_{isotope\_inc}(Q) = I_{NSF}(Q) - \frac{1}{2} I_{SF}(Q) \tag{5.17}$$

$$I_{spin\_inc}(Q) = \frac{3}{2} I_{SF}(Q) \tag{5.18}$$

Using polarised neutrons with polarisation analysis, one can then work around the “high-background problem” and experimentally separate the coherent and incoherent cross sections from two independent measurements of the spin flip and non-spin flip scattering intensities. Recently, this method has been developed on D3 diffractometer [248] and successfully applied to mixtures of light and heavy water [249]. It was thus used in this thesis to get rid of the huge incoherent scattering signal, and the samples were thus not deuterated before the measurements.

The incoherent scattering due to isotopic disorder in Eq. 5.17 can be easily removed by a simple fitting procedure [72, 250].

The different amorphous samples have been measured on two different neutron diffractometers at ILL: D3 and D7. The results obtained are presented below.

5.2.1 Diffraction on D3 diffractometer: short range order

5.2.1.a) D3 instrument

D3 is a two-axis neutron polarised diffractometer (see figure 5.3) initially designed for magnetic structure analysis. It has been recently upgraded for the structure determination of

hydrogenous liquids and glasses, by separating coherent and spin-incoherent scattering.

The neutron beam on D3 comes from the hot beam H4 tube at the ILL, and covers wavelength from 0.4 Å to 0.84 Å. A Heusler polarising monochromator, Cu_2MnAl, single crystal, supplied D3 with a polarised monochromatic beam. Guide fields along the beam path ensure the preservation of the neutron polarisation. A monitor put just before the sample serves to normalise the measured intensities. The neutron polarisation is flipped before the sample using a nutator. Helmholtz coils surround the sample in order to be in a zero magnetic field environment. The ^{3}He spin filter situated just before the single ^{3}He detector absorbs all the non-polarised up neutrons, and only up polarised neutrons are detected. The detector is scanned over a total angular range of 4° to 120°, with typical data acquisition times of 1-2 min/angular step, both polarisation channels being measured at each step.

It is worth mentioning that since the ^{3}He polarisation in the spin filter decays over time, typically losing about 5-10% per day, the analysing power has to be monitored. For this purpose, a silicon single crystal is glued to the top of the sample cell and regularly driven into the beam via a motorised vertical translation. The polarisation of the beam is measured by comparing the SF and NSF intensities of a Si Bragg peak [248].

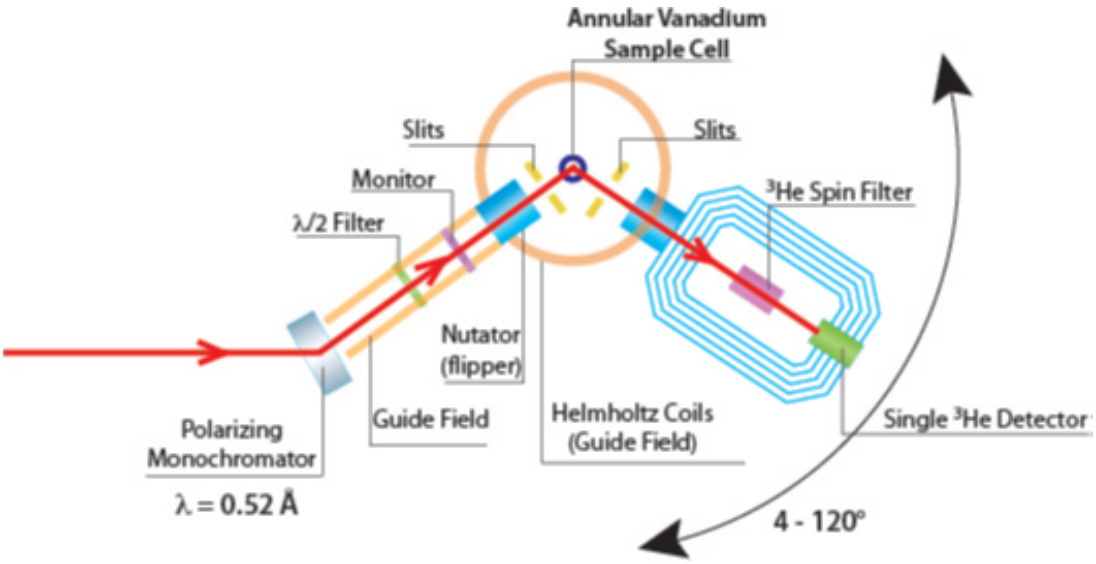

Figure 5.3 – Layout of the D3 diffractometer, modified for the study of hydrogenous liquids and glasses. The scattered neutrons are collected by one detector, which is gradually moved during the experiment in order to cover the different scattering angles. The I(2θ) spectrum is thus measured, and can be further treated to obtain the F(q) scattering function of the sample (see annex B).

5.2.1.b) Experimental details

To investigate the short-range order of the glassy samples, diffraction patterns were measured with a wavelength of λ = 0.52 Å, which yielded to a covered Q-range from 0.8 to 21 $Å^{-1}$. During the experiment, samples were filled into an annular cylindrical vanadium cell, with 1 mm thick annular space. These cells have been chosen to scale down multiple scattering. The measured transmission was between 80% and 85%. For the experiment, five lactulose samples have been measured:

- The anhydrous lactulose crystal
- The quenched from the melted lactulose (QFTM)
- The milled lactulose (MIL)
- The spray-dried lactulose (SD)
- The freeze-dried lactulose (FD)

The QFTM and FD samples were slightly crushed into fine powder, to have the same granulometry than other samples. This approach also ensured that the samples in the beam were of uniform geometry. Each sample was measured at 300 K. Roughly 48 h were needed to collect each diffraction pattern. The data treatment is presented in annex B.

5.2.1.c) Results and discussion

D3 results Figure 5.4 a) shows the static structure factors of amorphous lactulose samples: MIL (red line), QFTM (green line), FD (blue line), SD (pink line). The results do not reveal any remarkable difference of the structure factors S(Q) of the different amorphous samples within the experimental errors. **Although the amorphous compounds have different tautomeric compositions (see chapter 3, table 3.7), they have identical static structure factors**.

The static structure factor of the anhydrous crystal is represented in figure 5.4 b). It resembles very much to that of the amorphous samples, except below 6 $Å^{-1}$ where two peaks are clearly visible at 2.53 $Å^{-1}$ and 3.80 $Å^{-1}$. These peaks are due to the long range order existing in the crystal.

It is worth mentioning that the first peak in all those patterns is not very well defined below 1 $Å^{-1}$. Indeed, on D3, the incident beam comes at low angles and creates an important background, whose subtraction decreases the reliability of the result obtained in this Q-region. Fortunately, this Q-region has been better measured on D7, and will be presented later (see section 5.2.2.c)).

Static structure factors from MD simulations Three lactulose boxes composed of only tautomer A, tautomer B or tautomer C were generated by placing 216 molecules in a pseudo crystal. The boxes were then melted at 700 K during 3 ns in NPT (P = 1 atm) to eliminate any orientational or translational order, and to obtain a liquid. These equilibrated liquids have been subsequently hyper-quenched (from 700 K to 300 K) at 20K/200ps. The obtained boxes were further equilibrated at 300 K, during 5 ns (including 4 ns in NPT (P = 1 atm) followed by 1 ns in NVT) for boxes made of tautomers A and C, and during 7 ns (including 6 ns in NPT (P = 1 atm) followed by 1 ns in NVT) for the box composed of tautomer B. The effective density in the equilibrated boxes was equal to 1.45 g/cm^3 for tautomers A and C, and 1.46 g/cm^3 for tautomer B. Those densities are almost equal to 94%[3] of the density of the crystal, for which there is a good agreement between numerical and experimental values (ρ_{exp} = 1.53 g/cm^3, ρ_{simul} = 1.54 g/cm^3). A MD trajectory of 200 ps with frames saved every 50 fs has been generated from each of those equilibrated boxes. The static structure factor of each tautomer was then obtained using those MD trajectories, by calculating S(Q) every 0.05 $Å^{-1}$ thanks to the following equation:

[3]Experimental measurements on sucrose [251] gave a similar ratio.

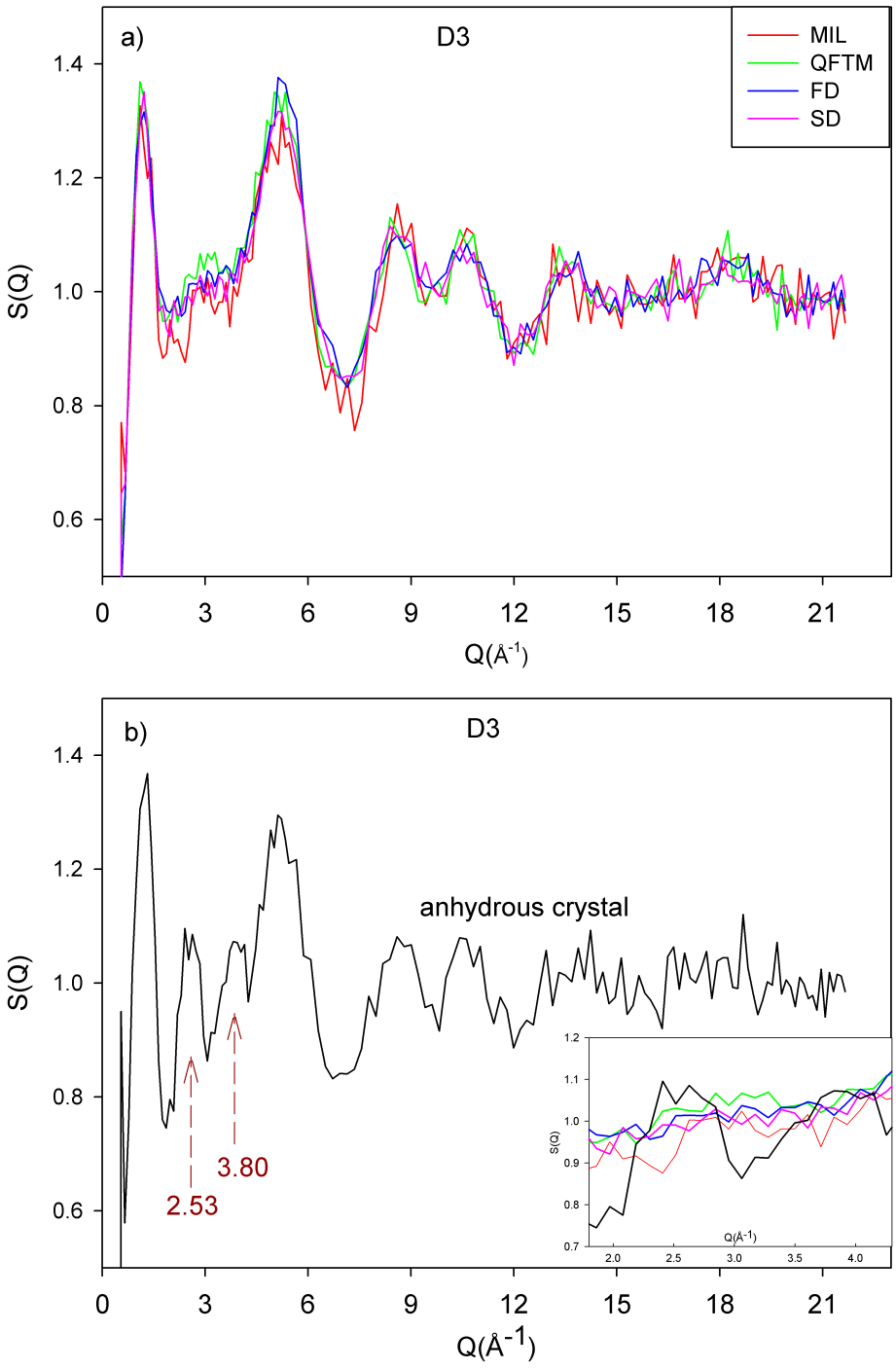

Figure 5.4 – Static structure factors of lactulose samples. Each sample was measured at room temperature on D3, and the measured intensity has been treated to obtain the static structure factors (see annex B). D3 data are not reliable below 1 Å^{-1} (see text for details).
a) The amorphous lactulose patterns are represented: MIL (red line), QFTM (green line), FD (blue line), SD (pink line)
b) The anhydrous crystal pattern (black line) is represented. All the samples are represented in the inset, in the Q-range 1.8 Å^{-1} to 4.3 Å^{-1}.

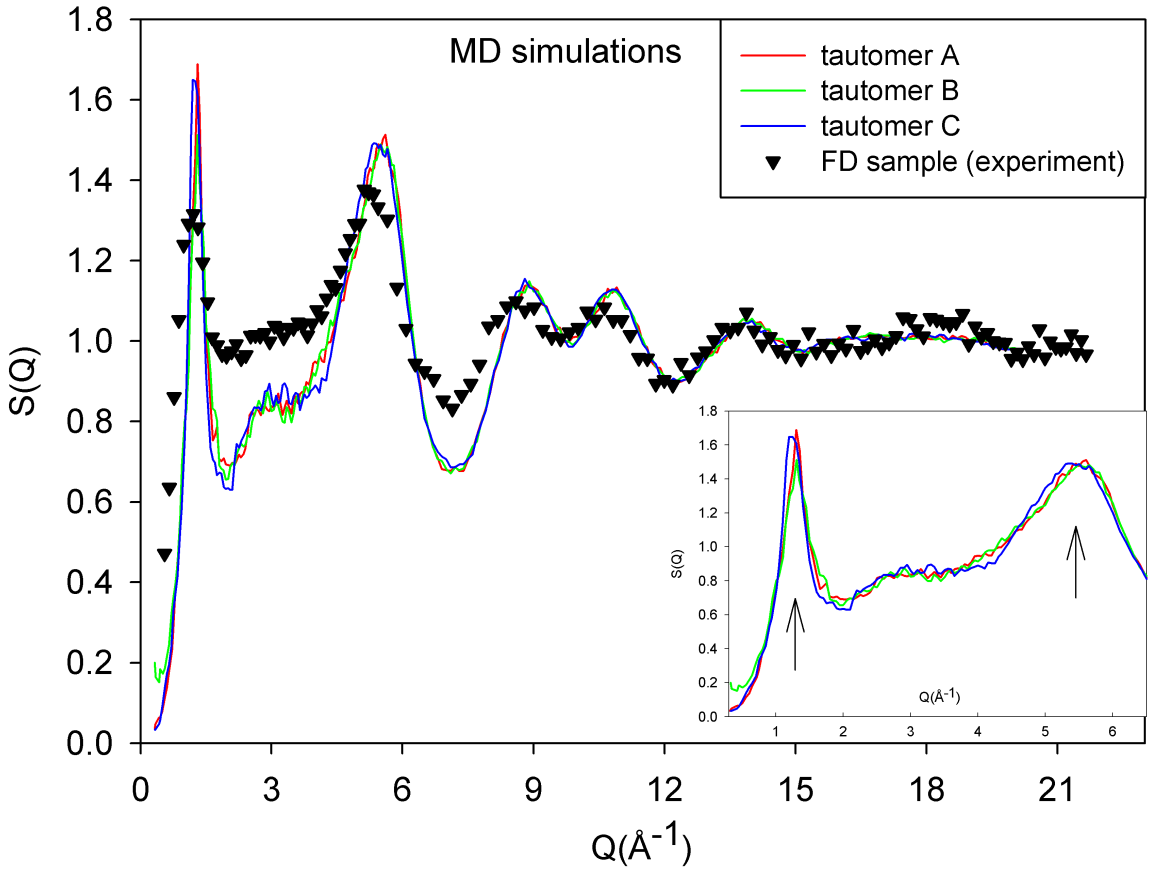

Figure 5.5 – Static structure factors of lactulose tautomer A (red line), tautomer B (green line) and tautomer C (blue line) calculated using Eq. 5.19. The experimental static structure factor of one of the amorphous samples, arbitrary FD sample (black triangles down), is also added for a comparison between numerical and experimental results. The numerical static structure factors are represented in the inset, between Q = 0.3 Å^{-1} and Q = 6.5 Å^{-1}.

$$S(Q) = \sum_{j \neq j'} b_j b_{j'} \exp(iQ(r_j - r_{j'})) \tag{5.19}$$

The results obtained are represented in figure 5.5, and zoomed between Q=0.3 Å^{-1} and Q=6.5 Å^{-1} in the inset: tautomer A (red line), tautomer B (green line) and tautomer C (blue line). The experimental static structure factor of an amorphous sample (black triangles down) is also added for a comparison between numerical and experimental results. Since S(Q) of amorphous samples are similar, we have arbitrary chosen the FD sample.

In the figure, one can notice that:

- Apart from some small differences in height and position of the peaks below 12 Å^{-1}, there is a fairly good agreement between experimental and numerical results, showing realism of MD simulations.

- The static structure factors of the three different tautomers are almost perfectly identical above 6 Å^{-1}, and only slight differences are found below. In particular, there are

some differences in the height and position of the first and second diffraction peaks. Their values have been reported in table 5.1, and show that:

i) **The first peak** is at the same position for tautomer A and B, but at a slightly different position for tautomer C. This difference is probably due to the differences in topology between tautomer C (2 cycles of 6 C) on the one hand and tautomers A and B (1 cycle of 6 C and one of 5 C) on the other hand. Tautomer C molecule is longer than tautomers A and B molecules, and its first sharp diffraction peak (FSDP) is thus at a lower Q. There is also a small difference between the height of the first peak of tautomer B and that of the other tautomers.

ii) **The second peak** is at the same position for tautomer A and B, but at a slightly different position for tautomer C. It is also a direct consequence of the intramolecular differences between the tautomer C on the one hand and tautomers A and B on the other hand.

Table 5.1 – Position and height of the first and second diffraction peaks of the different tautomers. Position and height were determined diectly from the data without fitting procedure.

	1^{st} peak position (Å)	1^{st} peak height (a. u.)	2^{nd} peak position (Å)	2^{nd} peak height (a. u.)
Tautomer A	1.30	1.68	5.58	1.50
Tautomer B	1.30	1.65	5.57	1.48
Tautomer C	1.22	1.51	5.44	1.49

Discussion The diffraction patterns measured on D3 allows probing a large Q-range where two main regions are distinguishable: a low Q-region (below 4 $Å^{-1}$) corresponding mainly to intermolecular correlations and a high Q-region (above 4 $Å^{-1}$) corresponding mainly to intramolecular correlations:

- In the low Q-region, because of the complexity of the molecule, it is difficult to separate inter and intramolecular correlations. Taking into account the size of the lactulose molecule (about 10 Å), pure intermolecular contributions are only expected below Q = $\frac{2\pi}{r}$ = 0.6 $Å^{-1}$. However, as seen on the crystal diffraction pattern, intermolecular correlations are majority below 4 $Å^{-1}$. There are no differences between amorphous samples in this Q-region. In particular, their FSDP (around 1.3 $Å^{-1}$) looks similar. This peak has been better measured on D7 (higher resolution), and the results will be presented later.

- In the high Q-range, intramolecular correlations are in majority. The peaks in this Q-range are identical in the four amorphous samples within the experimental errors. **This means that the eventual modifications in the structure of the molecule itself due to the preparation method are very little to be detectable on D3**. The numerical results obtained (see figure 5.5) show that the small differences in molecular structure of tautomers A and B do not lead to differences (above 4 $Å^{-1}$) on the obtained S(Q). It would therefore be necessary to have more important structural differences to observe differences on the measured S(Q).

5.2.2 Diffraction on D7 diffractometer: medium range order

5.2.2.a) D7 instrument

D7 is a neutron polarised diffuse scattering diffractometer (see figure 5.6) designed to study nuclear and magnetic short range ordered materials [252].

The neutron beam on D7 comes from the H15 cold neutron guide. A vertically and horizontally focusing pyrolytic graphite monochromator selects neutrons of wavelengths of 3.1, 4.8 or 5.8 Å. The beam is polarised using a focusing, m = 2.8 Co/Ti Scharpf bender-type supermirror polariser. A magnetic guide field of around 10–20 G exists everywhere within D7 to ensure that the neutron beam polarisation is efficiently transported through the instrument. The neutron polarisation is manipulated using a Mezei-type flipper, followed by a set of orthogonal xyz field coils situated around the sample position. These coils rotate the incoming beam polarisation in each of the x, y and z directions alternately. The scattered neutrons are analysed by m = 2.8 Co/Ti supermirrors over a 132° angular range. The complete instrument contains over 260 m^2 of supermirror.

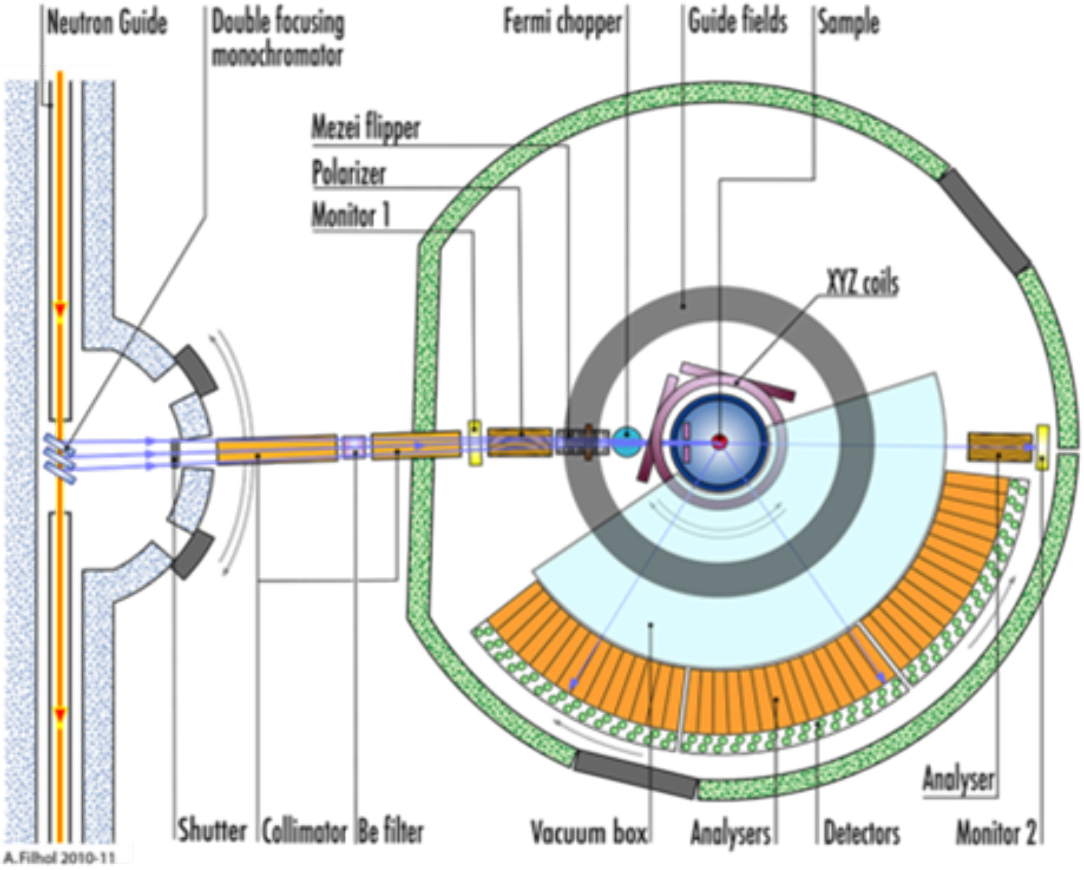

Figure 5.6 – Layout of the diffuse scattering diffractometer D7. The different detectors collect the scattered neutrons. The I(2θ) spectrum is thus measured, and can be further treated to obtain the S(Q) scattering function of the sample (see annex B).

5.2.2.b) Experimental details

An incident wavelength of 4.8 Å was used during the experiment. Samples were filled in flat aluminum cells, with 1 mm thickness, in order to scale down multiple scattering. The mea-

sured transmission was between 80% and 85%. For the experiment, five lactulose samples have been measured:

- The anhydrous lactulose crystal
- The quenched from the melted lactulose (QFTM)
- The milled lactulose (MIL)
- The spray-dried lactulose (SD)
- The freeze-dried lactulose (FD)

The QFTM and FD samples were slightly crushed into fine powder, to have the same granulometry than other samples. This approach also ensured that the samples in the beam were of uniform geometry. Each sample was measured at 300 K. Roughly 2 h were needed to collect each diffraction pattern. The data treatment is presented in annex B.

5.2.2.c) Results and discussions

D7 results Figure 5.7 represents the static structure factors of amorphous and crystalline lactulose samples. The patterns of the MIL (red line), QFTM (green line), FD (blue line), SD (pink line) and anhydrous crystal (black line) lactulose are represented. These patterns have a better resolution than that measured on D3, but are only defined below Q = 2.5 $Å^{-1}$. In figure a), all patterns are superimposed, and in figure b), they are shifted for a better visualisation of each of their specificities. The black line in plots of figure 5.7 b) corresponds to the data smoothed with Savitzky-Golay filter, using a third degree polynomial.

As expected, the first sharp diffraction peak (FSDP) of amorphous samples is broader than peaks in the crystal pattern. Below 1.0 $Å^{-1}$, the pattern of the FD sample is lower than that of the other amorphous samples. This could be an effective density effect. Since the FD sample has higher porosity than the other ones as usually reported [253], it has an effective density much smaller than them.

We have tried to fit the FSDP of all amorphous samples with several functions (Gaussian, Lorentzian, Voigt, pseudo-Voigt), but none of them gave satisfactory results. Therefore, the parameters of those FSDP were directly estimated from the data. In table 5.2, Q_{FSDP} (peak position) corresponds to the Q coordinate of the maximum intensity of the FSDP, A_{FSDP} (peak height) corresponds to the maximum intensity of the FSDP and Δ_{FSDP} (peak width) corresponds to the full width at 60% of the maximum intensity of the FSDP.

From both figure 5.7 and table 5.2, one can notice that:

- The FSDP of the FD sample is broad. It has no bump below 1 $Å^{-1}$.
- The FSDP of the SD sample is almost as broad as that of the FD sample. In addition, it seems to have two bumps at 0.74 $Å^{-1}$ and 0.92 $Å^{-1}$.
- The FSDP of the QFTM sample is sharper than that of the SD and FD samples. In addition, it seems to have one bump at 0.76 $Å^{-1}$.
- The MIL sample has:

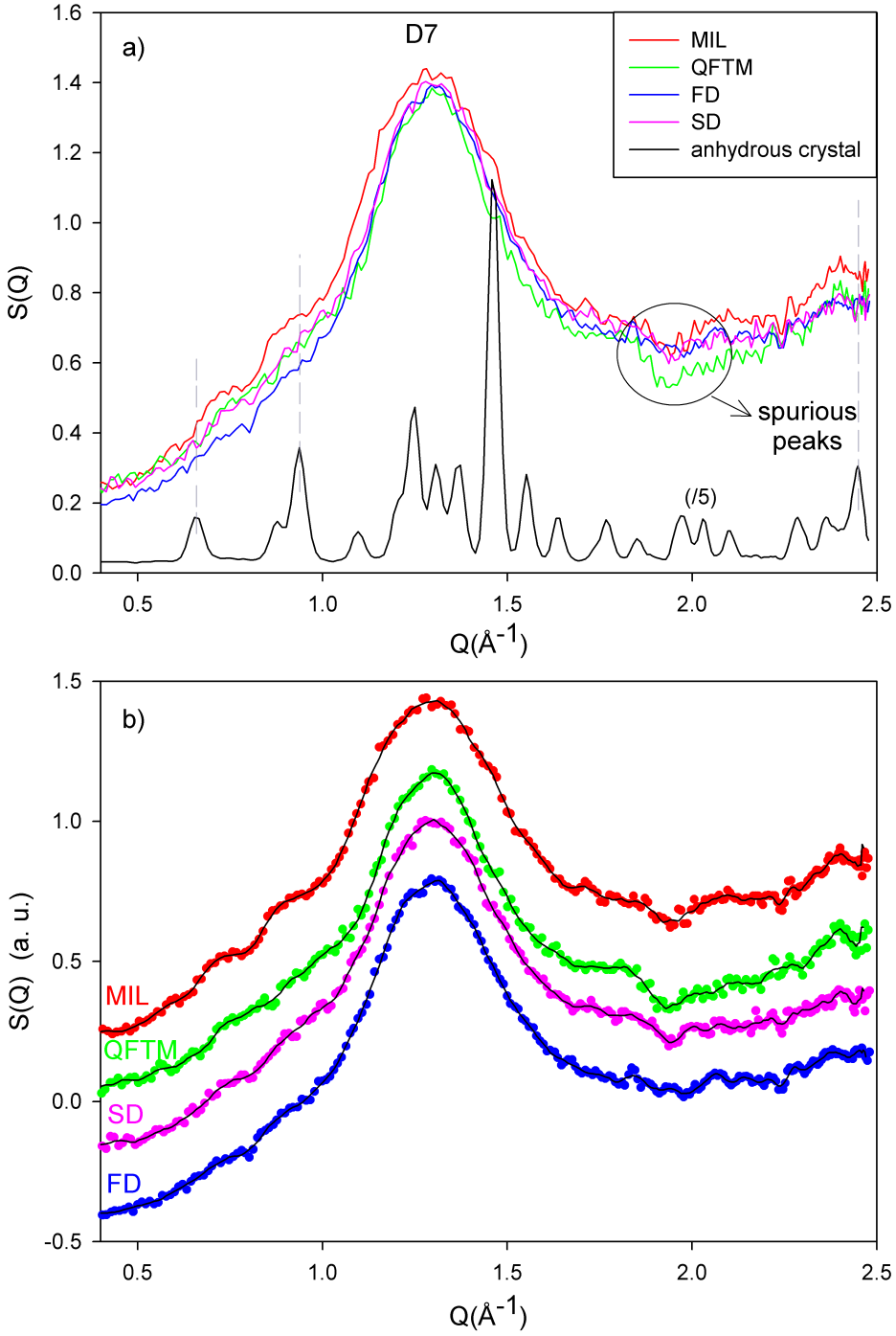

Figure 5.7 – Static structure factors of amorphous and crystalline lactulose samples. Each sample was measured at room temperature on D7, and the measured intensity has been treated to obtain the static structure factors (see annex B). The patterns of the MIL (red line), QFTM (green line), FD (blue line), SD (pink line) and anhydrous crystal (black line) lactulose are represented. In figure a), all patterns are superimposed, and in figure b), they are shifted in order to better visualise each of their specificities.

i) the broadest and highest FSDP.

ii) three bumps at 0.73 $Å^{-1}$, 0.90 $Å^{-1}$, 2.40 $Å^{-1}$, and a shoulder at 1.44 $Å^{-1}$. They are

at Q positions close to Bragg peaks in the crystal pattern. Therefore, it is clearly **the most ordered amorphous sample**.

It can also be noted that all S(Q) have a "hollow" around 1.93 $Å^{-1}$. This is an artefact, due to the fact that the efficiency of the analysers decreases when the incident neutrons become hotter [252].

It is important to remind here that all the amorphous compounds were measured less than 72 h after their preparation, and were kept under vacuum before being measured. DSC and X-ray experiments (laboratory in Lille) done before and after the experiment on D7 showed no evolution of the samples.

In order to understand the differences that the MIL sample shows with respect to the other amorphous samples, we have carried out several analyses whose results are presented below.

Table 5.2 – Position, height and width of the FSDP of the different amorphous samples.

Samples	Q_{FSDP} (peak positon, in $Å^{-1}$)	A_{FSDP} (peak height, a. u.)	Δ_{FSDP} (peak width, in $Å^{-1}$)
MIL	1.30	1.42	0.57
QFTM	1.30	1.37	0.46
FD	1.30	1.38	0.50
SD	1.30	1.39	0.51

Is there any crystalline fraction present in the MIL sample? Investigation by fast DSC A "fast DSC" experiment was performed on the MIL compound in order to get an idea of the crystalline fraction existing in this compound. The advantage of doing fast DSC is that the endotherms and exotherms present in the signal are amplified. Therefore, even very small fractions of crystal melting at T_m would be detectable.

Figure 5.8 shows the thermograms of the MIL lactulose (black line), and a physical mixture containing 97.3% of MIL lactulose and 2.7% of crystalline lactulose (blue line). These thermograms were recorded during heating at 200 °C/min after calorimeter calibration at this rate. Such a high heating rate was used to tentatively reveal a tiny crystalline fraction in the MIL sample.

The two thermograms show a C_p jump at T_g = 110 °C characteristic of a glassy state, which ends by a weak relaxation endotherm. They also have a small endotherm at higher temperatures. Concerning the physical mixture, this endotherm is around 170 °C. and the associated enthalpy is 4.59 J/g. This endotherm therefore roughly corresponds to the melting of the 2.7% of crystal contained in the physical mixture. In the case of the MIL sample, the endotherm is hardly perceptible, and occurs about ten degrees lower. It could correspond to the melting of the residual crystallites depressed because of the small size of these crystallites (Gibbs Thomsom effect [232, 233]). The enthalpy associated with this endotherm (ΔH = 0.39 J/g) indicates the presence of a residual crystalline fraction of about 0.4% in the MIL sample. Such a fraction is probably too small to be detectable by X-ray or neutron diffraction.

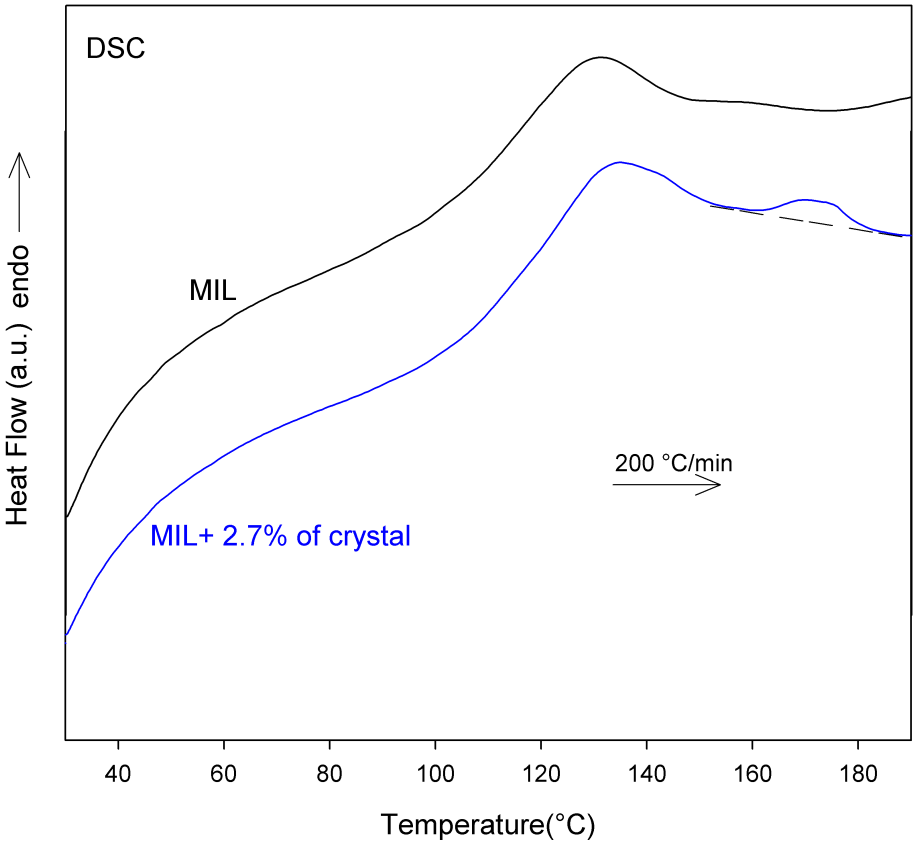

Figure 5.8 – Fast heating DSC scans (200 °C/min) of MIL lactulose (black line) and a physical mixture made of 97.3% of MIL lactulose and 2.7% of crystalline lactulose (blue line).

Region of the diffraction pattern the most impacted by the hydrogen bonds (HBs) network: investigation by MD simulations. The goal of this section is to determine which Q-region of the diffraction pattern is more influenced by the HBs network present in the system. To this end, the total and OH-OH partial (OH is an O atom bonded to a H atom) static structure factors have been calculated in a crystalline box. We have chosen to calculate the OH-OH partial static structure factor since it is the one characteristic of the HBs (the HBs in our samples are mainly O-H…O bonds). Moreover, the calculations were performed in a crystalline box because it has more HBs than an amorphous box, and so effects of the HBs on the static structure factor will be better revealed.

One monocrystalline box containing 648 lactulose molecules has been generated and equilibrated at 300 K during 10 ns, including 8 ns in NPT (P = 1 atm) followed by 2 ns in NVT. A MD trajectory of 200 ps with frames saved every 50 fs, has been generated from this equilibrated box. The total and partial static structure factors were then calculated using this MD trajectory. The results obtained are represented in figure 5.9: total (black line) and OH-OH (red line) static structure factors.

Below 1 $Å^{-1}$, the ratio of the peak height between the partial and the total static structure factors are (only the three main peaks are considered): 47.2% for the peak at 0.65 $Å^{-1}$, 47.5% for the peak at 0.86 $Å^{-1}$ and 63.8% for the peak at 0.97 $Å^{-1}$. Therefore, the peaks below 1 $Å^{-1}$ in experimental diffraction patterns mainly reflect the presence of HBs network in the

measured sample.

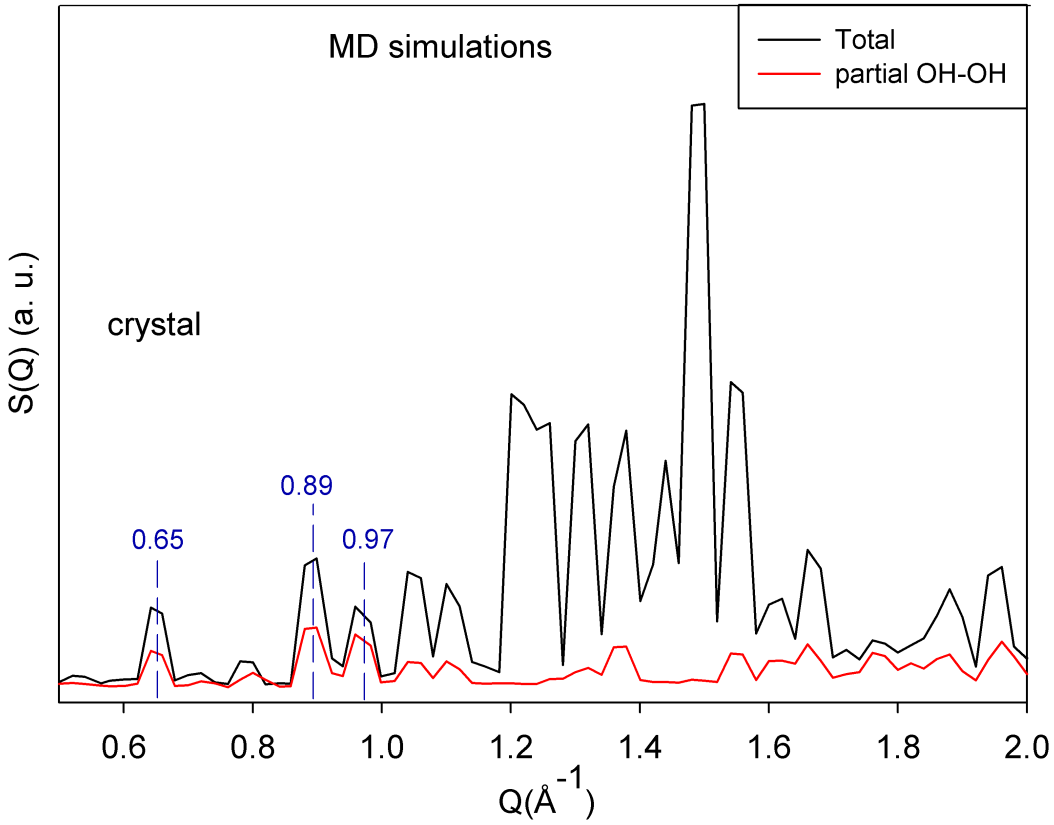

Figure 5.9 – Total (black line) and OH-OH (red line) static structure factors calculated on lactulose molecules. The calculations were performed on an equilibrated MD trajectory of 200 ps.

Milled (MIL) and anhydrous crystal: neutrons vs X-ray Figure 5.10 represents the X-ray (a)) and neutron (b)) diffraction patterns of the MIL and anhydrous crystalline lactulose.

Both X-ray and neutron diffraction patterns of the MIL sample are roughly similar. The FSDP is centred at Q=1.35 $Å^{-1}$ in X-ray diffraction pattern, and Q=1.30 $Å^{-1}$ in neutron diffraction pattern. However, unlike the neutron diffraction pattern, no bump is visible below 1.0 $Å^{-1}$ from the X-ray diffraction pattern of the MIL sample. Moreover, the ratio between the height of the peak at 0.92 $Å^{-1}$ and the main one at 1.45 $Å^{-1}$ present in the diffraction pattern of the crystal is 0.32 for neutron, and 0.25 for X-ray. This means that correlations are more revealed with neutron than X-ray. This is of course due to the fact that the correlations involving H atoms are revealed with neutrons, which is not the case with X-ray. It could explain why there are bumps on the neutron diffraction pattern of the MIL sample, but not on the X-ray one.

Discussion At the medium range [0.5 $Å^{-1}$ - 2.5 $Å^{-1}$], the FD sample appears to be the most disordered amorphous sample. The molecular organisation in this sample may be similar to that in the QFTM sample, but this organisation is more spatially extended in the QFTM

sample (this is why the QFTM sample has the sharpest FSDP). The FSDP widths of the FD and SD samples are close. However, since the FSDP of the SD sample shows in addition two bumps below 1.0 $Å^{-1}$, it may not be true to conclude that FD and SD samples have similar order. The SD sample may well be considered as a mixture of locally ordered structures surrounded by real amorphous phase, the addition of their patterns resulting in a broad FSDP having some bumps (below 1.0 $Å^{-1}$) due to the locally ordered structures.

At the opposite, the MIL sample is the most ordered amorphous sample. The signature of H-bonds molecular association in this sample is the presence of two bumps at scattering vectors Q = 0.74 $Å^{-1}$ and Q = 0.90 $Å^{-1}$ in its diffraction pattern. Those molecular associations also exist in the crystal, on a larger range, and are identified by the Bragg peaks seen at similar Q values in the crystal pattern. Furthermore, the pattern of the MIL sample is the broadest one. Therefore, one may suggest that it is a superposition of a "fully" amorphous sample pattern, and a local order structure pattern. This local order structure is very similar to a crystallite. One can then see the MIL sample as a mixture of local order structures surrounded by fully amorphous phases.

It should be mentioned that we have also performed PDF calculations of the different samples on S(Q) functions obtained after combining the results from D7 and D3. The resulting PDFs did not provide any new information, and will therefore not be presented.

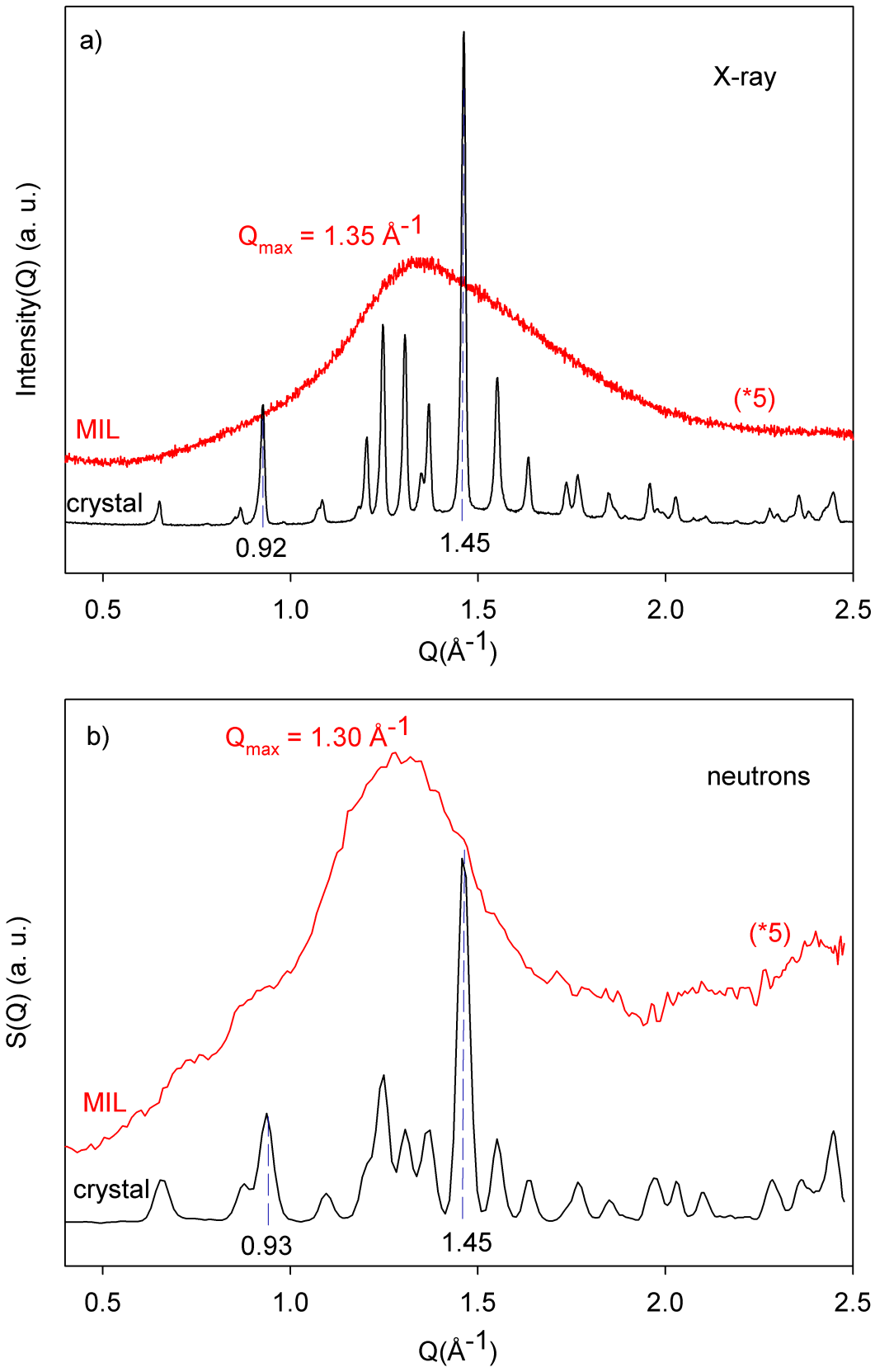

Figure 5.10 – MIL lactulose (red line) and crystalline lactulose (black line) diffraction patterns recorded at room temperature.
a) X-ray diffraction patterns.
b) Neutron diffraction patterns.

5.3 Neutron spectroscopy: instruments and results

Disaccharides have been already measured by INS experiments. Magazu et al. [254] have measured the Boson peak (on IRIS and OSIRIS spectrometers at ISIS, UK) of different trehalose/glycerol mixtures at different glycerol concentrations, in order to get information about the bio-protective effect of glycerol on amorphous trehalose. One year later, they measured (on TOSCA spectrometer at ISIS, UK) the high energy vibrational spectra of the same mixtures [255]. This recent work allows getting specific information about the changes induced by the glycerol on the trehalose H-bonds network. From both experiments, it emerges that the bio-protective effect of glycerol on trehalose is higher at 2.5% content of glycerol. INS spectra of trehalose dihydrate [256], lactose [257], and sucrose [257] have also already been measured.

The different amorphous lactulose samples have been measured on two neutron spectrometers: FOCUS (PSI, Villigen), and IN1-LAGRANGE (ILL, Grenoble). The results obtained are presented below.

5.3.1 FOCUS: instrument, experimental details, and results

The direct geometry spectrometer FOCUS (PSI, Swiss Spallation source, SINQ, Villigen) has been used to investigate collective excitations (1-10 meV) in the different amorphous samples of lactulose.

5.3.1.a) Instrument: principle and description

Principle FOCUS is a direct geometry time of flight (TOF) spectrometer. Direct geometry means that the incident neutrons have a constant energy (wavelength) - generally selected by a crystal monochromator - and the final energy is variable. TOF spectrometer means that the number of neutrons scattered by the sample in a certain solid angle are measured as a function of time. The kinetic energy of each scattered neutron is determined by its time of flight, i.e., the time the neutron takes to cover the sample to detector distance, which can be tracked back to its speed and then its energy. One can thus access the energy transfer $\hbar\omega$ between the neutron and the sample, knowing the initial energy of the neutron.

Description FOCUS (see figure 5.11) is a thermal or cold neutrons spectrometer located at the end of the curved guide RNR 11 of PSI. A « white » beam of neutrons coming from the guide is transported and reduced in a vertically converging neutron guide. The first chopper (pre-selector disc chopper) chops the incident beam and provides long pulses. This chopper also acts as anti-overlap chopper. Afterwards, a horizontally and vertically focusing monochromator (size 18cm × 18cm), made of several single crystals, with variable curvature in both directions makes the beam monochromatic, and focuses it through a Fermi-chopper. Bragg law is used to select the wavelength of the incident neutrons:

$$2dsin(\frac{2\theta}{2}) = n\lambda$$

Where, d is the inter-reticular distance of the monochromator, θ the angle between the lattice planes and the incident neutron beam, n an integer indicating the order of reflection and λ the desired wavelength.

The Fermi-chopper chops the monochromatic beam: it transforms the long pulses into sharp monochromatic flashes of neutrons. Another function of the Fermi chopper is to define the time reference for measuring the travel time of the neutron from the Fermi chopper to the ^{3}He detectors through the sample: the time of flight of the neutrons.

After the Fermi-chopper, the beam hits the sample. The scattered neutrons pass a 2.5 m flight distance through a radial collimator and an argon filled flight box before being detected in 375 ^{3}He counter tubes of rectangular shape. The scattering angle covers a range from 10° to 132°.

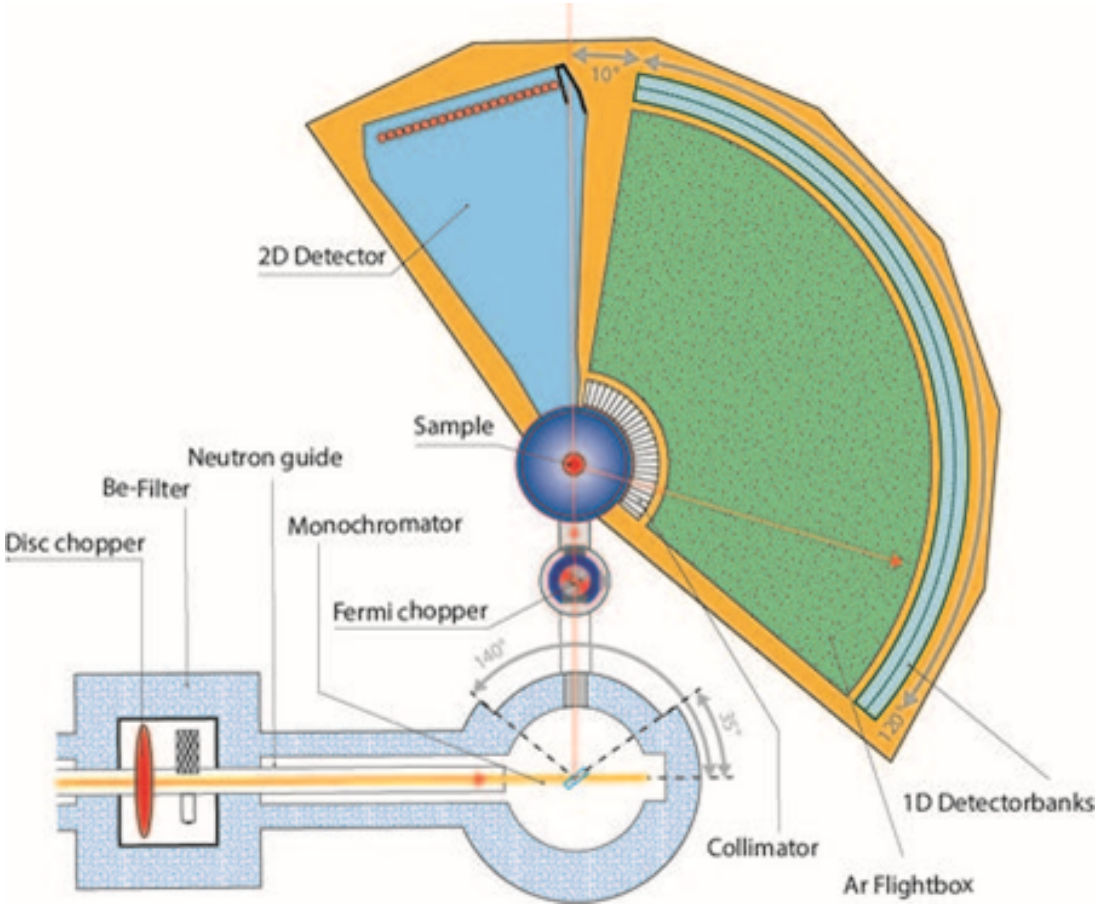

Figure 5.11 – FOCUS instrument layout. The detectors at different angles collect the scattered neutrons as a function of their TOF. The I(2θ,TOF) spectrum is thus measured, and can be further treated to obtain the S(Q,ω) scattering function of the sample (see annex B).

5.3.1.b) Experimental details

A pyrolytic graphite monochromator was used to select incident neutrons of wavelength 4.8 Å. This corresponds to an elastic peak around 538 microsecond at each detector of the instrument. Thanks to a vanadium spectrum measurement, the energy resolution (FWHM) of the instrument in this configuration was measured to 0.1 meV.

Figure 5.12 shows the kinematical range (Q,ω) covered on FOCUS instrument during our experiment.

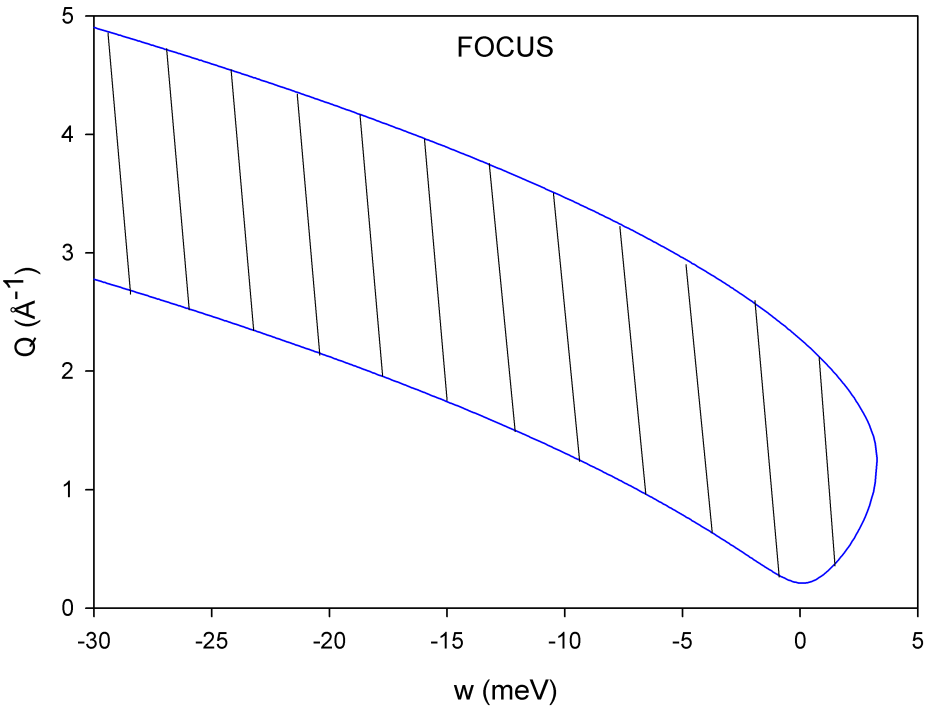

Figure 5.12 – The hatched area represents the kinematical range covered during the INS experiment on FOCUS, using an incident wavelength of 4.8 Å.

One can see that the kinematical range starts above Q = 0.2 $Å^{-1}$. Moreover the elastic signal is not seen over the whole range in Q. It is just between 0.2 $Å^{-1}$ and 2.3 $Å^{-1}$.

During the experiment, samples were filled in flat aluminum cells 40*47 mm^2 with 1 mm thickness. These cells have been chosen to scale down multiple scattering. The measured transmission was between 80% and 85%. For the experiment, five lactulose samples have been measured:

- The anhydrous lactulose crystal
- The quenched from the melted lactulose (QFTM)
- The milled lactulose (MIL)
- The spray-dried lactulose (SD)
- The freeze-dried lactulose (FD)

The QFTM and FD samples were slightly crushed into fine powder, to have the same granulometry than other samples. This approach also ensured that the samples in the beam were of uniform geometry. Each sample was measured at two different temperatures (100 K and 200 K), besides the SD sample for which we have experienced a technical problem during the measurement at 100 K. Roughly 6 h were needed to collect each spectrum. The data treatment is presented in annex B.

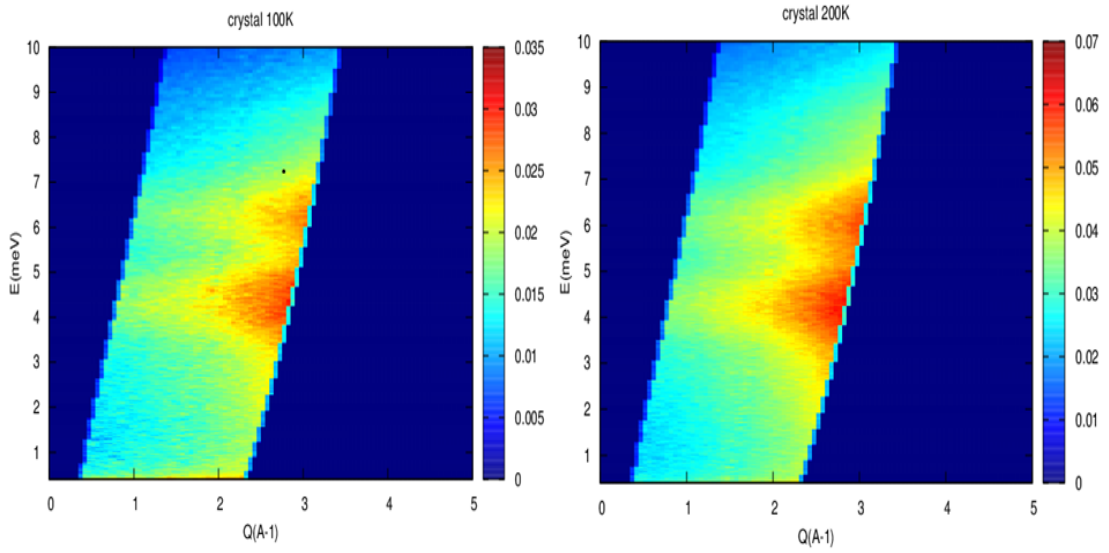

(a) Crystal, 100K

(b) Crystal, 200K

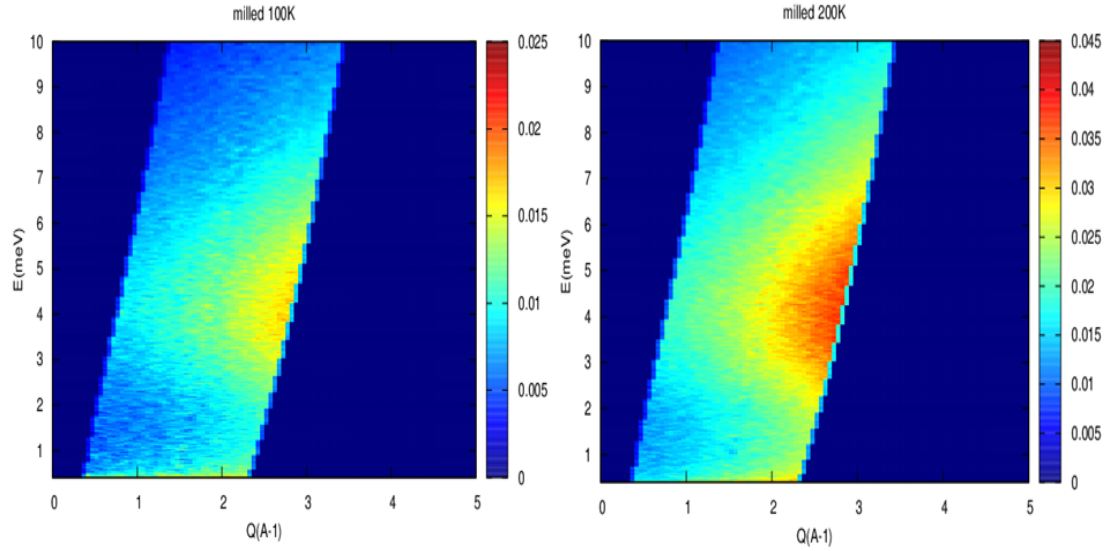

(c) MIL, 100K

(d) MIL, 200K

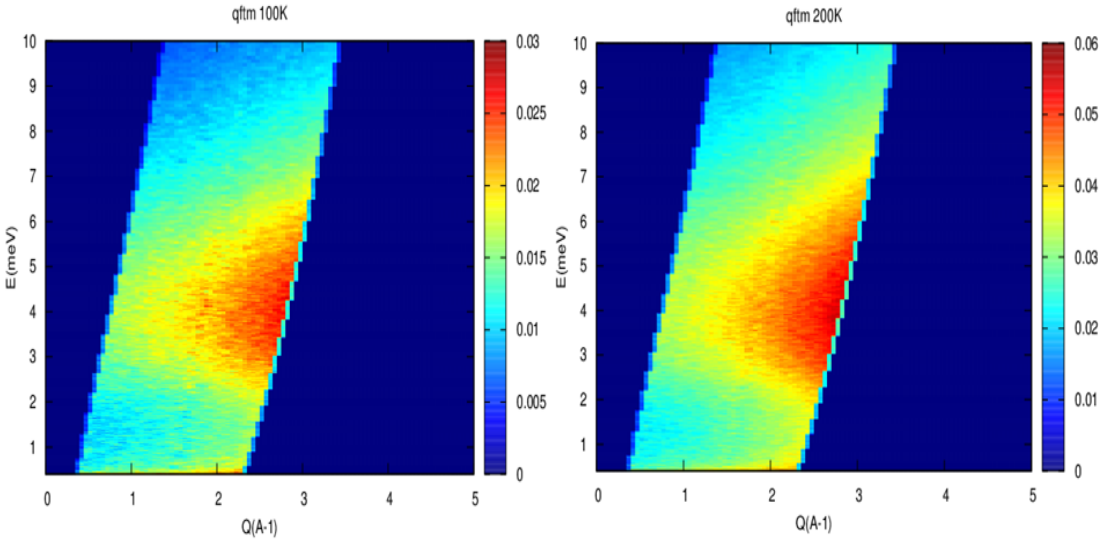

(e) QFTM, 100K

(f) QFTM, 200K

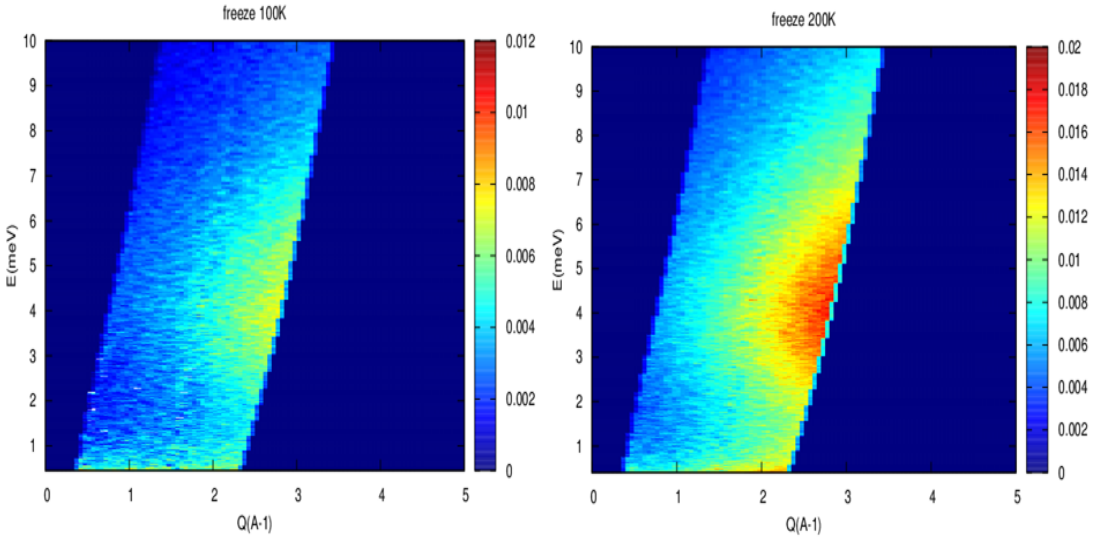

(g) FD, 100K **(h) FD, 200K**

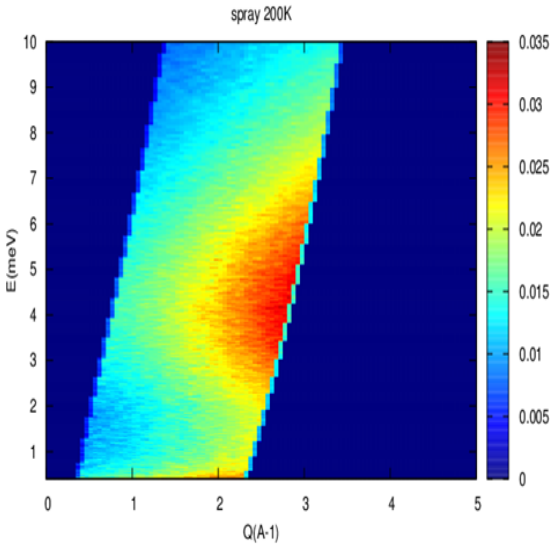

(i) SD, 200K

Figure 5.13 – Contour maps representing the incoherent dynamic structure factor S(Q,ω) of five different lactulose samples. Each sample has been measured at two different temperature (besides the SD sample) on FOCUS, and the measured intensity has been treated to obtain the incoherent dynamic structure factor S(Q,ω) (see annex B). Plots on the left are those of the samples measured at 100 K, and on the right those of the samples measured at 200 K. From top to bottom: the crystal, the MIL, the QFTM, the FD and the SD.

5.3.1.c) FOCUS results

Figure 5.13 represents the incoherent dynamic structure factor S(Q,ω) of five different lactulose samples: the anhydrous crystal, the MIL, the QFTM, the FD and the SD. The intensity of the map is given by the amplitude of the incoherent dynamic structure factor S(Q,ω). All the plots are represented from ω = 0.4 meV, in order to hide the elastic line, and thus to well visualise the phonons in the different samples.

In the figure, one can see:

- The dynamical range covered on the FOCUS instrument. All the dark blue area is the range not covered on the FOCUS instrument.
- That the amplitude of the contour map on the different samples is not the same. This is mainly due to the fact that we were not able to fill the same amount of sample in the containers, because samples do not have the same texture.
- Two clear humps, characteristic of two different « family » of phonons on the crystal dynamic structure factor. For all the amorphous samples, there is just one broad hump, characteristic of one « family » of phonons.

By doing MD simulations, we have tried to identify the atoms involved in the motions responsible of the two different « families » of phonons that were seen on the crystal. Positions of the particles were extracted from MD simulations and used to calculate the time-dependent dynamic structure factor S(Q,t). This function was further Fourier transformed to obtain S(Q,ω). The Fourier transform induces some errors on the result, and the S(Q,ω) obtained was not similar to that measured on FOCUS.

5.3.1.d) The density of states: experiment and MD simulations

First of all, it is important to clarify the difference between the density of states measured by INS, and the one calculated by MD simulations.

On the one hand, the density of states measured by INS is the generalised density of states (GDOS). It is a density of states weighted by the neutron scattering cross sections. For highly hydrogenated compounds such as lactulose, this density of states is mainly due to H atoms. GDOS(ω) has been calculated from the inelastic incoherent scattering function $S_{inc}(Q,\omega)$ by averaging it over the full accessible Q-range (it is the angle average approximation; this approximation is good for mainly incoherent scatterer) [254, 258]:

$$\mathrm{GDOS}(\omega) = \int_{\mathrm{all\,Q}} \left(\frac{\omega}{\mathrm{Q}^2} \frac{1}{n(\omega,\mathrm{T}) * \mathrm{DW}} \right) * \mathrm{S}_{inc}(\mathrm{Q},\omega) d\mathrm{Q} \tag{5.20}$$

where n(ω,T) is the temperature Bose factor, DW the Debye Waller factor, and $S_{inc}(Q,\omega)$ the inelastic incoherent scattering function.

On the other hand, the density of states calculated by MD simulations is the vibrational density of states (VDOS). It is obtained by a Fourier transform of the velocity autocorrelation function. In order to have a density of states comparable with the experimental one, the calculations were performed taking into account only velocities of H atoms. Therefore, VDOS(ω) is calculated using the following equation:

$$\mathrm{VDOS}(\omega) = \int_0^{\infty} (< v_{\mathrm{H}}(t).v_{\mathrm{H}}(0) >) \exp(i\omega t) dt \tag{5.21}$$

where v_H is the velocity of H atoms.

Figure 5.14 shows the GDOS of the four amorphous lactulose (MIL, QFTM, FD, SD) and the anhydrous crystal. The results of the measurement at 100 K (figure a)) and 200 K (figure b)) are represented. The total number of states was normalised to unity in the energy range 0 to 25 meV. There is a spurious peak around ω = 0.05 meV coming from the elastic signal.

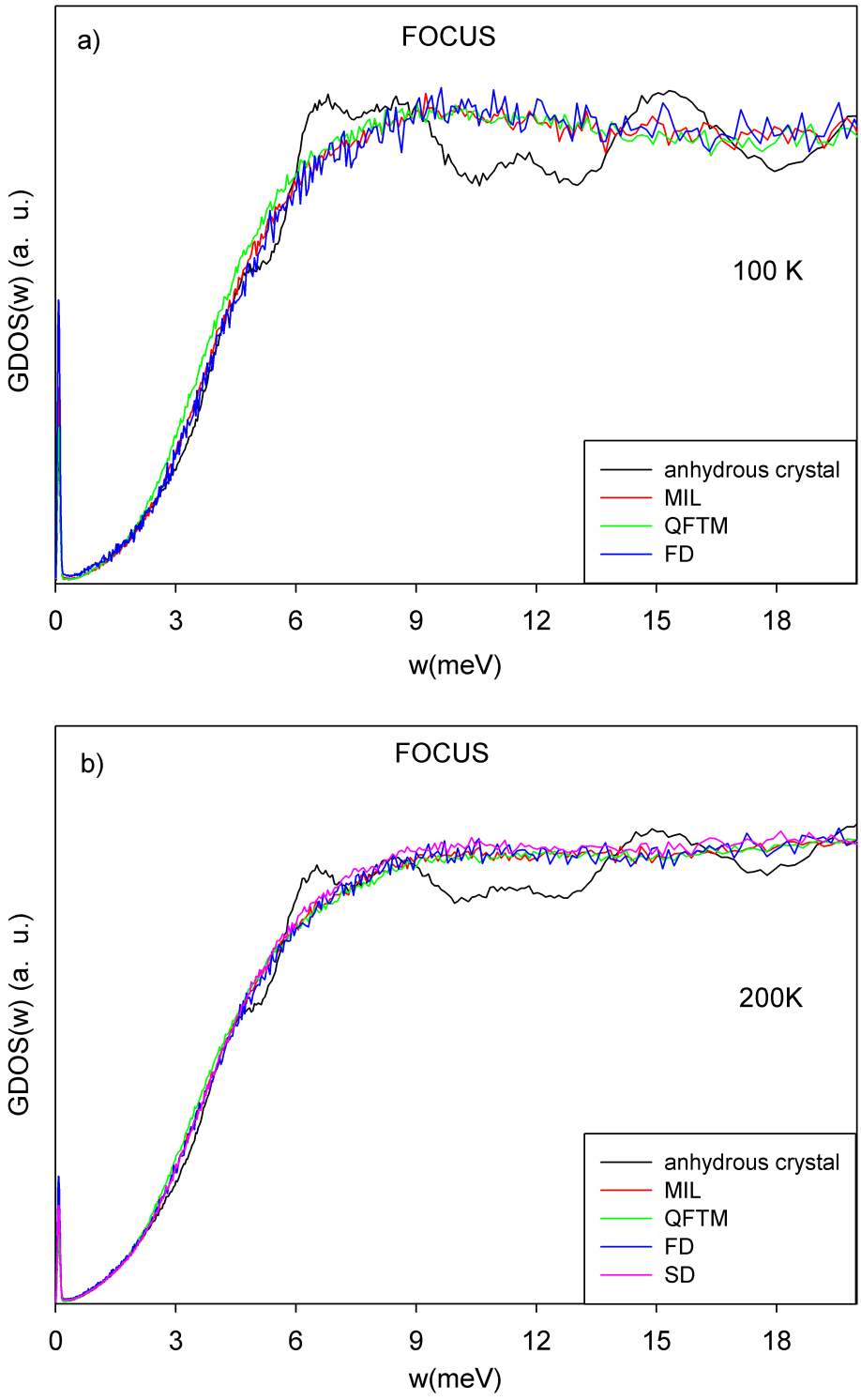

Figure 5.14 – GDOS of the MIL lactulose (red line), QFTM lactulose (green line), FD lactulose (blue line), SD lactulose (pink line) and the anhydrous crystalline lactulose (black line).
a) All the samples (besides the SD lactulose) measured at T= 100K.
b) All the samples measured at T = 200K.
The spectra were normalised to unity in the energy range 0 to 25 meV. There is a spurious peak around ω = 0.05 meV coming from the elastic signal.

In the figure, one can notice that the GDOS(ω) of the four amorphous samples (QFTM, MIL, FD and SD) are very similar. Furthermore:

- Above 6 meV, the curve of the crystal is more structured than that of the amorphous samples. It is the consequence of the long-range order present in the crystal, where phonon modes do not « merge » as in the case of amorphous samples. The humps seen are more amplified at 100 K than at 200 K.

- Between 2 meV and 6 meV, the curves of the amorphous samples are above that of the crystal. This means that amorphous samples have more vibrational modes than the crystal in this energy range. This is more important at 100 K than at 200 K.

To better visualise the excess of vibrational modes present in the amorphous samples compared to those predicted by the Debye theory [82, 83], it is usual to plot the reduced density GDOS(ω)/ω^2 function. This will be done in the next section. Looking at the plot of GDOS functions, the Debye theory should hold true up to 6 meV.

One crystalline box composed of 224 lactulose molecules was generated and equilibrated during 5 ns, including 4 ns in NPT (P = 1 atm) followed by 1 ns in NVT. The initial box was equilibrated both at 100 K, and at 200 K. One amorphous box composed of 240 lactulose molecules was generated after hyper-quenching (from 700 K to 300 K) an equilibrated liquid box at 20K/200ps. This amorphous box was further equilibrated at 100 K and 200K, in the same conditions than the crystalline one. A MD trajectory of 20 ps with frames saved every 2 fs was generated from each of those equilibrated boxes. The VDOS were then calculated using those MD trajectories, by a Fourier transform (FT) of the velocity autocorrelation function of H atoms. The low rate of frames saving (2 fs) was chosen in order to avoid aliasing effect during the FT calculation [162].

The results obtained at 100 K and 200 K were very similar. We have thus chosen to only show the results obtained at 100K (see figure 5.15). In figure 5.15, the black line represents the VDOS calculated in the crystalline box, and the green line that calculated in the amorphous box. The GDOS of the anhydrous crystal (black triangle down) and of one the amorphous samples (green triangle down) are also represented for a comparison between numerical and experimental results. Since GDOS(ω) of amorphous samples are similar, we have arbitrary chosen the FD sample.

In the figure, one can notice that:

- Between 2 meV and 6 meV, the VDOS of the amorphous sample and the crystalline one are almost superimposed. It was therefore not possible to reproduce the experimental findings (i.e., GDOS of the amorphous samples higher than that of the crystal).

- The shape of the numerical curves is roughly similar to that of the experimental ones, but the agreement is not that good. For example, the humps in the GDOS of the crystal are not seen in its VDOS.

5.3.1.e) The Boson peak

Figure 5.16 shows the reduced GDOS of the four amorphous lactulose (MIL, QFTM, FD, SD) and the anhydrous crystal. In the figure one can notice that:

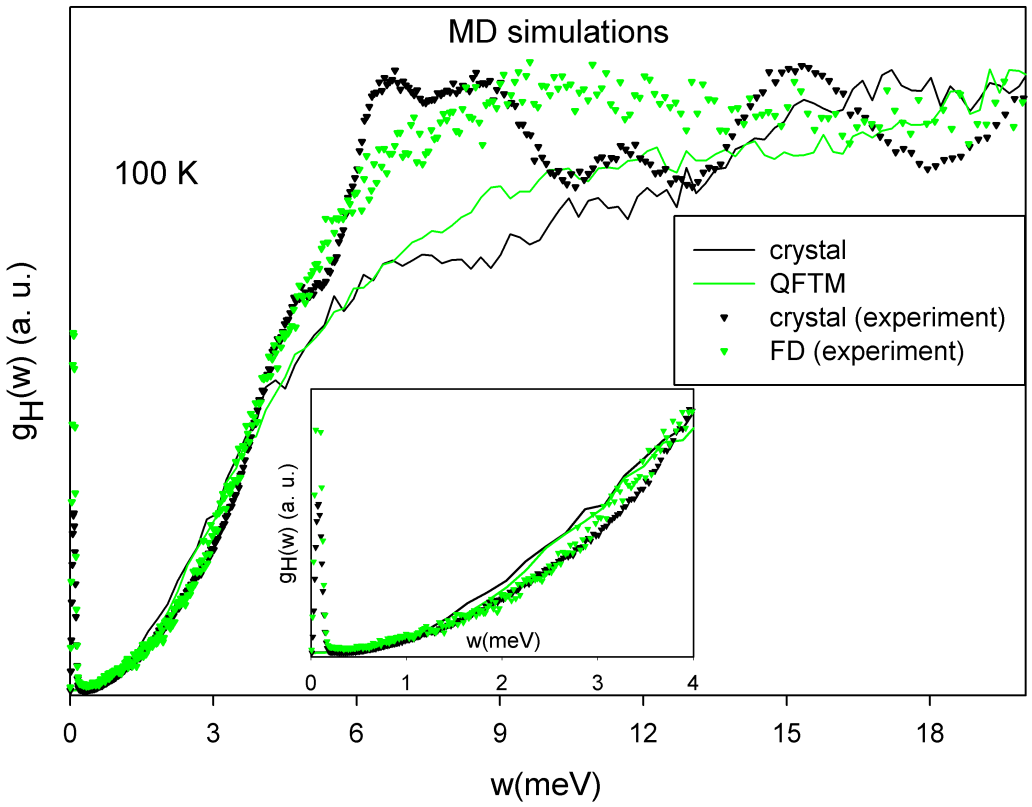

Figure 5.15 – VDOS of the QFTM lactulose (green line) and the anhydrous crystalline lactulose (black line) calculated by MD simulations. The calculations were performed at 100 K on an equilibrated MD trajectory of 20 ps. The GDOS of the anhydrous crystal (black triangles down) and one of the amorphous samples, arbitrary FD sample (green triangles down), are also added for a comparison between numerical and experimental results. All the spectra are represented in the inset, between ω = 0.0 meV and ω = 4.0 meV.

- Between 2 meV and 4 meV, the curves of all the amorphous samples show a hump. This means that amorphous samples have excess of the VDOS compared to that predicted by the Debye theory. This excess of the VDOS is named Boson peak (BP).

- The BP intensity of the QFTM is higher compared with the other amorphous samples. This is more important at 100 K than at 200 K. This result is in contradiction with Angell results [259], which showed for a glass of $PbGeO_3$ that the BP intensity of the MIL is higher than that of the QFTM (see figure 5.17). As it will be later seen, the increase of the BP intensity of the QFTM lactulose sample may be due to degradation.

- At 200 K, the BP of the MIL, FD and SD lactulose are identical within the experimental error bars. The BP frequency is around 3.42 meV.

- At 100 K, the BP frequencies of the MIL and FD lactulose are identical within the experimental error bars. The BP frequency is around 3.97 meV.

- The crystal also has an excess scattering over the Debye expectation. This excess occurs at somewhat higher frequency (around 4.1 meV at 200 K, and 4.3 meV at 100 K)

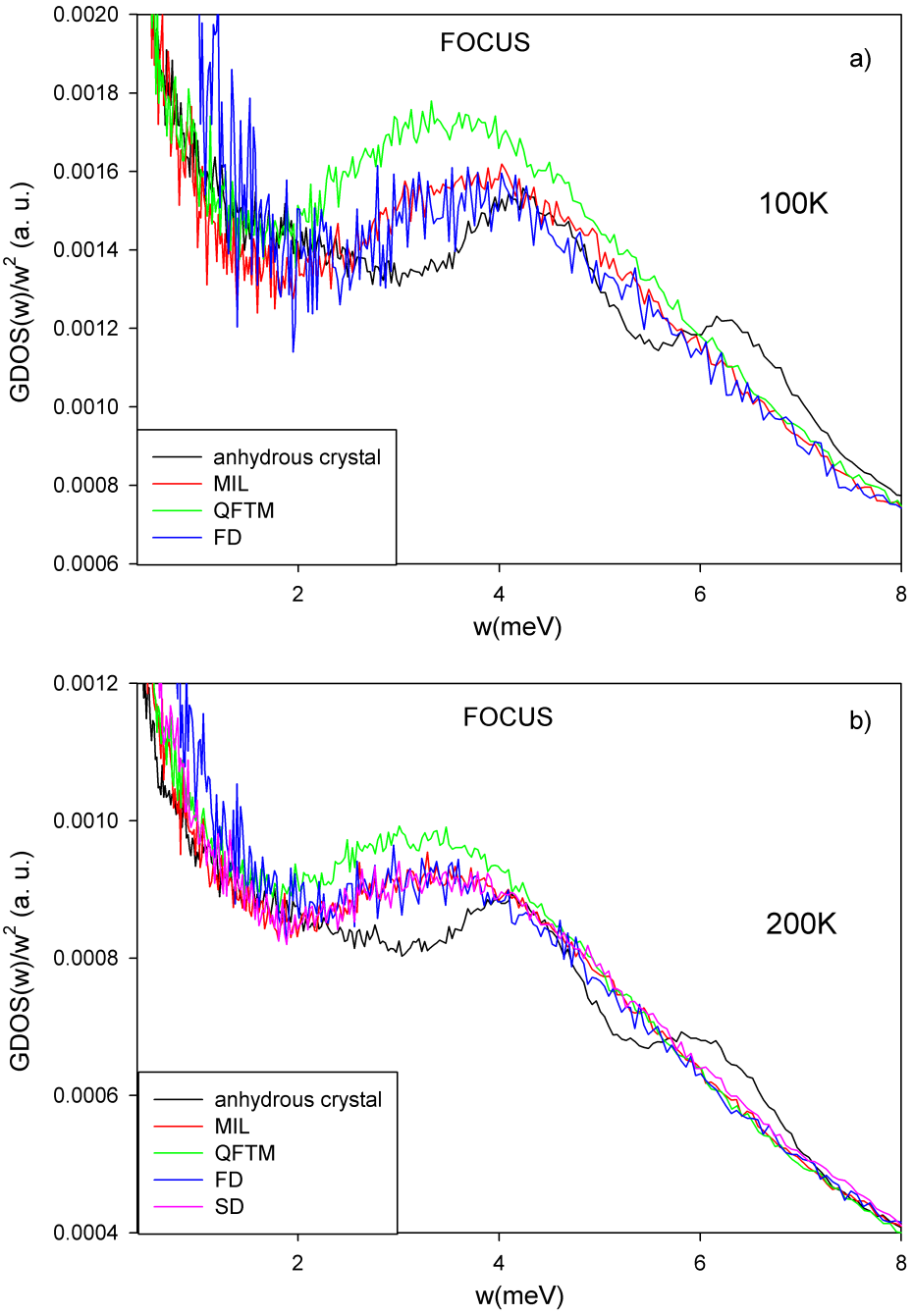

Figure 5.16 – Reduced GDOS (GDOS(ω)/ω^2) of the MIL lactulose (red line), QFTM lactulose (green line), FD lactulose (blue line), SD lactulose (pink line) and the anhydrous crystalline lactulose (black line).
a) All the samples (besides the SD sample) measured at T = 100 K.
b) All the samples measured at T = 200 K.
None of the results has been scaled by the temperature Bose factor.

compared to the amorphous samples. Crystalline glass formers are pre-disposed to become defective since they usually have poor lattice energies, and this may be the reason why the crystal also shows an excess VDOS [259, 260].

All the motions involved in the excess of the GDOS are between 2-4 meV, which means that they typically take place within 1 ps.

NB: The hump at 6.3 meV in the plot of the crystal comes from an increase of the number of phonons in that energy region as seen in figure 5.14 of the GDOS, and is probably not to consider as an excess of vibrational modes compared to that predicted by the Debye theory.

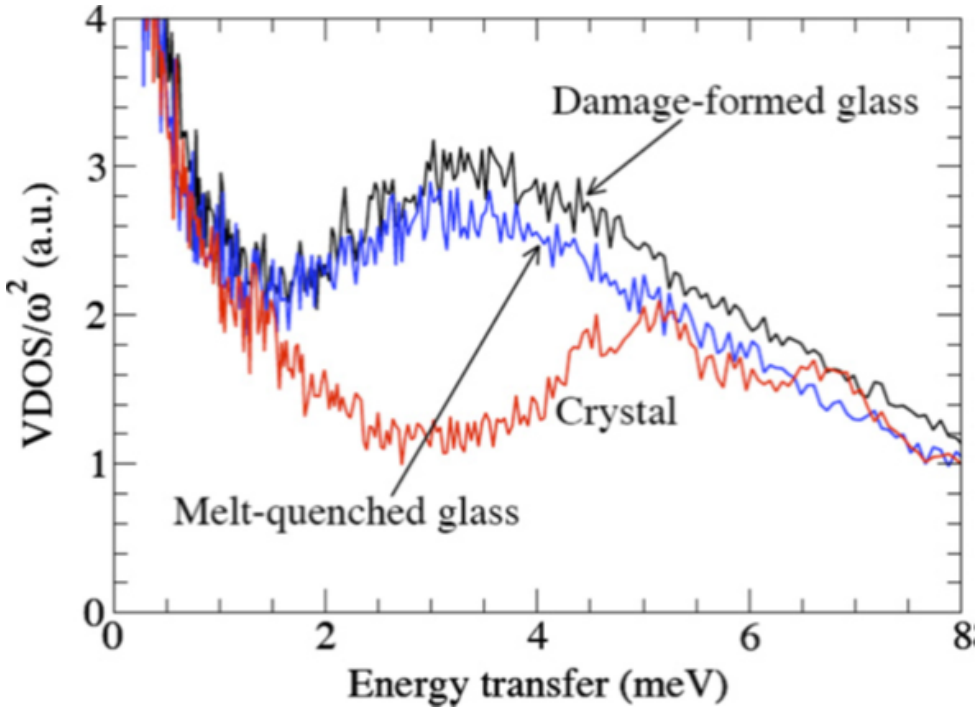

Figure 5.17 – Reduced GDOS of the crystal, melt-quenched glass and damage-formed glass of $PbGeO_3$. Taken from [259].

Effect of degradation on the QFTM density of states: investigations by MD simulations
The purpose of this section is to determine how the thermal degradation affects the BP.

It is quite difficult to determine the BP by MD simulations. This is mainly due to the fact that there are a lot of spurious peaks on the graph of the reduced VDOS, due to size effects [98]. To attenuate them considerably and to thus obtain a reasonable BP, the simulation must be performed on a rather large box. After performing some tests, we found that it is necessary to have at least 72,000 atoms in the box, i.e., more than 1600 molecules, to obtain a reasonable BP.

As a reminder, the thermal degradation of lactulose is a complicated process [261]:

- Lactulose can hydrolyse to its constituent monosaccharides fructose and galactose.
- Lactulose or its released monosaccharides equilibrate with their ring-opened isomers and the α-hydroxyl can air oxidize to produce an α-dicarbonyl.
- As all sugars, lactulose can also oligomerise to produce a variety of viscous products (caramel).

To estimate how degradation affects BP, two different amorphous boxes were generated:

- The first, composed of 2600 lactulose molecules, was generated after hyper-quenching (from 700 K to 100 K) an equilibrated liquid box at 20K/200ps.

- The second, composed of 1300 lactulose molecules, 1300 fructose molecules and 1300 galactose molecules, was generated after hyper-quenching (from 700 K to 100 K) an equilibrated liquid box at 20K/200 ps. This second box was considered as "degraded lactulose" although the real degraded sample is clearly more complex.

The two boxes were equilibrated at 100 K during 10 ns, including 8 ns in NPT (P = 1 atm) followed by 2 ns in NVT. A MD trajectory of 20 ps with frames saved every 2 fs was generated from each of those equilibrated boxes. The VDOS were then calculated using those MD trajectories, by a Fourier transform of the velocity auto-correlation function of H atoms. It is worth mentioning that the simulations were performed at 100 K in order to better reveal the BP, whose amplitude is always higher at low temperature.

Figure 5.18 represented the reduced VDOS calculated in the two previous boxes. The black line represents the result on the QFTM lactulose (first box), and the red line represents the result on the QFTM degraded lactulose (second box). The spectra are represented between 0.4 meV and 8 meV.

One can notice that:

- The simulation roughly reproduces the experimental results. However the BP seen from MD simulations is significantly less defined than that seen experimentally, and appears at lower energy (ω_{simul} = 2.8 meV, ω_{exp} = 3.97 meV).

- The QFTM degraded curve is above that of the QFTM. This means that there are more low-energy vibrational modes in the degraded system. Degradation thus probably plays a role in the increase of the BP intensity of the QFTM sample compared to that of the other amorphous samples, as it has been seen on the FOCUS results.

NB: In the inset, the reduced VDOS calculated in a QFTM box having 216 molecules (blue line) is compared with that of the QFTM having 2600 molecules (black line). It can be seen that with N = 216 molecules, there is no BP, and a lot of spurious peaks. With N = 2600 molecules, a bump emerges, even though there is still a spurious peak at ω = 0.84 meV. All those spurious peaks are size effects since they tend to finish while increasing box size. The bump seen with N = 2600 molecules corresponds to BP, and could be better defined for N $\gg$ 2600.

Comparison of the BP of the different samples It is difficult to compare the BP of the QFTM sample with those of the other amorphous samples, since it is highly influenced by the degradation that occurs during its preparation. Therefore, only the results obtained on the MIL, FD and SD samples will be compared. This comparison mainly shows that the three amorphous samples (MIL, FD and SD lactulose) have identical BP, even though they do not have the same tautomeric composition. This means that the BP is due to local (non-propagating) vibrations. It is a general feature of the BP [99, 101, 262]. From 100 K to 200 K, the BP differences are only due to the temperature Bose factor.

5.3.2 IN1-LAGRANGE: instrument, experimental details, and results

The IN1-LAGRANGE (Institut Laue-Langevin, Grenoble) spectrometer [263] has been used to measure high-energy vibrations (20-450 meV) in the different lactulose amorphous samples.

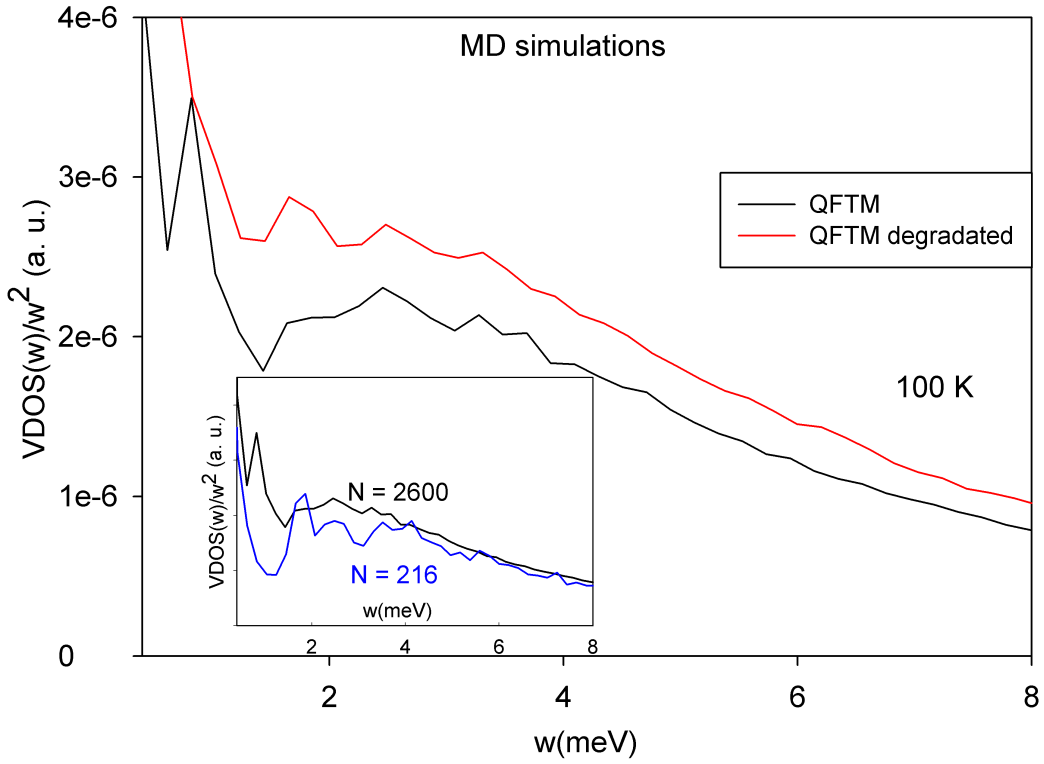

Figure 5.18 – Reduced VDOS of the QFTM lactulose (black line), QFTM degraded lactulose (red line) determined by MD simulations. The calculations were performed on an equilibrated MD trajectory of 20 ps. The spectra are represented between 0.4 meV and 8 meV. In the inset, the reduced VDOS calculated in a QFTM box having 216 molecules (blue line) is compared with that of the QFTM having 2600 molecules (black line).

5.3.2.a) Instrument: principle and description

Principle IN1-LAGRANGE (Large Array GRaphite ANalyser for Genuine Excitations) is an inverse geometry spectrometer. The final energy (energy of the neutron after scattering by the sample) detected is constant (E_f = 4.5 meV), and the incident energy E_i varies in a wide energy range. It is a continuous « point-by-point » spectrometer, since the instrument changes its configuration at each incident energy step (E_i) to select a different value. The energy transfer $\hbar\omega$ corresponding to an excitation energy in the sample is obtained by a subtraction of the final energy E_f from the energy E_i of the incident monochromatic neutrons.

Description IN1-LAGRANGE (see figure 5.19) is located on the hot beam H8 tube at the ILL. A large double-focusing multi-face crystal monochromator supplies the LAGRANGE spectrometer with a monochromatic beam in the intermediate and high neutron energy ranges (a mosaic Cu220 or Cu331 crystal faces can be used to select the incident energy), and also in the lower energy range (the incident energy is selected using Si111 or Si311 monochromator). The incident energy E_i is selected following the Bragg law, and depends on the angle between the monochromator face and the sample, and also on the inter-reticular distance of the monochromator.

Then the monochromatic beam hits the sample. A cold Be-filter is placed after the sample and it filters the scattered neutrons with energy less than 5.2 meV. In that way, the high order reflections of the crystal analysers are removed. Afterwards, a large area space focusing crystal analyser focuses them onto the detector. This analyser is a 1 m^2 reflecting surface built around the vertical sample-detector axis with 612 pyrolytic graphite (PG) crystals, and set to reflect neutrons with a fixed final energy of 4.5 meV. The focused scattered neutrons are thus recorded with a small single counter (a ^{3}He gas detector).

A carefully designed B_4C screen is installed on the sample detector axis in order to absorb the elastically scattered neutrons from the sample. Supplementary diminution of the instrument background, polluted by the high neutron energy components, is achieved through massive polyethylene shielding built around the whole analyser.

It is worth mentioning that there is no Q-dependence on the scattering signal measured on this spectrometer, because the « small » Q domain available to the instrument at each energy transfer is integrated at the detector, thus giving an intense signal. Therefore, the intensity measured during the experiment is directly the generalised density of vibrational states GDOS(ω).

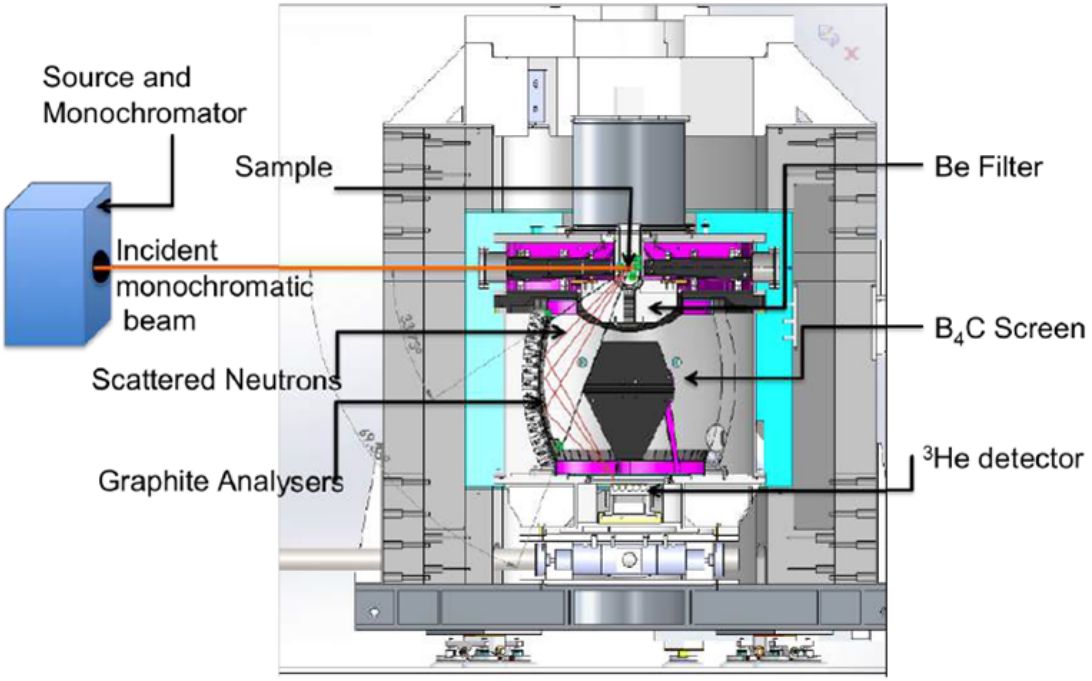

Figure 5.19 – Vertical cut of the LAGRANGE spectrometer: the scattered neutrons with final energy of 4.5 meV are focussed to the ^{3}He detector by the arrangement of HOPG analyser mounted on an ellipsoidal surface. The spectra are obtained by varying the incident neutron energy.

5.3.2.b) Experimental details

A Cu220 monochromator was used to select incident neutrons of energy in the range [26.5-450]meV. With this monochromator, the energy resolution (FWHM) of the instrument is about 2-3% of the incident energy. Incident neutrons of energy below 26.5 meV have been

selected using the Si311 monochromator.

Figure 5.20 shows the kinematical range (Q,ω) covered on IN1 instrument during our experiment. In contrast to FOCUS, IN1 probes a quite sharp kinematical range, mainly because the final energy is very small compared to the initial one (see Eq. 5.3 to understand why a large energy exchange induces a sharper kinematical range). This kinematical range spreads between 22 meV and 450 meV.

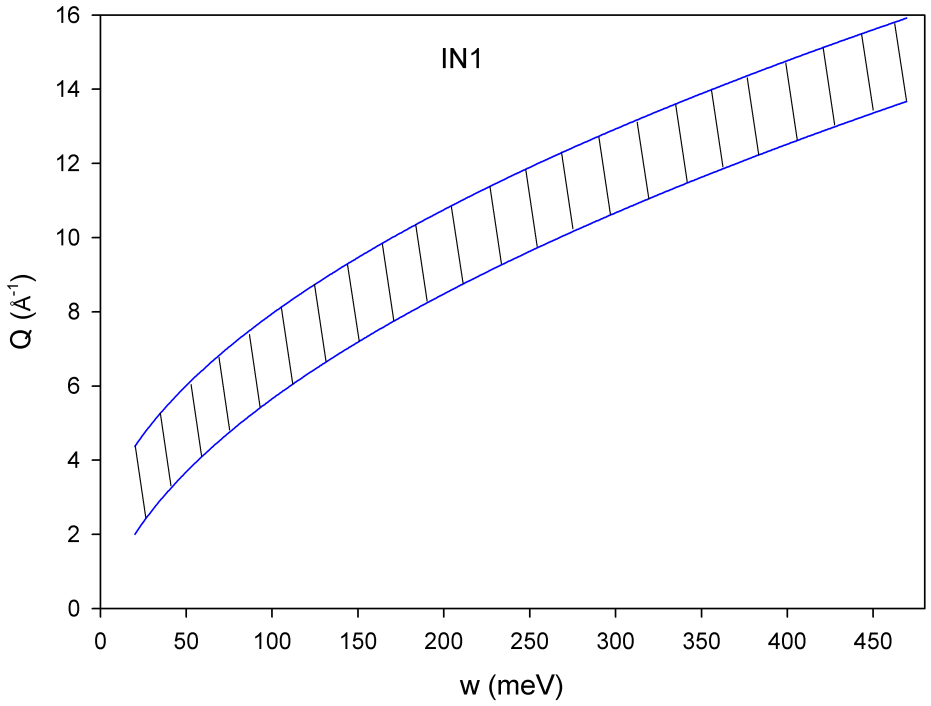

Figure 5.20 – The hatched area represents the kinematical range covered during the INS experiment on IN1.

During the experiment, samples were filled into an aluminum foil. Six lactulose samples have been measured:

- The anhydrous lactulose crystal
- The trihydrate lactulose crystal
- The quenched from the melted lactulose (QFTM)
- The milled lactulose (MIL)
- The spray-dried lactulose (SD)
- The freeze-dried lactulose (FD)

The QFTM, FD and trihydrate crystal samples were slightly crushed into fine powder, to have the same granulometry than other samples. This approach also ensured that the samples in the beam were of uniform geometry. All samples were measured at 10 K, in order to scale down the DW factor. Roughly 12 h were needed to collect each spectrum. The data treatment is presented in annex B.

5.3.2.c) Results

Figure 5.21 a) represents the GDOS of the two different lactulose crystals: the anhydrous one (black line) and the trihydrate one (cyan line). The spectra were normalised to unity in the energy range 20 to 460 meV.

In the figure, one can see that:

- The amplitude of the vibrational modes around 70 meV is higher in the trihydrate crystal than in the anhydrous crystal. Those modes correspond to librational modes of water. A higher amplitude of these vibrational modes on the trihydrate crystal compared to the anhydrous one thus reflects a higher amount of water in the trihydrate sample, as expected.

- The frequency of the vibrational mode around 370 meV is slightly lower in the trihydrate crystal compared to the anhydrous crystal. This vibrational mode corresponds to the CH stretching mode [183, 255]. There is thus a softening of the CH stretching mode in the trihydrate crystal compared to the anhydrous crystal.

Figure 5.21 b) represents the GDOS of four different lactulose amorphous samples: the MIL (red line), the QFTM (green line), the FD (blue line) and the SD (pink line). The spectra were normalised to unity in the energy range 20 to 460 meV. The four spectra are similar, but the spectrum of the SD sample shows some differences compared to that of the others amorphous samples:

- Below 120 meV, the spectrum of the SD sample is more structured than that of the other amorphous samples: it has some sharp peaks on the main broad peak.

- The amplitude of the two vibrational modes between 160 meV and 180 meV is higher in the SD sample than in the other amorphous samples. The hybridised H-C-H, C-C-H and C-O-H bending modes are known to be responsible for the peaks in this energy region [183, 255].

- There is a softening of the CH stretching mode of the SD sample compared to the others.

It is important to mention that multiphonon terms do significantly affect the shape of the GDOS in the high-energy range (above 250 meV). For example, the « shoulder » around 340 meV (just before the CH stretching mode) is a harmonic (overtone) of the OH and CH bending modes located around 170 meV. In general, the multiphonons (overtones or combination of modes) are responsible, above 250 meV, of the increase of the background of the plot.

5.3.2.d) DFT calculations of the density of states of the lactulose tautomers

As a reminder, the position of all atoms in tautomer A has already been well determined by XRD, but the position of most of the H atoms in tautomers B and C is unknown [51]. We have thus performed structure optimisations using DFT calculations, in order to predict the position of the undetermined H atoms. Geometry optimisations were performed on the three different tautomers using the B3LYP functional, in DMol3. Despite our multiple attempts, it was not possible to well optimise the structure of the tautomer A, and the calculation of

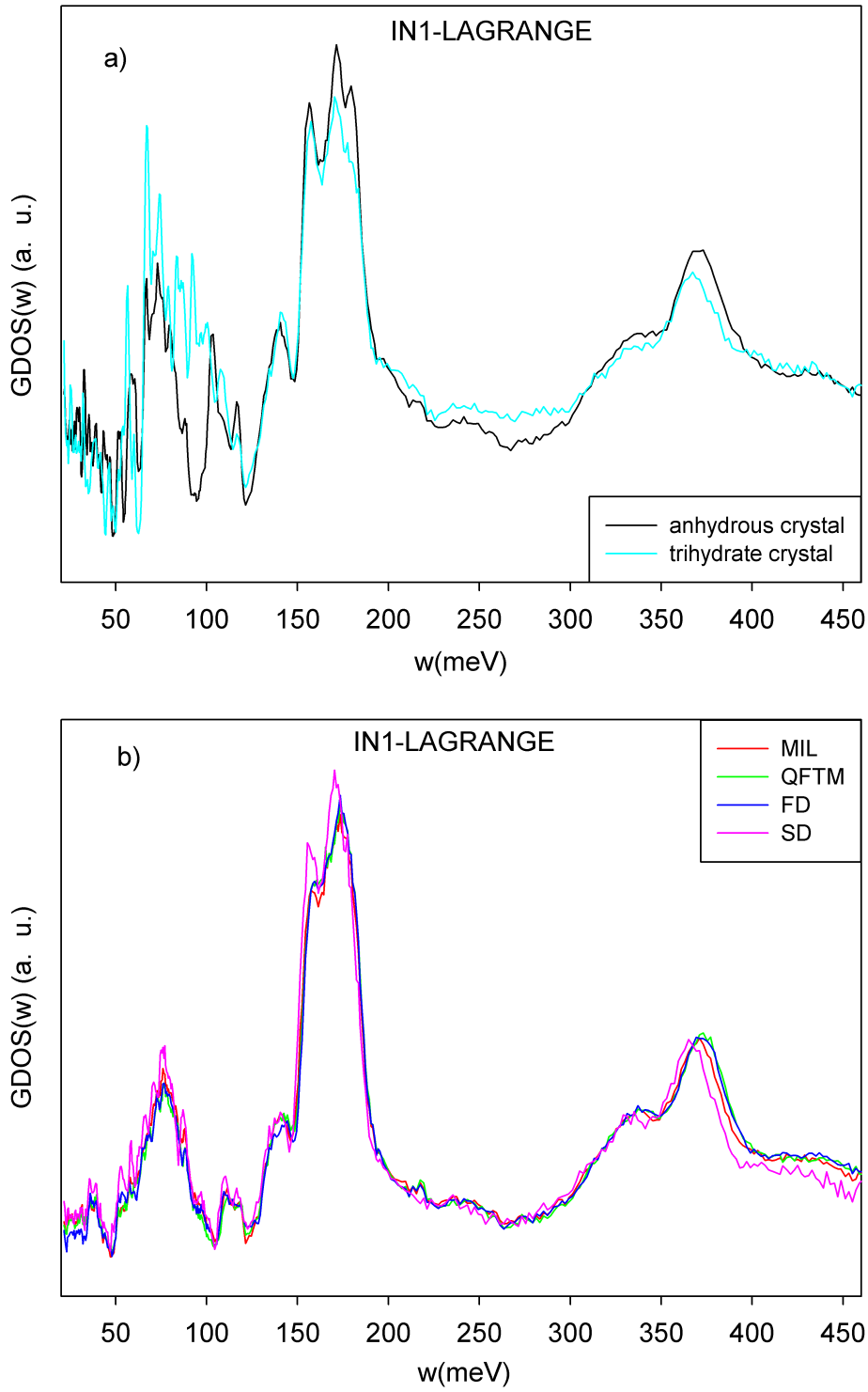

Figure 5.21 – GDOS of different samples of lactulose represented between 20 meV and 460 meV. Each sample was measured at 10 K on IN1-LAGRANGE, and the measured intensity has been treated to obtain the GDOS (see annex B). The spectra were normalised to unity in the energy range 20 to 460 meV.
a) The anhydrous (black line) and trihydrate (cyan line) crystals are represented.
b) The MIL (red line), QFTM (green line), FD (blue line) and SD (pink line) samples are represented.

its VDOS always gave negative frequencies. Works are in progress to solve this issue. Therefore, the VDOS of the tautomer A will not be presented. On the other hand, the structures of the tautomers B and C have been well optimised. The normal modes of the latter were determined afterwards by diagonalising their Hessian matrix, and from there the VDOS was calculated. Only H atoms were considered. The obtained VDOS was convolved by a Gaussian resolution function of FWHM equal to 3% of the vibration energy, in order to be easily comparable to the GDOS measured on IN1. The results obtained are presented in figure 5.22.

It can be seen that:

- Below 100 meV, the vibrational spectra are different. The differences seen are however not meaningful. Indeed, calculations were performed on isolated molecules, and therefore the intermolecular part of the spectra is not calculated correctly.
- Above 150 meV, there are three main bands: one centred at 175 meV, another centred at 370 meV, and the last one centred at 470 meV. The amplitude and position of those three bands are roughly the same.

This calculation of the VDOS allowed to make an identification of the vibrational modes, and showed that:

- The vibrational mode around 450 meV is the OH stretching.
- The vibrational mode around 370 meV is the CH stretching.
- The OH and CH bending modes are between 150 meV and 200 meV. It was not possible to separate the contribution from the OH bending only, or the CH bending only, or the OH and CH bending modes coming only from one of the monosaccharides constituting the lactulose molecule.

5.3.2.e) The CH stretching band in the different samples

Figure 5.23 represents the GDOS of the four different amorphous samples (MIL, red line ; QDFTM, green line ; FD, blue line ; SD, pink line) of lactulose and the two crystalline forms (anhydrous, black line ; trihydrate, cyan line) as measured on IN1-LAGRANGE. All plots are represented between 300 meV and 460 meV to emphasize the CH stretching band. This band is surrounded by the OH stretching band (centred at 440 meV), and the overtone of the OH and CH bending bands (centred at 340 meV).

These different spectra were fitted with three Gaussians, in order to determine the exact FWHM and position of the CH stretching band. The background was assumed constant in this energy range (from 300 meV to 460 meV). We only consider the physical implications and report the results (see table 5.3) from the CH stretching band, and so the fits to the two other bands only serve to give a more accurate estimation of the CH stretching band parameters. The CH stretching band position obtained directly from the data as the x coordinate of the maximum of the band (or the middle point of the top of the bump, for flat-tops) tracks the fits rather well (see grey column in table 5.3). This gives confidence on the fitting protocol.

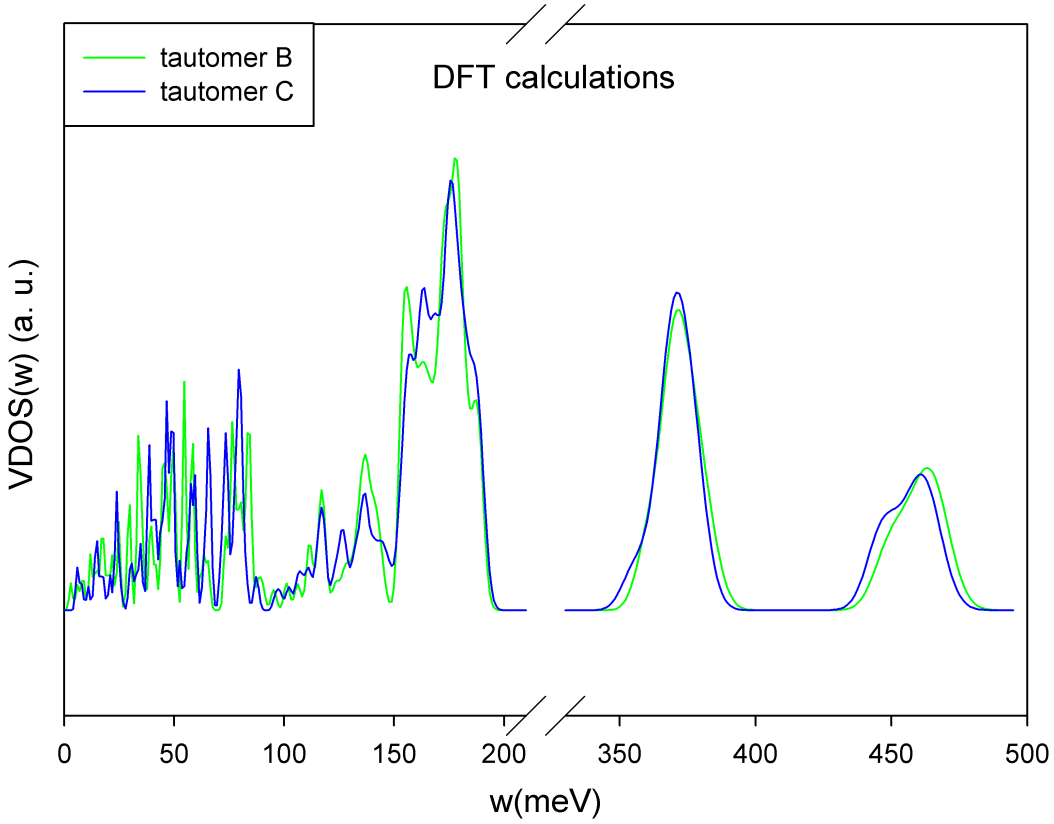

Figure 5.22 – VDOS of the tautomer B (green line) and tautomer C (blue line) obtained after DFT calculations. The original DFT spectra were convolved by a Gaussian resolution function of FWHM equal to 3% of the vibration energy.

Table 5.3 – Position and FWHM of the CH stretching band in the different lactulose samples. The grey column represents the CH stretching band position obtained directly from the data as the x coordinate of the maximum (or the middle point of the top of the bump, for flat-top) of the band.

Samples	CH stretching band FWHM (± 1.00 meV)	CH stretching band position (± 0.50 meV)	CH stretching band position (± 0.50 meV)
Anhydrous crystal	23.79	370.56	370.49
MIL	25.55	370.63	371.14
QFTM	25.93	373.27	373.51
FD	25.79	372.85	372.18
SD	25.36	366.48	365.42
Trihydrate crystal	21.79	368.06	367.43

From the table, it can be seen that the FWHM of the CH stretching bands are similar in the different amorphous samples. Those of the crystalline samples are slightly smaller because crystalline samples are more ordered. Moreover:

- The trihydrate crystal has a lower vibration frequency than the anhydrous crystal. This softening of the CH stretching vibration in the trihydrate crystal compared to the an-

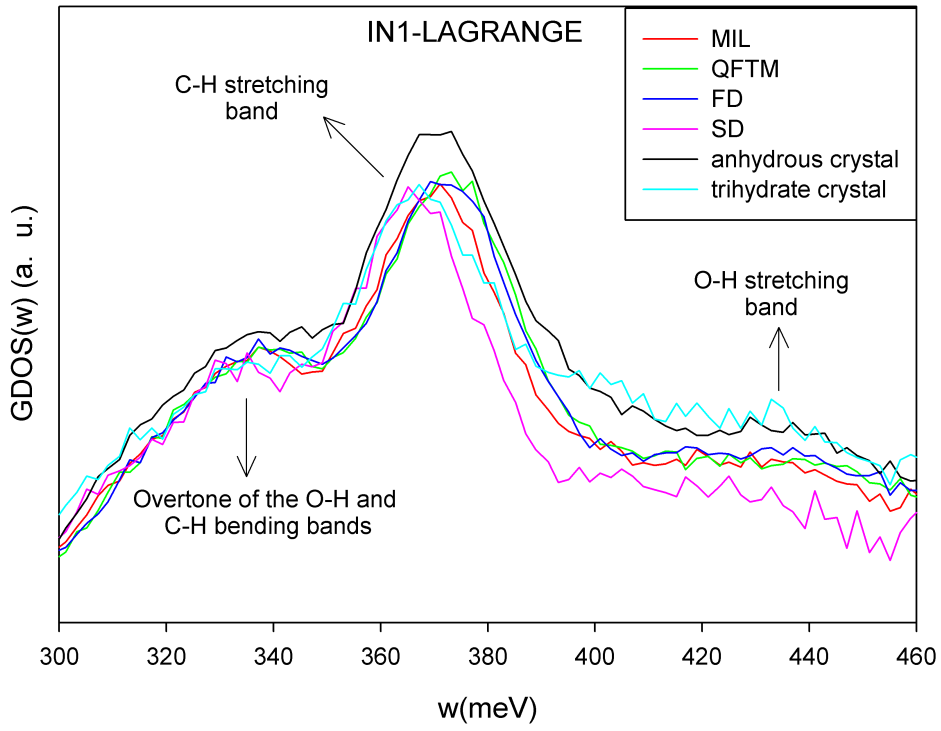

Figure 5.23 – GDOS of the four different amorphous samples (MIL, red line ; QDFTM, green line ; FD, blue line ; SD, pink line) of lactulose and the two crystalline forms (anhydrous, black line ; trihydrate, cyan line) as measured on IN1-LAGRANGE. All plots are represented between 300 meV and 460 meV to emphasize the CH stretching band. The OH stretching band and the overtone of the OH and CH bending bands surround this band.

hydrous one is due to HBs network. Since the trihydrate crystal has water, it has many more HBs than the anhydrous one, and its CH stretching vibration may soften. Such behaviour has already been observed in the case of the OH stretching vibration [264] (see figure 5.24), where softening is expected to be more important than in the CH stretching vibration.

- The anhydrous crystal and the MIL have equal vibration frequencies. This indicates that they locally have the same intermolecular arrangement and the same number of intermolecular HBs, as suggested by D7 results.

- The vibrational frequencies of the QFTM and FD are higher than those of the other compounds. They thus have locally less intermolecular HBs than the previous samples.

- The SD sample has the lowest vibrational frequency. This is an uncommon behaviour.

A detailed analysis of SD sample is carried out in the next section.

5.3.2.f) Analysis of the bending and stretching modes of the SD sample

The IN1-LAGRANGE results previously presented shown some interesting differences between the SD lactulose sample and the other amorphous samples:

i) Softening of the CH stretching mode.

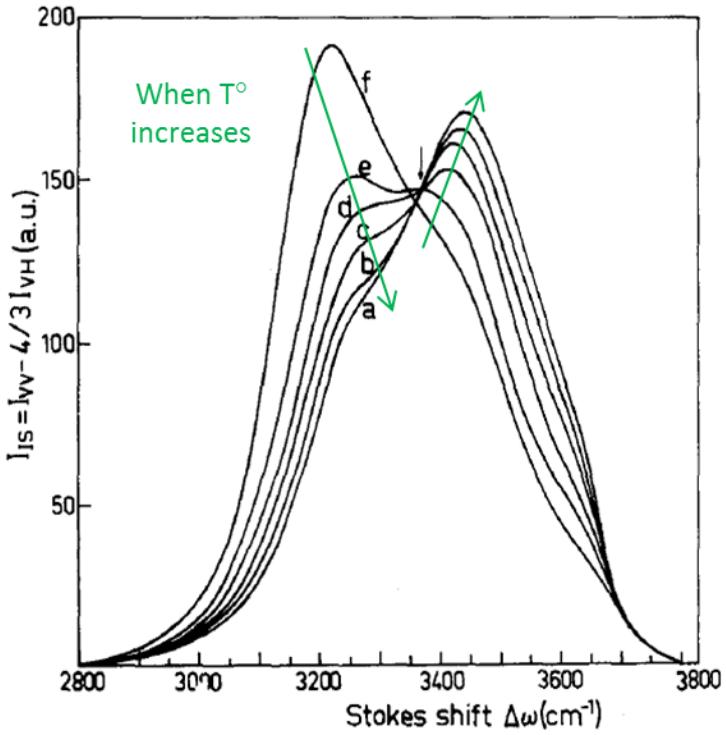

Figure 5.24 – Raman spectra of the OH stretching of water at different temperatures. a: T=95 °C, b: T=80 °C, c: T=60 °C, d: T=40 °C, e: T=20 °C, f: T=-24 °C. As the temperature increases, the vibrational mode at 3150 cm^{-1} shifts toward higher frequencies with a decrease of its amplitude, while the vibrational mode at 3450 cm^{-1} shifts toward higher frequencies with an increase of its amplitude. This means that the decrease in the number of HB induces an increase of the OH stretching frequency. Taken from [264].

ii) Higher OH and CH bending mode amplitudes.

iii) Presence of sharp peaks on the main broad peak below 120 meV.

Those differences require thorough investigations.

First of all, we must emphasize that:

- DSC and X-ray experiments were performed just after the preparation of the samples and after their measurement on IN1-LAGRANGE. The results were identical, thus indicating that the samples did not evolve between their preparation and their measurement.

- The differences found are not due to the tautomeric differences between samples. Indeed, the MIL and the FD lactulose samples for example do not have the same tautomeric composition, thus having interchangeable spectra. The SD and the FD lactulose samples have very close tautomeric compositions, but do not show the same spectra.

- It is tempting to assert that the softening of the CH stretching mode of SD sample compared to the other amorphous samples is due to the presence of water, since a similar effect is seen (see figure 5.24) between the trihydrate crystal and the anhydrous crystal. However, the amplitude of the librational mode of water (around 75 meV) is similar in all amorphous samples spectra, thus indicating that they roughly contain the same

amount of water. More precisely, by TGA, we have detected almost 3.4 % of water in the MIL and SD samples, and 2 % in the FD sample. The previous assertion should then be forgotten.

- The four amorphous samples were measured in succession. The SD sample was the third to be measured. Therefore, these differences are probably not due to any dysfunction of the instrument itself.

To understand those differences between the SD sample and the other amorphous samples, we have investigated if the SD sample contains a small crystalline fraction just after its preparation, and if the water used during the spray-drying preparation indirectly affected the state of the SD sample obtained. The obtained results are presented below.

Is there any crystalline fraction in the SD lactulose? A fast DSC experiment was carried out on the SD lactulose in order to remove any suspicion of the presence of crystallites within it immediately after its preparation.

Figure 5.25 shows the thermograms of SD lactulose (black line), and a physical mixture containing 98% of SD lactulose and 2% of crystalline lactulose (cyan line). These thermograms were recorded during heating at 200 °C/min after calorimeter calibration at this rate.

The two thermograms show a C_p jump at T_g = 125 °C characteristic of a vitreous state, which ends in a weak relaxation endotherm. Concerning the physical mixture, it has an endotherm at about 170 °C, having an enthalpy of 3.18 J/g. This endotherm therefore corresponds well to the melting of the 2% of crystalline lactulose contained in the physical mixture. Regarding the SD lactulose, no endotherm is seen in the melting temperature region. **There are thus clearly no crystallites in the SD lactulose**.

Is there any "water memory" effect? Investigation by MD simulations The purpose of this section is to determine by MD simulations whether the SD compound exhibits a sort of "water memory" effect.

To this end, two different amorphous boxes were generated:

- A box composed of 64 lactulose molecules. It was generated after hyper-quenching (from 700 K to 300 K) an equilibrated liquid box at 20 K/200 ps. This box will be named "anhydrous box".

- A box composed of 64 lactulose molecules and 640 water molecules. This other box will be named "diluted box". We have put ten times more water molecule than lactulose molecule for a better dilution of the lactulose, and a good homogenisation of the mixture. The SCP flexible water model was used [265].

The anhydrous box was equilibrated at 300 K during 3 ns, including 2 ns in NPT (P = 1 atm) followed by 1 ns in NVT. The diluted box was equilibrated at 300 K during 5 ns, including 4 ns in NPT (P = 1 atm) followed by 1 ns in NVT. The effective density was about 1.45 g/cm^3 in the anhydrous box, and 1.35 g/cm^3 in the diluted box.

Afterwards, all the water molecules have been removed at once from the diluted box. This new box (diluted box without water) will be named "dried box". The dried box was also equilibrated at 300 K during 3 ns, including 2 ns in NPT (P = 1 atm) followed by 1 ns in NVT. The effective density in the dried box was nearly 1.40 g/cm^3. It is worth mentioning that the small difference of the effective density between the anhydrous box and the dried box does not induce changes in system properties that will be presented later. Indeed, we have

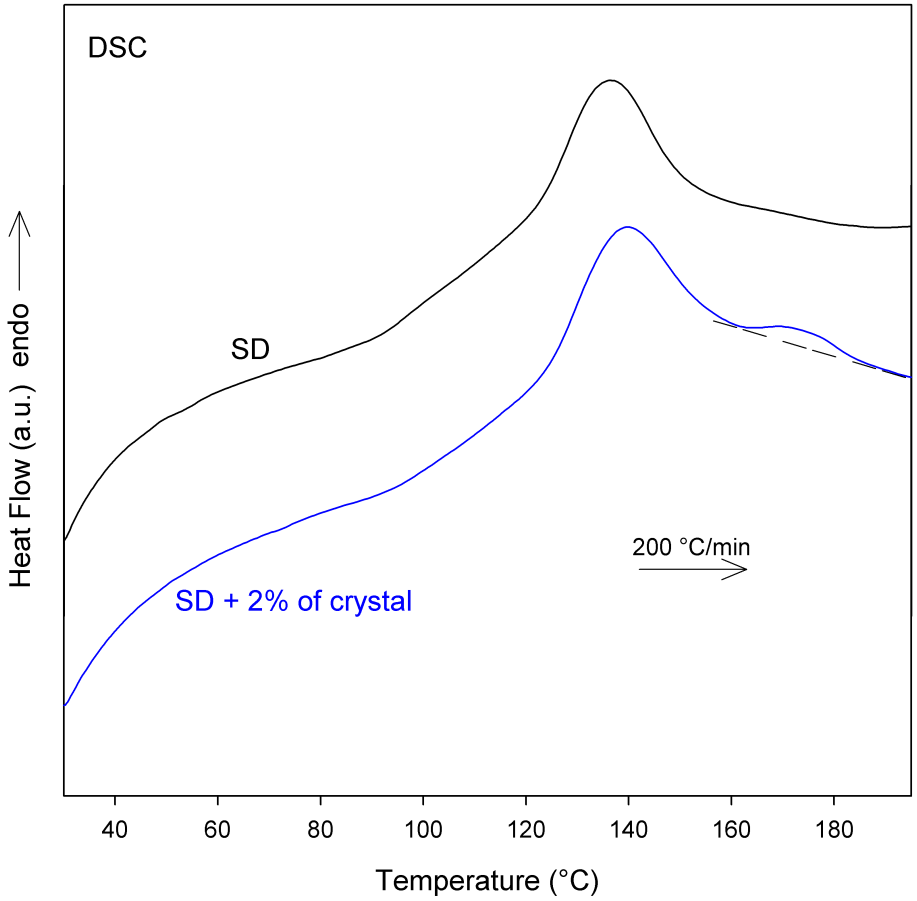

Figure 5.25 – Fast DSC heating scans (200 °C/min) of SD lactulose (black line) and a physical mixture made of 98% of SD lactulose and 2% of crystalline lactulose (blue line).

slightly compressed the dried box to have an effective density equal to that of the anhydrous box, i.e. 1.45 g/cm^3, and the results obtained in both boxes (the slightly compressed and the uncompressed) were similar.

Water molecules have been removed at once from the diluted box in order to reproduce the spray-drying process. **The dried box can then be assimilated to a spray-dried amorphous box**.

The previous equilibrated boxes (anhydrous and dried boxes) were further used to analyse the properties of the lactulose molecules after the passage of water (i.e., molecules in the dried box), in comparison with the properties of the lactulose molecules without any water effect (i.e., molecules in the anhydrous box). For this purpose, a MD trajectory of 1 ns with frames saved every 0.1 ps was generated from each of those boxes. Those MD trajectories are used for all the results presented afterwards.

i) The number of HBs

In the present study, two lactulose molecules are considered to be H-bonded if the oxygen–oxygen distance d(O-O) is less than 3.4 Å and the O-H...O angle larger than 150.0°. This geometric criterion included well-formed and strong HBs. Attempts to compute distribution of HBs with a less stringent criterion (O-H...O angle > 120.0°), including well-formed and strong HBs and quite deformed and weaker HBs, have given similar

results, and are thus not presented here.

The total (including intermolecular and intramolecular) and intermolecular numbers of HBs per molecule were calculated over 500 ps of simulation in the anhydrous box and the dried box, using the MD trajectories previously generated. The distributions of the numbers obtained are represented in figure 5.26.

In figure 5.26 a), the distributions of the total number of HBs per molecule in the anhydrous box (black line) and the dried box (blue line) are represented. The distributions of the intermolecular number of HBs in the same boxes are represented in figure 5.26 b).

It can be seen that the molecules in the anhydrous box develop 4.5 HBs on average, and those in the dried box develop 4.3 HBs on average. The molecules in the anhydrous box therefore develop slightly more HBs than those in the dried box. Similarly, the average number of intermolecular HBs in the anhydrous box, n = 4.3, is slightly larger than the one in the dried box, n = 4.0. A similar difference in the number of HBs has been seen in chapter 3 (see figure 3.30) between tautomer A and tautomer B. However, the experimental and DFT results presented before indicate that the CH stretching frequency is the same in all tautomers. **The small differences in the number of HBs that the molecules develop in the anhydrous box and the dried box are therefore not expected to induce changes in the CH stretching frequency**.

ii) The nature of the HBs

Instead of counting the number of HBs, the properties of the HBs computed above are analysed in this section.

Figure 5.27 shows the contour maps of the characteristics (O-O distance and O-H...O angle) of the HBs calculated in the anhydrous box (picture on the top) and the dried box (picture on the bottom). Calculations were performed on equilibrated MD trajectories, using 100.000 HBs. The colour at a given point represents the number of HBs having the corresponding property. The results were subsequently normalised, to have the highest intensity equal to one. Both intermolecular and intramolecular HBs are considered.

In the dried box and in the anhydrous box, one can see that the signal is concentrated between 156.5° and 168°. To better visualise if the nature of the HBs developed by the molecules in both boxes has changed, we have calculated the distribution of the d(O-O) distances of the HBs for OH...O angles varying between 150° and 180°, and the distribution of the OH...O angles of the HBs for d(O-O) distances varying between 2.4 Å and 3.2 Å. The results obtained are shown in figure 5.28.

In figure 5.28, one can see that the distributions - of the HBs characteristics - calculated in both boxes are almost identical: the medium d(O-O) distance of the HBs is around 2.7 Å and the medium O-H...O angle is around 163.6°. Therefore, **the nature of the HBs developed in both boxes is the same**.

iii) The HCCH dihedral angles

The aim of this section is to determine if lactulose molecules adopt different conformations in the anhydrous box and the dried box. For this purpose, the set of conformations explored by two HCCH dihedral angles of the molecules in both boxes was calculated. Among these two angles, one is on the cycle of 6 C atoms (Phi) and the other is on the cycle of 5 C atoms (Psi). Both of them can be visualised in figure 5.29.

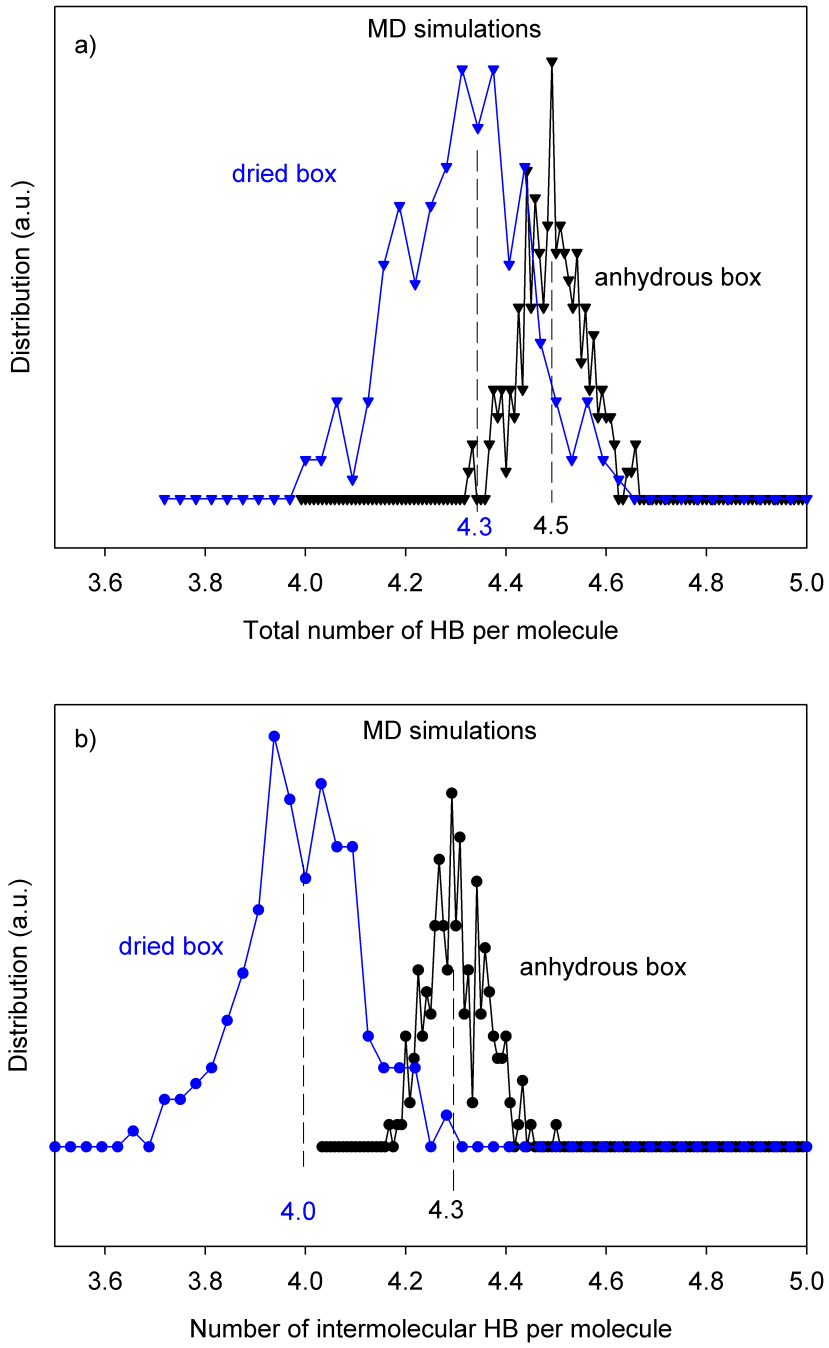

Figure 5.26 – Distribution of the number of HBs developed by each molecule in the anhydrous box (black lines) and the dried box (blue lines). The calculations were performed on an equilibrated MD trajectory of 500 ps.
a) All HBs (intermolecular and intramolecular).
b) Only intermolecular HBs.

It is worth mentioning that we have chosen to investigate the HCCH dihedral angles explored by the molecules in both boxes since the C-H stretching vibration of the SD sample measured on IN1 is different from that of the other samples.

In figure 5.30, one dihedral angle value is the value of the dihedral angle calculated on

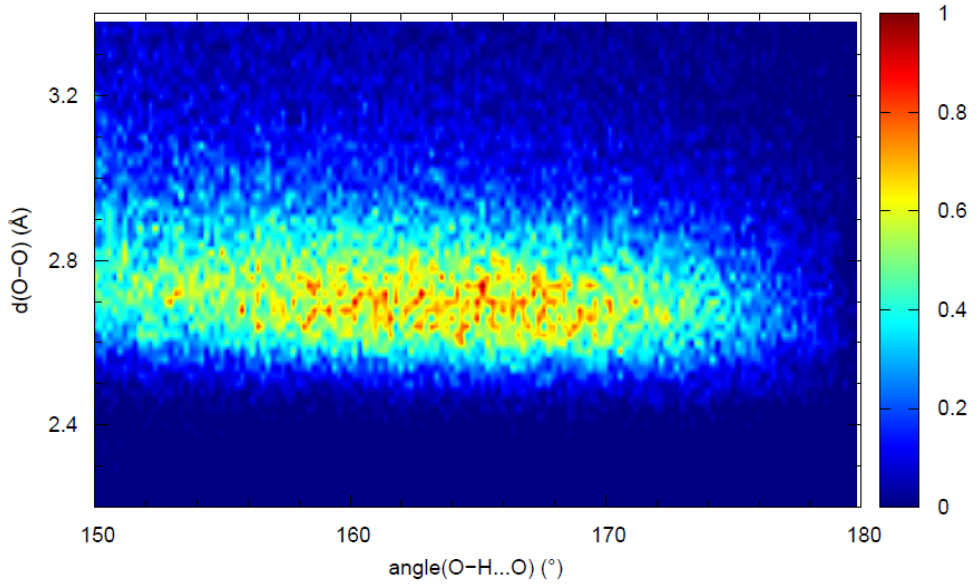

(a) Case of the anhydrous box

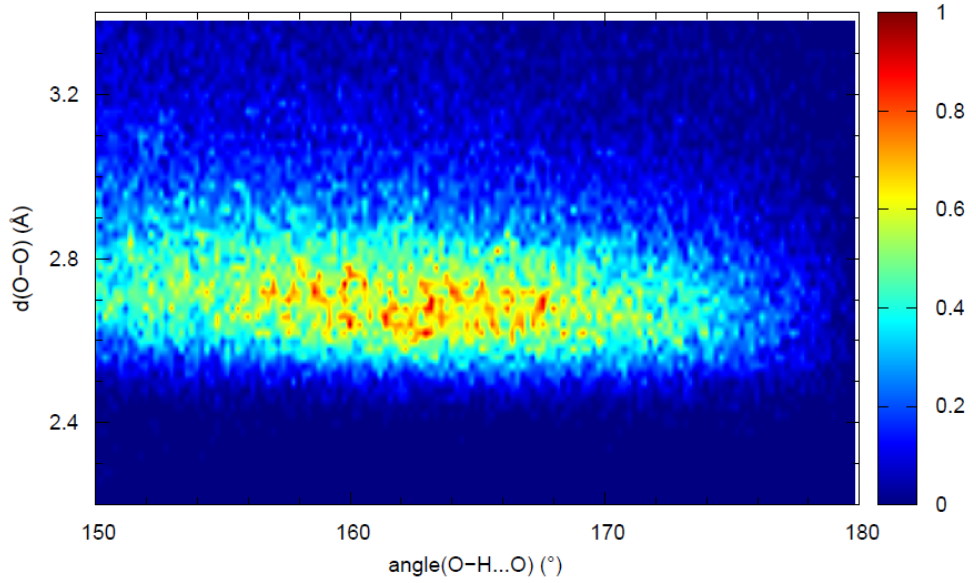

(b) Case of the dried box

Figure 5.27 – Contour maps of the characteristics (O-O distance and O-H…O angle) of the HBs calculated in the boxes on equilibrated MD trajectories, using 100000 HBs.

one molecule. Any plot represented in the figure is thus the distribution of these dihedral angle values over all the molecules in the box, and all the frames saved during 100 ps of simulation. Figure 5.30 a) represents the distribution of the Phi dihedral angle values that have been explored by the molecules. The black line stands for the distribution of values of the Phi dihedral angle calculated on lactulose molecules coming from the anhydrous box, and the blue line stands for the distribution of values of the Phi dihedral angle calculated on lactulose molecules coming from the dried box. The same distributions for the case of the Psi dihedral angle values are depicted in figure 5.30 b).

In figure 5.30 a), one can see that lactulose molecules have explored slightly different Phi dihedral angle in the two different boxes. The medium value of the Phi dihedral

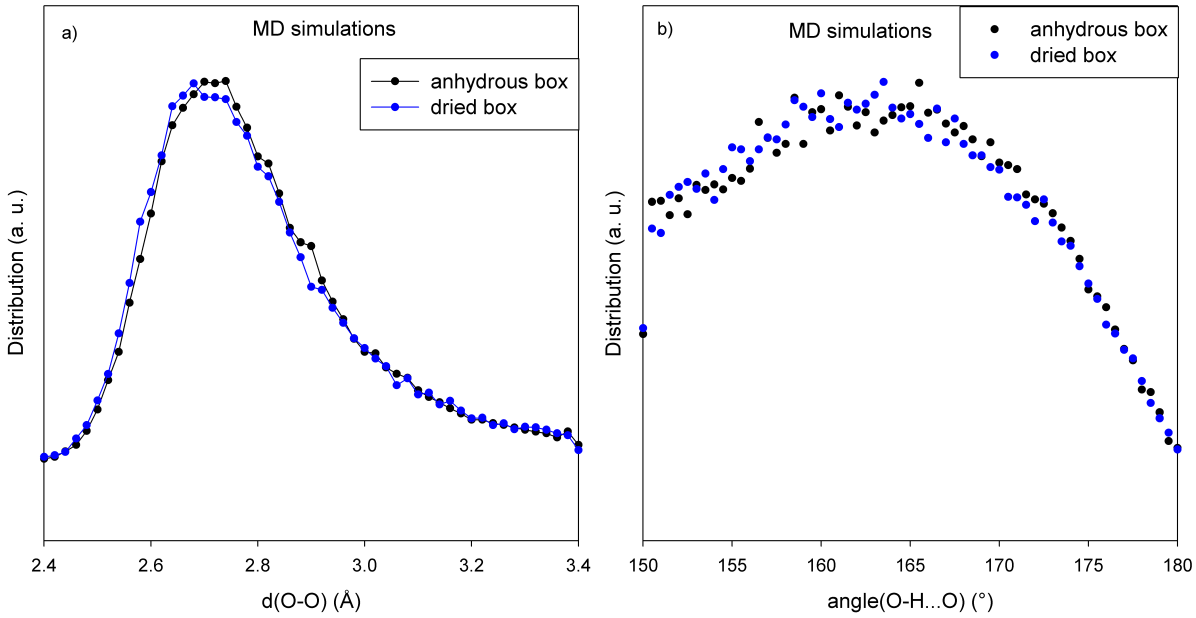

Figure 5.28 – Distribution of the characteristics of the HBs developed by the molecules in the anhydrous box and in the dried box, calculated using 100000 HBs.
a) Case of the d(O-O) distance.
b) Case of the O-H...O angle.

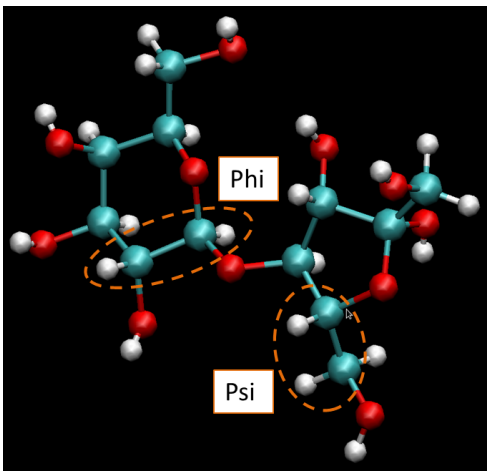

Figure 5.29 – Phi and Psi HCCH dihedral angles chosen for the investigations.

angle is -168° for lactulose molecules coming from the anhydrous box, and -171° for lactulose molecules coming from the dried box.

In figure 5.30 b), a more striking difference can be viewed for the case of the Psi dihedral angle. There is a shift of the main value of the dihedral angle, which is around 64° for lactulose molecules coming from the anhydrous box, and 58° for lactulose molecules coming from the dried box. The other peak is around -52° for lactulose molecules coming from the anhydrous box, and -58° for lactulose molecules coming from the dried box. We have performed several simulations, which shown that these differences are reproducible. **These shifts clearly indicate that the passage of water has induced some changes of the conformation of lactulose molecule**.

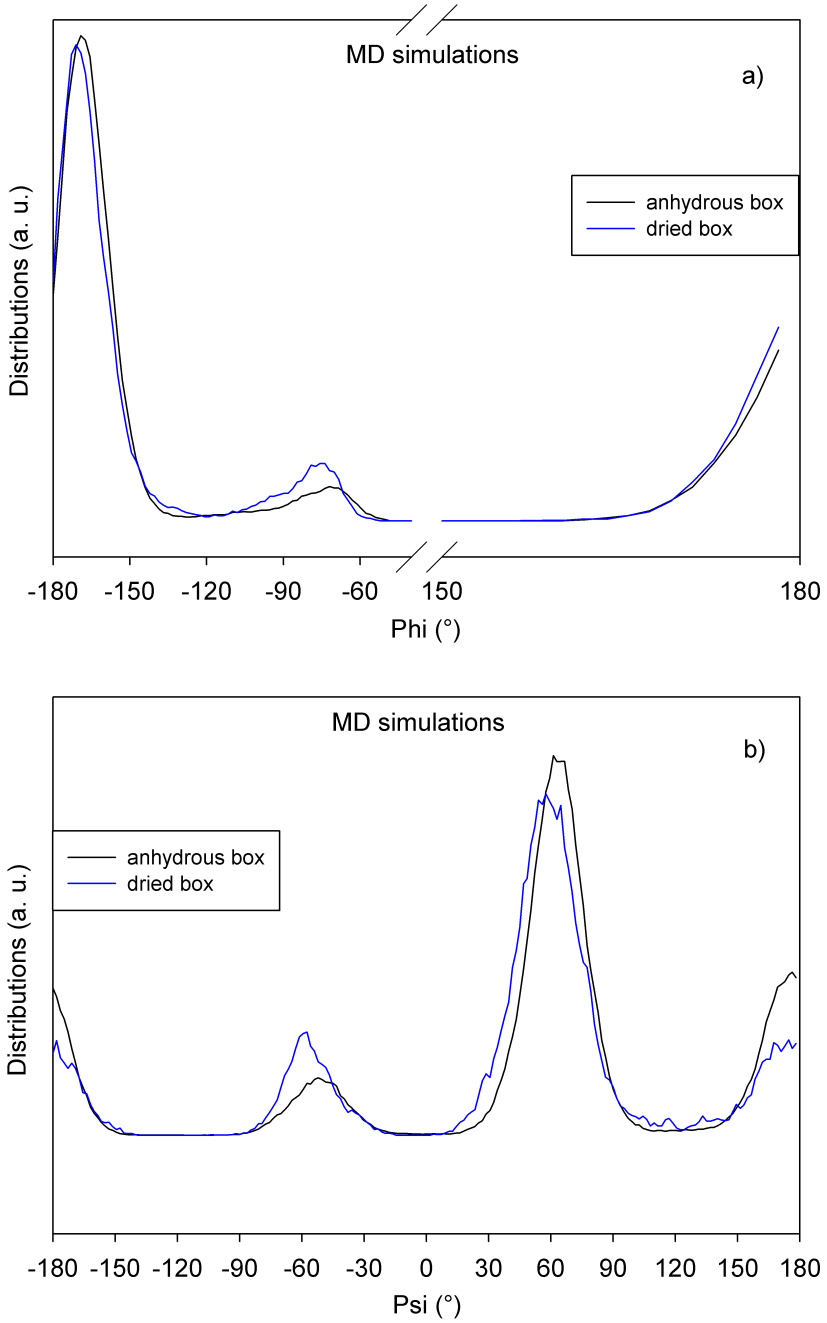

Figure 5.30 – Distribution of values of two dihedral angles explored by lactulose molecules in the anhydrous box (black line) and in the dried box (blue line). The calculations were performed on an equilibrated MD trajectory of 100 ps.
a) Case of the Phi dihedral angle.
b) Case of the Psi dihedral angle.

iv) The q6 order parameter

The IN1 spectrum of the SD sample showed some sharp peaks at low energy (below 120 meV) suggesting that it is more ordered than other amorphous samples. It therefore appeared interesting to determine the order level in the anhydrous box and in the dried box.

To this end, we have chosen the q6 order parameter. It is a simple rotational-invariant order parameter, based on a spherical harmonics development of vectors joining the centre of mass of neighbouring molecules [266–268]. Generally this order parameter is used for systems having a cubic symmetry and allows distinguishing between different crystal cubic systems, but it can be used as well for non-cubic symmetries [269, 270].

In figure 5.31, one q6 value is the average of the q6 values calculated in all the "Voronoi" cells around each molecule of the box, in one simulation frame. Only centres of mass of the molecules are considered for the calculations. Any plot represented in the figure is thus the distribution of these average q6 values over all the frames saved during 100 ps of simulation. The distribution of q6 order parameter calculated in the anhydrous box (black points), in the dried box (blue points), and in a crystalline box (dark red points) are represented.

As seen in the figure, the mean value of q6 is 0.57 in the crystalline box, 0.18 in the dried box, and 0.14 in the anhydrous box. The mean value of q6 in the dried box is therefore greater than that in the anhydrous box, but remains much lower than in the crystal. This means that the dried box is locally more ordered than the anhydrous box, while remaining completely amorphous. The passage of water has thus favoured the development of a particular local order in the system. **This order could be responsible of the appearance of the peaks seen at low energy on the SD sample spectrum**.

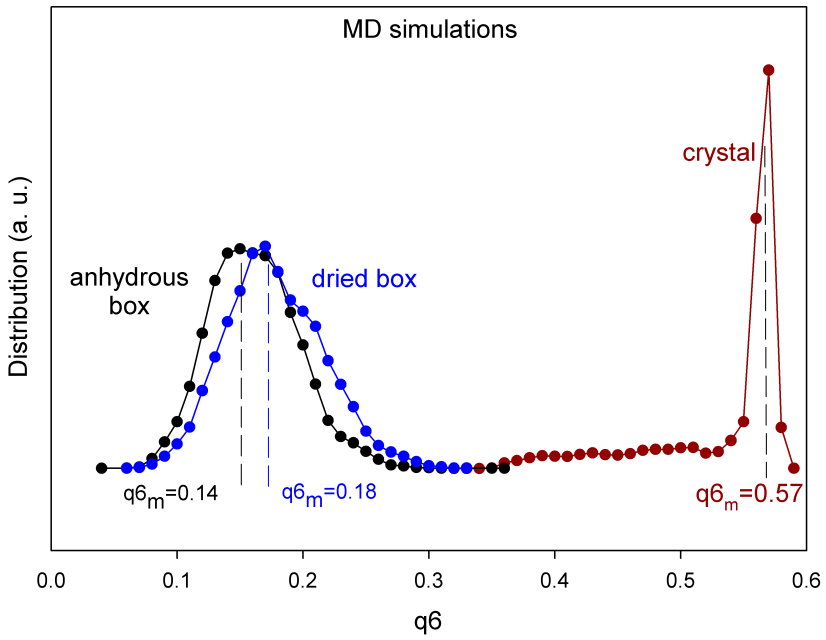

Figure 5.31 – Distribution of q6 order parameter calculated in the anhydrous box (black points), in the dried box (blue points), and in a crystalline box (dark red points). All calculations were performed over 100 ps of simulation.

5.3.2.g) Proposition of a model

The SD sample spectrum shows some differences compared to the one of other amorphous samples. Such a spectrum was not expected since it does not agree with that of the FD

sample, which has a similar tautomeric composition and initial state (water in solution) during the preparation method. First of all, it is important to recall the differences between these two preparation methods. For both of them, the crystalline power is diluted in water. Then:

- In the spray-drying method, water is removed at the liquid state, by a hot drying of the droplets. Therefore, it is a sudden removing of water (see figure 5.32).

- In the freeze-drying method, there is an intermediate freezing step. In this intermediate step, new lactulose clusters are formed as there was initially no water, since all water molecules aggregate to form ice crystals. Those lactulose clusters are slightly compacted by the surrounding ice crystals which are later removed by sublimation (see figure 5.32).

The FD compound is thus made of local “true” amorphous phases of lactulose, surrounded by “large” voids left by ice crystals. The effective density of the FD compound is then quite small (probably the smallest of all the amorphous compounds) because of those voids. However, the local density of the FD might be close to that of the QFTM, with similar local arrangements. This could explain why the FD and QFTM compounds have similar spectra.

Oppositely, the SD compound is globally more homogeneous. It forms one single phase made of lactulose molecules “mixed” with small voids left by liquid water. Its local density might then be smaller than the one in any other amorphous compound. The reduction of the number of HBs in the the dried box compared to the anhydrous box is well in line with this hypothesis. Because it has locally more space than any other amorphous compound, the SD compound succeeds in adopting a locally more ordered configuration than the other amorphous ones. This was seen by simulation between the anhydrous box and the dried box, and explains the presence of sharp peaks on the main broad peak below 120 meV in the SD compound spectrum. Moreover, the molecules might have adopted specific conformations in the presence of void, as it has been seen by simulation. These conformations could have different vibrational frequencies (CH stretching vibration, OH and CH bending vibrations) than that in the other amorphous states. This latter assumption must be verified by DFT calculations. It could justify the softening of the CH stretching vibration of the SD compound. The increase in the amplitude of the OH and CH bending vibrations could also be due to these specific conformations, or due to the fact that the molecules have more void around.

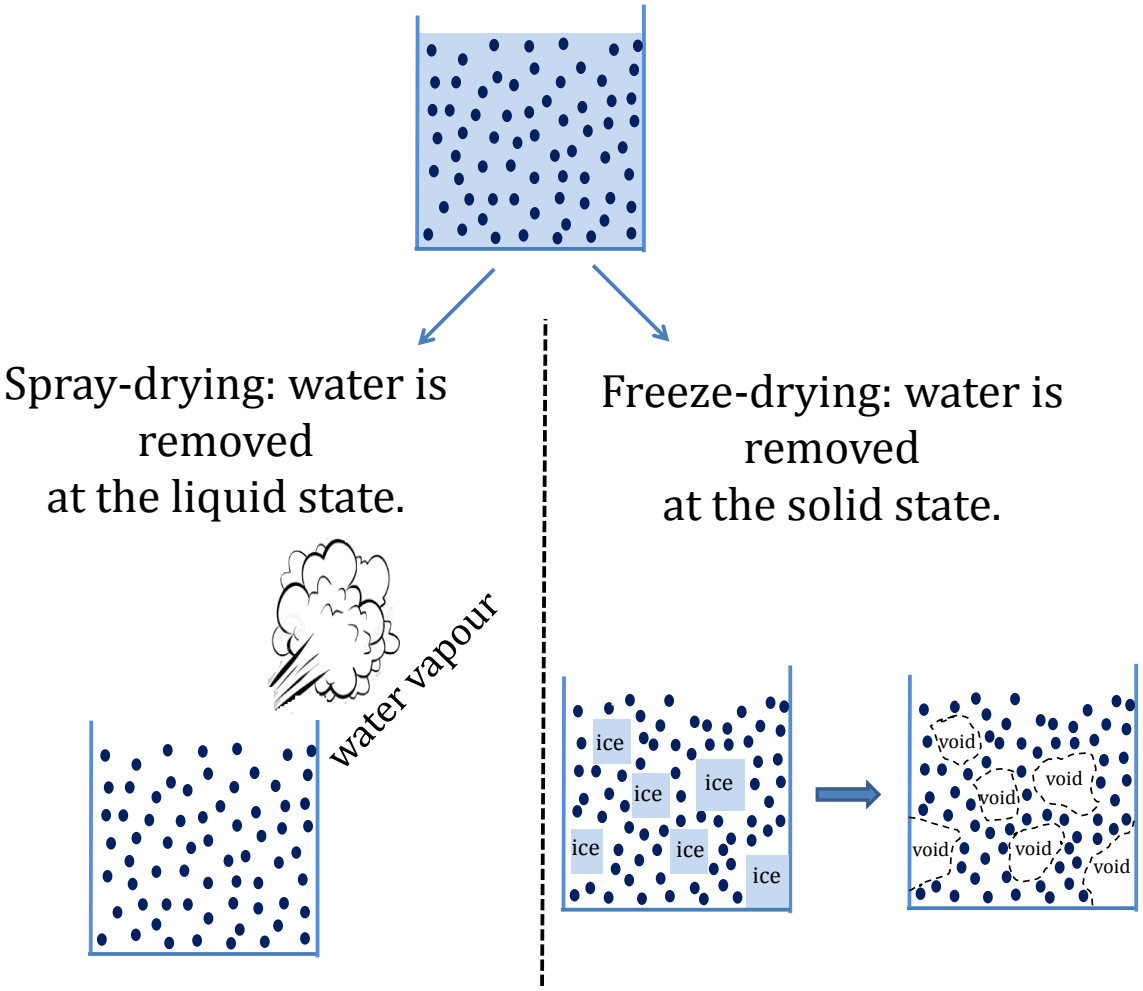

Figure 5.32 – Schematic representation of the differences between spray-drying and freeze-drying amorphisation methods.

Summary

In this chapter, we have studied the structural and vibrational properties of amorphous lactulose obtained by different amorphisation routes, by means of neutron scattering experiments combined with MD and DFT calculations. The obtained results revealed differences which appear to originate more from the amorphisation method itself than the chemical differences between compounds (tautomers, thermal degradation) mentioned in chapter 3.

Structure (D3 and D7 diffractometers)

On D3, the results do not reveal any remarkable difference of the structure factor S(Q) of the different amorphous compounds within the experimental errors. Interestingly, this latter result confirms that there is no important modification in the structure of the molecule itself due to the preparation method.

On D7 however, the S(Q) of the milled sample is different from that of the other amorphous samples. In particular, it has two bumps at Q = 0.74 $Å^{-1}$ and Q = 0.90 $Å^{-1}$ which indicates that the local intermolecular arrangement between molecules in the milled compound is similar to that of the crystal. However, the too low crystallites fraction (0.4 %) detected by fast DSC in the milled sample probably does not affect the neutron diffraction pattern. Therefore, the milled sample appears to be a mixture of local order structures (similar to crystallites) surrounded by real amorphous phases.

Vibration (FOCUS and IN1 spectrometers)

On FOCUS, the goal was to measure the BP of the different compounds. The results showed that the BP of the quenched from the melt compound is different from that of the other amorphous compounds. This difference appears to be due to the thermal degradation that took place during the preparation of the quenched from the melt compound.

On IN1, the results reveal some striking differences between the vibrational spectrum of the spray-dried sample and that of the other amorphous samples: presence of sharp peaks below 120 meV, more intense OH and CH bending modes and softening of the CH stretching mode. This is a puzzling result. By reproducing the spray-drying process by MD simulations, we demonstrated that the spray-dried compound (obtained after the sudden removal of water) was locally more ordered than a “conventional” amorphous compound. This justifies the presence of sharp peaks below 120 meV. The MD simulations results also show that the molecules in the spray-dried compound adopt particular conformations which could be at the origin of the increase of OH and CH bending modes amplitude, as well as the softening of the CH stretching mode. DFT calculations will be made to verify this assumption.

General Conclusion and Perspectives

"*Lorsque vous avez éliminé l'impossible, ce qui reste, si improbable soit-il, est nécessairement la vérité.*"

Arthur Conan Doyle

In this thesis, the main fundamental question was to determine whether the amorphous state of the same material obtained by different routes has different properties or not. To answer to this question, we have investigated how various amorphisation techniques impact on the physico-chemical properties of a model disaccharide compound: the lactulose. We have used four amorphisation techniques which present themselves potential marked differences on how the physical state of a material is manipulated: milling, quenching from the melt, spray-drying and freeze-drying. They can be classified as a-thermal/thermal and/or require or not the use of a solvent (water). A broad range of experimental (X-ray diffraction, DSC, NMR, neutron scattering) and numerical (MD and quantum simulations) approaches were used to obtain structural, dynamical, and thermodynamic information.

Using the four amorphisation techniques (milling, quenching from the melt, spray-drying or freeze-drying), an amorphous state was successfully produced but none of them is strictly similar to the others. They all clearly exhibit differences on either their physical or chemical states and it was demonstrated that some physical changes are direct consequences of a chemical change.

Difference of the chemical states between the amorphous states (tautomeric disorder & degradation) and their consequences on the physical states

Degradation

The quench of the liquid produces unavoidably a thermally degraded amorphous lactulose (seen by NMR). This is due to the fact that crystalline lactulose starts to degrade before melting. We have established that thermal degradation increases the glass transition temperature of lactulose. This explains why the T_g values of the QFTM published in the literature vary from authors to authors. However, thermal degradation did not seem to have any effect on the structure and vibrational dynamics as measured by neutron scattering (D7 and IN1).

Tautomeric disorder

As many sugar molecules, the lactulose molecule possesses many isomeric forms. At least three main tautomeric conformations - noted A, B and C in this work - have been detected, whose concentrations have been determined by NMR and found to be dependent of the amorphisation techniques.

The milled compound (MIL) has a tautomeric composition identical to that of the crystal (%A = 79.3, %B = 10.3, %C = 10.4). The milling technique thus does not induce tautomeric changes. Milling has the great advantage of being the only amorphisation method that does not induce thermal degradation or tautomerisation. This is important for pharmaceutical applications, since the compound obtained after thermal degradation or tautomerisation may have side effects.

The quenched from the liquid compound (QFTM) has the tautomeric composition of the liquid (%A = 48.9, %B = 33.6, %C = 17.5) which is slightly different from that of the MIL compound.

The freeze-dried (FD) and spray-dried (SD) compounds have a similar tautomeric composition (for the FD: %A = 23.4, %B = 68.4, %C= 8.2; for the SD: %A = 29.4, %B = 61.8, %C= 8.8), which is very different from that of the other amorphous samples. This is due to the mutarotation which occurred when crystalline lactulose has been put in aqueous solution. We have been able to establish experimentally and by MD simulations that the tautomer B (majority tautomer in the SD and FD samples) has an anti-plasticising effect on the system, whereas the tautomer A (majority tautomer in the MIL sample) has a plasticising effect. MD simulations particularly revealed that the molecular mobility of tautomer B molecules is significantly lower than that of tautomer A since tautomer B molecules form more intermolecular HBs due to the geometry of the molecule. The difference in chemical composition between these compounds (SD and FD) and the MIL one thus resulted in an increase of the T_g of the material.

True physical differences between the amorphous states: stability, residual crystallinity, local hydrogen bonds organisations

The chemical differences between the different amorphous compounds did not appear to impact the structure of those compounds probed by neutron scattering (D7 and IN1). We thus had the possibility of studying the effects of the amorphisation technique on the physical state of the compound, independently of any chemical change.

The milled compound is the only amorphous system which probably contains local order structures very similar to crystals. This has been revealed:

- by the presence of two well-defined bumps at Q = 0.74 $Å^{-1}$ and Q = 0.92 $Å^{-1}$ corresponding almost to Bragg peaks of the crystal diffraction pattern measured by neutron diffraction (D7, ILL).
- by the fact that MIL and anhydrous crystalline samples have the same CH stretching frequency as measured by inelastic neutron scattering (IN1, ILL).

These local order structures are also probably responsible for the easier recrystallisation propensity of the milled material over the other amorphous compounds upon annealing.

The structural information obtained by neutron scattering (D7 and IN1) does not reveal any particular order in the QFTM compound.

Neutron scattering experiments combined with MD simulations suggest the following:

- The FD compound locally (first neighbour shell) has the same structure than that of the QFTM compound (both have the same CH vibrational frequency, as seen on IN1).

However, this structure seems to be less extended in the FD sample than in the QFTM sample (the first sharp diffraction peak (FSDP) of the FD sample is broader than that of the QFTM sample).

- The SD compound has a structure globally different from that of the other amorphous compounds. It appears to have a specific local order, which gives rise to low energy peaks (below 120 meV) on the spectrum measured on IN1. Moreover, the molecules may have adopted particular conformations in this compound (CH stretching softening, as seen on IN1).

During the quenching of the liquid, a local order precursor of a stable (or metastable) crystalline phase at low temperature is generally developed. However, neutron scattering results showed that the local order in the QFTM compound is different from that of the SD compound. Speculatively, this difference of local order in the SD compound is likely to induce a frustration of the recrystallisation process. We can therefore expect that the spray-drying method is the amorphisation method creating the least unstable amorphous compound. Long annealing experiments of the different amorphous forms should be implemented to check that point. It is worth noticing that our assumption is well in line with experimental results obtained on trehalose materials [271], which showed that amorphous samples produced by different routes crystallise upon heating (10 °C/min), except the SD one.
Therefore:

$$\text{MIL} < \text{FD} \; ; \; \text{QFTM} < \text{SD} \longrightarrow \text{increasing physical stability}$$

In addition, α-relaxation time below and above T_g, as well as porosity, bulk density and true (local) density of the different amorphous materials have to be measured, in order to confirm our different interpretations.

Stability of the milled sample

Our results also demonstrated that it was possible to produce an amorphous compound upon milling that does not recrystallise during heating at 5 °C/min. This has been achieved on a crystalline compound milled during only 8 hours. This is a very exceptional result, which reflects the great ease of lactulose to be amorphised during milling. The characteristic time of the amorphisation kinetic during milling was estimated to be 11 min. This time is much shorter than that of other sugars (typically 1 h for identical milling conditions) such as lactose or trehalose, disaccharides of the same chemical formula having conformations close to that of lactulose.

Trihydrate crystal

We have succeeded to formulate trihydrate crystalline lactulose by an unprecedented method of co-milling of a anhydrous crystal/water mixture in the molar proportions [1:3]. Unlike anhydrous crystal, it has the property of being made up of a single tautomer (tautomer A). It is quite remarkable that milling makes it possible to increase the tautomeric purity of a material. The identification of the physico-chemical mechanisms favouring this chemical purification would be an interesting extension of this work. In addition it was possible to produce an amorphous lactulose by dehydrating the trihydrate crystal. Dehydration of the

trihydrate crystal thus provides a fifth amorphisation route. A thorough study of this amorphisation route appears to be another promising work to perform in the near future.

Perspectives on further studies from neutron scattering and simulations

By means of neutron diffraction experiments (performed on D3, ILL), no difference of the molecule structure in the different amorphous compounds has been detected. However, it will be interesting to probe these compounds on synchrotron diffractometers even if the correlations due to H atoms are absent. Since synchrotron diffractometers have better resolution than neutron ones, eventual intramolecular differences between the amorphous compounds might be revealed.

Our results showed that thermal degradation might have an influence on the Boson peak (BP) of the QFTM sample measured on FOCUS (PSI, Villigen). At the time of the FOCUS experiment, we had not yet set up this rather exotic way to produce a kind of "non-degraded quenched from the melt" compound (actually, it is a quenched from the softened MIL, SD or FD sample, see chapter 3 for details). The BP of this "non-degraded quenched from the melt" compound should be measured later, in order to complete our study.

Moreover, neutron spectroscopy experiments (performed on IN1, ILL) revealed a puzzling softening of the CH stretching vibration. We have performed MD simulations which suggest that molecular conformations might be different in the SD sample than in the others. This new molecular conformations are likely to have different vibration frequencies from the others. DFT calculations must be performed to verify this assumption. In addition, infrared experiments might be performed on the different compounds to supplement neutron results.

By MD simulations, an amorphous box is usually generated by hyper-quenching a liquid box. In this thesis, we have also tried to generate an amorphous box comparable to a MIL sample, by shearing a crystalline box. The results obtained are satisfactory, since the "sheared box" obtained is completely disordered. Works are in progress to analyse the physical changes that occurred during the shearing. They might give supplement information on the differences between a QFTM sample and a MIL sample.

Throughout this work, we have studied the amorphous compounds as produced under the conditions described in chapter 2. The MIL, SD and FD compounds contained almost 3% w/w of water. However, several works [272–276] have pointed out the important role of water on the stability of amorphous pharmaceutical compounds. A study of the evolution of the structural, dynamic and thermodynamic properties of the different amorphous lactulose according to their water content would be interesting to do in the future.

Appendix A

Modulated DSC

Temperature Modulated Differential Scanning Calorimetry (MDSC) is a technique that uses a non-linear variation of temperature (sinusoidal variation) which is added to the linear part of the "conventional" DSC [277]. This technique appeared some twenty years ago thanks to the works of Reading et al. [278]. MDSC has also been the subject of several other studies [277, 279–281]. In this annex we will briefly recall the main lines concerning MDSC, as it has been done in previous theses in our laboratory.

In a MDSC experiment, the temperature evolution of the oven as a function of time is given by Eq. A.1:

$$T(t) = T_i + qt + A\sin(\omega t) \tag{A.1}$$

Where:

- T(t) is the oven temperature at time t
- T_i is the initial temperature
- t is the time
- q is the linear scanning speed
- A is the modulation amplitude
- ω is the modulation pulsation

Eq. A.1 can be divided in two parts. The first part includes the first two terms, and is characteristic of a conventional DSC experiment. On the other hand the second part, Asin(ωt), represents a temperature sinusoidal oscillation of low-amplitude.
The time derivative of the oven temperature reflects the perturbation undergone by the sample:

$$\dot{T}(t) = q + A\omega\cos(\omega t) \tag{A.2}$$

The response of the sample is a modulated heat flow of the same period (but out of phase with respect to the perturbation):

$$\dot{Q}(t) = qC_p(q, qt) + \dot{Q}_{cin}(qt, t) + \dot{Q}_0(\omega)\cos(\omega t - \varphi) \tag{A.3}$$

As Eq. A.1, Eq. A.3 can be divided in two parts. The first part ($qC_p(q,qt) + \dot{Q}_{cin}(qt,t)$) is identical to the response of the sample during a conventional DSC experiment. The second part ($\dot{Q}_0(\omega)\cos(\omega t - \varphi)$) is the response of the sample during a MDSC experiment. These two parts are estimated by MDSC, by doing the time average of the modulated heat flow over four modulation cycles. The information retrieved by a conventional DSC technique is therefore achievable with a MDSC experiment thanks to the mean heat flow, which is written as:

$$\dot{Q} = \left\langle \dot{Q}(qt,t) \right\rangle = qC_p(q,qt) + \dot{Q}_{cin}(qt,t) \tag{A.4}$$

The first term ($qC_p(q,qt)$) is characteristic of a conventional DSC experiment. This term comes from the fact that, when a sample is subjected to a temperature variation, it exchanges a heat flow which is proportional to its specific heat C_p, with the source. The second term ($\dot{Q}_{cin}(qt,t)$) is due to the fact that certain transformations, in particular those involving enthalpy catch-up during the heating of a glass, or latent heat, bring an additional heat flow, noted $\dot{Q}_{cin}$.

Using the complex notation, the perturbation of a modulated signal is given by Eq. A.5, and the complex susceptibility - defines by the ratio between the complex amplitude of the response and the perturbation - is given by Eq. A.6:

$$\dot{T}_{mod} = \dot{T}_0 \cos(\omega t) = \mathrm{Re}\left(\dot{T}_0 \exp(-i\omega t)\right) \tag{A.5}$$

$$\chi^*(\omega) = \frac{\dot{Q}_{\omega,\varphi}}{\dot{T}_0} = C_p^*(\omega) + \chi_{inc}^*(\omega) \tag{A.6}$$

Where:

- $C_p^*(\omega)$ represents the complex specific heat of the material. It indicates how the material responds to the sinusoidal temperature perturbation, without any kinetic process.

- $\chi_{inc}^*(\omega)$ is associated with kinetic transformations (structural relaxations, crystallisations ...). It is the imaginary term of Eq. A.6.

Experimentally, the complex susceptibility $\chi_{inc}^*(\omega)$ is easily accessible. It corresponds to the ratio between the amplitudes of the oscillations of the heat flux and of the modulation of temperature. Its modulus is given by Eq. A.7:

$$\left|\chi^*(\omega)\right| = \frac{\dot{Q}_0}{\dot{T}_0} \tag{A.7}$$

An example of the information accessible by MDSC is illustrated in figure A.1. This shows results obtained on maltitol [279].

In the figure, one can see that:

- the phase shift φ has an extremum at T_ω = 48 °C.

- there is a specific heat jump at T_g = 44 °C characteristic of a glass transition.

- A jump of the modulated specific heat amplitude at T_ω = 48 °C.

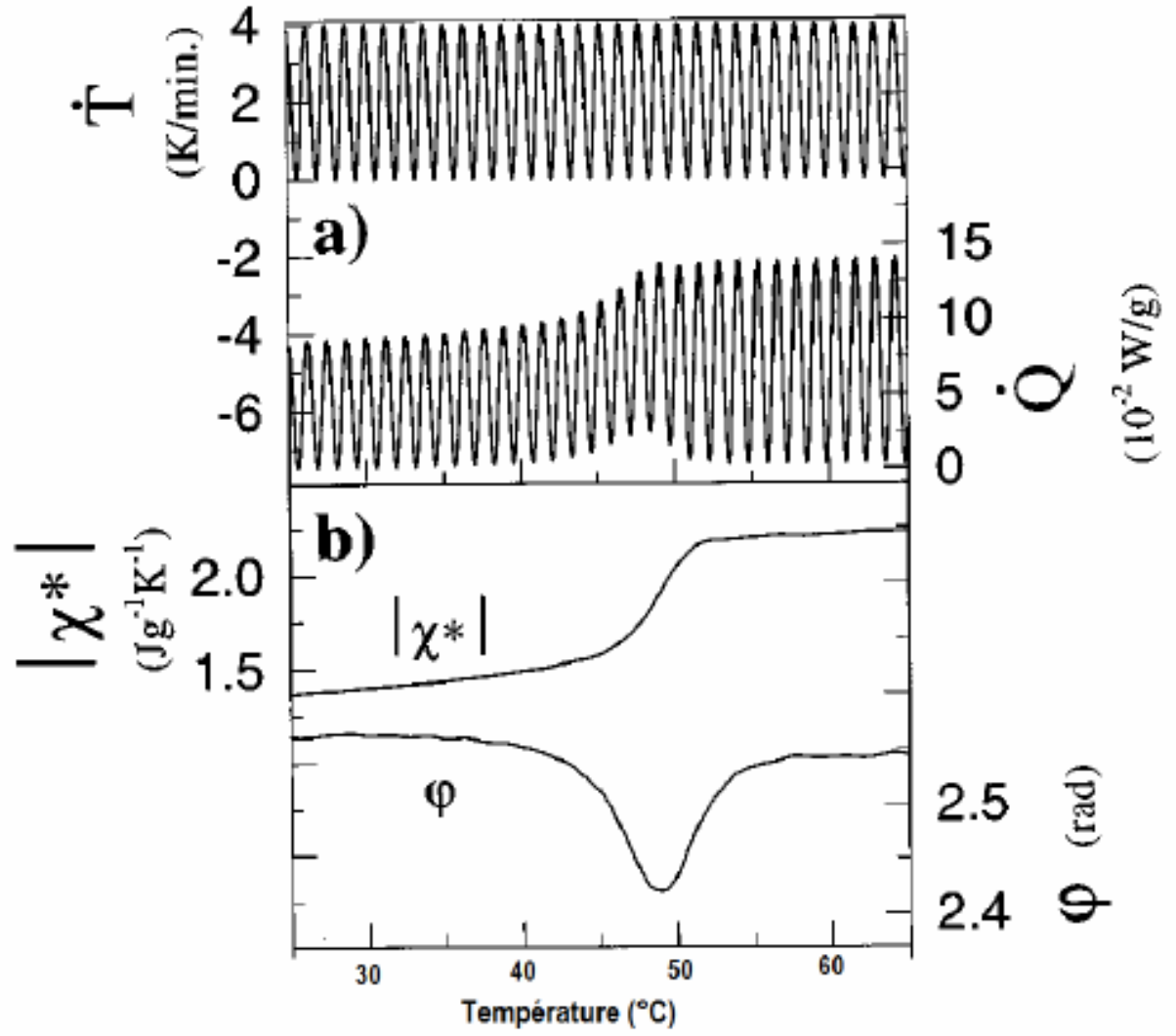

Figure A.1 – a) Raw MDSC signals: evolution of the derivatives of the modulated heat flow and the modulated temperature, as a function of temperature.
b) Evolution of the specific heat and the phase shift that occurs in the glass transition region, as a function of temperature.
The curves were recorded during heating at 2 °C/min, with a modulation amplitude A = 0.2 °C. Taken from [279].

T_ω is function of the modulation frequency whereas, T_g is function of the average scanning speed. This explains the difference between the two temperatures at the glass transition.

In a MDSC experiment, the total heat flow can be decomposed into a reversible heat flow and a non reversible heat flow:

- **the reversible heat flow** corresponds to the response of the sample in term of heat capacity. It is proportional to the specific heat of the material.
- **the non reversible heat flow** shows the kinetic contributions (physical aging or recrystallisation) of the thermal response. It is obtained from the subtraction between the reversible heat flow and the total heat flow.

Appendix B

Neutron data treatment

B.1 Data corrections from scratch: "instrumental" corrections

When doing a neutron scattering experiment, the intensity $I^{meas}(2\theta)$ recorded is proportional to the experimental differential cross-section per atom of the sample and its surroundings. This measured intensity does not exactly represent the number of neutrons scattered by the sample ($I^{sca}(2\theta)$). Indeed, the number of neutrons detected at the different detectors should be corrected knowing some features of the instruments, in order to be reliable and more realistic (i.e. closer to $I^{sca}(2\theta)$). The instrument responsible usually does these operations. They account for the detector dead time correction, normalisation to monitor counts and correction of the different efficiencies of each detector. The experimental error is also determined, and for some cases, numor grouping have to be performed.

- **Detector dead time correction:** The detector dead time is the minimum amount of time that must separate two neutrons arriving to the detector so that they will be recorded as distinct events. There are thus some hot neutrons that are not detected, and a correction should be applied.

- **Normalisation to monitor:** The neutron flux can have small fluctuations and may differ at different moments of the experiment. All measurements thus have to be normalised to the number of neutrons detected by the monitor (the monitor counts the number of neutrons just before the sample).

- **Detector efficiency:** Because detectors are not perfectly identical, they do not have the same efficiency. The different detectors can detect a different number of neutrons when the same incident flux is impinging on them. The different detectors thus have to be calibrated.

- **Numor grouping:** Due to the angular separation between detectors, several measurements have to be performed with the detector bank at different offset angles, to be able to measure the whole scattering (this is done for many diffractometers). Each one of these single measurements is called numor (it represents the NUMber Of Runs) and yields an incomplete spectrum. The grouping and averaging of the different numors into a single measurement thus have to be performed.

- **Experimental error:** after each experiment, it is always important to know the experimental error, i.e. how much the measurement differs from the average value of the magnitude. Errors are usually estimated using the fact that the standard deviation in a

counting experiment is predicted to tend to $\sigma = \sqrt{N}$ as the number of counts N tends to infinity.

B.2 Diffraction

When all those instrumental corrections are applied, the diffraction pattern of the neutrons scattered by the sample and its surroundings I(2θ) is obtained. It can be easily convert to I(Q):

$$Q = \frac{4\pi}{\lambda} \sin(2\theta/2) \tag{B.1}$$

I(Q) should be corrected in order to obtain the scattering function S(Q) of the sample in absolute units, that can be compared with others techniques, or to experiments performed with other instruments on the same material in similar conditions. Therefore, one should:

- Carefully subtract the non-sample contributions from the background (due to electronic noise for example, or radiations), from the neutrons scattered by the sample environment and the sample holder, in order to extract the sample contribution. In our case, we have measure the empty sample environment (empty instrument $I_{MTI}(Q)$) as the background. Further measurement of an absorbing specimen (e.g. cadmium, $^{10}B_4C$) and of the sample holder within the sample environment (the empty can $I_{can}(Q)$) have to be carried out. They are useful for performing attenuation corrections.

- Correct the signal from attenuation (resulting from both scattering and absorption) and multiple scattering events.

When considering the sample as having several point-like, the mean free path of the neutrons before interacting with the sample is much larger than the sample dimensions. Then, most of them will go through the sample without interacting, and only a few will be scattered (likely just once) or absorbed. In such situation, there is almost no need to perform attenuation and multiple scattering corrections. Unfortunately, the flux of neutrons is very low, even in a reactor source, and one usually needs to fill a big amount of sample in the container in order to reduce the counting time. Therefore, attenuation and multiple scattering events can become non negligible and may be to correct.

Paalman and Pings [282] have treated attenuation corrections arising from absorption and scattering of a completely and uniformly illuminated sample of cylindrical geometry in an annular container. They provide coefficients, which depend on the scattering angle, and allow a proper subtraction of the empty container diffractogram taking into account the attenuation of the sample and its container. This method can be extended to other sample and container geometry [283]. However, it is important to precise that its approach does not take into account multiple scattering events. It should therefore be used after correcting the signal from multiple scattering.

Multiple scattering is quite difficult to correct, and highly depends on the sample and the sample container geometry. It is always better to avoid them at more by choosing appropriate sample container geometry (annular container for example). Nevertheless, if needed, one can treat them thanks to numerical approaches (Monte Carlo simulations in general),

which commonly assume isotropic and elastic scattering [284–287].

After the signal has been treated from non-sample contributions, attenuation and multiple scattering, the new I(Q) is a single-scattering non attenuated signal of the sample, without any background. Some further treatments should be performed to extract the S(Q) function:

- **Normalisation:** The normalisation of a sample diffraction intensity to an absolute cross section can be performed by comparing it to another sample of known cross-section and volume in the beam. In our case, a vanadium rod was measured for this purpose. Vanadium is commonly used as a normalisation standard because its accurately known cross-section is almost completely incoherent and therefore isotropic. Its diffraction pattern is quite a horizontal line, quite appropriate for normalisation purposes. The normalisation by vanadium does also "treat", in a very simple way, the resolution in the intensity measured.

- **Inelasticity:** In practice, in diffraction experiments, the detectors integrate all the neutrons regardless of their energy exchanges with the sample (this is why the scattering function measured on a diffractometer is named total scattering function). However, inelastic events should be avoided, or treated in order to fulfill the static approximation [250]. The breakdown of the static approximation happens for samples that contain light atoms such as H, more subject to large recoil after the scattering event, or for higher scattering angles, where the energy and momentum exchange is greater. If inelasticity effects are not well corrected, too short interatomic distances may be obtained in the PDF function [250]. The common way to treat inelasticity effects is by applying Placzek corrections [288].

After having done all those treatments, the total scattering function S(Q) is therefore obtained.

D3 data treatment

Spin flip and non-spin flip intensities have been measured for each sample, using D3 polarised neutron diffractometer. However, some of the corrections previously mentioned have to be done only on the total intensity. We have used the following procedure:

1) We obtain $I^{total} = I^{spinflip} + I^{non\text{-}spinflip}$ of the sample, the vanadium (vana), the empty can (can) and the empty instument (MTI). For the case of the sample, using Eqs. 5.17 5.18, we obtained the I_{coh} and I_{inc} not yet corrected. This calculation is useful to know the ratio of the coherent and incoherent contributions in the total scattering. This information will be needed afterwards.

2) We remove the MTI signal from the total signal of the sample, the vanadium and the empty can signals:

$$\begin{cases} I^{new}_{sample} = I_{sample} - I_{MTI} \\ I^{new}_{vana} = I_{vana} - I_{MTI} \\ I^{new}_{can} = I_{can} - I_{MTI} \end{cases} \tag{B.2}$$

3) Thereafter, the sample and empty can intensities are normalised with the vanadium to obtained the differential scattering cross section

$$\begin{cases} \sigma_{\text{sample}} = c1 * \frac{I^{\text{new}}_{\text{sample}}}{I^{\text{new}}_{\text{vana}}} \\ \sigma_{\text{can}} = c2 * \frac{I^{\text{new}}_{\text{can}}}{I^{\text{new}}_{\text{vana}}} \end{cases} \tag{B.3}$$

Where c1 is the ratio between the number of vanadium atoms "seen" by the neutrons during the vanadium measurement, and the number of atoms (sample + container) seen by the neutrons during the sample measurement. Similarly, c2 is the ratio between the number of vanadium atoms seen by the neutrons during the vanadium measurement, and the number of atoms seen by the neutrons during the empty can measurement.

4) We thus remove the empty can contribution in σ_{sample}:

$$\sigma^{\text{new}}_{\text{sample}} = \sigma_{\text{sample}} - 0.90 * \sigma_{\text{can}} \tag{B.4}$$

This new σ_{sample} is thus separated into the coherent and incoherent contribution at each Q value, following the ratio previously determined. We thus obtained the coherent scattering cross section σ_{coh}, where there still have inelastic contribution, and a small amount of incoherent scattering due to isotopic disorder. Both are treated with Placzek corrections [288]: a Placzek polynomial is fitted on the data, and removed from the data to obtained the total scattering function S(Q).

NB: We have also tried to correct D3 data from multiple scattering, attenuation and inelasticity effects in a consistent way using Monte Carlo (MC) simulations. MC simulations perform all those three corrections as a whole, and might be more accurate. However, our tests have shown that the results obtained are very close to that obtained with the "classic" treatment method. The results presented in chapter 5 have thus been obtained after having reduce data in the "classic" approach, for obvious reason of simplicity. The interested reader is referred to articles of Dawidowski [287, 289] for a better understanding of the MC simulations method.

D7 data treatment

As in the case of D3 measurements, spin-flip and non spin-flip signals have been measured and treated following the same logic, in order to extract the coherent scattering cross section. We have used several routines available in the LAMP platform developed by the CS group at ILL, to reduce D7 data. A data treatment script can be found below. The new point in the script is the polarisation analysis of the incident beam. Indeed, data must be corrected for the finite polarisation of the incident beam. They must also be corrected for the analysing power of the analysers in the scattered beam, since the efficiency of the analyser highly depends on the wavelength of the detected neutron [252]. This is achieved by doing a measurement of the diffuse scattering from an amorphous silica (quartz) rod. The scattering from amorphous silica is entirely nuclear, so that for a perfectly polarised beam and perfect analysers, there should be no spin-flip scattering. Another advantage of amorphous silica is that, since it is a glass, it gives a good scattering intensity over the whole multi-detector simultaneously.

```
; Lactulose measurement, Nov 2016
V= 8.539   ; Vanadium mass
D= 20161115   ; D7 calibration file
Q= 277999   ; Quartz calibration for (X,Y,Z)
W= 278051   ; Vanadium calibration
Z=[]            ; Zero detector 2
; Isotopic incoherent from sample  (2.0*1.1 + 4.0*0.32)
   /(4.0*!pi)
;RDSET,path='/net/serdon/illdata/data/d7/exp_6-05-974/
   processed'

; Load empties
w1=rdand(277978,277988)
w1=w1(*,0:1,*) & p1(2)=2
w1=d7_calibration(w1,calib=d)

; Load cadmium
w2=rdand(278022,278032)
w2=w2(*,0:1,*) & p2(2)=2
w2=d7_calibration(w2,calib=d)

;RDSET,path='/net/serdon/illdata/data/d7/exp_6-05-974/rawdata
   /'

; QFTM
S= 2.7    ; Sample mass
F= 12.0*12.011+22.0*1.0079+11.0*15.999; Formula weight

; Transmission
A=(mean([7696.0,9552.0,7437.0,7504.0])-86.0)/(mean
   ([12787.0,12768.0])-86.0)
B=A

; Load Data
w4=rdand(279189,279199) ; Run 1
w5=rdand(279200,279210) & w4=w4+w5 & n4=n4+n5   ; Run 2
w5=rdand(279211,279221) & w4=w4+w5 & n4=n4+n5   ; Run 3
w5=rdand(279222,279232) & w4=w4+w5 & n4=n4+n5   ; Run 4
w5=rdand(279233,279243) & w4=w4+w5 & n4=n4+n5   ; Run 5
w40=w4
@standard_reduction_6pt
w20=w56     ; Data vs Q
w30=w55     ; All data vs twotheta
;d17_save,w20,'QFTM.txt',header='Lactulose QFTM @ 300K. [Tot
   NSI NC]',outformat='xye'
```

B.3 Spectroscopy

FOCUS data treatment

We have used several routines available in the LAMP platform developed by the CS group at ILL, to reduce FOCUS data. A data treatment script of the can be found below. Basically, it has the following steps:

- Suppression of bad detectors.
- Normalisation of the data to the rate counts of the monitor mounts in front of the sample (i.e. normalise to the number of incident neutrons).
- Time of flight (TOF) correction (wavelength calibration) at the different cycles of the experiment.
- Subtraction of sample container contribution, taking into account the sample transmission.
- Detector efficiency correction. This is done by normalising the data with the integrated intensity of a vanadium sample with identical to the sample container geometry. This normalisation also "corrects" the Debye-Waller (DW) decrease at high Q. The vanadium being a dominant incoherent scatterer, its spectrum should not be angular dependent (no coherent signal), and any change in the value obtained at the different detectors is due to a different detector efficiencies, but also to the DW factor.
- Detector grouping of the data to improve the statistics of the signal.
- Conversion from TOF to ω, and 2θ to Q, in order to obtain S(Q,ω).
- Further energy (ω) and wave vector (Q) transfer binning are applied.

We have assumed the data overlapping negligible (i.e. there are a negligible amount of neutrons per pulse which are counted at the next pulses), and have thus not corrected them. Multiple scattering has also been considered negligible.

```
;;;;;;;;;;;;;;;;;;;;;;;;;;;;
; Fred Ngono, FOCUS data treatment
;;;;;;;;;;;;;;;;;;;;;;;;;;;;

; list of bad detectors
s = '1-9,13-14,16-17,19-20,22-23,25-26,255,368-369,371-375'

w1 = rdopr('2561>2570')  ; sample
w1 = normalise(w1)
w1 = lineup(w1)
w1 = remove_spectra(w1, badSpectra=s, /verbose)
w1 = sumbank(w1)

w2 = rdopr('2506>2510')  ; vana
w2 = normalise(w2)
w2 = lineup(w2)
```

```
w2 = remove_spectra(w2, badSpectra=s, /verbose)
w2 = sumbank(w2)

w3 = rdopr('2465>2466')  ; empty cell
w3 = normalise(w3)
w3 = lineup(w3)
w3 = remove_spectra(w3, badSpectra=s, /verbose)
w3 = sumbank(w3)

w4 = w1 - 0.9*w3
e4 = sqrt(e1^2 + (0.9*e3)^2)

w5 = w2 - 0.9*w3
e5 = sqrt(e2^2 + (0.9*e3)^2)

w7 = vnorm(w4, w5, min=500,max=565) ; bords de la ligne
   elastique, given in TOF
w8 = corr_tof(w7, /det_eff) ; relation detector efficiency vs
    energy, as on D7

w9 = t2e(w8)  ; This is S(2theta,w)
w20 = w9*1e6
w18=reb(w20, dE=0.01, /force) ; This gives S(2theta,w) where
   w is rebinned.

w11 = gdos(w9, emin=-25, emax=0, /inverse)
w12 = total(w11,2) ; This is g(w)
w15 = w12/int_tabulated(x12,w12)  ; w15 is the normalised
   gdos(w) function
```

IN1-LAGRANGE data treatment

We have used several routines available in the LAMP platform developed by the CS group at ILL, to reduce IN1-LAGRANGE data. A data treatment script of the can be found below. Basically, it has the following steps:

- Subtraction of the sample container contribution.
- Efficiency correction of the monitor.
- Subtraction of the background.
- Normalisation of the integrated signal to unity.

```
;;;;;;;;;;;;;;;;;;;;;;;;;;;
; Frederic Ngono, IN1 data treatment
;;;;;;;;;;;;;;;;;;;;;;;;;;;
```

```
; The workspace w50 should have the water file result
   measured with the monochromator used during the experiment

; T=10K
w1=rdrun(9850)  ; sample
w1=w1/n1 & x1=x1 & e1=e1/n1 & n1[*] = 1.0
w2=rdrun(9851)  ; sample
w2=w2/n2 & x2=x2 & e2=e2/n2 & n2[*] = 1.0
w3=rdrun(9852)  ; sample
w3=w3/n3 & x3=x3 & e3=e3/n3 & n3[*] = 1.0
w5=[w1,w2,w3] & x5=[x1,x2,x3] & e5=[e1,e2,e3] & n5=[n1,n2,n3]
w6=interpol(w50,x50,x5) & x6=interpol(x50,x50,x5) & n6=
   interpol(n50,x50,x5) & e6=interpol(e50,x50,x5)
w7=w5*w6 & x7=x5 & n7=n5 & e7=e5
w10=rdopr('9916>9918') ; empty cell
w10=w10/n10 & x10=x10 & e10=e10/n10 & n10[*] = 1.0
w16=interpol(w50,x50,x10) & x16=interpol(x50,x50,x10) & n16=
   interpol(n50,x50,x10) & e16=interpol(e50,x50,x10)
w17=w10*w16 & x17=x10 & n17=n10 & e17=e10
w20=w7-w17 & x20=x7-4.5 & e20=sqrt(e7^2+e17^2) ; e is the
   errorbar, x is the energy, we always have a shift of 4.5
   meV to do.
w40=w20/int_tabulated(x20,w20) ; w40 is the normalised gdos(w
   ) function.
```

Appendix C

The OPLS force field

In the matter, atoms interact together. The idea behind a force field (FF) is to model the true interatomic potential by a mathematical expression. It must be simple enough to be quickly evaluated (with the available computational power), but sufficiently detailed to reproduce the properties of interest. The FF consists of an analytical form of the interatomic potential energy, $U(\vec{r}_1, \vec{r}_2, \ldots, \vec{r}_N)$, and a set of parameters entering into this form. These parameters can be obtained:

- from ab initio calculations
- from semi-empirical quantum mechanical calculations
- by fitting to experimental data such as neutron, X-ray, NMR, etc.

There are many FF available in the literature, oriented to treat different kinds of systems. Almost all of them are always composed of intramolecular terms - used to describe bonded interactions[1] (stretching, bending and dihedral) -, and "intermolecular" terms - used to model non-bonded interactions (Van der Waals, electrostatic) -. For the most complex of them, there are also additional terms (cross terms, describing the coupling between motions as stretching and bending, etc.) that allow to better reproduce the experimental results.

The OPLS-AA (optimised potentials for liquid simulations all-atom) FF is a second generation force field designed for organic molecules. Bond stretching and angle bending parameters have been adopted mostly from the AMBER all-atom FF (it is a FF primarily developed for protein and nucleic acid systems) [290–292]. Torsional parameters were primarily determined by fitting to rotational energy profiles obtained from ab initio calculations [194]. Torsional parameters were later refined using better fitting techniques and accurate ab initio calculations [293]. Non-bonded parameters were developed in conjunction with Monte Carlo statistical mechanics simulations (performed with the BOSS program [294], version 3.6) by computing the structures and thermodynamic properties of more than 30 pure organic liquids (methanol, propanol, 2-propanol, 2-methyl-2-propanol, ethyl methyl sulfide, etc.) [194].

Some parts of the FF parameters used during the MD simulations performed in this work (with the DL_POLY software) are shown below.

[1] Interactions between atoms linked by covalent bonds.

```
lactulose
UNITS kcal
MOLECULES     1
lactulose
nummols      64
atoms       45
 OH0171     15.999400    -0.700000     1     0
 OH0171     15.999400    -0.700000     1     0
 OH0171     15.999400    -0.700000     1     0
 OS0186     15.999400    -0.400000     1     0
 HC0194      1.008000     0.100000     1     0
.
.
.
 HO0172      1.008000     0.418000     1     0
 HO0172      1.008000     0.435000     1     0
 CT0173     12.010000     0.145000     1     0
 HO0172      1.008000     0.418000     1     0
 HO0172      1.008000     0.418000     1     0
bonds    46
harm     1    19 1106.000000     0.945000
harm     1    21  640.000000     1.410000
harm     2    22 1106.000000     0.945000
harm     2    23  640.000000     1.410000
harm     3    24 1106.000000     0.945000
.
.
.
harm    35    40  680.000000     1.090000
harm    36    38  536.000000     1.529000
harm    37    43  680.000000     1.090000
harm    38    40  536.000000     1.529000
harm    39    43  680.000000     1.090000
harm    40    43  536.000000     1.529000
angles    83
harm    19     1    21   110.000000   108.500000
harm    22     2    23   110.000000   108.500000
harm    24     3    27   110.000000   108.500000
harm    20     4    29   120.000000   109.500000
harm    28     6    33   110.000000   108.500000
harm    20     8    38   120.000000   109.500000
harm    25    10    41   110.000000   108.500000
harm    31    12    42   110.000000   108.500000
harm    36    14    44   110.000000   108.500000
harm    31    16    40   120.000000   109.500000
.
.
.
```

```
harm    16    40    43   100.000000   109.500000
harm    35    40    38    75.000000   110.700000
harm    35    40    43    75.000000   110.700000
harm    38    40    43   116.700000   112.700000
harm    18    43    37    70.000000   109.500000
harm    18    43    39    70.000000   109.500000
harm    18    43    40   100.000000   109.500000
harm    37    43    39    66.000000   107.800000
harm    37    43    40    75.000000   110.700000
harm    39    43    40    75.000000   110.700000
dihedrals   189
cos    19     1    21     7     0.176200     0.000000     3.000000
0.500000     0.500000
cos    19     1    21    23     1.337000     0.000000     1.000000
0.500000     0.500000
cos    19     1    21    23    -1.441500   180.000000     2.000000
0.500000     0.500000
cos    19     1    21    23     0.513000     0.000000     3.000000
0.500000     0.500000
cos    22     2    23     9     0.176200     0.000000     3.000000
0.500000     0.500000
cos    22     2    23    21     1.337000     0.000000     1.000000
0.500000     0.500000
cos    22     2    23    21    -1.441500   180.000000     2.000000
0.500000     0.500000
cos    22     2    23    21     0.513000     0.000000     3.000000
0.500000     0.500000
cos    22     2    23    27     1.337000     0.000000     1.000000
0.500000     0.500000
cos    22     2    23    27    -1.441500   180.000000     2.000000
0.500000     0.500000
cos    22     2    23    27     0.513000     0.000000     3.000000
0.500000     0.500000
.
.
.
cos    16    40    43    18     2.159500     0.000000     1.000000
0.500000     0.500000
cos    16    40    43    37     0.234000     0.000000     3.000000
0.500000     0.500000
cos    16    40    43    39     0.234000     0.000000     3.000000
0.500000     0.500000
cos    35    40    43    18     0.234000     0.000000     3.000000
0.500000     0.500000
cos    35    40    43    37     0.150000     0.000000     3.000000
0.500000     0.500000
cos    35    40    43    39     0.150000     0.000000     3.000000
0.500000     0.500000
```

```
cos    38    40    43    18     0.855500     0.000000     1.000000
0.500000     0.500000
cos    38    40    43    18    -0.250000   180.000000     2.000000
0.500000     0.500000
cos    38    40    43    18     0.331500     0.000000     3.000000
0.500000     0.500000
cos    38    40    43    37     0.150000     0.000000     3.000000
0.500000     0.500000
cos    38    40    43    39     0.150000     0.000000     3.000000
0.500000     0.500000
finish
VDW    36
OH0171   OH0171     lj      0.170000     3.070000
OH0171   OS0186     lj      0.154272     2.983790
OH0171   HC0194     lj      0.071414     2.770379
OH0171   HC0176     lj      0.071414     2.770379
OH0171   CO0193     lj      0.105925     3.277957
OH0171   CT0174     lj      0.105925     3.277957
OH0171   CT0173     lj      0.105925     3.277957
.
.
.
CO0193   CO0198     lj      0.066000     3.500000
CT0174   CT0174     lj      0.066000     3.500000
CT0174   CT0173     lj      0.066000     3.500000
CT0174   CO0198     lj      0.066000     3.500000
CT0173   CT0173     lj      0.066000     3.500000
CT0173   CO0198     lj      0.066000     3.500000
CO0198   CO0198     lj      0.066000     3.500000
CLOSE
```

References

[1] M. Descamps and J. F. Willart. *Some Facets of Molecular Disorder in Crystalline and Amorphous Pharmaceuticals*, pages 1–56. Wiley-VCH Verlag, 2016. 1

[2] Sharad B. Murdande, Michael J. Pikal, Ravi M. Shanker, and Robin H. Bogner. Solubility advantage of amorphous pharmaceuticals: I. a thermodynamic analysis. *Journal of Pharmaceutical Sciences*, 99(3):1254–1264, 2010. 1

[3] D. Q. M. Craig, P. G. Royall, V. L. Kett, and M. L. Hopton. The relevance of the amorphous state to pharmaceutical dosage forms: glassy drugs and freeze dried systems. *International Journal of Pharmaceutics*, 179(2):179–207, 1999.

[4] K. A. Graeser, J. E. Patterson, and T. Rades. Physical stability of amorphous drugs: Evaluation of thermodynamic and kinetic parameters. *Journal of Pharmacy and Pharmacology*, 60:116, 2008. 1

[5] Sisir Bhattacharya and Raj Suryanarayanan. Local mobility in amorphous pharmaceuticals-characterization and implications on stability. *Journal of Pharmaceutical Sciences*, 98(9):2935–2953, 2009. 1

[6] D. Bahl, J. Hudak, and R.H. Bogner. Comparison of the ability of various pharmaceutical silicates to amorphize and enhance dissolution of indomethacine upon co-grinding. *Pharm. Dev. Technol.*, 13(3):255–269, 2008. 1

[7] Bruno C. Hancock and George Zografi. Characteristics and significance of the amorphous state in pharmaceutical systems. *Journal of Pharmaceutical Sciences*, 86(1):1–12, 1997. 1

[8] B.C. Hancock and M. Parks. What is the true solubility advantage for amorphous pharmaceuticals? *Pharmaceutical Research*, 17(4):397–404, 2000.

[9] Jared A. Baird and Lynne S. Taylor. Evaluation of amorphous solid dispersion properties using thermal analysis techniques. *Advanced Drug Delivery Reviews*, 64(5):396–421, 2012. 1

[10] Ketan T. Savjani, Anuradha K. Gajjar, and Jignasa K. Savjani. Drug solubility: Importance and enhancement techniques. *ISRN Pharmaceutics*, 2012:1–10, 2012. 1

[11] N. Jagadeesh Babu and Ashwini Nangia. Solubility advantage of amorphous drugs and pharmaceutical cocrystals. *Crystal Growth & Design*, 11(7):2662–2679, 2011. 1

[12] C. Leuner and J. Dressman. Improving drug solubility for oral delivery using solid dispersions. *European Journal of Pharmaceutics and Biopharmaceutics*, 50(1):47–60, 2000. 1

[13] J. F. Willart and M. Descamps. Solid state amorphization of pharmaceuticals. *Molecular Pharmaceutics*, 5(6):905–920, 2008. xii, 2, 3, 24, 25

[14] D.P. Singh. Solid dispersions: Promising feature : A review. *International Journal of Drug Formulation & Research*, 1(2):65–82, 2010. 2

[15] T. Vasconcelos, B. Sarmento, and P. Costa. Solid dispersions as strategy to improve oral bioavailability of poor water soluble drugs. *Drug Discovery Today*, 12(23-24):1068–1075, 2007.

[16] W. L. Chiou and S. Riegelman. Pharmaceutical applications of solid dispersion systems. *Journal of Pharmaceutical Sciences*, 60(9):1281–1302, 1971.

[17] Christopher J. Roberts and Pablo G. Debenedetti. Engineering pharmaceutical stability with amorphous solids. *AIChE Journal*, 48(6):1140–1144, 2002. 2

[18] S. Jaskirat, W. Manpreet, and S. L. Harikumar. Solubility enhancement by solid dispersio method: a review. *Journal of Drug Delivery & Therapeutics*, 3(5):148–155, 2013. 2

[19] M. T. Cicerone, M. J. Pikal, and K. K. Qian. Stabilization of proteins in solid form. *Advanced Drug Delivery Reviews*, 93:14–24, 2015. 2

[20] M. Descamps and J. F. Willart. Perspectives on the amorphisation/milling relationship in pharmaceutical materials. *Advanced Drug Delivery Reviews*, 100:51–66, 2016. 2

[21] Harry G. Brittain. Effects of mechanical processing on phase composition. *Journal of Pharmaceutical Sciences*, 91(7):1573–1580, 2002. 2

[22] Peter Balaz, Marcela Achimovicova, Matej Balaz, Peter Billik, Zara Cherkezova-Zheleva, Jose Manuel Criado, Francesco Delogu, Erika Dutkova, Eric Gaffet, Francisco Jose Gotor, Rakesh Kumar, Ivan Mitov, Tadej Rojac, Mamoru Senna, Andrey Streletskii, and Krystyna Wieczorek-Ciurowa. Hallmarks of mechanochemistry: from nanoparticles to technology. *Chemical Society Reviews*, 42(18):7571–7637, 2013. 2

[23] Laszlo Takacs. The historical development of mechanochemistry. *Chemical Society Reviews*, 42(18):7649–7659, 2013.

[24] C. Suryanarayana. *Mechanical Alloying And Milling*. Marcel Dekker Incorporated, 2004. 2

[25] J. F. Willart, A. De Gusseme, S. Hemon, M. Descamps, F. Leveiller, and A. Rameau. Vitrification and polymorphism of trehalose induced by dehydration of trehalose dihydrate. *Journal of Physical Chemistry B*, 106(13):3365–3370, 2002. 2, 3, 76

[26] N. Onodera, H. Suga, and S. Seki. Glass transition in dehydrated amorphous solid. *Bulletin of the Chemical Society of Japon*, 41:2222–2222, 1968. 2

[27] N. Dujardin, J. F. Willart, E. Dudognon, A. Hédoux, Y. Guinet, L. Paccou, B. Chazallon, and M. Descamps. Solid state vitrification of crystalline α and β-D-glucose by mechanical milling. *Solid State Communications*, 148(1-2):78–82, 2008. 2, 3, 24, 89, 130

[28] J.F. Willart, V. Caron, R. Lefort, F. Danede, D. Prevost, and M. Descamps. Athermal character of the solid state amorphization of lactose induced by ball milling. *Solid State Communications*, 132(10):693–696, 2004.

[29] N. Dujardin, E. Dudognon, J. F. Willart, A. Hédoux, Y. Guinet, L. Paccou, and M. Descamps. Solid state mutarotation of glucose. *Journal of Physical Chemistry B*, 115(7):1698–1705, 2011. 2, 88, 106

[30] M. Descamps, J. F. Willart, E. Dudognon, and V. Caron. Transformation of pharmaceutical compounds upon milling and comilling: The role of tg. *Journal of Pharmaceutical Sciences*, 96(5):1398–1407, 2007. 2, 3

[31] Pablo G. Debenedetti and Frank H. Stillinger. Supercooled liquids and the glass transition. *Nature*, 410(6825):259–267, 2001. 2

[32] M. D. Ediger, C. A. Angell, and Sidney R. Nagel. Supercooled Liquids and Glasses. *The Journal of Physical Chemistry*, 100(31):13200–13212, jan 1996. 2, 20

[33] M. M. Crowley, F. Zhang, M. A. Repka, S. Thumma, S. B. Upadhye, S. K. Battu, J. W. McGinity, and C. Martin. Pharmaceutical applications of hot-melt extrusion: Part i. *Drug Development and Industrial Pharmacy*, 33(9):909–926, 2007. 2

[34] J. Broadhead, S.K. Edmond Rouan, and C.T. Rhodes. The spray drying of pharmaceuticals. *Drug Development and Industrial Pharmacy*, 18(11-12):1169–1206, jan 1992. 2, 27

[35] Xiaolin Tang and Michael J Pikal. Design of freeze-drying processes for pharmaceuticals: practical advice. *Pharmaceutical research*, 21(2):191–200, feb 2004. 3, 30

[36] J. E. Patterson, M. B. James, A. H. Forster, R. W. Lancaster, J. M. Butler, and T. Rades. Preparation of glass solutions of three poorly water soluble drugs by spray drying, melt extrusion and ball milling. *International Journal of Pharmaceutics*, 336(1):22–34, 2007. 3

[37] O. Mishima, L. D. Calvert, and E. Whalley. An apparently first-order transition between two amorphous phases of ice induced by pressure. *Nature*, 314(6006):76–78, mar 1985. 3, 10

[38] H. Eugene Stanley and Osamu Mishima. The relationship between liquid, supercooled and glassy water. *Nature*, 396(6709):329–335, nov 1998. 3, 10

[39] Men Zhu, Jun Qiang Wang, John H. Perepezko, and Lian Yu. Possible existence of two amorphous phases of d -mannitol related by a first-order transition. *Journal of Chemical Physics*, 142(24), 2015. 3

[40] Men Zhu and Lian Yu. Polyamorphism of D-mannitol. *Journal of Chemical Physics*, 146(24), 2017. 3

[41] Alice Ha, Itai Cohen, Xiaolin Zhao, Michelle Lee, and Daniel Kivelson. Supercooled Liquids and Polyamorphism †. *The Journal of Physical Chemistry*, 100(1):1–4, jan 1996. 3

[42] A. Hédoux, Y. Guinet, and M. Descamps. Raman signature of polyamorphism in triphenyl phosphite. *Physical Review B*, 58(1):31–34, jul 1998.

[43] G. Tarjus, C. Alba-Simionesco, M. Grousson, P. Viot, and D. Kivelson. Locally Preferred Structure and Frustration in Glass-forming Liquids: A Clue to Polyamorphism? *Journal of Physics: Condensed Matter*, 15(January 2014):S1077–S1084, 2003. 3

[44] J. F. Willart, N. Dujardin, E. Dudognon, F. Danède, and M. Descamps. Amorphization of sugar hydrates upon milling. *Carbohydrate Research*, 345(11):1613–1616, 2010. 3, 24, 106

[45] Jean-Francois Willart, Morgan Durand, Lars-Erik Briggner, Anke Marx, Florence Danède, and Marc Descamps. Solid-State Amorphization of Linaprazan by Mechanical Milling and Evidence of Polymorphism. *Journal of Pharmaceutical Sciences*, 102(7):2214–2220, jul 2013. 24, 89

[46] Ahmed Mourad SALAH. *Effets du broyage mécanique sur l'état physique des matériaux pharmaceutiques vitreux*. PhD thesis, Université Lille 1, 2015. xii, 30, 87, 95, 99

[47] Nicolas DUJARDIN. *Vitrification à l'état solide du glucose et maîtrise de la mutarotation*. PhD thesis, Université Lille 1, 2009. 3, 74, 111

[48] D P Miller and J J de Pablo. Calorimetric solution properties of simple saccharides and their significance for the stabilization of biological structure and function. *Journal of Physical Chemistry B*, 104(37):8876–8883, 2000. 4, 38, 80, 125, 126

[49] K. Kaminski, E. Kaminska, P. Wlodarczyk, S. Pawlus, D. Kimla, A. Kasprzycka, M. Paluch, J. Ziolo, W. Szeja, and K. L. Ngai. Dielectric studies on mobility of the glycosidic linkage in seven disaccharides. *Journal of Physical Chemistry B*, 112(40):12816–12823, 2008. 38

[50] Y.H. Roos. Frozen State Transitions in Relation To Freze Drying. *Journal of thermal analysis*, 48:535–544, 1997. 4, 38

[51] G. A. Jeffrey, Richard A. Wood, Philip E. Pfeffer, and Kevin B. Hicks. Crystal structure and solid-state NMR analysis of lactulose. *Journal of the American Chemical Society*, 105(8):2128–2133, apr 1983. xii, xix, 4, 36, 37, 39, 65, 69, 74, 172

[52] Dan a. Neumann. Neutron scattering and hydrogeneous materials. *Materials Today*, 9(1-2):34–41, 2006. 4

[53] Thomas Steiner. The Hydrogen Bond in the Solid State. *Angew. Chem. Int. Ed.*, 41:48–76, 2002. 4

[54] Adrien Lerbret, Patrice Bordat, Frédéric Affouard, Yannic Guinet, Alain Hédoux, Laurent Paccou, Dominique Prévost, and Marc Descamps. Influence of homologous disaccharides on the hydrogen-bond network of water: Complementary Raman scattering experiments and molecular dynamics simulations. *Carbohydrate Research*, 340(5):881–887, 2005. 4, 107

[55] Kenichiro Koga, G. T. Gao, Hideki Tanaka, and X. C. Zeng. Formation of ordered ice nanotubes inside carbon nanotubes. *Nature*, 412(6849):802–805, 2001. 9

[56] Christoph G. Salzmann, Paolo G. Radaelli, Ben Slater, and John L. Finney. The polymorphism of ice: five unresolved questions. *Physical Chemistry Chemical Physics*, 13(41):18468, 2011. 9

[57] Lian Yu. Polymorphism in Molecular Solids: An Extraordinary System of Red, Orange, and Yellow Crystals. *Accounts of Chemical Research*, 43(9):1257–1266, sep 2010. 10

[58] Lynne S. Taylor and Peter York. Characterization of the Phase Transitions of Trehalose Dihydrate on Heating and Subsequent Dehydration. *Journal of Pharmaceutical Sciences*, 87(3):347–355, mar 1998. 10

[59] M. M. Koza, B. Geil, K. Winkel, C. Köhler, F. Czeschka, M. Scheuermann, H. Schober, and T. Hansen. Nature of Amorphous Polymorphism of Water. *Physical Review Letters*, 94(12):125506, apr 2005. 10

[60] D. Turnbull. Kinetics of Heterogeneous Nucleation. *The Journal of Chemical Physics*, 18(2):198–203, feb 1950. 11

[61] K. F. Kelton, A. L. Greer, and C. V. Thompson. Transient nucleation in condensed systems. *The Journal of Chemical Physics*, 79(12):6261–6276, dec 1983.

[62] D W Oxtoby. Homogeneous nucleation: theory and experiment. *Journal of Physics: Condensed Matter*, 4(38):7627–7650, sep 1992. 11

[63] K. F. Kelton and A. L. Greer. Test of classical nucleation theory in a condensed system. *Physical Review B*, 38(14):10089–10092, nov 1988. 13

[64] David Turnbull. *Phase Changes*. Solid State Phys., 1956. 13

[65] H. M. Rietveld. Line profiles of neutron powder-diffraction peaks for structure refinement. *Acta Crystallographica*, 22(1):151–152, jan 1967. 15

[66] A R Stokes. A Numerical Fourier-analysis Method for the Correction of Widths and Shapes of Lines on X-ray Powder Photographs. *Proceedings of the Physical Society*, 61(4):382–391, oct 1948.

[67] George M. Sheldrick. Crystal structure refinement with SHELXL. *Acta Crystallographica Section C Structural Chemistry*, 71(1):3–8, jan 2015. 15

[68] S. J L Billinge and T. Egami. *Underneath the Bragg Peaks: Structural Analysis of Complex Materials*. Pergamon Materials Series, 2003. 15

[69] Th Proffen, S. J L Billinge, T. Egami, and D. Louca. Structural analysis of complex materials using the atomic pair distribution function - A practical guide. *Zeitschrift fur Kristallographie*, 218(2):132–143, 2003. 15

[70] B. E. Warren. *X-Ray Diffraction*. Dover Publications Inc., 1990.

[71] Seema Thakral, Maxwell W. Terban, Naveen K. Thakral, and Raj Suryanarayanan. Recent advances in the characterization of amorphous pharmaceuticals by X-ray diffractometry. *Advanced Drug Delivery Reviews*, 100:183–193, 2016. 15

[72] Gabriel J Cuello. Structure factor determination of amorphous materials by neutron diffraction. *Journal of Physics: Condensed Matter*, 20(24):244109, 2008. 15, 143

[73] J. M. Ziman. *Models of disorder: the theoretical physics of homogeneously disordered systems*. Cambridge University Press, 1979. xi, 15, 16

[74] J. A. Barker and D. Henderson. What is "liquid"? Understanding the states of matter. *Reviews of Modern Physics*, 48(4):587–671, oct 1976. 15

[75] Wikipedia. Molecular vibrations. https://en.wikipedia.org/wiki/Molecularv, 2013. 17

[76] José Baruchel ; Jean-Louis Hodeau ; Mogens S. Lehmann ; Jean-René Regnard ; Claire Schlenker. *Neutron and Synchrotron Radiation for Condensed Matter Studies*. Springer-Verlag Berlin Heidelberg, 1994. 17, 138

[77] A. C. Ferrari, J. C. Meyer, V. Scardaci, C. Casiraghi, M. Lazzeri, F. Mauri, S. Piscanec, D. Jiang, K. S. Novoselov, S. Roth, and A. K. Geim. Raman spectrum of graphene and graphene layers. *Physical Review Letters*, 97(18), oct 2006. 17

[78] Derek Steele. *Infrared Spectroscopy: Theory*. John Wiley & Sons, Ltd, 2006. 17

[79] A. J. Ramirez-Cuesta P. C. H. Mitchell, S. F. Parker and J. Tomkinson. *Vibrational Spectroscopy with Neutrons: With Applications in Chemistry, Biology, Materials Science and Catalysis*. World Scientific Publishing Co. Pte. Ltd., 2006. xi, 17

[80] Charles Kittel. *Introduction to Solide State Physics*. John Wiley & Sons, Inc, 1996. 17, 19

[81] P. Debye. Zur Theorie der spezifischen Wärmen. *Annalen der Physik*, 344(14):789–839, 1912. 17

[82] V.K. Malinovsky and A.P. Sokolov. The nature of boson peak in Raman scattering in glasses. *Solid State Communications*, 57(9):757–761, mar 1986. 18, 164

[83] V. K Malinovsky, V. N Novikov, P. P Parshin, A. P Sokolov, and M. G Zemlyanov. Universal Form of the Low-Energy (2 to 10 meV) Vibrational Spectrum of Glasses. *Europhysics Letters (EPL)*, 11(1):43–47, jan 1990. 18, 164

[84] Mikhail Shubin and Toshikazu Sunada. Geometric Theory of Lattice Vibrations and Specific Heat. *Pure and Applied Mathematics Quarterly*, 2(3):745–777, 2006. 17

[85] U. Buchenau, N. Nücker, and A. J. Dianoux. Neutron Scattering Study of the Low-Frequency Vibrations in Vitreous Silica. *Physical Review Letters*, 53(24):2316–2319, dec 1984. 18

[86] N. Theodorakopoulos and J. Jäckle. Low-frequency Raman scattering by defects in glasses. *Physical Review B*, 14(6):2637–2641, sep 1976. 18

[87] A. P. Sokolov, E. Rossler, A. Kisliuk, and D. Quitmann. Dynamics of strong and fragile glass formers: Differences and correlation with low-temperature properties. *Physical Review Letters*, 71(13):2062–2065, 1993. 18

[88] W. A. Phillips. *Amorphous Solids: Low-Temperature Properties*. Springer-Verlag Berlin, 1981. 18

[89] A. P. Sokolov, R. Calemczuk, B. Salce, A. Kisliuk, D. Quitmann, and E. Duval. Low-Temperature Anomalies in Strong and Fragile Glass Formers. *Physical Review Letters*, 78(12):2405–2408, mar 1997. 18

[90] K. L. Ngai, A. Sokolov, and W. Steffen. Correlations between boson peak strength and characteristics of local segmental relaxation in polymers. *The Journal of Chemical Physics*, 107(13):5268–5272, oct 1997. 18

[91] Y Inamura, M Arai, O Yamamuro, A Inaba, N Kitamura, T Otomo, T Matsuo, S.M Bennington, and A.C Hannon. Peculiar suppression of the specific heat and boson peak intensity of densified SiO2 glass. *Physica B: Condensed Matter*, 263-264:299–302, mar 1999. 18

[92] M Yamaguchi and T Yagi. Anharmonicity of low-frequency vibrations in a -Ge S 2 studied by light scattering. *Europhysics Letters (EPL)*, 47(4):462–467, aug 1999. 18

[93] C. McIntosh, J. Toulouse, and P. Tick. The Boson peak in alkali silicate glasses. *Journal of Non-Crystalline Solids*, 222:335–341, dec 1997. 18

[94] V. N. Novikov, E. Duval, A. Kisliuk, and A. P. Sokolov. A model of low-frequency Raman scattering in glasses: Comparison of Brillouin and Raman data. *The Journal of Chemical Physics*, 102(11):4691–4698, mar 1995. 18

[95] S. N. Taraskin and S. R. Elliott. Nature of vibrational excitations in vitreous silica. *Physical Review B*, 56(14):8605–8622, oct 1997. 18

[96] Hajime Tanaka. Physical Origin of the Boson Peak Deduced from a Two-Order Parameter Model of Liquid. *Journal of the Physics Society Japan*, 70(8):2492–2492, 2001. 18

[97] Hua Tong, Peng Tan, and Ning Xu. From Crystals to Disordered Crystals: A Hidden Order-Disorder Transition. *Scientific Reports*, 5(1):15378, dec 2015. 18

[98] Pradeep Kumar, K. Thor Wikfeldt, Daniel Schlesinger, Lars G. M. Pettersson, and H. Eugene Stanley. The Boson peak in supercooled water. *Scientific Reports*, 3(1):1980, 2013. 18, 167

[99] Hiroshi Shintani and Hajime Tanaka. Universal link between the boson peak and transverse phonons in glass. *Nature Materials*, 7(11):870–877, nov 2008. 168

[100] J. Horbach, W. Kob, and K. Binder. High frequency sound and the boson peak in amorphous silica. *The European Physical Journal B*, 19(4):531–543, feb 2001. 18

[101] A. I. Chumakov, G. Monaco, A. Monaco, W. A. Crichton, A. Bosak, R. Rüffer, A. Meyer, F. Kargl, L. Comez, D. Fioretto, H. Giefers, S. Roitsch, G. Wortmann, M. H. Manghnani, A. Hushur, Q. Williams, J. Balogh, K. Parliński, P. Jochym, and P. Piekarz. Equivalence of the boson peak in glasses to the transverse acoustic van, hove singularity in crystals. *Physical Review Letters*, 106(22):1–5, 2011. 18, 168

[102] Shlomo Alexander. Amorphous solids: their structure, lattice dynamics and elasticity. *Physics Reports*, 296(2-4):65–236, mar 1998. 19

[103] S. Hunklinger. PHONONS IN AMORPHOUS MATERIALS. *Le Journal de Physique Colloques*, 43(C9):C9–461–C9–474, dec 1982. 19

[104] R. Böhmer, K. L. Ngai, C. A. Angell, and D. J. Plazek. Nonexponential relaxations in strong and fragile glass formers. *The Journal of Chemical Physics*, 99(5):4201–4209, sep 1993. 19

[105] R. Böhmer. Non-linearity and non-exponentiality of primary relaxations. *Journal of Non-Crystalline Solids*, 172-174:628–634, sep 1994. 20

[106] G. W. Scherer. *Relaxation in Glass and Composites*. Wiley, 1986. 20

[107] I. M. Hodge. Enthalpy relaxation and recovery in amorphous materials. *Journal of Non-Crystalline Solids*, 169(3):211–266, 1994.

[108] I. Avramov. Kinetics of structural relaxation of glass-forming melts. *Thermochimica Acta*, 280-281:363–382, jul 1996. 20

[109] B. Ruta, Y. Chushkin, G. Monaco, L. Cipelletti, E. Pineda, P. Bruna, V. M. Giordano, and M. Gonzalez-Silveira. Atomic-scale relaxation dynamics and aging in a metallic glass probed by X-ray photon correlation spectroscopy. *Physical Review Letters*, 109(16):1–6, 2012. 21

[110] Amy Y.-H. Liu and Jörg Rottler. Physical aging and structural relaxation in polymer nanocomposites. *Journal of Polymer Science Part B: Polymer Physics*, 47(18):1789–1798, sep 2009. 21

[111] R. Casalini and C. M. Roland. Aging of the secondary relaxation to probe structural relaxation in the glassy state. *Physical Review Letters*, 102(3):1–4, 2009. 21

[112] Jerzy Zarzycki. *Les verres et l'état vitreux*. Masson, 1982. xi, 22

[113] Walter Kauzmann. The Nature of the Glassy State and the Behavior of Liquids at Low Temperatures. *Chemical Reviews*, 43(2):219–256, 1948. 22, 23

[114] G. J. Fan, F. Q. Guo, Z. Q. Hu, M. X. Quan, and K. Lu. Amorphization of selenium induced by high-energy ball milling. *Phys. Rev. B*, 55(17):11010–11013, 1997. 24

[115] W. J. Weber, R. C. Ewing, and L. M. Wang. The radiation-induced crystalline-to-amorphous transition in zircon. *Journal of Materials Research*, 9(February 2015):688–698, 1994. 24

[116] Tomaž Einfalt, Odon Planinšek, and Klemen Hrovat. Methods of amorphization and investigation of the amorphous state. *Acta Pharmaceutica*, 63(3), jan 2013. 24

[117] Shrawan Baghel, Helen Cathcart, and Niall J. O'Reilly. Polymeric Amorphous Solid Dispersions: A Review of Amorphization, Crystallization, Stabilization, Solid-State Characterization, and Aqueous Solubilization of Biopharmaceutical Classification System Class II Drugs. *Journal of Pharmaceutical Sciences*, 105(9):2527–2544, 2016. 24

[118] Alejandro Costoya, Angel Concheiro, and Carmen Alvarez-Lorenzo. Electrospun fibers of cyclodextrins and poly(cyclodextrins). *Molecules*, 22(2), 2017. 24

[119] Leena Peltonen, Hanna Valo, Ruzica Kolakovic, Timo Laaksonen, and Jouni Hirvonen. Electrospraying, spray drying and related techniques for production and formulation of drug nanoparticles. *Expert Opinion on Drug Delivery*, 7(6):705–719, jun 2010. 24

[120] J. F. Willart, M. Descamps, and V. Caron. Direct crystal to glass transformations of trehalose induced by milling, dehydration and annealing. *AIP Conference Proceedings*, 982:108–113, 2008. 24, 89

[121] Jean-François Willart, Laurent Carpentier, Florence Danède, and Marc Descamps. Solid-State Vitrification of Crystalline Griseofulvin by Mechanical Milling. *Journal of Pharmaceutical Sciences*, 101(4):1570–1577, apr 2012. 24

[122] P. Papon Meijer and J. Leblond P.H.E. *The Physics of Phase Transitions*. Springer, 2006. 24

[123] H. J. Fecht. Defect-induced melting and solid-state amorphization. *Nature*, 356(6365):133–135, mar 1992. 25

[124] G. Martin. Phase stability under irradiation: Ballistic effects. *Physical Review B*, 30(3):1424–1436, 1984. 27

[125] Georges Martin and Pascal Bellon. *Driven Alloys*. Solid State Physics - Advances in Research and Applications, 1996. 27

[126] Laurent Chaffron, Yann Le Bouar, and Georges Martin. Driven phase transformations: A useful concept for wear studies? *Comptes Rendus de l'Academie des Sciences - Series IV: Physics, Astrophysics*, 2(5):749–759, 2001. 27

[127] C J Aundhia, J A Raval, M M Patel, N V Shah, S P Chauhan, G U Sailor, A R Javia, and R A Mahashwari. Spray Drying in the Pharmaceutical Industry – A Review. *Indo American Journal of Pharmaceutical Research Indo American Journal of Pharm Research Aundhia C.J. et al. Indo American Journal of Pharmaceutical Research*, 212(111):125–13863, 2011. 27

[128] Krzysztof Cal and Krzysztof Sollohub. Spray Drying Technique. I: Hardware and Process Parameters. *Journal of Pharmaceutical Sciences*, 99(2):575–586, feb 2010. 28

[129] Sandra Guns, Aswin Dereymaker, Pieterjan Kayaert, Vincent Mathot, Johan A. Martens, and Guy Van den Mooter. Comparison Between Hot-Melt Extrusion and Spray-Drying for Manufacturing Solid Dispersions of the Graft Copolymer of Ethylene Glycol and Vinylalcohol. *Pharmaceutical Research*, 28(3):673–682, mar 2011. 28

[130] Reinhard Vehring. Pharmaceutical particle engineering via spray drying. *Pharmaceutical Research*, 25(5):999–1022, 2008. 28

[131] Linna Wu, Xu Miao, Ziyun Shan, Ying Huang, Lu Li, Xin Pan, Qinghe Yao, Ge Li, and Chuanbin Wu. Studies on the spray dried lactose as carrier for dry powder inhalation. *Asian Journal of Pharmaceutical Sciences*, 9(6):336–341, dec 2014. xii, 29

[132] Graham Buckton, Owen C Chidavaenzi, and Fariba Koosha. The effect of spray-drying feed temperature and subsequent crystallization conditions on the physical form of lactose. *AAPS PharmSciTech*, 3(4):E37, 2002. 29

[133] Eva Maria Littringer, Axel Mescher, Susanna Eckhard, Hartmuth Schröttner, Christoph Langes, Manfred Fries, Ulrich Griesser, Peter Walzel, and Nora Anne Urbanetz. Spray Drying of Mannitol as a Drug Carrier—The Impact of Process Parameters on Product Properties. *Drying Technology*, 30(1):114–124, jan 2012. 29

[134] Patrick P. DeLuca. Freeze drying of pharmaceuticals. *Journal of Vacuum Science and Technology*, 14(1):620–629, jan 1977. 29

[135] Chalat Santivarangkna, Mathias Aschenbrenner, Ulrich Kulozik, and Petra Foerst. Role of Glassy State on Stabilities of Freeze-Dried Probiotics. *Journal of Food Science*, 76(8):R152–R156, oct 2011. 30

[136] Louis Rey Joan C. May. *Freeze Drying/Lyophilization of Pharmaceutical and Biological Products*. Informa Healthcare, 2006. 30

[137] Michael F. Kozempel, Michael J. Kurantz, James C. Craig, and Kevin B. Hicks. Development of a continuous lactulose process: separation and purification. *Biotechnology Progress*, 11(5):592–595, sep 1995. 35

[138] He Wang, Ruijin Yang, Xiao Hua, Wei Zhao, and Wenbin Zhang. Enzymatic production of lactulose and 1-lactulose: current state and perspectives. *Applied Microbiology and Biotechnology*, 97(14):6167–6180, jul 2013. 35

[139] Amara Aït-Aissa and Mohammed Aïder. Lactulose: production and use in functional food, medical and pharmaceutical applications. Practical and critical review. *International Journal of Food Science & Technology*, 49(5):1245–1253, may 2014. 35

[140] D H Patil, D Westaby, Y R Mahida, K R Palmer, R Rees, M L Clark, A M Dawson, and D B Silk. Comparative modes of action of lactitol and lactulose in the treatment of hepatic encephalopathy. *Gut*, 28(3):255–9, mar 1987. 35

[141] Parmjit S. Panesar and Shweta Kumari. Lactulose: Production, purification and potential applications. *Biotechnology Advances*, 29(6):940–948, nov 2011. 35

[142] J. M. Nelson and Frank M. Beegle. MUTAROTATION OF GLUCOSE AND FRUCTOSE. *Journal of the American Chemical Society*, 41(4):559–575, apr 1919. 35

[143] Ronan Lefort, Vincent Caron, Jean-François Willart, and Marc Descamps. Mutarotational kinetics and glass transition of lactose. *Solid State Communications*, 140(7-8):329–334, nov 2006. 35, 106

[144] T.E. Acree, R.s. Shallenberger, C.Y. Lee, and J.W. Einset. Thermodynamics and kinetics of D-galactose tautomers during mutarotation. *Carbohydrate Research*, 10(3):355–360, jul 1969. 35

[145] H.S. Isbell and W.W. Pigman. Pyranose-furanose interconversions with reference to the mutarotations of galactose, levulose, lactulose,and turanose. *Journal of Research of the National Bureau of Standards*, 20(6):773, 1938. 36

[146] G A Jeffrey, D B Huang, P E Pfeffer, R L Dudley, K B Hicks, and E Nitsch. Crystal structure and n.m.r. analysis of lactulose trihydrate. *Carbohydrate research*, 226(1):29–42, mar 1992. xix, 36, 38, 39, 50, 68, 74, 75, 76, 106, 111

[147] FRITSCH. Pulverisette 7. http://www.fritsch-international.com/sample-preparation/milling/planetary-mills/details/product/pulverisette-7-classic-line/, 2017. 39

[148] BUCHI. B 290. https://www.buchi.com/en/products/spray-drying-and-encapsulation/mini-spray-dryer-b-290, 2017. 41

[149] CHRIST. Epsilon 2-4 lsc. https://www.martinchrist.de/en/products/pilot/epsilon-1-4-lscplus.html, 2017. 42

[150] R. E. Dinnebier and S. J. L. Billinge. *Powder Diffraction: Theory and Practice*. The Royal Society of Chemistry, 2008. xii, 44, 45

[151] PANalytical. X'celerator. http://www.panalytical.com/XCelerator.htm, 2017. 45

[152] M. Evain, P. Deniard, A. Jouanneaux, and R. Brec. Potential of the INEL X-ray position-sensitive detector: a general study of the Debye–Scherrer setting. *Journal of Applied Crystallography*, 26(4):563–569, aug 1993. 45

[153] J. Rodriguez-Carvajal. Crystallographic tools for rietveld, profile matching and integrated intensity refinements of x-ray and/or neutron data. https://www.ill.eu/sites/fullprof/, 2017. 46, 65, 75

[154] TA Instruments. Q 500. http://www.tainstruments.com/tga-q50-and-q500-packing/, 2017. 46

[155] TA Instruments. Q 2000. http://www.tainstruments.com/dsc-q20aq2000-pack/, 2017. 47

[156] SETARAM. C 80. http://us.setaram.com/en/setaram-products/calorimetry/calorimetry-calorimetry/c80/, 2017. 48

[157] Harald Gunther. *NMR Spectroscopy: Basic Principles, Concepts and Applications in Chemistry*. Wiley-VCH Verlag, 2013. 49, 50

[158] BRUKER. Nmr 400. https://www.bruker.com/, 2017. 50

[159] Stephen J. Angyal. The Composition of Reducing Sugars in Solution. *Elsevier*, pages 15–68, 1984. 50

[160] SJ Angyal and VA Pickles. Equilibria between pyranoses and furanoses. II. Aldoses. *Australian Journal of Chemistry*, 25(8):1695, 1972. 50

[161] S Garnier. *Contribution à l'étude de la cristallisation en solution. Application à la purification et à l'étude de composés moléculaires: Un thiocarboester et le* α*-lactose monohydrate*. PhD thesis, University of Rouen, 2001. 50, 68

[162] MP Allen and DJ Tildesley. *Computer Simulation of Liquids*. Oxford Science Publications, 1987. xii, 51, 59, 60, 164

[163] JM Haile. *Molecular Dynamics Simulation: Elementary Methods*. John Wiley & Sons, 1992. 51

[164] DC Rapaport. *The Art of Molecular Dynamics Simulation*. Cambridge University Press, 1995. 51, 59

[165] D Frenkel and B Smit. *Understanding Molecular Simulation: From Algorithms to Applications*. Elsevier, 2002. 51

[166] DS Sholl and JA Steckel. *DENSITY FUNCTIONAL THEORY: A Practical Introduction*. John Wiley & Sons, 2009. 51

[167] RM Dreizler and EKU Groos. *Density Functional Theory - An Approach to the Quantum Many-Body Problem*. Springer Berlin Heidelberg, 1990. 51

[168] RG Parr and W Yang. *Density Functional Theory of Atoms and Molecules*. Oxford University Press, 1989. 51

[169] P. Hohenberg and W. Kohn. Inhomogeneous Electron Gas. *Physical Review*, 136(3B):B864–B871, nov 1964. 54

[170] W Kohn and L J Sham. Self-Consistent Equations Including Exchange and Correlation Effects. *Physical Review*, 140(4A):A1134–A1138, 1965. 55

[171] D. M. Ceperley and B. J. Alder. Ground State of the Electron Gas by a Stochastic Method. *Physical Review Letters*, 45(7):566–569, aug 1980. 55

[172] Perdew, Chevary, Vosko, Jackson, Pederson, Singh, and Fiolhais. Atoms, molecules, solids, and surfaces: Applications of the generalized gradient approximation for exchange and correlation. *Physical review. B, Condensed matter*, 46(11):6671–6687, sep 1992. 55

[173] John P Perdew, Kieron Burke, and Matthias Ernzerhof. Generalized Gradient Approximation Made Simple. *Physical Review Letters*, 78(7):1396–1396, 1996. 55

[174] AD Becke. Density-functional exchange-energy approximation with correct asymptotic behavior. *Physical review. A, General physics*, 38(6):3098–3100, sep 1988. 55

[175] AD Becke. Density-Functional Thermochemistry. I. The effect of the exchange-only gradient correction. *The Journal of Chemical Physics*, 96(3):2155–2160, feb 1992.

[176] AD Becke. Density-Functional Thermochemistry . III. the Role of Exact Exchange. *Journal of Chemical Physics*, 98(7):5648–5652, 1993.

[177] John P. Perdew and Yue Wang. Accurate and simple analytic representation of the electron-gas correlation energy, 1992.

[178] Lee, Yang, and Parr. Development of the Colle-Salvetti correlation-energy formula into a functional of the electron density. *Physical review. B, Condensed matter*, 37(2):785–789, jan 1988. 55

[179] B. Delley. From molecules to solids with the DMol3 approach. *The Journal of Chemical Physics*, 113(18):7756–7764, nov 2000. 56

[180] J L Momany, FA and Willett. Computational Studies on Carbohydrates: I. Density Functional Ab Initio Geometry Optimization on Maltose Conformations. *Journal of Computational Chemistry*, 21(13):1204–1219, 2000. 56

[181] Francis Cloran, Ian Carmichael, and Anthony S. Serianni. Density Functional Calculations on Disaccharide Mimics: Studies of Molecular Geometries and Trans- O -glycosidic 3 J COCH and 3 J COCC Spin-Couplings. *Journal of the American Chemical Society*, 121(42):9843–9851, oct 1999. 56

[182] D R Hamann. H2O hydrogen bonding in density-functional theory. *Physical Review B*, 55(16):R10157–R10160, 1997. 56

[183] Pietro Ballone, Massimo Marchi, C. Branca, Salvatore Magazù, S. Magazu, and S. Magazú. Structural and Vibrational Properties of Trehalose: A Density Functional Study. *The Journal of Physical Chemistry B*, 104(26):6313–6317, 2000. 56, 172

[184] R Fletcher and M J D Powell. A Rapidly Convergent Descent Method for Minimization. *The Computer Journal*, 6(2):163–168, 1963. 57

[185] Roberto Battiti. First- and Second-Order Methods for Learning: Between Steepest Descent and Newton's Method. *Neural Computation*, 4(2):141–166, mar 1992.

[186] C. T. Kelley. *Iterative Methods for Optimization*. Siam, 1999. 57

[187] M.R. Hestenes and Eduard Stiefel. Methods of conjugate gradients for solving linear systems, 1952.

[188] J. Gilbert and J. Nocedal. Global Convergence Properties of Conjugate Gradient Methods for Optimization. *SIAM Journal on Optimization*, 2(1):21–42, 1992. 57

[189] Hans-Joachim Werner and Peter J. Knowles. A second order multiconfiguration SCF procedure with optimum convergence. *The Journal of Chemical Physics*, 82(11):5053–5063, jun 1985. 57

[190] R Momany, FA and Rone. Validation of the general purpose QUANTA ®3.2/CHARMm® force field. *Journal of Computational Chemistry*, 13(7):888–900, sep 1992. 58

[191] J Wang, RM Wolf, and JW Caldwell. Development and testing of a general amber force field. *Journal of*, 2004. 58

[192] W.F. van Gunsteren and H.J.C. Berendsen. Algorithms for macromolecular dynamics and constraint dynamics. *Molecular Physics*, 34(5):1311–1327, nov 1977. 58

[193] Chris Oostenbrink, Alessandra Villa, Alan E. Mark, and Wilfred F. Van Gunsteren. A biomolecular force field based on the free enthalpy of hydration and solvation: The GROMOS force-field parameter sets 53A5 and 53A6. *Journal of Computational Chemistry*, 25(13):1656–1676, oct 2004. 58

[194] William L. Jorgensen, David S. Maxwell, and Julian Tirado-Rives. Development and Testing of the OLPS All-Atom Force Field on Conformational Energetics and Properties of Organic Liquids. *J. Am. Chem. Soc.*, 118(15):11225–11236, 1996. 58, XIII

[195] H. Sun. COMPASS: An ab Initio Force-Field Optimized for Condensed-Phase ApplicationsOverview with Details on Alkane and Benzene Compounds. *The Journal of Physical Chemistry B*, 102(38):7338–7364, sep 1998. 58

[196] H. J. C. Berendsen, J. P. M. Postma, W. F. van Gunsteren, A. DiNola, and J. R. Haak. Molecular dynamics with coupling to an external bath. *The Journal of Chemical Physics*, 81(8):3684–3690, oct 1984. 58

[197] William G. Hoover. Canonical dynamics: Equilibrium phase-space distributions. *Physical Review A*, 31(3):1695–1697, mar 1985. 58

[198] D. J. Evans and B. L. Holian. The Nose–Hoover thermostat. *The Journal of Chemical Physics*, 83(8):4069–4074, oct 1985.

[199] Shuichi Nosé. A unified formulation of the constant temperature molecular dynamics methods. *The Journal of Chemical Physics*, 81(1):511–519, jul 1984. 58

[200] Nicholas Metropolis, Arianna W. Rosenbluth, Marshall N. Rosenbluth, Augusta H. Teller, and Edward Teller. Equation of State Calculations by Fast Computing Machines. *The Journal of Chemical Physics*, 21(6):1087–1092, 1953. xii, 59

[201] Loup Verlet. Computer "Experiments" on Classical Fluids. I. Thermodynamical Properties of Lennard-Jones Molecules. *Physical Review*, 159(1):98–103, jul 1967. 59

[202] R.W. Hockney. The potential calculation and some applications. *Methods Comput. Phys.*, 9:135–211, 1970. 59

[203] William C. Swope, Hans C. Andersen, Peter H. Berens, and Kent R. Wilson. A computer simulation method for the calculation of equilibrium constants for the formation of physical clusters of molecules: Application to small water clusters. *The Journal of Chemical Physics*, 76(1):637–649, jan 1982. 59

[204] W Smith. The computer simulation of liquids by molecular dynamics. *Physics Education*, 22(6):005, nov 1987. 60

[205] W Smith and T R Forester. DL_POLY_2.0: a general-purpose parallel molecular dynamics simulation package. *Journal of molecular graphics*, 14(3):136–41, jun 1996.

[206] Ilian T. Todorov and William Smith. DL_POLY_3: the CCP5 national UK code for molecular-dynamics simulations. *Philosophical Transactions of the Royal Society A: Mathematical, Physical and Engineering Sciences*, 362(1822):1835–1852, sep 2004.

[207] Ilian T. Todorov, William Smith, Kostya Trachenko, and Martin T. Dove. DL_POLY_3: new dimensions in molecular dynamics simulations via massive parallelism. *Journal of Materials Chemistry*, 16(20):1911, 2006. 60

[208] Wolfgang Damm, Antonio Frontera, Julian Tirado–Rives, and William L. Jorgensen. OPLS all-atom force field for carbohydrates. *Journal of Computational Chemistry*, 18(16):1955–1970, 1997. 60

[209] D. Kony, W. Damm, S. Stoll, and W. F. Van Gunsteren. An improved OPLS-AA force field for carbohydrates. *Journal of Computational Chemistry*, 23(15):1416–1429, nov 2002. 60

[210] Jonathan Richard Shewchuk. An Introduction to the Conjugate Gradient Method Without the Agonizing Pain. *Science*, 49(CS-94-125):64, 1994. 60

[211] W. Smith and T.R. Forester. Parallel macromolecular simulations and the replicated data strategy. *Computer Physics Communications*, 79(1):63–77, feb 1994. 60

[212] Jean Paul Ryckaert, Giovanni Ciccotti, and Herman J.C. Berendsen. Numerical integration of the cartesian equations of motion of a system with constraints: molecular dynamics of n-alkanes. *Journal of Computational Physics*, 23(3):327–341, 1977. 60

[213] ACD/Labs. Acd/nmr predictors. http://www.acdlabs.com/products/adh/nmr/, 2016. 68

[214] Varanavasi Govindaraju, Karl Young, and Andrew A. Maudsley. Proton NMR chemical shifts and coupling constants for brain metabolites. *NMR in Biomedicine*, 13(3):129–153, 2000. 70

[215] Vincent CARON. *Mecanosynthese et vitrification à l'état solide d'alliages moléculaires*. PhD thesis, Université Lille 1, 2006. 86, 88, 111, 130

[216] Yuanzheng Yue and C. Austen Angell. Clarifying the glass-transition behaviour of water by comparison with hyperquenched inorganic glasses. *Nature*, 427(6976):717–720, 2004. 88, 103, 104

[217] Jiang Fan and C. Austen Angell. Relaxational transitions and ergodicity breaking within the fluid state: the sugars fructose and galactose. *Thermochimica Acta*, 266(C):9–30, 1995. 98

[218] E. Tombari, G. Salvetti, C. Ferrari, and G. P. Johari. Structural unfreezing and endothermic effects in liquids, β-D-fructose. *Journal of Physical Chemistry B*, 108(43):16877–16882, 2004.

[219] A. Magoń and M. Pyda. Apparent heat capacity measurements and thermodynamic functions of D(-)-fructose by standard and temperature-modulated calorimetry. *Journal of Chemical Thermodynamics*, 56:67–82, 2013. 98

[220] C. A. Angell. Liquid Fragility and the Glass Transition in Water and Aqueous Solutions. *Chemical Reviews*, 102(8):2627–2650, aug 2002. 103

[221] C Austen Angell, Yuanzheng Yue, Li-Min Wang, John R D Copley, Steve Borick, and Stefano Mossa. Potential energy, relaxation, vibrational dynamics and the boson peak, of hyperquenched glasses. *Journal of Physics: Condensed Matter*, 15(11):S1051–S1068, 2003.

[222] Li Min Wang, Steve Borick, and C. Austen Angell. An electrospray technique for hyperquenched glass calorimetry studies: Propylene glycol and di-n-butyl phthalate. *Journal of Non-Crystalline Solids*, 353(41-43):3829–3837, 2007.

[223] Tonu Reinot, Nhan C. Dang, and Ryszard Jankowiak. Hyperquenched glassy water and hyperquenched glassy ethanol probed by single molecule spectroscopy. *Journal of Physical Chemistry B*, 113(13):4303–4313, 2009. 103

[224] Y. Z. Yue, S. L. Jensen, and J. Dec Christiansen. Physical aging in a hyperquenched glass. *Applied Physics Letters*, 81(16):2983–2985, 2002. 103, 104

[225] Angeline AUMELAS. *Broyage de composés pharmaceutiques : changements d'états physiques et manipulation de la stabilité*. PhD thesis, Université Lille 1, 2008. 103

[226] Devin Averett, Marcus T. Cicerone, Jack F. Douglas, and Juan J. de Pablo. Fast relaxation and elasticity-related properties of trehalose-glycerol mixtures. *Soft Matter*, 8(18):4936, 2012. 106

[227] Armand Soldera and Noureddine Metatla. Glass transition of polymers: Atomistic simulation versus experiments. *Physical Review E - Statistical, Nonlinear, and Soft Matter Physics*, 74(6):1–6, 2006. 106

[228] John C Mauro, Yuanzheng Yue, Adam J Ellison, Prabhat K Gupta, and Douglas C Allan. Viscosity of glass-forming liquids. *Proceedings of the National Academy of Sciences of the United States of America*, 106(47):19780–4, 2009.

[229] Qian Qin and Gregory B. McKenna. Correlation between dynamic fragility and glass transition temperature for different classes of glass forming liquids. *Journal of Non-Crystalline Solids*, 352(28-29):2977–2985, aug 2006. 106

[230] C. Alba-Simionesco, A. Toelle, D. Morineau, B. Farago, and G. Coddens. "de Gennes" narrowing in supercooled molecular liquids : Evidence for center-of-mass dominated slow dynamics. *Condensed Matter*, 2001. 107

[231] Peter Kleban. Toward a microscopic basis for the de Gennes narrowing. *Journal of Statistical Physics*, 11(4):317–322, 1974. 107

[232] A. Keller, M. Hikosaka, S. Rastogi, A. Toda, P. J. Barham, and G. Goldbeck-Wood. An approach to the formation and growth of new phases with application to polymer crystallization: effect of finite size, metastability, and Ostwald's rule of stages. *Journal of Materials Science*, 29(10):2579–2604, 1994. 117, 152

[233] J H Strange and J B W Webber. Spatially resolved pore size distributions by nmr. *Measurement Science & Technology*, 8(5):555–561, 1997. 117, 152

[234] Teruhiko Mizota, Itsuko Suzawa, Nobuo Seki, Yoshitaka Tamura, and Seiichi Shimamura. Solubility of lactulose trihydrate. *Carbohydrate Research*, 263(1):163–166, oct 1994. 124

[235] H. Huemer, E. Platzer, and K. Rehak. A new Calvet-type calorimeter for excess enthalpies. *Thermochimica Acta*, 231:21–30, jan 1994. 126

[236] Beata Salamon, Jan Kapala, and Marcelle Gaune-Escard. Instrumentation and calibration of the Calvet calorimeter: Enthalpy of solution of PrBr 3 at standard conditions. *Journal of Thermal Analysis and Calorimetry*, 108(2):421–424, 2012. 126

[237] R. V. Jasra and J. C. Ahluwalia. Enthalpies and heat capacities of dissolution, apparent molar heat capacities, and apparent molar volumes of some mono-, di-, tri-, and tetra-saccharides in water. *The Journal of Chemical Thermodynamics*, 16(6):583–590, 1984. 126

[238] Elena Elisei, Jean-François Willart, Florence Danède, Jürgen Siepmann, Florence Siepmann, and Marc Descamps. Crystalline Polymorphism Emerging From a Milling-Induced Amorphous Form: The Case of Chlorhexidine Dihydrochloride. *Journal of Pharmaceutical Sciences*, jul 2017. 130

[239] G.L. Squires. *Introduction to the Theory of Thermal Neutron Scattering*. Cambridge University Press, 1978. 138, 140, 141, 142

[240] S.W. Lovesey. *Theory of neutron scattering from condensed matter*. Oxford Clarendon Press, 1984. 142

[241] N.W. Ashcroft and N.E. Mermin. *Solid State Physics*. Hartcourt College, 1976. 138

[242] E. Merzbacher. *Ouantum Mechanics*. John Wiley & Sons, Inc, 1970. 140

[243] Varley F. Sears. Neutron scattering lengths and cross sections. *Neutron News*, 3(3):26–37, jan 1992. 141, 143

[244] H. Schober. Diffusion des neutrons par la matière cristalline ou amorphe non-magnétique. In *JDN 16 – Diffusion Inélastique des Neutrons pour l'Etude des Excitations dans la Matiére Condensée*, pages 159–336, Les Ulis, France, jun 2010. EDP Sciences. 142

[245] A. H. NARTEN, W. E. THIESSEN, and L. BLUM. Atom Pair Distribution Functions of Liquid Water at 25 C from Neutron Diffraction. *Science*, 217(4564):1033–1034, sep 1982. 143

[246] A. K. Soper. The Radial Distribution Functions of Water as Derived from Radiation Total Scattering Experiments: Is There Anything We Can Say for Sure? *ISRN Physical Chemistry*, 2013:1–67, 2013. 143

[247] R. M. Moon, T. Riste, and W. C. Koehler. Polarization Analysis of Thermal-Neutron Scattering. *Physical Review*, 181(2):920–931, may 1969. 143

[248] A Stunault, S Vial, L Pusztai, G J Cuello, and L Temleitner. Structure of hydrogenous liquids: separation of coherent and incoherent cross sections using polarised neutrons. *Journal of Physics: Conference Series*, 711(1):012003, 2016. 143, 144

[249] László Temleitner, Anne Stunault, Gabriel J. Cuello, and László Pusztai. Neutron diffraction of hydrogenous materials: Measuring incoherent and coherent intensities separately. *Physical Review B*, 92(1):014201, jul 2015. 143

[250] Henry E Fischer, Adrian C Barnes, and Philip S Salmon. Neutron and x-ray diffraction studies of liquids and glasses. *Reports on Progress in Physics*, 69(1):233–299, jan 2006. 143, VII

[251] Koreyoshi Imamura, Yoshinobu Maruyama, Kazuhiro Tanaka, Tohru Yokoyama, Hiroyuki Imanaka, and Kazuhiro Nakanishi. True density analysis of a freeze-dried amorphous sugar matrix. *Journal of Pharmaceutical Sciences*, 97(7):2789–2797, 2008. 145

[252] J. R. Stewart, P. P. Deen, K. H. Andersen, H. Schober, J.-F. Barthélémy, J. M. Hillier, A. P. Murani, T. Hayes, and B. Lindenau. Disordered materials studied using neutron polarization analysis on the multi-detector spectrometer, D7. *Journal of Applied Crystallography*, 42(1):69–84, feb 2009. 149, 152, VIII

[253] O. A. Caparino, J. Tang, C. I. Nindo, S. S. Sablani, J. R. Powers, and J. K. Fellman. Effect of drying methods on the physical properties and microstructures of mango (Philippine 'Carabao' var.) powder. *Journal of Food Engineering*, 111(1):135–148, 2012. 150

[254] S. Magazù, F. Migliardo, F. Affouard, M. Descamps, and M. T.F. Telling. Study of the relaxational and vibrational dynamics of bioprotectant glass-forming mixtures by neutron scattering and molecular dynamics simulation. *Journal of Chemical Physics*, 132(18):1–9, 2010. 157, 162

[255] Salvatore Magazù, Federica Migliardo, and Stewart F. Parker. Vibrational properties of bioprotectant mixtures of trehalose and glycerol. *Journal of Physical Chemistry B*, 115(37):11004–11009, 2011. 157, 172

[256] S. Magazù, F. Migliardo, and A.J. Ramirez-Cuesta. Concentration dependence of vibrational properties of bioprotectant/water mixtures by inelastic neutron scattering. *Journal of The Royal Society Interface*, 4(12):167–173, feb 2007. 157

[257] ISIS. Tosca database. http://wwwisis2.isis.rl.ac.uk/INSdatabase/Theindex.asp, 2017. 157

[258] M. Bée. *Quasielastic Neutron Scattering: Principles and Applications in Solid-State Chemistry*. Bristol, Hilger, 1988. 162

[259] M Harish Bhat, Inmaculada Peral, John R D Copley, and C Austen Angell. The boson peak in melt-formed and damage-formed glasses : A defect signature ? *Journal of Non-Crystalline Solids*, 352:4517–4524, 2006. xvii, 165, 166, 167

[260] A. Meyer, J. Wuttke, W. Petry, O. G. Randl, and H. Schober. Slow Motion in a Metallic Liquid. *Physical Review Letters*, 80(20):4454–4457, may 1998. 166

[261] P.L.H. McSweeney and P.F. Fox. *Advanced Dairy Chemistry: Volume 3: Lactose, Water, Salts and Minor Constituents*. Springer, 1990. 167

[262] Osamu Yamamuro, Kiyoshi Takeda, Itaru Tsukushi, and Takasuke Matsuo. Boson peaks in hydrogen-bonded molecular glasses. *Physica B*, 311:84–89, 2002. 168

[263] Alexandre Ivanov, Mónica Jimenéz-Ruiz, and Jiri Kulda. IN1-LAGRANGE – the new ILL instrument to explore vibration dynamics of complex materials. *Journal of Physics: Conference Series*, 554:012001, nov 2014. 168

[264] G. D'Arrigo, G. Maisano, F. Mallamace, P. Migliardo, and F. Wanderlingh. Raman scattering and structure of normal and supercooled water. *The Journal of Chemical Physics*, 75(9):4264–4270, 1981. xvii, 176, 177

[265] Yujie Wu, Harald L. Tepper, and Gregory A. Voth. Flexible simple point-charge water model with improved liquid-state properties. *The Journal of chemical physics*, 124(2):024503, 2006. 178

[266] Paul J. Steinhardt, David R. Nelson, and Marco Ronchetti. Bond-orientational order in liquids and glasses. *Physical Review B*, 28(2):784–805, 1983. 185

[267] R. E. Rozas and J. Horbach. Capillary wave analysis of rough solid-liquid interfaces in nickel. *EPL (Europhysics Letters)*, 93(2):26006, 2011.

[268] Aleks Reinhardt, Jonathan P. K. Doye, Eva G. Noya, and Carlos Vega. Local order parameters for use in driving homogeneous ice nucleation with all-atom models of water. *Journal of Chemical Physics*, 194504(2012), 2012. 185

[269] Yaroslav Chushak and Lawrence S. Bartell. Crystal Nucleation and Growth in Large Clusters of SeF 6 from Molecular Dynamics Simulations. *The Journal of Physical Chemistry A*, 104(41):9328–9336, oct 2000. 185

[270] Walter Mickel, Sebastian C. Kapfer, Gerd E. Schröder-Turk, and Klaus Mecke. Shortcomings of the bond orientational order parameters for the analysis of disordered particulate matter. *Journal of Chemical Physics*, 138(4), 2013. 185

[271] Rahul Surana, Abira Pyne, and Raj Suryanarayanan. Effect of Preparation Method on the Physical Properties of Amorphous Trehalose. *Pharmaceutical Research*, 21(5), 2004. 191

[272] Satoshi Ohtake and Evgenyi Shalaev. Effect of Water on the Chemical Stability of Amorphous Pharmaceuticals: I. Small Molecules. *Journal of Pharmaceutical Sciences*, 102(4):1139–1154, apr 2013. 192

[273] Evgenyi Y. Shalaev and George Zografi. How Does Residual Water Affect the Solid-state Degradation of Drugs in the Amorphous State? *Journal of Pharmaceutical Sciences*, 85(11):1137–1141, nov 1996.

[274] R. Ergun, R. Lietha, and R. W. Hartel. Moisture and Shelf Life in Sugar Confections. *Critical Reviews in Food Science and Nutrition*, 50(2):162–192, jan 2010.

[275] Liuquan (Lucy) Chang, Deanna Shepherd, Joanna Sun, Xiaolin (Charlie) Tang, and Michael J. Pikal. Effect of sorbitol and residual moisture on the stability of lyophilized antibodies: Implications for the mechanism of protein stabilization in the solid state. *Journal of Pharmaceutical Sciences*, 94(7):1445–1455, jul 2005.

[276] Marcus T Cicerone, Andrew Tellington, Landon Trost, and Alexei Sokolov. Substantially Improved Stability of Biological Agents in Dried Form The Role of Glassy Dynamics in Preservation of Biopharmaceuticals. *BioProcess International*, 1(December), 2003. 192

[277] Bernhard Wunderlich, Yimin Jin, and Andreas Boller. Mathematical description of differential scanning calorimetry based on periodic temperature modulation. *Thermochimica Acta*, 238:277–293, jun 1994. I

[278] M. Reading, A. Luget, and R. Wilson. Modulated differential scanning calorimetry. *Thermochimica Acta*, 238:295–307, jun 1994. I

[279] O. Bustin and M. Descamps. Slow structural relaxations of glass-forming Maltitol by modulated DSC calorimetry. *The Journal of Chemical Physics*, 110(22):10982–10992, jun 1999. xviii, I, II, III

[280] K.J. Jones, I. Kinshott, M. Reading, A.A. Lacey, C. Nikolopoulos, and H.M. Pollock. The origin and interpretation of the signals of MTDSC. *Thermochimica Acta*, 304-305:187–199, nov 1997.

[281] Els Verdonck, Ko Schaap, and Leonard C Thomas. A discussion of the principles and applications of Modulated Temperature DSC (MTDSC). *International Journal of Pharmaceutics*, 192(1):3–20, dec 1999. I

[282] H. H. Paalman and C. J. Pings. Numerical evaluation of X-ray absorption factors for cylindrical samples and annular sample cells. *Journal of Applied Physics*, 33(8):2635–2639, 1962. VI

[283] E. W. J. Mitchell, P. F. J. Poncet, and R. J. Stewart. The ion pair distribution functions in molten rubidium chloride. *Philosophical Magazine*, 34(5):721–732, nov 1976. VI

[284] I. A. Blech and B. L. Averbach. Multiple scattering of neutrons in vanadium and copper. *Physical Review*, 137(4A):1–4, 1965. VII

[285] V.F. Sears. Slow-neutron multiple scattering. *Advances in Physics*, 24(1):1–45, jan 1975.

[286] Alan K. Soper and P.A. Egelstaff. Multiple scattering and attenuation of neutrons in concentric cylinders: I. Isotropic first scattering. *Nuclear Instruments and Methods*, 178(2-3):415–425, dec 1980.

[287] L.A. Rodríguez Palomino, J. Dawidowski, J.J. Blostein, and G.J. Cuello. Data processing method for neutron diffraction experiments. *Nuclear Instruments and Methods in Physics Research Section B: Beam Interactions with Materials and Atoms*, 258(2):453–470, may 2007. VII, VIII

[288] G. Placzek. The Scattering of Neutrons by Systems of Heavy Nuclei. *Physical Review*, 86(3):377–388, may 1952. VII, VIII

[289] L A Rodríguez Palomino, A Stunault, J Dawidowski, L Temleitner, L Pusztai, and G J Cuello. A Monte Carlo simulation code applied to diffraction experiments with polarization analysis. *Journal of Physics: Conference Series*, 663:012002, 2015. VIII

[290] Scott J. Weiner, Peter A. Kollman, David A. Case, U. Chandra Singh, Caterina Ghio, Guliano Alagona, Salvatore Profeta, and Paul Weiner. A new force field for molecular mechanical simulation of nucleic acids and proteins. *Journal of the American Chemical Society*, 106(3):765–784, feb 1984. XIII

[291] Scott J. Weiner, Peter A. Kollman, Dzung T. Nguyen, and David A. Case. An all atom force field for simulations of proteins and nucleic acids. *Journal of Computational Chemistry*, 7(2):230–252, apr 1986.

[292] Wendy D. Cornell, Piotr Cieplak, Christopher I. Bayly, Ian R. Gould, Kenneth M. Merz, David M. Ferguson, David C. Spellmeyer, Thomas Fox, James W. Caldwell, and Peter A. Kollman. A Second Generation Force Field for the Simulation of Proteins, Nucleic Acids, and Organic Molecules. *Journal of the American Chemical Society*, 117(19):5179–5197, may 1995. XIII

[293] George A. Kaminski, Richard A. Friesner, Julian Tirado-Rives, and William L. Jorgensen. Evaluation and reparametrization of the OPLS-AA force field for proteins via comparison with accurate quantum chemical calculations on peptides. *Journal of Physical Chemistry B*, 105(28):6474–6487, 2001. XIII

[294] William L. Jorgensen and Julian Tirado-Rives. Molecular modeling of organic and biomolecular systems usingBOSS andMCPRO. *Journal of Computational Chemistry*, 26(16):1689–1700, dec 2005. XIII